To the Graduate Council:

I am submitting herewith a dissertation written by K. Vasudevan entitled "Transmission Electron Microscopy Study of Phase Transformations in Ternary Ni_4Mo-Based Alloys Containing 0 to 4 Weight Percent Chromium." I have examined the final copy of this dissertation for form and content and recommend that it be accepted in partial fulfillment of the requirements for the degree of Doctor of Philosophy, with a major in Metallurgical Engineering.

E. E. Stansbury

E. E. Stansbury, Major Professor

We have read this dissertation and recommend its acceptance:

C R Brooks

J. E. Spruiell

B. S. Bose

G. M. Stocks

Accepted for the Council:

Vice Provost
and Dean of the Graduate School

TRANSMISSION ELECTRON MICROSCOPY STUDY OF PHASE TRANSFORMATIONS IN TERNARY Ni_4Mo-BASED ALLOYS CONTAINING 0 to 4 WEIGHT PERCENT CHROMIUM

A Dissertation

Presented for the

Doctor of Philosophy

Degree

The University of Tennessee, Knoxville

K. Vasudevan

June 1986

DEDICATION

This dissertation is dedicated to my family members: Appa, Amma, Rama, Nandu, Anuradha, Abhijit, Popsee and Pati. Without their love, support, and encouragement, this graduate education would have been impossible.

ACKNOWLEDGEMENTS

The author would like to express deep gratitude to his major professor, Dr. E. E. Stansbury, for his unceasing guidance, patience, and support through the entire duration of this research.

The financial support provided through research grants by the Cabot Corporation, and through teaching assistantships by the Department of Materials Science and Engineering, University of Tennessee, Knoxville is gratefully acknowledged.

The author would like to deeply thank Dr. C. R. Brooks for many enlightening and helpful discussions.

The help received from Mr. Ted A. Long, head of the departmental electronic shop, and his efficient group: Mr. Stephen A. Stiner, Mr. Michael R. Neal and Mr. Ronald L. Johnson in maintaining the electronic, computer and furnace equipment is deeply appreciated.

Thanks are extended to Mr. H.B. Thompson, head of the departmental machine shop and his amiable group: Mr. Raymond Bellamy, Mr. Jack French, and Mr. Doug Fielden for their help in solving mechanical equipment problems.

Special gratitude is expressed to Mr. Bob L. McGill for his help with the scanning and transmission electron microscope, and to Mr. Albert W. J. Carter and Ms. Aileen Cagle for supplying laboratory materials.

Use of the electron microscopic facilities at the Oak Ridge National Laboratory is appreciated. Special appreciation is expressed to Mr. Jerry Lehman and to Dr. J. A. Horton for their assistance with the electron microscope.

The author is grateful to the ladies of the departmental office: Ms. Sancy Hail, Ms. Betty Frazier, Ms. Phyllis Davis, Ms. Kay Davis, Ms. Inez McDonald, Ms. Phyllis Klindt and Ms. Sue Turner for their goodwill, support and help with official matters.

The author would like to express his deep gratitude to Ms. Damayanti Patel for her support and understanding throughout this research endeavor.

Last but not the least, the author would like to thank his fellow graduate students for their friendship and support, and for providing a congenial work atmosphere.

ABSTRACT

Phase transformations in the binary Ni_4Mo alloy and ternary Ni_4Mo alloys containing 0 to 4 weight percent chromium are reported using electrical resistivity and microhardness measurements, optical, scanning, and transmission electron microscopy (TEM). The transformation behavior was studied by resistivity measurements during continuous heating, cooling, or isothermally in alloys in various initial states. The isothermal transformation behavior was also investigated in alloys aged at 600, 700, 800 and 850°C for times to 4500 hours. Prepared TEM thin foils of the heat treated alloys were examined in detail and the results correlated to changes in resistivity, hardness and optical microstructure.

The resistivity changes associated with short range order (SRO) and long range order (LRO) in Ni_4Mo have been completely characterized. Fast cooling from above the LRO-SRO transition temperature results in retention of SRO with resistivities of 144 and 139 micro-ohm-cm at 25 and -269°C, respectively. The corresponding resistivities of the fully LRO state obtained by slow cooling are 48 and 8 micro-ohm-cm, respectively. Increase in cooling rate within the range permitting LRO, results in an increase in the room temperature resistivity and a decrease in domain size. This increase in resistivity is attributed to the primary influence of a decrease in the degree of LRO with cooling rate. A negative temperature coefficient of resistivity is observed in the SRO state above the critical temperature and is attributed to the interaction between the

change in the degree of SRO with temperature and s-d electron scattering. The slope of the LRO resistivity- temperature curve decreases in the temperature range -150 to 600°C and is attributed to the temperature dependence of s-d electron scattering.

The {111} fcc striations observed in the optical microstructure of ordered Ni_4Mo are intrinsic stacking faults/twins, and are primarily generated by quenching stresses. The presence of these faults is explained on the basis of structural and nearest neighbor bond considerations.

The {110} fcc striations appearing in the optical microstructure of ordered Ni_4Mo are perpendicular twin boundaries. Each striation consists of groups of antiparallel twin-related domains. An atomistic mechanism is proposed for the change in morphology of these striations from tapered at short aging times to straight at longer aging times.

Domain growth in Ni_4Mo can be described by the relationship $D^n = kt$, in a manner parallel to metallurgical grain growth. The value of the exponent n (1/slope of the logD versus logt plot) changes from 2 at 850 and 800°C to 3 at 600°C. This change is attributed to constraints imposed on growing domains by neighboring domains in other orientations. The activation energy for domain growth is obtained as 80 kcal/mole.

A domain coarsening reaction is observed at the grain boundaries on low temperature aging (700 and 600°C) of Ni_4Mo and involves formation of groups of large domains separated by antiphase boundaries (APB's) on low energy {110} fcc planes. The primary driving force for this reaction is the reduction in interfacial energy obtained by

elimination of the APB's between the small intragrain domains. The difference in the degree of order between the coarse and fine domains also provides a contribution, at least initially, whereas ordering strains play a relatively insignificant role.

Resistivity changes associated with ordering in ternary Ni_4Mo-Cr alloys on continuous heating and slow cooling have been explained using TEM. The Ni_4Mo domain size is decreased markedly by addition of chromium. The increase in LRO resistivity to 2.08 wt pct Cr is attributed to the influence of increased electron scattering caused by chromium in solid solution, a decreased degree of LRO, and scattering caused by increased domain boundary area. The high resistivity of the 3.84 wt pct Cr alloy is caused by a completely SRO state. In the 2.08 wt pct Cr alloy, both Ni_2Mo and Ni_3Mo are observed.

The isothermal transformation behavior of ternary Ni_4Mo alloys containing chromium in the range 2 to 4 wt pct aged at 850, 800, 700 and 600^{o}C has been studied. A variety of Mo-rich second phases, such as DO_{22}, Ni_3Mo, Ni_2Mo, and eta-carbides is observed.

Prior grain size plays a significant role in governing the type, volume and distribution of phases. In coarse-grained specimens, a discontinuous precipitation of α and eta-carbides of type Mo_6Ni_6C (that is, $M_{12}C$) is observed on aging at 800 and 850^{o}C. Other than the absence of this reaction in the fine-grained specimens, the types of phases observed in both cases are the same; only the amount of Ni_3Mo is greater in the fine-grained specimens, its formation is seen at shorter times, and the equilibrium state is attained faster.

The Ni_3Mo forms by two mechanisms. One mechanism observed at 850, 800 and 700°C involves direct transformation from bands of DO_{22} aligned parallel to {111} fcc planes. A second mechanism occurs at the grain boundaries on aging at 700 and 600°C, and closely follows the conventional sequence observed at lower temperatures (<800°C) in the binary Ni_3Mo alloy. Large domains of Ni_4Mo form at the grain boundaries. These domains subsequently transform to Ni_3Mo, with the simultaneous presence of stacking faults on (010) Ni_3Mo planes. In contrast to the binary Ni_3Mo, no evidence was obtained for the long period superstructure, $Ni_{3.4}Mo$, during this step.

Composition analyses of the phases has established that chromium predominantly substitutes for the molybdenum in Ni_4Mo-Cr alloys.

At 700°C, the DO_{22} forms from bands composed of Ni_4Mo and Ni_2Mo aligned parallel to {111} fcc planes. The relative stability of the DO_{22} with respect to the Ni_2Mo (ε) is probably associated with the reduction in the V_2/V_1 ratio (ratio of second to first pair interaction energies) caused by substitution of the molybdenum by the chromium.

With increase in chromium content, the phase relationships at equilibrium progressively change from β to $\alpha + \beta + \gamma$ to $\alpha + \gamma$ at 850 and 800°C, and from β to $\beta + \gamma + \varepsilon$ to $\alpha + \gamma$ at 700°C. Isothermal sections at 800 and 850°C of the ternary Ni-Mo-Cr phase diagram near the Ni_4Mo composition have been proposed. With increasing chromium content in the alloy, the compositions of phases in the phase diagram shift toward lower molybdenum and higher chromium; the nickel content remains relatively unchanged.

TABLE OF CONTENTS

CHAPTER		PAGE
I.	INTRODUCTION	1
	General Comments	1
	Nickel-Molybdenum Alloys	2
	Objectives	7
II.	REVIEW OF LITERATURE	9
	Background	9
	Elementary Concept of Order-Disorder	10
	Notations for Ordered Structures	11
	Definitions of Degree of Order	12
	Theory and Mechanism of Ordering	13
	Thermodynamics of Ordering	18
	Experimental Techniques for Order-Disorder Studies	22
	X-ray Diffraction	22
	Thermal Measurements--Specific Heat	23
	Electrical Resistivity	23
	Microscopy	24
	Neutron Diffraction	26
	Mechanical Property Testing	27
	Kinetics of Ordering	27
	The Nickel-Molybdenum System	31
	β Phase--Ni_4Mo	32
	Crystal structure and atomic arrangement	32
	Inter-domain interfaces	38
	APB	38

CHAPTER PAGE

II. (Continued)

APTB 39

PTB 41

Reciprocal lattice and electron diffraction pattern . 42

γ Phase--Ni_3Mo 47

Crystal structure and atomic arrangement 47

Inter-domain interfaces 50

Reciprocal lattice and electron diffraction pattern . 51

δ Phase--NiMo 53

The Metastable Ordered Ni_2Mo Phase 53

The Metastable Ordered DO_{22} Phase 54

The Metastable Long-Period Superstructure $Ni_{3.4}Mo$ (LPAPB) 58

The Ordered Ni_8Mo Phase 58

Short Range Ordered α Phase 62

The K-state effect 62

The nature of SRO in Ni-Mo alloys 65

Clapp-Moss model 69

Microdomain model 69

Cluster model 74

Static concentration wave model 74

Static concentration wave packet model 79

Rationalization of models for SRO in Ni-Mo alloys based on latest experimental evidence 80

CHAPTER PAGE

II. (Continued)

The SRO to LRO Transformation in Ni_4Mo 83
Continuous heating and cooling kinetics 83
Temperature dependence of structural changes during isothermal annealing 89
Effect of cold work on ordering kinetics 94
Transformation mechanisms 95
Correlation with theoretical predictions 97
Ordering in Nickel-Molybdenum Alloys Containing Less than 20 at pct Mo 101
Microstructural Features of Ordered Ni_4Mo 102
General Features 102
The nature of the {111} fcc striations 108
The nature of the {110} fcc striations 110
Domain morphology, growth, and contrast 111
Boundary instabilities 112
Morphology of single ordered Ni_4Mo domains 114
The SRO to LRO Transformation in Ni_3Mo 119
Ordering in Nickel-Molybdenum Ternary Alloys 128
The Ni-Mo-Fe System 128
Continuous Heating and Cooling Kinetics in Ni-Mo-Fe and Ni-Mo-Cr Alloys 131
Isothermal Kinetics of Ordering in Ni_4Mo-Based Ternary Alloys 136
Effect of Vanadium and Niobium 137

CHAPTER PAGE

II. (Continued)

Effect of iron and chromium 138

Effect of chromium at 850°C 142

Effect of chromium at 800°C 142

Effect of chromium at 700°C 142

Effect of chromium at 600°C 145

Effect of iron and chromium on the microstructure . 145

Changes in structure and properties in commercial Ni_4Mo-based alloys 152

Order Strengthening in Ni_4Mo 156

III. EXPERIMENTAL METHODS 164

Alloy Preparation 164

Heat Treatments 166

Optical Metallography, Hardness and Electrical Resistivity Measurements 166

Transmission Electron Microscopy 167

Specimen Preparation 167

Basic considerations 167

Ni-Mo-Cr alloys 170

Observations of Thin Foils 173

Convergent beam electron diffraction (CBED) 174

Thin film x-ray microanalysis 180

IV. RESULTS AND DISCUSSIONS 187

Ordering in Ni_4Mo During Continuous Heating and Cooling . 187

Electrical Resistivity Behavior 187

CHAPTER PAGE

IV. (Continued)

Effect of reheating and rapid quenching on resistivity 191
Electron Microscopy 191
Discussions on Resistivity and Structure 197
SRO resistivity 197
LRO resistivity and structure 201
Ordering in Ni_4Mo During Isothermal Annealing 204
The Nature of the {111} Fcc Striations 205
Rationalization for the existence of the faults/twins based on structural considerations 224
The Nature of the {110} Fcc Striations 230
Mechanisms involved in the straightening of the striations 238
Domain Growth in Ni_4Mo 242
Aging at 850°C 242
Aging at 800°C 243
Aging at 700°C 246
Aging at 600°C 251
Summary of domain size measurements 254
Mechanism of domain growth 257
Domain Coarsening at Grain Boundaries in Ni_4Mo 262
Mechanism and driving force for the domain coarsening reaction 275
Ordering in Ni_4Mo-Cr Alloys During Continuous Heating and Cooling 281

CHAPTER PAGE

IV. (Continued)

Electrical Resistivity 281

Electron Microscopy 283

Ordering in Ni_4Mo-Cr Alloys During Isothermal Annealing . 289

Optical Microscopy 289

Aging at 850°C 290

Aging at 800°C 290

Aging at 700°C 292

Electron Microscopy 295

Identification of grain boundary precipitates in coarse-grained samples 295

Aging at 850°C 306

Aging at 800°C 308

Aging at 700°C 316

Aging at 600°C 336

Composition Analyses of Phases by TEM-EDAX 344

Discussions on the Effect of Chromium on Phase Relationships in Ternary Ni_4Mo-Based Alloys 346

Mechanisms of Transformations 346

Relative Stability of Phases 349

Ternary Ni-Mo-Cr Phase Diagram 354

V. CONCLUSIONS 358

Binary Ni_4Mo 358

Ternary Ni_4Mo-Cr Alloys 360

CHAPTER PAGE

LIST OF REFERENCES 363

APPENDIX 379

VITA 383

LIST OF TABLES

TABLE		PAGE
II-1.	Typical Values of Resistivity of Ni-Mo-Cr Alloys	133
III-1.	Chemical Compositions of Alloys	165
IV-1.	Domain Size as a Function of Aging Temperature and Time in Ni_4Mo	255
IV-2.	Time Required to Attain a Certain Domain Size as a Function of Temperature	258
IV-3.	Chemical Compositions of Phases as a Function of Chromium Content in Alloy and Temperature	345
A-1.	Magnification Calibration of Philips EM300	380
A-1.	Rotation Calibration of Philips EM300	381
A-3.	Camera Constant Calibration of Philips EM300	382

LIST OF FIGURES

FIGURE		PAGE
II-1.	Curves of S as a function of V	16
II-2.	Nickel-rich portion of the nickel-molybdenum phase diagram	33
II-3.	Crystal structure of ordered Ni_4Mo	34
II-4.	Atomic arrangement in the (001) plane of fully ordered Ni_4Mo	36
II-5.	Atomic arrangement in the (001) plane of fully ordered Ni_4Mo	37
II-6.	Atomic models of Ni_4Mo domain boundaries	40
II-7.	Three-dimensional reciprocal lattice representations of ordered Ni_4Mo	43
II-8.	(001) reciprocal lattice representations of ordered Ni_4Mo	44
II-9.	[001] electron diffraction pattern showing APT-related Ni_4Mo superlattice spots	46
II-10.	Crystal structure of ordered Ni_3Mo	48
II-11.	Domain boundaries in ordered Ni_3Mo	50
II-12.	Reciprocal lattice sections of fully ordered Ni_3Mo	52
II-13.	Crystal structure of ordered Ni_2Mo	55
II-14.	Crystal structure of the ordered DO_{22} structure	57
II-15.	Atomic model in the (010) plane of the long-period superstructure $Ni_{3.4}Mo$	59
II-16.	Crystal structure of ordered Ni_8Mo	60

FIGURE PAGE

II-17. Variation of resistivity with cold work in as-quenched Ni_4Mo alloys 64

II-18. Distribution of diffuse x-ray intensity at 86°K in the (h1,h2,0) plane of reciprocal space for Ni_4Mo 67

II-19. (001) reciprocal lattice section and corresponding diffraction pattern of as-quenched Ni_4Mo 71

II-20. Variation of resistivity with temperature on continuous heating and cooling in Ni_4Mo 84

II-21. Resistivity (a) and microhardness (b) as a function of aging time for Ni_4Mo 90

II-22. Isothermal time-temperature-transformation behavior of Ni_4Mo based on resistivity measurements 93

II-23. Diagram of the alloy state and ordering mechanism map in Ni_4Mo 99

II-24. Optical microstructures of ordered Ni_4Mo aged at 850°C . . 105

II-25. Optical microstructures of ordered Ni_4Mo aged at 800°C . . 106

II-26. Optical microstructures of ordered Ni_4Mo aged at 700 and 600°C 107

II-27. The relationship between anti-parallel twins in real and reciprocal space in Ni_4Mo 116

II-28. Bright field micrographs of single Ni_4Mo domains 117

II-29. Ideal three-dimensional model of Ni_4Mo domains with habit planes and perspective sections 118

II-30. Optical microstructures of domain morphology at 850°C . . 120

FIGURE PAGE

II-31. TEM micrographs showing the sequential development of intermediate structures during ordering of Ni_3Mo 123

II-32. Mechanism of ordering of Ni_3Mo 124

II-33. Possible sequence for the shearing mechanism from Ni_4Mo to Ni_3Mo 127

II-34. Isothermal sections of the Ni-Mo-Fe ternary phase diagram 129

II-35. Schematic depiction of the Ni-rich region of the Ni-Mo-Fe phase diagram 130

II-36. Variation of SRO resistivity at 25°C of Ni-Mo-Cr alloys 134

II-37. Variation of resistivity of Ni-Mo-Cr alloys with temperature on slow cooling 135

II-38. Phase present in Ni-Mo-Fe alloys after aging 4500 hrs at 600 and 800°C and 2000 hrs at 700 and 850°C 140

II-39. Effect of iron on kinetics of α-phase transformation in Ni_4Mo-based alloys 141

II-40. Resistivity (a) and microhardness (b) as a function of chromium content in Ni_4Mo alloys 143

II-41. Phases present in Ni-Mo-Cr alloys after aging 4500 hrs at 600, 700, 800 and 850°C 144

II-42. Optical microstructures of the 2.08 wt pct Cr alloy . . . 147

II-43. Optical microstructures of the 3.84 wt pct Cr alloy . . . 148

III-1. Ray diagrams illustrating the formation of convergent beam patterns 176

FIGURE PAGE

III-2. Schematic illustration of the basic principles of conventional and convergent beam electron diffraction . . 177

IV-1. Variation of resistivity with temperature in Ni_4Mo under different indicated conditions 188

IV-2. Variation of resistivity with time at 700°C in Ni_4Mo . . . 192

IV-3. Effect of cooling rate from 950°C on the microstructure of ordered Ni_4Mo 193

IV-4. Effect of reheating on the microstructure of fully ordered Ni_4Mo 195

IV-5. Effect of reheating on the microstructure of fully ordered Ni_4Mo 196

IV-6. SRO $d\rho/dT$ versus temperature 200

IV-7. LRO $d\rho/dT$ versus temperature 203

IV-8. Optical micrographs showing the effect of cooling rate and grain size on the formation of the {111} fcc striations in ordered Ni_4Mo 206

IV-9. TEM micrographs of the {111} fcc striations imaging as twins 208

IV-10. TEM micrographs of the {111} fcc striations imaging as stacking faults 210

IV-11. Illustration of the two possible senses of inclination of a stacking fault 212

IV-12. Schematic diagram to enable determination of whether a stacking fault is intrinsic or extrinsic 214

FIGURE PAGE

IV-13. TEM micrographs of the {111} fcc striations imaging as overlapping stacking faults 216

IV-14. TEM micrographs of the {111} fcc striations showing one-to-one correspondence between overlapping stacking faults and twins 219

IV-15. TEM micrographs of the {111} fcc striations in large domain size Ni_4Mo 220

IV-16. Schematic drawing showing contrast expected from overlapping stacking faults in fcc crystals with $\alpha=2\pi/3$ . . . 222

IV-17. TEM micrographs showing the creation of perpendicular twins when a twin passes through antiphase domains 225

IV-18. The close-packed plane of ordered Ni_4Mo 227

IV-19. The positions of Mo atoms on three successive (111) planes in fully ordered Ni_4Mo 229

IV-20. TEM micrographs of the {110} fcc striations in ordered Ni_4Mo 232

IV-21. TEM micrographs of the domain structure between the {110} fcc striations in Figure IV-20 235

IV-22. TEM micrographs showing the tapered nature of the {110} fcc striations at short times 236

IV-23. TEM micrographs showing the straightening of the {110} fcc striations at longer times 237

IV-24. Schematic idealization of the tapered morphology of the {110} fcc striation 239

FIGURE PAGE

IV-25. Mechanism for the narrowing and straightening of the {110} fcc striation 241

IV-26. Domain growth in Ni_4Mo aged at 850°C 244

IV-27. Domain growth in Ni_4Mo aged at 800°C 247

IV-28. Domain growth in Ni_4Mo aged at 700°C 249

IV-29. Domain growth in Ni_4Mo aged at 600°C 252

IV-30. Log-log plot of domain size, D, against aging time, t, for Ni_4Mo aged at the indicated temperatures 256

IV-31. Plot of $\log(D^n/t)$ against 1/T 259

IV-32. Mechanism for the preferential elimination of APTB's . . . 263

IV-33. Domain coarsening reaction at grain boundaries in Ni_4Mo aged at 700°C 265

IV-34. Domain coarsening reaction at grain boundaries in Ni_4Mo aged at 600°C 268

IV-35. TEM micrographs showing the interaction between the coarsening reaction and annealing twins 272

IV-36. Another example of the domain coarsening reaction at grain boundaries in Ni_4Mo aged at 600°C 274

IV-37. Reciprocal lattice sections identifying the relative locations of different indicated reflections 284

IV-38. TEM micrographs of continuously cooled Ni_4Mo-Cr alloys . . 286

IV-39. Optical micrographs showing effect of grain size on the microstructure of Ni_4Mo-Cr alloys aged at 850°C . . . 291

IV-40. Optical micrographs showing effect of grain size on the microstructure of Ni_4Mo-Cr alloys aged at 800°C . . . 293

FIGURE PAGE

IV-41. Optical micrographs showing effect of grain size on the microstructure of Ni_4Mo-Cr alloys aged at 700°C . . . 294

IV-42. TEM micrographs of the discontinuous precipitation reaction 296

IV-43. Diffraction patterns of the precipitates labelled 1 to 5 in Figure IV-42 298

IV-44. Micrographs showing precipitates on annealing twin boundaries 299

IV-45. TEM micrograph of grain boundary precipitates 301

IV-46. Diffraction and composition analyses of particle A in Figure IV-45 302

IV-47. Diffraction and composition analyses of particle B in Figure IV-45 304

IV-48. Micrographs of the 2.08 wt pct Cr alloy aged at 850°C . . 307

IV-49. Micrographs showing DO_{22} and Ni_3Mo in the 2.08 wt pct Cr alloy aged at 800°C 309

IV-50. Micrographs showing the coexistence of DO_{22} and Ni_3Mo in the 2.08 wt pct Cr alloy aged at 800°C 310

IV-51. Micrographs showing the secondary coarsening reaction of Ni_3Mo at grain boundaries in the 2.08 wt pct Cr alloy aged at 800°C 312

IV-52. Micrographs showing the morphology of Ni_4Mo domains in the 2.08 wt pct Cr alloy aged at 800°C 313

IV-53. Micrographs showing the change in morphology of Ni_4Mo domains in the 2.08 wt pct Cr alloy aged for longer times at 800°C 314

FIGURE PAGE

IV-54. Micrographs illustrating the DO_{22} structure in the 2.97 wt pct Cr alloy aged at 800°C 315

IV-55. Micrographs showing the formation of Ni_3Mo in the 2.97 wt pct Cr alloy aged at 800°C 317

IV-56. Micrographs showing the formation of Ni_3Mo in the 3.84 wt pct Cr alloy aged at 800°C 318

IV-57. [112] SADP of the 2.08 wt pct Cr alloy aged at 700°C for 16 hrs 319

IV-58. Microstructures of the 2.08 wt pct Cr alloy aged at 700°C for intermediate times 321

IV-59. Micrographs showing the morphologies of Ni_4Mo and Ni_2Mo in the 2.08 wt pct Cr alloy aged at 700°C 322

IV-60. Micrographs illustrating the formation mechanism of DO_{22} in the 2.08 wt pct Cr alloy aged at 700°C 327

IV-61. Micrographs illustrating the formation mechanism of Ni_3Mo from DO_{22} in the 2.08 wt pct Cr alloy aged at 700°C . . . 328

IV-62. Micrographs illustrating the formation of Ni_3Mo at grain boundaries in the 2.08 wt pct Cr alloy aged at 700°C . . . 331

IV-63. Microstructures of the 2.97 wt pct Cr alloy aged at 700°C 334

IV-64. Microstructures of the 3.84 wt pct Cr alloy aged at 700°C 337

IV-65. Microstructures of the 2.97 wt pct Cr alloy aged at 600°C 339

FIGURE PAGE

IV-66. Micrographs illustrating the formation of Ni_3Mo at grain boundaries in the 2.97 wt pct Cr alloy aged at 600°C . . . 341

IV-67. Example of stacking faults and APB's in grain boundary Ni_3Mo in the 2.97 wt pct Cr alloy aged at 600°C 343

IV-68. Ground state structures for fcc ordering alloys 351

IV-69. Temperature-composition phase diagrams calculated for three values of the ratio of second to first pairwise interaction parameters (V_2/V_1) 352

IV-70. Isothermal sections of the ternary Ni-Mo-Cr phase diagram near the Ni_4Mo composition 356

CHAPTER I

INTRODUCTION

General Comments

The order-disorder transformation has been the subject of numerous theoretical and experimental investigations since the early part of this century. Many solid solutions undergo long range ordering below a certain critical temperature. In a long range ordered (LRO) state, the component atoms of the alloy system occupy specific sets of sites in the lattice; the arrangement of atoms is regular and long ranged periodic in three dimensions. This type of order generally occurs at simple stoichiometric compositions. In a short range ordered (SRO) state, in contrast, the structure is neither completely random nor long range ordered; rather non-random atomic arrangements occur statistically throughout the lattice.

Our most common encounter with ordered phases is in the form of strengthening precipitates in numerous commercial alloys; γ' in nickel-base superalloys is a prime example. However, there are many other esoteric and less commonly encountered applications where alloys are used in the fully long range ordered condition for one or more positive features associated with the ordering phenomenon itself. Important examples of these can be found in alloys for permanent magnets (Fe-Co, Fe-Al, Fe-Si, Fe-Rh, Co-Pt and the Heusler alloy), electrical contacts (Pd-Cu) and precision potentiometers (Au-Pd-Fe). Hardening associated with ordering has also been used to advantage in alloys for jewelry, dental, chronometric and brazing applications (1).

While ordered alloys possess many attractive properties, widespread commercial exploitation has been complicated by extreme intergranular brittleness. This has, in turn, engendered the notion that the ordering phenomenon is a subject rich in academic and intellectual content, but limited in potential for practical applicability. However, in recent years, significant progress in overcoming the embrittlement problem is causing a reversal of such notions, with the result that commercial viability of ordered alloys is being viewed favorably. This is well demonstrated in experiments showing the beneficial, ductilizing effects of boron in Ni_3Al (2-4). This alloy is a candidate material for high-temperature applications. Judicious alloy design is also being applied to many other ordering alloys such as Fe-Al, Ti-Al and Co-Fe-V. The future for ordered alloys is bright and the day when these become a commercial reality is awaited.

Nickel-Molybdenum Alloys

Nickel-molybdenum alloys, particularly the Ni-20 and Ni-25 at pct Mo compositions, are another class of ordering alloys which have been the subject of interest since the mid 1930's. The Ni-20 at pct (29 wt pct) Mo alloy is well known for its corrosion resistance in non-oxidizing, acid chloride environments (5). This alloy exists as a short range ordered face centered cubic (fcc) structure, α, above $868^{o}C$, but transforms below this temperature to a long range ordered body centered tetragonal (bct) structure, β, (6,7), and exhibits a wide range of physical and mechanical properties which correlate well

with internal structure (8-19). Besides the binary Ni_4Mo alloy, ternary alloys containing iron (8,20), chromium (9,21), silicon (22), aluminum (22), vanadium (23), and niobium (23,24), have also been studied.

Several commercial alloys are closely related to the Ni-20 at pct Mo alloy. The initial commercial alloy, Hastelloy B, contained about 5 wt pct Fe (25), which was sufficient to suppress long range ordering of Ni_4Mo and hence possible low ductility. This decrease in ductility associated with long range ordering of Ni_4Mo has been reported by several investigators (12-18,26,27). Although Hastelloy B was fabricable, problems were encountered with intergranular corrosion caused by precipitation of Mo-rich carbides at the grain boundaries of the heat affected zone during welding (5,28). To restore the corrosion resistance, a solution treatment followed by rapid cooling after welding was required, thus limiting the size of fabricated parts. Subsequent research led to Hastelloy B-2, a low carbon, low iron, low silicon version of Hastelloy B which is supplied quenched from 1066^{o}C to retain the fcc structure (25), and can be used in the as-welded condition. Although alloy B-2 resists grain boundary precipitation of carbides and has excellent corrosion resistance, it can develop decreased ductility if cooled or reheated too slowly, either treatment leading to long-range ordering of Ni_4Mo allowed by the decreased iron content.

Comparison of properties, response to heat treatment and the microstructure of the binary Ni_4Mo alloy (8,9,19) with those of Hastelloy B (28,29) and Hastelloy B-2 (8,30-32) shows that there is a

major effect of third elements on the physical metallurgy and corrosion properties of these alloys. Norem and Stansbury (20) investigated the phase relationships in the Ni-Mo-Fe ternary system, including alloys near and at the Ni_4Mo composition. They observed that about 4 wt pct Fe was sufficient to suppress the ordering transformation and also proposed isothermal sections for the phases present at various temperatures.

Lei (8) carried out a systematic research effort on the influence of iron on phase transformations in Ni_4Mo-based alloys using electrical resistivity, microhardness, optical metallography and scanning and transmission electron microscopy. In agreement with Norem and Stansbury (20), he found that about 4.4 wt pct Fe was sufficient to suppress long range ordering of Ni_4Mo on slow cooling from above the ordering temperature. Vasudevan (9), in studying the effect of 0 - 4 wt pct chromium on transformations in Ni_4Mo-based alloys, using similar techniques, found that about 4 wt pct Cr was sufficient to suppress long range ordering in alloys cooled slowly from above the ordering temperature. Chromium had a somewhat greater effect in slowing down the kinetics of ordering of Ni_4Mo than iron. Increasing iron (8) and chromium (9) contents caused an increase in resistivity, decrease in hardness and decrease in the ordering temperature on continuous cooling. The changes in hardness and resistivity on isothermal aging were dependent on the iron and chromium content and on the temperatures and times of heat treatment, and these measurements were used to pinpoint differences in behavior between the binary and ternary alloys.

The microstructures which result upon ordering in Ni_4Mo (8-10), Ni-Mo-Fe (8) and Ni-Mo-Cr (9) alloys are quite remarkable and complicated. One outstanding aspect characteristic of the optical microstructure of ordered Ni_4Mo is the frequent appearance on etching of a distinct thin, striated, Widmanstatten type structure. Spruiell (33), Lei (8), Vasudevan (9) and Stansbury et al. (10) suggested these were parallel to {111} fcc planes since they formed parallel to annealing twins. In addition, Vasudevan (9) and Stansbury et al. (10) suggested these striations were mechanical twins in an ordered lattice arising due to the stresses generated by the tetragonality of the ordered phase. However, the exact nature of these striations and factors leading to their formation are still not fully clear. The microstructural changes during the ordering of Ni_4Mo are also accompanied by the evolution of a distinct domain structure, together with instabilities at grain and annealing twin boundaries (10). The development of these over extended periods of time need elucidation.

Both iron (8) and chromium (9), cause rather complicated, but similar, changes to the microstructure. Addition of these tends to suppress the formation of the Ni_4Mo phase while simultaneously stabilizing the formation of Ni_3Mo. Even in alloys containing low iron and chromium contents (<1 wt pct), the Ni_3Mo phase was observed on aging for extended times at 850 and 800°C. At 800°C, the relative proportions of Ni_3Mo over Ni_4Mo in the chromium alloys increased with chromium content, eventually leading to no Ni_4Mo at chromium levels beyond 2.08 wt pct. In alloys containing over 2 wt pct Fe or Cr, a discontinuous precipitation of α and NiMo occurred at 800 and 850°C.

At 700°C, similar to the behavior at 800°C, the initial Ni_4Mo structure progressively changed to Ni_3Mo with increase in chromium to 3.84 wt pct. In contrast, some Ni_4Mo was still present at 4500 hours. At chromium levels at the upper end of the range studied, substantial amounts of the fcc α phase were also present together with small amounts of Widmanstatten NiMo. At both 800 and 700°C, the Ni_3Mo formed in two morphologies: namely, thin, Widmanstatten striations and massive, lamellar plates. The formation of the latter morphology was accompanied by further increase in hardness (9).

In this research (9), preliminary phase identification was carried out by SEM-EDAX. Although this technique allows determination of the compositions of phases in a multi-phase microstructure, neither the method nor extent of its use led to conclusive identification of the phases in the alloys under study. One uncertainty was related to the composition of the Mo-rich phase observed at the grain boundaries at the higher temperatures and within the grains at 700°C in the higher chromium alloys. Although it was interpreted as NiMo, the observed variations in composition from very high to moderately high in molybdenum indicated the possible presence of the metastable phase Ni_2Mo. Also, the presence of other metastable phases such as the DO_{22}, reported in ternary Ni_4Mo alloys containing vanadium (28) and in the commercial alloys Hastelloy B (29) and Hastelloy B-2 (31), could not be precluded. Several Widmanstatten precipitates, which appeared at the earlier stages of annealing in the higher chromium alloys at 800 and 700°C as probable precursors of later structures, also remained unidentified.

Major problems arise in determining or even estimating the phases at equilibrium in the Ni_4Mo alloys containing chromium. Although some estimate of the phases that will be present at equilibrium can be obtained by following changes in the microstructure with time, sufficiently accurate compositions of the various phases, which are required to map out the phase diagram, cannot be determined by SEM-EDAX. As a result, Vasudevan (9) was unable to positively identify the observed phases and to establish a ternary Ni-Mo-Cr phase diagram. In contrast, thin film EDAX in the TEM is capable of determining phase compositions within a percent; this technique can be used to advantage for establishing the ternary phase diagram.

Objectives

Despite the considerable progress that has been made towards understanding the physical metallurgy of both Ni_4Mo and Ni_4Mo-based ternary alloys, there remain several features that need better understanding. The areas warranting indepth research are listed below and are the objectives of this dissertation. The majority of the research here is directed towards the application of electron diffraction and transmission and scanning electron microscopy to better understand the optical microstructures, resistivity and hardness of ternary Ni_4Mo- based alloys containing 0 to 4 wt pct chromium. Specific structural features examined are:

1. Extension of electrical resistivity measurements of short range and long range order changes in Ni_4Mo to cover the temperature range of -269 to 1300^{o}C.

2. Examination of the behavior of the resistivity in the vicinity of the ordering temperature of 868°C to determine whether a discontinuous, that is, first order change occurs.
3. Investigation of the long observed negative deviation in the resistivity-temperature curve.
4. Determination if there are significant differences in structural changes when transformations occur during continuous cooling as compared to isothermal conditions.
5. Better understanding of the {111} and {110} fcc striations long observed in the optical microstructure of ordered Ni_4Mo, particularly to investigate a correlation with strain-induced mechanical twinning due to ordering.
6. Correlation of the irregular, progressively enlarging but difficult to etch regions presumed to be ordered Ni_4Mo domains based on optical microscopy with transmission electron microscopy.
7. Better elucidation of domain coarsening reactions at grain boundaries and annealing twin boundaries in Ni_4Mo.
8. Identification of the nucleation and growth morphology of second phases as they develop at increasing chromium contents.

CHAPTER II

REVIEW OF LITERATURE

Background

Order-disorder phenomena have fascinated materials scientists since the early part of this century. The discovery of ordering is generally credited to Tammann (34-37) and Kurkanov and co-workers (38,39). The earliest x-ray diffraction evidence for ordering was obtained by Bain (40,41) in 1923, who observed extra "superlattice" lines in the diffraction patterns of Cu_3Au, and the first analysis of these lines was performed by Johannson and Linde (42) in 1925. Since that time, a prodigious volume of literature in the form of publications, review papers (43-46), chapters in books (47-49), books (50,51) and symposia proceedings (52-54) support the diverse aspects of the order-disorder transformation. Specialized monologues devoted to mechanical properties of ordered alloys (55,56), the application of static concentration wave methods to ordering (57), use of modern analytical tools for order-disorder studies (58) and ordered alloys for high-temperature applications (59) have also appeared.

The earliest review by Nix and Shockley (43) is a scholarly treatise on the theoretical and conceptual aspects of order-disorder and their relationship to thermodynamics. Lipson (44) and Guttmann (45) published more general descriptions providing a balance between theory, concepts and experiment. Muto and Takaji (46) reviewed the statistical thermodynamic theory and the relationship between ordering

and physical properties. The book by Krivoglaz and Smirnov (50) deals exclusively with the theory of order-disorder, and the books edited by Westbrook (51) and Warlimont (52) contain articles on particular aspects of ordering from experts in the field. The major thrust of the symposium proceedings edited by Kear et al. (53) and the most recent one edited by Koch et al. (54) is towards structure-property relationships as they relate to the feasibility of commercial exploitation of ordered alloys.

Elementary Concept of Order-Disorder

A large number of solid solutions become ordered at low temperatures. The process of ordering involves a change from a statistically nearly random distribution of atoms among the atom sites to a more regular arrangement, whereby designated sites are occupied predominantly by one kind of atom. In a disordered alloy of composition AB, for instance, any given atom site is occupied indifferently by either A or B atoms, but on ordering, A and B atoms segregate more or less completely to designated sites, so that the resulting arrangement can be described as a lattice of A atoms interpenetrating a lattice of B atoms. This arrangement is often referred to as a "superlattice" or "superstructure," since ordered structures have larger unit cells (47).

The formation of superlattices, frequently described as long range order (LRO), takes place at relatively low temperatures and usually at compositions expressed by a simple formula such as AB or AB_3, or at compositions near these. At all temperatures above a

certain critical temperature, LRO disappears; when the temperature is lowered through the critical point, LRO is reestablished and increases as the temperature decreases, approaching perfection only at low temperatures. Bragg and Williams (60) were the first to develop a theory for long range ordering, including the temperature dependence.

Short range order (SRO), in contrast, can occur over certain ranges of composition and at temperatures above the LRO critical point; the structure is neither perfectly random nor perfectly ordered. This concept was introduced by Bethe (61) to obtain quantitative agreement with experiment. It is a local deviation from randomness in successive coordination shells about an atom and atoms of a given kind may or may not be related to long range sublattices.

Solid solutions may show SRO without undergoing LRO under any condition. On the other hand, alloys which can LRO, usually show SRO, observable when the LRO is suppressed or when the temperature is above the LRO critical temperature. Short range order, in contrast to long range order, does not have a critical transition temperature, as shown, for example, by Spruiell (33,62) and Chang (63); SRO exists in the Ni_4Mo composition alloy quenched from 1000^{o}C and probably exists up to the melting point.

Notations for Ordered Structures

Since many superstructures have been identified, the literature relating them has adopted symbols referred to as "Strukturbericht" notations (64). Examples of these notations for ordered structures are B2, $L1_2$, $L1_0$, $L2_0$, $D1_a$, DO_3, DO_{19}, DO_{22}, DO_{23} etc. For disordered

solid solutions, the conventional notation for pure metals is used: A1, A2, A3 for fcc, bcc and hcp structures, respectively. However, several superstructures have not been assigned a special name and for these the prototype is specified. For example, Pt_2Mo for Ni_2Cr, Ni_2Mo and Ni_2V, Al_3Ti for Ni_3Ta and Pt_3V, Ni_8Nb for Ni_8V and Ni_8Ta. For more complex superstructures, similar, but different notations are used (58). A more elaborate description of this "Strukturbericht" symbolism can be found in the book by Barrett and Massalski (47).

Definitions of Degree of Order

To quantify the extent of ordering, it is necessary to define one or more order parameters which allow description of atom positions in the crystal lattice. Suppose that in an alloy system A-B, α sites are appropriate for A atoms and β sites are appropriate for B atoms. Let r_α be the probability that an α site is occupied by an A atom and F_A be the fraction of A atoms in the system. Let r_β and F_B hold similar meanings, but for B atoms. Bragg and Williams (60) expressed the long range order parameter as:

$$S = (r_\alpha - F_A)/(1 - F_A) = (r_\beta - F_B)/(1 - F_B) \qquad \text{(II-1)}$$

For complete order, $r_\alpha = r_\beta = 1$, and therefore $S = 1$. For complete disorder, $r_\alpha = F_A$, $r_\beta = F_B$, and $S = 0$.

This definition of order does not, however, take short range order into account. Since the behavior of a pair of atoms taking part in the ordering process is more likely to be influenced by the atoms in the immediate surroundings rather than the distribution of all other atoms in the crystal as assumed by Bragg and Williams (60),

Bethe (61) introduced another parameter based on near-neighbor interactions. This parameter is defined as:

$$\sigma = (q - q_r)/(q_m - q_r) \qquad \text{(II-2)}$$

where, q is the fraction of atom pairs which are unlike, q_m is the maximum value (=1) of q, and q_r is the value for the random alloy. For a completely long range ordered alloy $\sigma = S = 1$ and only one parameter is required, but for a partially ordered alloy, both parameters must be specified (44).

Cowley (65-67) considered interactions between atoms extending beyond nearest neighbors to describe short range order and gave the following expression for a set of short range order parameters (also called Warren-Cowley SRO parameters):

$$\alpha_i = 1 - (n_i/(X_A C_i) \qquad \text{(II-3)}$$

where, C_i is the number of A atoms in the i-th shell about a given B atom, n_i is the average number of A atoms in the i-th shell and X_A is the atomic fraction of A atoms. This parameter can be determined experimentally using diffuse x-ray scattering measurements and provides insight into the structure of short range order (65-67).

Theory and Mechanism of Ordering

In the following, a simplistic view of the theories and mechanisms of ordering is provided. A more detailed exposition of all the different theories is not attempted.

Ordering results from the tendency of atoms to surround themselves with unlike neighbors. Thus, any theory of ordering must be able to explain how the disordered structure transforms to an ordered

one. The only rational explanation is that a few atoms come together and form an ordered arrangement and this predisposes the neighboring atoms to adopt a similar, lower free energy configuration, so that order spreads throughout the crystal (44). It is in this sense that Bragg and Williams (60) referred to ordering as a cooperative phenomenon. Put in other words, when a few atoms join forces to form an orderly arrangement, then disruptive influences such as thermal agitation are further overcome if other atoms follow suit to increase the degree of cooperation.

This cooperational tendency was expressed by Bragg and Williams (60) by ascribing an energy V to the process of interchange of two atoms. It is the energy of the crystal associated with interchanging two unlike atoms to incorrect sites. V depends on S such that it is zero when S is zero and increases as S increases (44). Bragg and Williams (60) assumed a linear relationship between V and S as:

$$V(S) = V_0 S \qquad \text{(II-4)}$$

When $S = 0$, $V = 0$ and when $S = 1$, $V = V_0$. Thus, as soon as any order is established, the internal energy of the crystal is further reduced by extension of the order (44). To obtain better agreement with experiment, Dienes (68) modified this simple expression for the energy to

$$V(S) = V_0(S + S^3/3) \qquad \text{(II-5)}$$

This tendency for ordering is opposed by the action of temperature. Increase in temperature, increases thermal vibrations, which causes atoms to be displaced from right to wrong sites. Thus, a dynamical equilibrium will exist and there will be a characteristic

degree of order for any given temperature. The fact that minimal internal energy is not the only consideration was taken into account by Bragg and Williams (60) by making S dependent on V. Thus, lower the ordering energy, the easier it is for atoms to exchange positions and hence the lower the degree of order. For an AB alloy, the expression relating S and V was derived by Bragg and Williams (60) as:

$$S(V) = \tanh(V/kT) \qquad \text{(II-6)}$$

where, k is the Boltzmann constant and T is temperature. Thus, the simultaneous solutions of the V(S) and S(V) against energy curves establishes the equilibrium degree of order for any given temperature. The point at which the V(S) curve becomes tangential to the S(V) curve gives the critical temperature, T_c (Figure II-1a).

For an A_3B alloy, the expression for S(V) is different and the S(V) versus energy curve shows an inflection. In this case, the intersection point between the V(S) and S(V) versus energy curves which makes the areas on either side and within these two curves equal, establishes the critical temperature (Figure II-1b). Thus, for certain temperatures three solutions are possible. For temperatures below T_c and the lower boundary of the S(V) curve, the disordered phase is metastable relative to the ordered phase, for temperatures above T_c and below the upper boundary of the S(V) curve, the ordered phase is metastable relative to the disordered phase (44). This means that a two-phase field, consisting of the ordered and disordered phases, will be present, at least in the initial stages.

As pointed out earlier, one defect in the Bragg-Williams (60) theory is the assumption that the behavior of a pair of atoms is

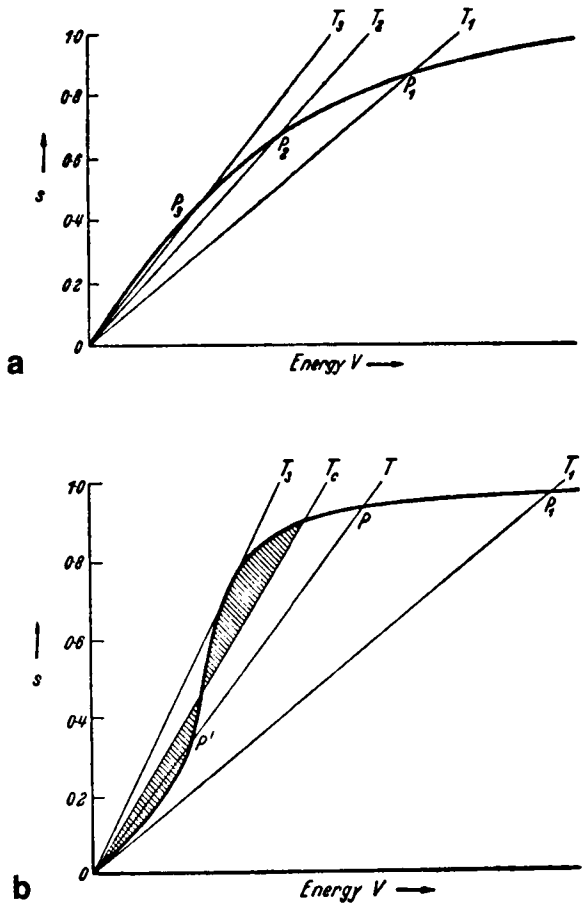


Figure II-1. Curves of S as a function of V. a) AB alloy; b) AB_3 alloy.

Source: H. Lipson, "Order-Disorder Changes in Alloys," Progr. Metal Phys., 2, 1-52 (1950).

governed by that of all the other atoms in the crystal (44). Bethe (61), therefore introduced the concept of short range order and developed a theory based on the more realistic grounds of nearest-neighbor interactions. His results were qualitatively similar to those of Bragg and Williams (60). Both these theories and that of Cowley (65-67) are statistical-mechanical approaches. Later theories such as Kikuchi's (69,70) cluster variation method, and the static concentration wave approach of Landau and Lifshitz (71) and Khachaturyan (57) have also been formulated to explain the ordering process; these have enjoyed a good amount of success. All these theories fall under the realm of classical physics. More recent approaches are based on the "new physics," that is, quantum mechanics (72-76), which involves electronic structure calculations. In this connection, the coherent potential approximation (CPA) has been applied to long range (73) and short range order (74) and the results have been compared to the Bragg-Williams theory (75). One aim of these theories (76) is to calculate the ordering energy from the electronic structure (58).

The nature of forces responsible for ordering has also received attention. The lattice strain theory of Hume-Rothery and Powell (77) and Brillouin Zone theory of Raynor (78) are eminent attempts at explaining these forces. The theory of Hume-Rothery and Powell (77), though qualitative, adequately accounts for many observed phenomena relating to ordering. In particular, it can account for the presence of a superlattice at the Cu_3Au composition and for the absence of one at the Au_3Cu composition. The Brillouin zone theory of Raynor (78),

though quite successful in explaining general structures in metals and alloys, has had limited success in explaining many features associated with ordering (44). The quantum-mechanical or electronic structure approach is directed towards a more fundamental understanding of the ordering phenomenon. Success has already been achieved as demonstrated by the linking of the existence of long-period superstructures to electronic structure (79).

Thermodynamics of Ordering

The order-disorder transition has been treated extensively from the usual thermodynamical standpoint of establishing expressions allowing calculations of the state of lowest energy, which the perfectly ordered state must possess. At sufficiently low temperatures, the contribution to the Helmholtz free energy (F) of the entropy (TS) term relative to the internal energy (E) term is negligible. Hence, the difference in free energy between the two phases, which governs the relative stability, becomes the difference in total energy, and the phase with the lower energy will be the stable one. At higher temperatures, the TS term will provide a greater contribution to the free energy, and the stable state will be the one having greater entropy. The entropy which is of interest here is the configurational entropy, that is, the entropy due to changes in atomic configurations. There is no contribution to the entropy from the ordered phase, since definite kinds of atoms are located at all lattice sites. However, a randomly disordered solid solution will have greater entropy, since there are no preferred sites for atoms. If

short range order is present, then the likelihood of atoms surrounding themselves by unlike neighbors, will tend to decrease the entropy somewhat relative to the random case, but the value will still be higher than that of the ordered phase. At higher temperatures therefore, the stable thermodynamic state will be the state with the greater entropy, that is, the disordered phase (random or short range ordered) (44,45).

It is expected from these considerations that on increasing the temperature, the alloy will progress from a state of perfect order at $0^{o}K$, through states of intermediate order, and eventually to complete disorder, past the critical temperature. The transition at the critical temperature could be smooth or abrupt, which brings up an important point on whether ordering is a First Order or Second Order transformation.

> Phase transformations may be classified in the thermodynamic sense according to the degree of the lowest derivative of the free energy that shows a discontinuity. A transformation is said to be of the first order if the molar free energies are equal at the transformation temperature but the entropies and volumes of the two phases differ, and of the second if the free energies, the entropies, and the volumes are equal but the heat capacities or compressibilities differ (47).

As a result, a first order transformation is characterized by an anomalous latent heat upon transition, whereas a second order transformation is not. The second order transformation also requires identical composition of the two phases. Thus, "a first order transformation appears on a phase diagram as two lines bounding the region where two phases of different compositions coexist in

equilibrium," or in certain cases as a single line, "but a second order transformation appears as a single line" (47). In the context of order-disorder transformations, first order transitions are characterized by a discontinuous change in the long range order parameter, S, from a finite value to zero, second order transitions by continuous variations in S, as the temperature of the system passes beyond T_c.

The question of whether superlattice changes are first or second order thermodynamic transformations has attracted much discussion. In the early stages of order-disorder theory, there was a tendency to regard almost all superlattices as second order transitions (based on the Bragg-Williams theory, 60), but it has become increasingly evident that many of these changes are first order. Insofar as it is possible to generalize from the limited number of types of transitions, it seems that changes from $L2_0$ or DO_3 structures to disordered bcc structures may be second order, and all others first order (45,49). One point in the Bragg-Williams theory which emerges as a consistency with a first order transformation, is the discontinuous drop in the degree of order at T_c for an A_3B alloy, but a gradual decrease for AB alloy (49).

Gibbs (80) pointed out that two types of transformations can occur in physical systems: I) those which are large in degree and small in extent, and II) those which are small in degree and large in extent. Christian (49) named the first type as "heterogeneous transformations" and the second type as "homogeneous transformations."

In Type I transformations, the formation of a superlattice is assumed to be a nucleation and growth process, beginning at discrete centers, and continuing outwards until the disordered regions are consumed (49). Thus, this transformation is characterized by microscopically distinct regions of fully transformed precipitates in the untransformed parent matrix (81). Since the precipitates are independently nucleated, they will not necessarily be in phase and a substructure of antiphase domains may result (49).

In Type II transformations, the reaction is treated as a continuous process of atomic interchange, proceeding simultaneously in all parts of the assembly, and being analogous to a homogeneous chemical reaction (49). No distinct interface exists between the parent and product phases.

The two mechanisms are related to corresponding descriptions of the nature of changes in thermodynamic parameters, a nucleation and growth reaction being more probable if there is a classical first order change, and a homogeneous reaction being more feasible if there is no discontinuity in volume in passing from the disordered to the ordered phase, that is, a second order change. Although the concept of a homogeneous reaction has some plausibility when applied to an order-disorder change, most experimental evidence suggests that superlattices have to be nucleated in the disordered lattice, at least at high temperatures. However, the change in long range order produced by a change of temperature within the region of stability of the superlattice is probably correctly regarded as a homogeneous reaction (49).

Experimental Techniques for Order-Disorder Studies

This section provides a brief review of the relative merits and shortcomings of different experimental techniques.

X-ray Diffraction

The scattering pattern of an incident wave or particle beam is a result of the arrangement of atoms on the lattice sites. An ordered arrangement of atoms will have a different atomic scattering factor and consequently different structure factors and lower symmetry than a random arrangement. As a result, the x-ray diffraction pattern is sensitive to the type and extent of order, which is quantified by measurement of the intensity and scattering angles observed for a given state of order. Thus, an ordered alloy will show besides fundamental lines, extra superlattice lines in the x-ray diffraction pattern. Guthrie and Stansbury (6) studied the ordered Ni_4Mo phase using the x-ray powder technique and confirmed its structure as body centered tetragonal in agreement with Harker's (7) earlier report. By using x-ray diffraction methods, from the width of x-ray reflections, domain sizes together with lattice strains can be calculated and from the integrated intensities of various diffraction lines, the degree of long range order can be determined (82).

The x-ray powder technique is limited in its ability to study short range order. Rather, a special x-ray technique (33,65-67) using a single crystal sample is required for this. Unfortunately, single crystal samples are very difficult to prepare and the experimental process is tedious. However, α_1, the SRO parameter can be determined

by this method (65-67). This was accomplished by Spruiell (33,62) in detail for the Nickel-10 and -20 at pct Mo.

Thermal Measurements--Specific Heat

Although x-ray diffraction gives direct evidence for ordering, it does not provide adequate quantitative measurements for testing theory. This can be achieved by calorimetry, that is, by measuring the specific heat and has been applied to many systems. On heating below the critical temperature, atoms jumping from right to wrong positions will require an increase in energy which is reflected in an increase in specific heat. Quantitative calorimetry yields specific heat (and change in internal energy) which can be related to the degree of order, but this does not help in understanding the atomic arrangement.

Electrical Resistivity

The changes in ordering as a function of temperature and time can also be studied by measuring the variation in electrical resistivity during heating, cooling or isothermal holding. The electrical resistivity of metals can be attributed to the degree of scattering of electrons; the greater the perfection in the periodicity of the lattice, the lower the resistivity. In a metal above $0^{o}K$, one source of scattering is the thermal vibration of the lattice. Since the amplitude of vibration increases with temperature, then electron scattering from this source should increase and therefore electrical resistivity increases with temperature. In disordered alloys, the random atomic arrangement will result in a higher resistivity than that of ordered alloys, because the periodicity of the lattice is

greater in the latter case. This appears always to be true for LRO; however, there may be states of SRO for which scattering is more effective than for a random solid solution and hence the SRO state exhibits the greater resistivity.

The measurement of electrical resistivity lends itself quite gracefully for studying order-disorder transformations. Large differences in resistivity are usually observed between LRO and SRO or random states and measureable differences may exist within both, states of SRO, as well as LRO. Moreover, the precision of the measurement is usually very high and the amount of metal required for specimens is small. Techniques are available to record the resistivity as a function of temperature and time for different heating and cooling rates and to accomplish such measurements on a number of alloys within a short time. Also, it is possible to indirectly relate the resistivity to the degree of long range order and to obtain information on the kinetics. One major drawback of the electrical resistivity technique is its inability to provide information on details relating to the crystal structure and the degree of order.

Microscopy

Many ordering systems have been studied using various microscopical techniques. For example, Newkirk et al. (83), compared optical microstructures of the CoPt alloy with a precipitation reaction. A better simile was suggested by Rudman (84) who compared the microstructure with a recrystallization process, on a qualitative basis. Generally speaking, the structural changes associated with

ordering usually occur on such a fine scale as to necessitate better resolution than that offerred by optical microscopy. Nevertheless, in many cases the finer details agglomerate into coarser structures which become resolvable optically. In such cases, optical microscopy can be used to great advantage to gain an overall, perspective view of the ordering process. In recent years, optical microscopy has been superseded by transmission electron microscopy because of its higher associated resolution and many predicted morphologies viewed directly.

Transmission electron microscopy (TEM) and electron diffraction are powerful techniques for studying order-disorder changes. Direct evidence for ordering, both long range and short range, can be obtained, since both structures give rise to extra spots in the electron diffraction patterns; these spots are sharp in the former, but generally diffuse in the latter. The diffraction patterns can be analyzed easily to deduce crystal structures and atomic arrangements. The degree of order can also be determined from electron diffraction patterns when coupled with a microdensitometer. Although such measurements are not very accurate, semi-quantitative information can be obtained. This barrier has been now overcome by application of modern techniques such as critical voltage effects in convergent beam electron diffraction (CBED) which can provide fairly accurate estimates of the degree of long range order (85). TEM observations can also provide information on whether the ordering is a first or second order transformation (58) and is a valuable tool for testing theories.

Contrast analysis can be used in the TEM to directly observe and analyze various defects such as superdislocations, antiphase domain

boundaries, order twins, stacking faults and others (58). Moreover, the displacement vectors associated with these types of defects can also be determined. One principal advantage of using TEM and electron diffraction over x-ray diffraction is the ease of identification of individual phases in a multiphase microstructure, and that too, on a fine scale. To identify very small second phase particles, CBED can be used (85-87); the composition of the phases can be fairly accurately determined with energy dispersive analysis of x-rays (EDAX) (88). Many modern electron microscopes are designed with these analytical capabilities. Other modern techniques such as high resolution electron microscopy (HREM) can provide direct, tangible information on the distribution of atoms (58). This can be used to study the changes in atomic configurations in the presence of line or planar defects.

Field ion microscopy has also been used in recent years for studying finer details of the ordering process (89-92). However, the preparation of samples for this technique is generally tedious.

Finally, optical microscopy and TEM when used in combination offer the greatest potential for obtaining information on the volume and distribution of phases, the kinetic processes and transformation mechanisms associated with ordering.

Neutron Diffraction

Neutron diffraction can be used effectively to get information on both SRO and LRO. Since the atomic scattering factors for neutrons does not depend on the atomic number, this technique is useful for detecting ordering in systems where the atomic scattering factors of

the two kinds of atoms are so close that their positions cannot be distinguished by x-ray diffraction (58). This technique has been applied successfully to detect ordering in Cu_2ZnNi (93) and Fe-Ni (94) alloys.

Mechanical Property Testing

Mechanical properties such as hardness, tensile strength and ductility change with ordering. These properties are useful for studying the kinetics of ordering and are also important from an industrial standpoint. The hardness test is easy to perform and is the most commonly tested property. However, other tests such as tensile, creep and fatigue are destructive in nature and hence a large quantity of material is required. The usual practice is to perform such tests on samples whose transformation behaviors have been pre-determined by other techniques such as electrical resistivity and microscopy.

Kinetics of Ordering

The parameters S and α_i can be used to describe the long range order and short range order at equilibrium for each temperature. The values of these parameters are not established instantaneously on change of temperature, but are time dependent in response to the diffusive rearrangement of atoms on lattice sites. This time for attaining equilibrium is system dependent, and relates to the usual kinetic factors of the actual temperature and the difference between the actual and the critical temperatures. For example, beta brass is completely ordered after cooling from above the critical temperature,

while Cu_3Au must be held for hours below the critical temperature in order to attain equlibrium.

As early as 1936, Sykes and Evans (95) studied the kinetics of ordering in Cu_3Au and concluded that the process of ordering was complex and took place by nucleation and growth. In the simplest treatment of kinetics three parameters are required to describe the state of the alloy: 1) the fraction of alloy that is ordered, 2) the domain size of the ordered material, and 3) the degree of long range order within the domains (96). To formulate a quantitative theory in terms of a kinetic approach has proved very difficult for a nucleation and growth model because experimentally only one property, namely, a function of all of the above is usually measured. Therefore, most of the earlier theories (68,97-99), notably that of Dienes (68), treated ordering as a homogeneous chemical reaction and derived equations for the homogeneous increase in order.

As pointed out in the preceding paragraph, Dienes (68) applied a simple chemical reaction rate theory to obtain the rate of ordering, dS/dt. On the basis of his theory (68), he could predict two transformation mechanisms: nucleation and growth (first order) and homogeneous or continuous (second order) ordering. For the continuous ordering case, positive values of dS/dt indicated alloy instability for temperatures below the critical temperature, T_c. For the first order transformation, on the other hand, a range of temperatures existed below T_c for which the transformation to the ordered state could not proceed in a homogeneous fashion ($dS/dt < 0$), but had to occur by the formation of ordered nucleii.

Classical nucleation and growth processes are characterized by a C-shaped time-temperature-transformation curve. The reaction rate is governed by a balance of two factors, namely, change in volume free energy (driving force) and diffusion. The transformation times are prolonged near and far below the transformation temperature because of a small driving force in the former and limited diffusion in the latter. As a consequence, a maximum rate (minimum time) for the reaction results, giving rise to the C shape. As pointed out earlier (page 20), most order-disorder transformations evince this behavior. This feature was well demonstrated by Lei (8) for the Ni_4Mo alloy.

The status of the kinetics of ordering was reviewed by Yamuchi and DeFontaine (100). They have pointed out that difficulties exist in evolving a kinetic model because of the inherent nature of ordering. In their words, "the subject presents great conceptual and mathematical difficulties so that a theoretical treatment that is both general and tractable is out of the question." In particular, there is difficulty in a) description of the state of order of a system, b) derivation and solution of partial differential equations of motion for the state of order, and c) the evaluation of fundamental rate constants. To solve the kinetic problem, they determined the time evolution of selected multiple-site probablities using certain simplifying assumptions, and derived a master equation. A nonlinear equation for long range ordering kinetics obtained from the master equation yielded good agreement when compared to the theories of Dienes (68) and Vineyard (98), and to experimental data.

From the results of measured quantities, in almost every ordering system, little doubt remains that the processes involved, regardless of the operative mechanisms, are diffusion controlled. The diffusion coefficients are lower in ordered than in disordered alloys, but since ordering has to be preserved in a superstructure, the normal mechanism of nearest neighbor exchange with vacancies is inapplicable because it is energetically unfavorable (82). Nevertheless, Sato and Kikuchi (101) adopted a path probability technique and considered the kinetics of the order relaxation process to occur via a vacancy mechanism in a manner parallel to atomic diffusion.

In recent years, theoretical attempts have been made to draw an analogy between continuous ordering and spinodal decomposition (102-104). The analytical treatment requires consideration of the discrete crystalline lattice and formulation of a diffusion equation to include a gradient energy contribution to the free energy of the atomistically inhomogeneous alloy. The diffusion equation is then linearized and solved by Fourier techniques to yield expressions for the time dependence of the amplitudes of the Fourier components of harmonic composition waves. The rate of growth is determined by the amplification factor, which appears in the expression for the amplitudes. For order-disorder transformations, d^2G/dX^2 is positive and the coefficient of the gradient energy is negative, implying that the free energy is reduced by the introduction of composition gradients at short wavelengths, which leads to the formation of LRO (105). Ling and Starke (104) used this approach and assumed a periodic composition fluctuation in the disordered state prior to subsequent

ordering. On applying Cahn's (106) earlier established spinodal decomposition relationships to this, they (104) obtained excellent fit of their theory with experimental results for Ni_4Mo, Mg_3Cd, CuAu and Cu_3Au.

X-Ray diffraction measurements have been largely used to determine the variation of the degree of order with time. However, this is possible only for samples quenched to room temperature. Resistivity measurements are useful for studying the kinetics on a continuous basis at elevated temperatures and attempts have been made to relate the resistivity to the degree of order. Muto (107) investigated this theoretically and proposed an equation of the form:

$$\rho = \rho' + \rho''S + \rho'''S^2 \qquad \text{(II-7)}$$

Using the relations $\rho = \rho_{dis}$ at S=0 and $\rho = \rho_{ord}$ at S=1 and further assuming $(d\rho/dS)_{S=0} = 0$, he arrived at

$$(\rho - \rho_{ord})/(\rho_{dis} - \rho_{ord}) = 1 - S^2 \qquad \text{(II-8)}$$

Dienes (108) performed a purely phenomenological analysis of isothermal resistivity of Cu_3Au and obtained an activation energy of 29 Kcal. Further kinetic analysis was done by transforming raw resistivity data into isothermal order parameter-time curves using the above relation; this approach led to an activation energy of 28.5 Kcal which was considered to be in agreement with the value just quoted.

The Nickel-Molybdenum System

Nickel-molybdenum alloys have been studied extensively since the mid 1930's. Quite recently, Brooks et al. (19) have extensively reviewed the current state of understanding of the physical metallurgy

and corrosion properties of these alloys. Four complete phase diagrams have been published. An early extensive report was published by Grube and Schlect (109), who reviewed the previous work of Baar (110), Dreibholz (111), and Koster and Schmidt (112) along with their own work. Subsequent reports were based on research by Ellinger (113), a diagram by Hansen (114) based on analysis of existing data and a more recent diagram by Casselton and Hume-Rothery (115). In the binary system, there are three ordered phases, commonly designated by β, γ, and δ, or respectively ordered Ni_4Mo, Ni_3Mo and NiMo. Throughout this dissertation, these designations will be used interchangeably. Guthrie and Stansbury (7) investigated the nickel-rich portion of this system using x-ray diffraction and optical metallography, and proposed the partial phase diagram shown in Figure II-2. The α phase is a short range ordered nickel-rich terminal solid solution having a face centered cubic (fcc) structure and a lattice expansion of about 0.00033 nm per weight percent molybdenum. A description of the phases occurring in this system is presented in the following.

β Phase--Ni_4Mo

Crystal structure and atomic arrangement. The crystal structure of the ordered Ni_4Mo phase was first determined by Harker (6) and assigned the space group C_{4h}^5 - I 4/m. This phase is often referred to by the "Strukturbericht" notation $D1_a$. The unit cell, which is depicted in Figure II-3, is a body centered tetragonal (bct) superstructure based on the fcc basic structure, with cell dimensions a = 0.5731 nm, c = 0.357,1 nm and c/a = 0.623. There are 2 Mo atoms in

Ni—Mo PHASE DIAGRAM

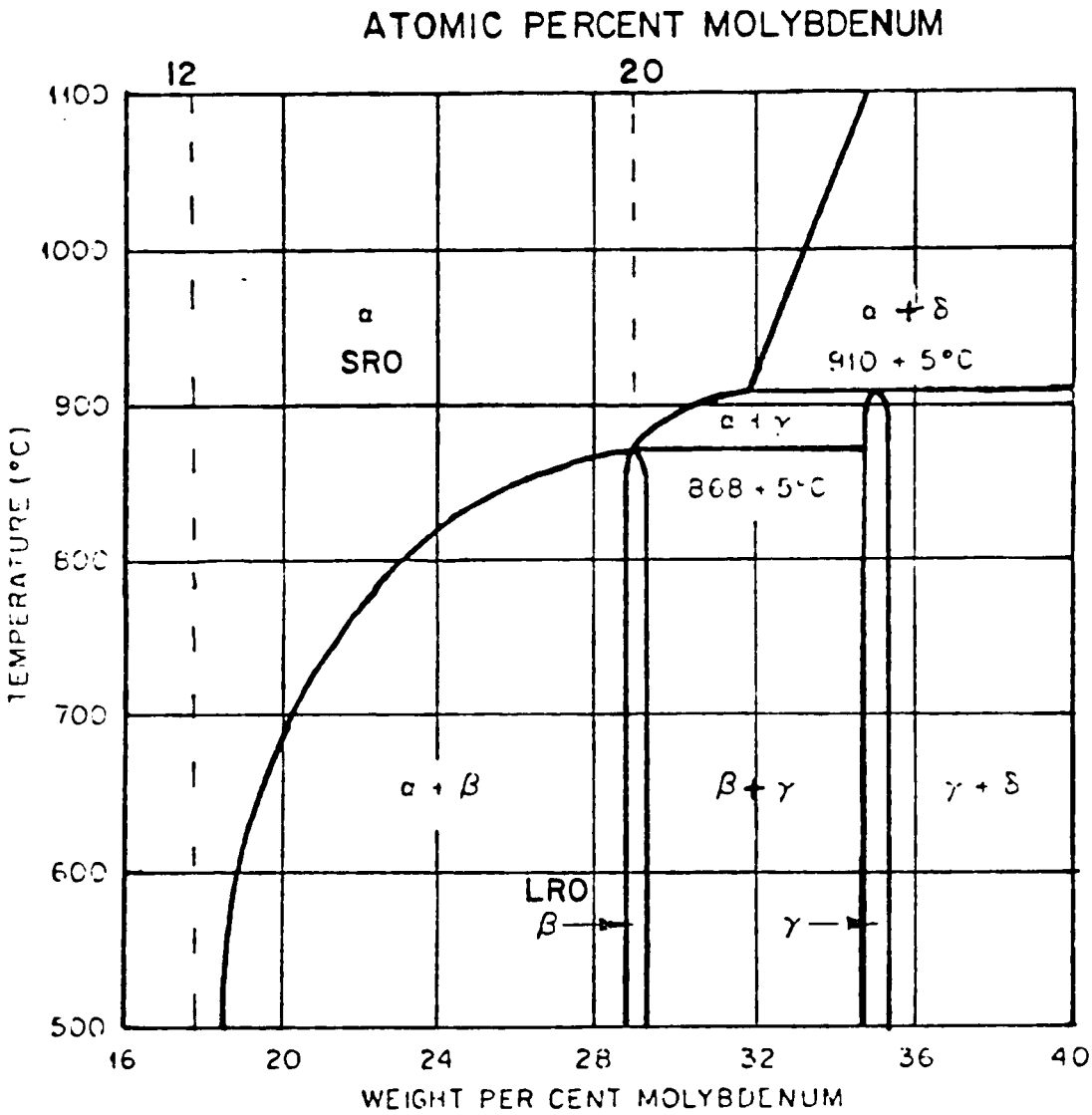


Figure II-2. Nickel-rich portion of the nickel-molybdenum phase diagram.

Source: P. V. Guthrie and E. E. Stansbury, "X-ray and Metallographic Study of the Nickel-Rich Alloys of the Nickel-Molybdenum System," ORNL-3078, Oak Ridge National Laboratory, Oak Ridge, Tennessee (1961).

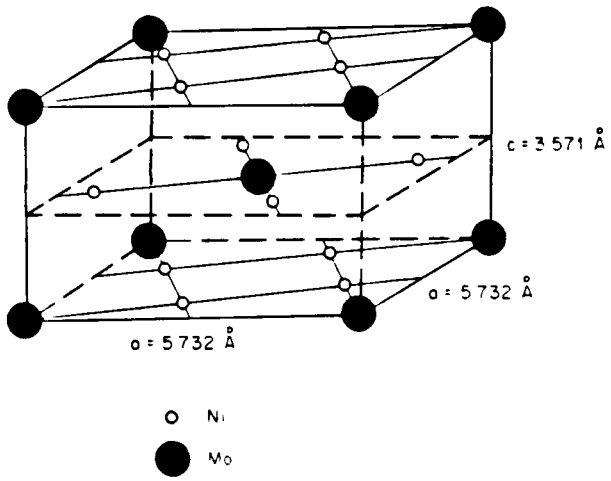


Figure II-3. Crystal structure of ordered Ni_4Mo.

Source: C. R. Brooks, J. E. Spruiell and E. E. Stansbury, "Physical Metallurgy of Nickel-Molybdenum Alloys," Inter. Met. Rev., 29, 210-248 (1984).

2(a) positions and 8 Ni atoms in 8(h) positions with x = 0.200 and y = 0.400. The volume of the ordered tetragonal cell is 2.5 times the volume of the disordered fcc cell. Subsequent researchers have confirmed this (7). Harker (6) and Guthrie and Stansbury (7) showed that the Ni_4Mo phase could be derived from the α phase by the equivalence of ordering of molybdenum atoms and allowing a slight shift in interplanar spacing. This structural model is shown in Figures II-4a, -4b and -5.

On a (001) plane of the fcc lattice, molybdenum atoms on successive [110] rows of atoms are arranged such that they are at the greatest distance from molybdenum atoms on a previous [110] row. When a second (001) plane of atoms is arranged on top of this, the molybdenum atoms occupy positions marked with an X in Figure II-4a. The third layer is arranged exactly as the first one and so on. Guthrie and Stansbury (7) in analyzing their x-ray diffraction data felt that the 20 at pct Mo alloy on aging below T_c first transformed to a face centered tetragonal structure with c/a = 0.986 and subsequently to the body centered tetragonal structure.

There are thirty possible ways for Ni_4Mo to nucleate from a single α lattice (6,7). The c-axis of the tetragonal cell can be any one of the three original cube axes of the fcc cell and the tetragonal a-axis can be inclined positively or negatively to the original cell (Figures II-4b and -5). Finally, each one of the first five atoms in the [110] row could serve equally well as the origin and hence there are 3x2x5 = 30 ways of nucleating Ni_4Mo. Of these, however, only six produce different orientations of Ni_4Mo, each having five starting positions. Each of these variants can result in a unique LRO domain.

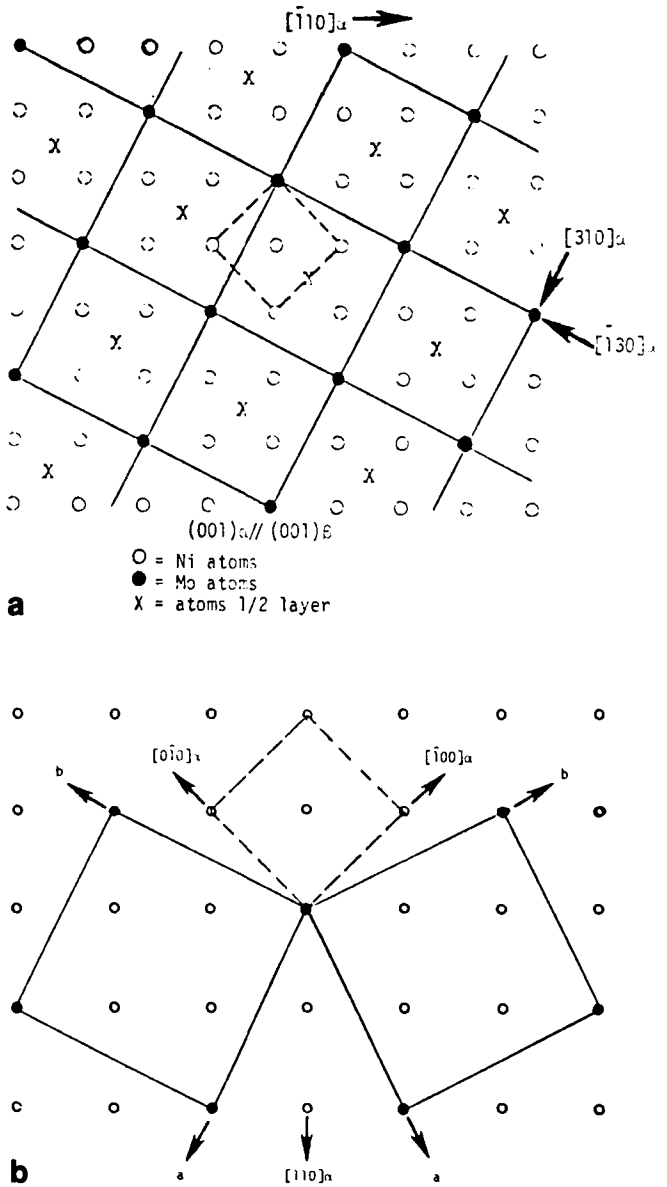


Figure II-4. Atomic arrangement in the (001) plane of fully ordered Ni_4Mo. a) Single domain; b) Anti-parallel twins. $[00\bar{1}]_\alpha // [001]_\beta$. Dashed lines outline fcc cell, solid lines the bct cell.

Source: T. S. Lei, "The Effect of 0-8 Wt.% Iron on Transformations of Alpha Phase Ni-Mo-Fe alloys with Ni:Mo Ratio Equal to 4:1," Ph.D. Dissertation, University of Tennessee (1979).

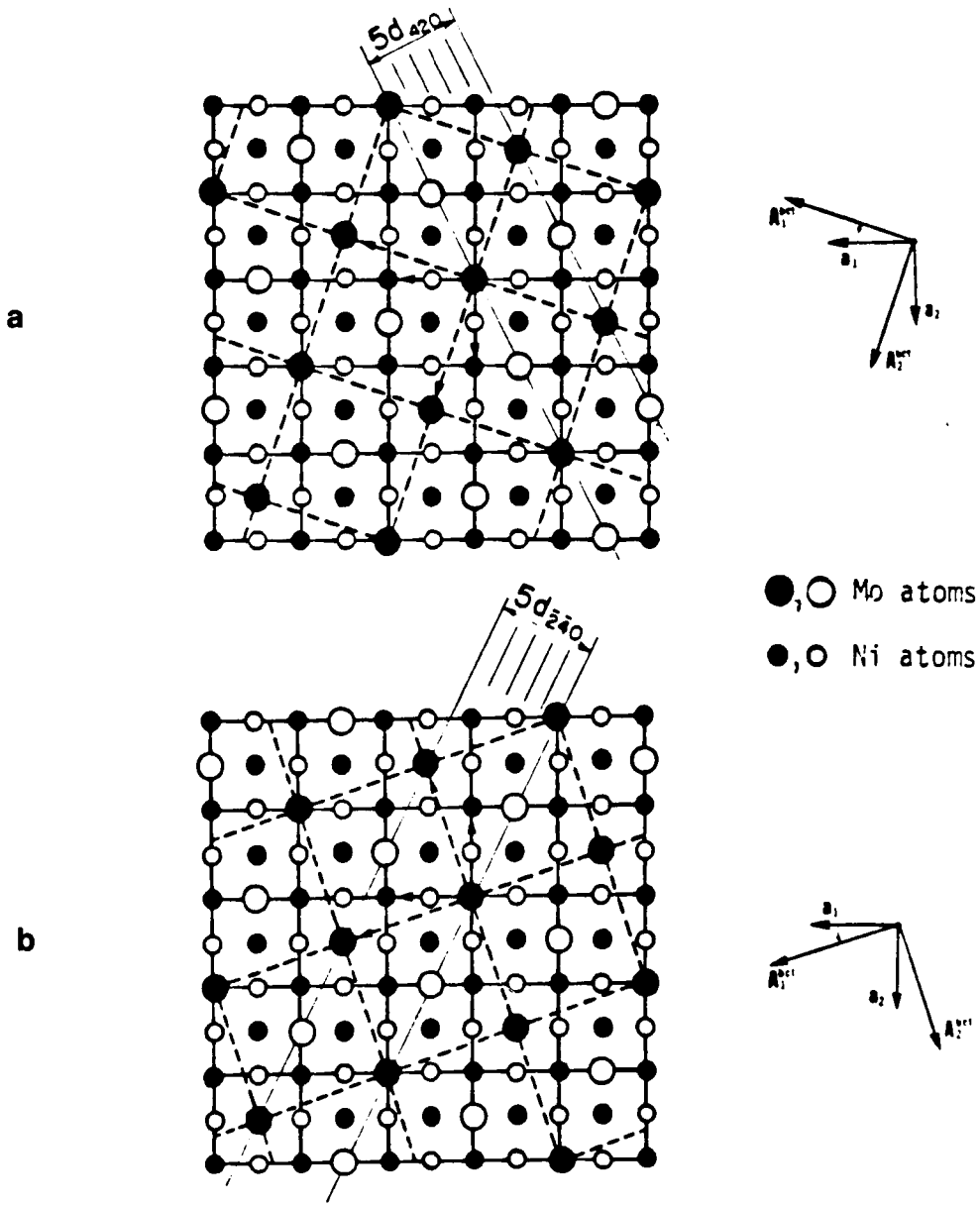


Figure II-5. Atomic arrangement in the (001) plane of fully ordered Ni_4Mo. a) Type I; b) Type II. Solid circles, top layer open circles, 1/2 layer; dashed lines outline bct cell.

Source: P. R. Okamoto and G. Thomas, "On Short Range Order and Microdomains in the Ni_4Mo System," Acta Met., 19, 825-841 (1971).

Okamoto and Thomas (92,116) have shown (Figure II-5) that the two twin orientations, referred to as type I and II structures, can be generated by a regular layering sequence of nickel and molybdenum atoms on the {420} fcc or {101} bct superstructure planes. The type I structure (Figure II-5a) can be generated by stacking on the $(4\bar{2}0)$ or (240) planes in which every fifth plane contains only molybdenum atoms, the intervening four only nickel atoms. The same layering mode on the (420) or $(2\bar{4}0)$ planes will generate the type II structure (Figure II-5b). Similar layering on the remaining mutually orthogonal pairs of planes of type {420} will generate type I or II structures with the c-axis along either the [010] or [100] cube axes. If such layering were to occur normal to each of the 12 {420} planes in different parts of a single crystal, the resulting structure will then be an assembly of domains or transformation twins having one of the six possible orientational variants relative to the parent fcc lattice.

Inter-domain interfaces. Ruedl et al. (117,118) identified three classes of interfaces that can arise due to ordering within a single crystal of the basic structure in Ni_4Mo. These are Anti-Phase Boundary (APB), Anti-Parallel Twin Boundary (APTB), and Perpendicular Twin Boundary (PTB).

APB. If two parts of a crystal can be derived, one from the other, by means of translation defined by a lattice vector of the disordered phase but not the ordered crystal, the interface between these parts is called an APB. The atomic model for this interface is

shown in Figure II-6a. The c-axes are parallel in the two crystals. Since these boundaries can be described by a pure displacement R, one expects α-fringes, that is, stacking fault type fringes in TEM images. The outermost fringes of these types of faults are symmetrical in bright field and asymmetrical in dark field when viewed under two-beam conditions. The displacement vectors R for the APB's can be of four types: $R_1 = 1/5[210]$, $R_2 = 1/5[130]$, $R_3 = 1/10[13\pm5]$, and $R_4 = 1/10[3\bar{1}\pm5]$ and their negatives. The number of fringes (depth periodicity) is inversely proportional to the superlattice extinction distance, which, in turn depends on the degree of long range order. Since nickel and molybdenum have widely different atomic scattering factors, the superlattice extinction distances are expected to be short in fully ordered Ni_4Mo, and therefore the APB's should be characterized by a number of fringes. However, generally, few fringes (upto three) are observed. The electron diffraction pattern is not affected by the presence of APB's except for a fine structure of the spots. The background intensity should be the same in the two domains separated by the APB, and furthermore, the APB fringes will be visible only when a superlattice reflection is excited (117,118).

APTB. An APTB is the name given to the interface that separates two crystal parts for which rows of molybdenum atoms enclose an angle of 2arctg1/3 ($2\times18.43 = 36.86^{o}$). The structures are mirror images, that is, twin related and the c-axes are anti-parallel. The structures can be derived, one from the other, by a rotation, but not by a rotation about the common c-axis. The atomic model for this interface is illustrated in Figure II-6b. The possible coherent APTB planes are

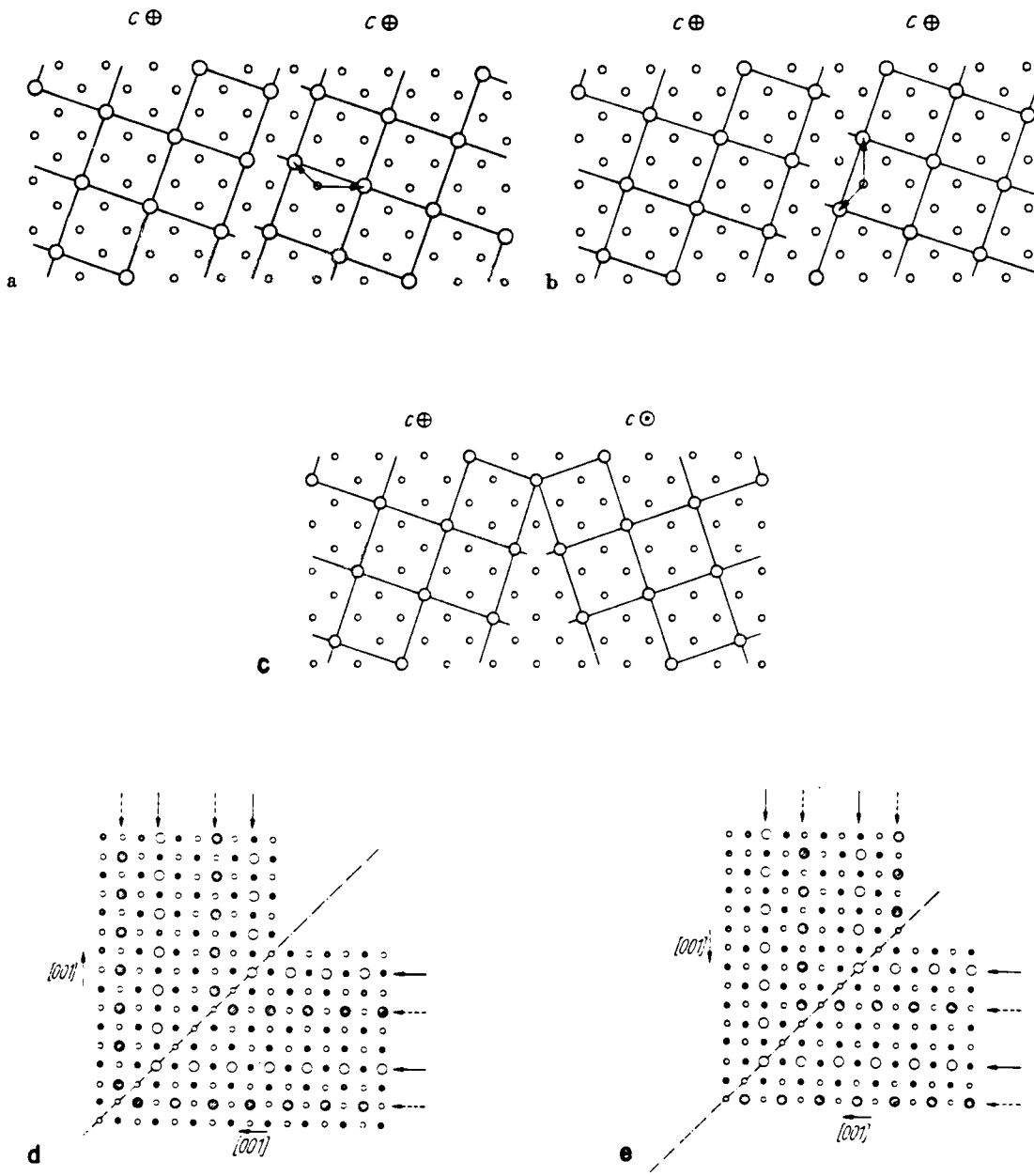


Figure II-6. Atomic models of Ni_4Mo domain boundaries. a), b) Anti-phase boundary; c) Anti-parallel twin boundary; d), e) Perpendicular twin boundary.

Source: E. Ruedl, P. Delavignette and S. Amelinckx, "Electron Diffraction Study of Long- and Short-Range Order in Ni_4Mo," Phys. Stat. Sol., 28, 305-328 (1968).

the (100), (010), (110) and (110) planes. The basic lattices of the two domains across the APTB are continuous. In general, the diffraction conditions for the two APT-related domains will be different, and as a result, the background intensities should be different. Inclined APTB's are characterized by wedge (thickness) type fringes in TEM images. The surface energy of the APTB is higher than that of the APB (117,118).

PTB. A PTB results when the c-axes in adjacent crystal parts are roughly perpendicular. In fact, they enclose an angle of 2arctg(c/a). Because of the slight contraction along the c-axis in the ordered structure, the basic lattice is no longer continuous; slight misorientations will be present on both sides of the interface. The two parts are actually mirror images relative to the coherent twin plane which is of the {101} type as referred to the average fcc structure. The atomic model for this type of interface is shown in Figure II-6c. Due to the misorientation of the basic lattice along the PTB, the deviation parameters (s values) and the operating reflection (g) will be slightly different in the two PT-related domains. As a result, δ-fringes are expected, even when considering diffraction by the fundamental lattice alone. The outermost fringes of the δ-type interface are asymmetrical in bright field and symmetrical in dark field when viewed under two-beam conditions. The depth period depends inversely on the extinction distance of the fundamental reflections, so that a number of fringes are expected. The slight misorientations will give rise to different background intensities in the two crystal parts. Moreover, the diffraction pattern will show spot splitting of

the fundamental spots, because of the slight difference in length and orientation of the two simultaneously operating reflections (g's). For fundamental reflections from planes parallel to the PTB, no contrast will be produced, that is the PTB's will be invisible (that is, g.R = 0). This property can be utilized to determine the the indices of the twin plane and also to confirm the presence of PTB's. All of the above features permit unambiguous identification of the PTB. The surface energy of the PTB is the highest among the three types of interfaces (117,118).

Reciprocal lattice and electron diffraction pattern. The three-dimensional reciprocal lattice containing one variant and all six variants of ordered Ni_4Mo are shown in Figures II-7a and -7b. When the electron beam is parallel to the c-axis, the [001] direction, Figure II-8a is the expected diffraction pattern for a fully ordered single Ni_4Mo domain. Spots on the four corners are the fundamental spots from the fcc matrix and the four other spots are superlattice spots. The spots can be alternatively indexed relative to the tetragonal Ni_4Mo cell as shown in Figure II-8a. When the electron beam lies along the [100] and [010] directions (a and b-axes), only the fundamental diffraction spots will be present; no ordered domains are detected if the beam direction is ninety degrees to the c-axis of the Ni_4Mo superlattice. This is also true for the <110> beam directions. For the <100> planar section passing through the (111) spot with l = 0.5, in general, the superlattice diffraction spots will not show up in the first zone diffraction. However, in case of a thin, extended

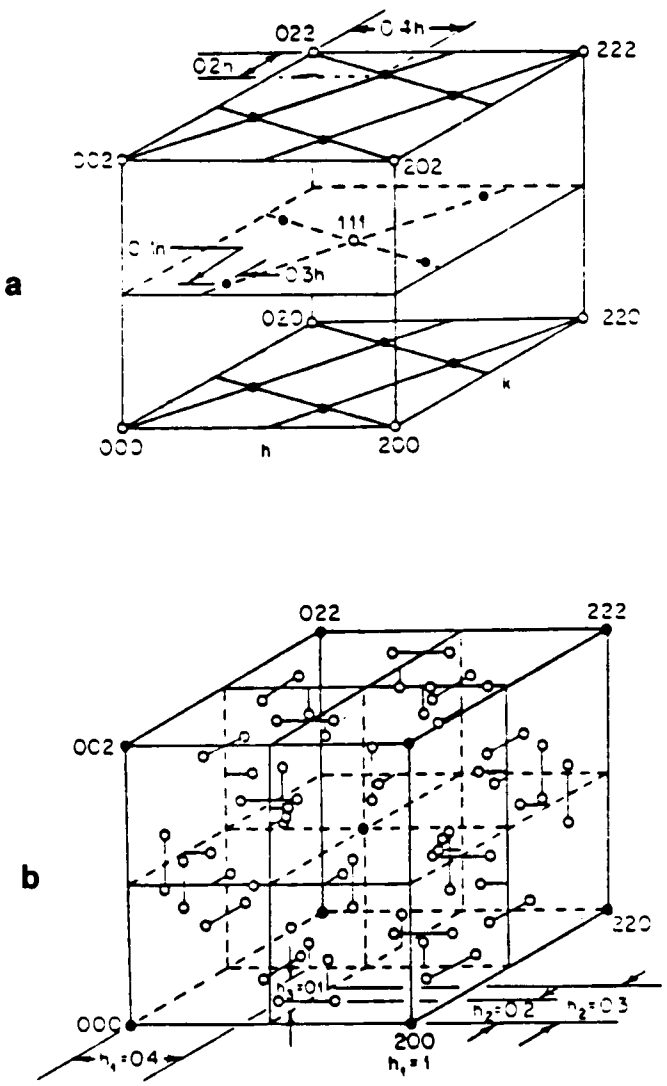


Figure II-7. Three-dimensional reciprocal lattice representations of ordered Ni_4Mo. a). Single variant; b) All six variants.

Source: T. S. Lei, "The Effect of 0-8 Wt.% Iron on Transformations of Alpha Phase Ni-Mo-Fe alloys with Ni:Mo Ratio Equal to 4:1," Ph.D. Dissertation, University of Tennessee (1979).

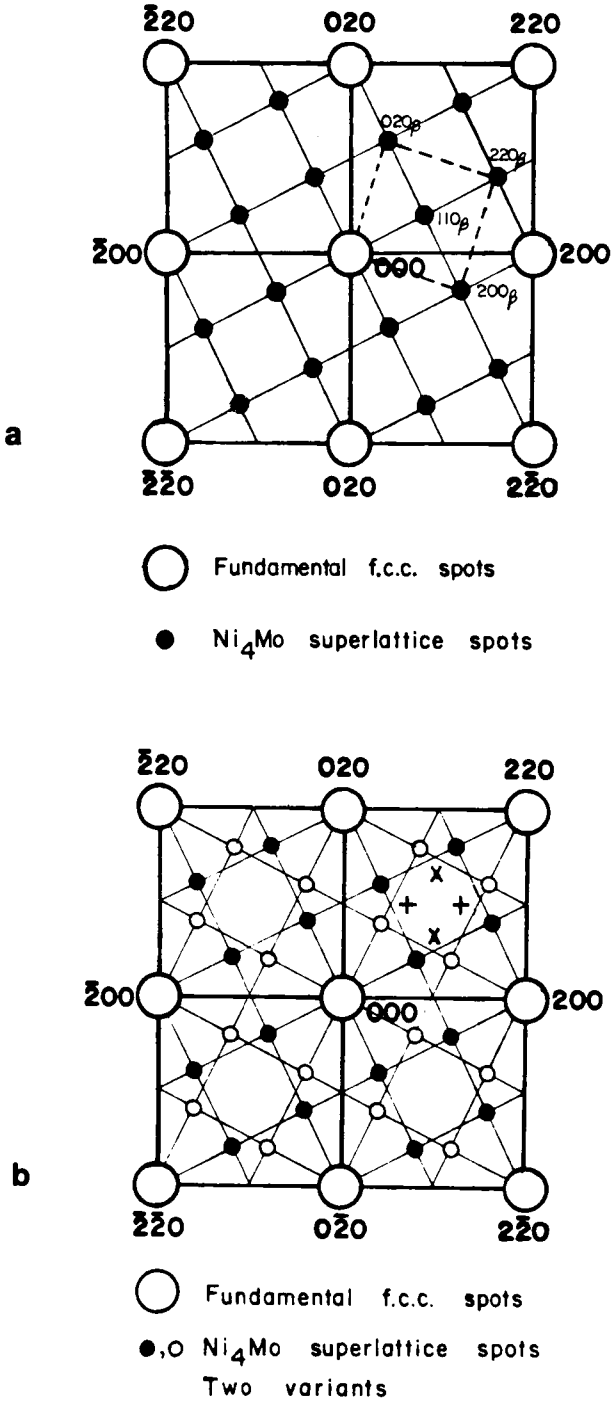


Figure II-8. (001) reciprocal lattice sections of ordered Ni_4Mo. a) One variant; b) Two variants.

single domain, reciprocal lattice spikes from out-of-plane spots may extend far enough to be detected in the first zone diffraction (8).

Figure II-7b depicts the three-dimensional reciprocal lattice for a region covering all the six variants of ordered Ni_4Mo and Figure II-8b shows the expected diffraction pattern when the electron beam is directed along a cube axis of the fcc lattice; again these are indexed relative to the reciprocal lattice of fcc α phase. In a particular cube axis lattice section, superlattice spots from only two variants will be present. The large open circles at the corners are fcc fundamental spots, and the small closed and open circles are superlattice spots from two APT-related orientations having their c-axis along the beam, that is, along the [001] direction. These are spots resulting from the type I and II structures identified in Figure II-5. It is evident from Figure II-8b, that the superlattice spots occur at every 1/5{420} positions, as pointed out by Okamoto and Thomas (92,116). This is a consequence of the occupancy of every fifth (420) plane solely by molybdenum atoms in ordered Ni_4Mo. The "+" and "x" are spots resulting from spiking from out-of-plane domains which have c-axes ninety degrees to the electron beam and their a- and b-axes along the beam direction. Both anti-parallel twins contribute spiking spots at the same locations with no way to distinguish between them in this specially oriented diffraction. However, if the domains are very small in all three dimensions, then there will be no spiking spots at all (8). A [001] electron diffraction pattern for a region containing two APT-related variants reproduced from the work of Ruedl et al. (117) is shown in Figure II-9. The network of faint spots forming an inner square grid are due to double diffraction (117,118).

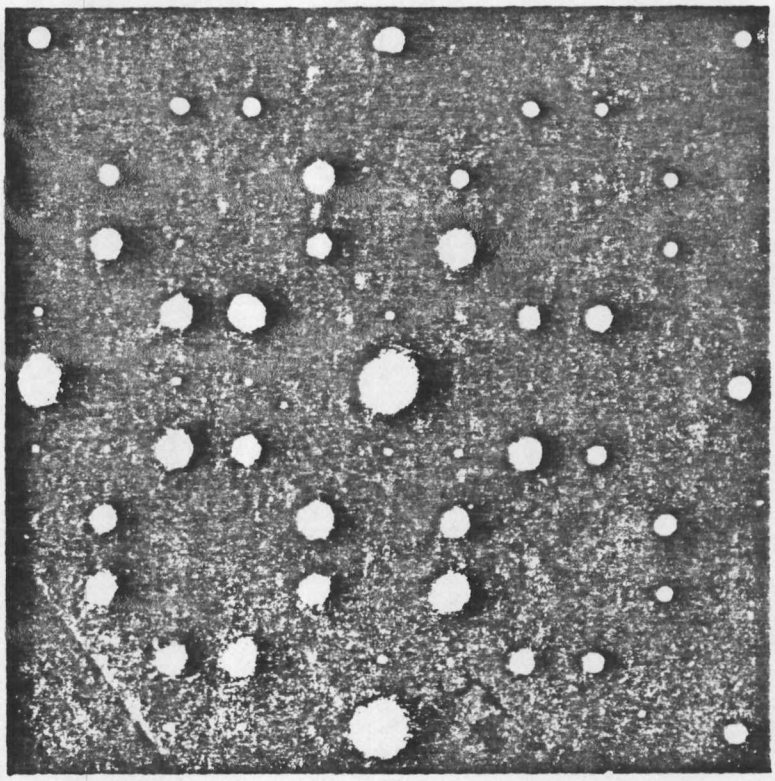


Figure II-9. [001] electron diffraction pattern showing APT-related Ni_4Mo superlattice spots.

Source: E. Ruedl, P. Delavignette and S. Amelinckx, "Electron Diffraction Study of Long- and Short-Range Order in Ni_4Mo," Phys. Stat. Sol., 28, 305-328 (1968).

γ Phase--Ni_3Mo

Crystal structure and atomic arrangement. Saito and Beck (119) first reported that the ordered Ni_3Mo phase has an orthorhombic crystal structure, isotypic with $TiCu_3$, and the space group Pmmm. The unit cell, which is shown in Figure II-10a, contains six nickel and two molybdenum atoms, and has dimensions: a = 0.5064 nm, b = 0.4448 nm and c = 0.4224 nm. This has been confirmed by Ruedl and Amelinckx (120). The relationship between the orthorhombic and hcp structures is also shown in Figure II-10a, and the atomic arrangement on the close-packed plane of ordered Ni_3Mo is illustrated in Figure II-10b. If the orthorhombic distortion (slight relative to the corresponding orthohexagonal cell) is disregarded, the structure may be described in terms of a hexagonal close packed (hcp) cell, stacked in the sequence abab.... (119,120).

The structure can be further built in the hexagonal matrix in three different orientations which differ roughly by 120^{o} (120). The ordered structure can therefore adopt 21 (3x7) different positions within the hexagonal matrix. However, there are twelve possible orientations for the Ni_3Mo superlattice with respect to the fcc α phase since the c face of the Ni_3Mo can assume three orientations and the basal plane of the hexagonal structure can be any one of the four {111} planes of the fcc lattice. Ruedl and Amelinckx (120) showed through TEM studies that the [111] direction of the fcc coincides with the [001] direction of the orthorhombic ordered cell, and the close packed directions in these planes are nearly parallel, suggesting that

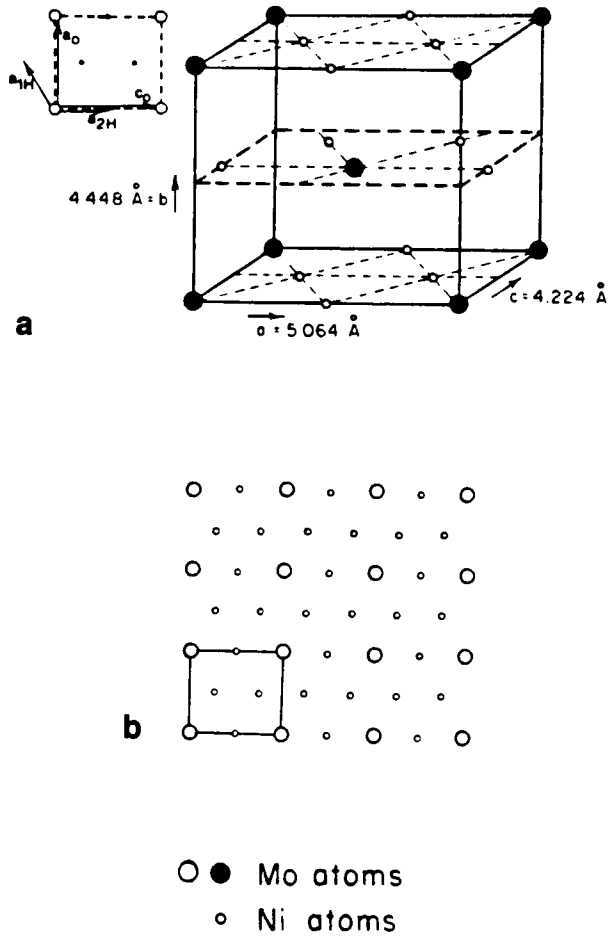


Figure II-10. Crystal structure of ordered Ni_3Mo. a) Orthorhombic unit cell and its relationship to the hcp structure; b) Close packed layer. Large circles denote Mo atoms, small circles Ni atoms.

Source: G. Van Tendeloo, P. Delavignette, R. Gevers and S. Amelinckx, "A Study of Dissociated Antiphase Boundaries in Ni_3Mo," Phys. Stat. Sol. (a), 18, 85-97 (1973).

the transition to Ni_3Mo is a shear transformation along close packed planes. The close packed plane in ordered Ni_3Mo was later stated to be (010) (121) instead of (001), as assumed previously (120).

Inter-domain interfaces. Three different kinds of antiphase boundaries (APB's) occur in ordered Ni_3Mo. The displacement vectors for these are R_1 = 1/4[102], R_2 = 1/2[100] and R_3 = 3/4[102] (120-113), and are illustrated in Figure II-11a; the resulting configuration of the APB's is represented in Figure II-11b. The two domains separated by the APB will exhibit the same background intensity in the TEM. Aside from these thermally produced APB's, another type referred to as non-conservative, dissociated antiphase boundaries also occur during the ordering of Ni_3Mo. These APB's form when there is an excess of molybdenum or nickel atoms, so that the composition deviates from stoichiometric Ni_3Mo; a majority of these boundaries form roughly in the (100) orientation (121).

A second type of domain interface, the twin interface, can also be deduced from structural considerations in ordered Ni_3Mo. As pointed out earlier, the Ni_3Mo structure can be built in the hexagonal matrix in three different orientations approximately differing by 120°C. This gives rise to three twin variants of Ni_3Mo; these can be visualized by looking at the (111) plane of α, which is a close packed plane in the hcp structure (Figure II-11c). The twin interfaces have a strong tendency to be coherent, and the twin planes are of type $(210)_o$ or $(230)_o$ referred to the orthorhombic Ni_3Mo. When inclined, these interfaces will exhibit δ-fringes in TEM images due to the difference

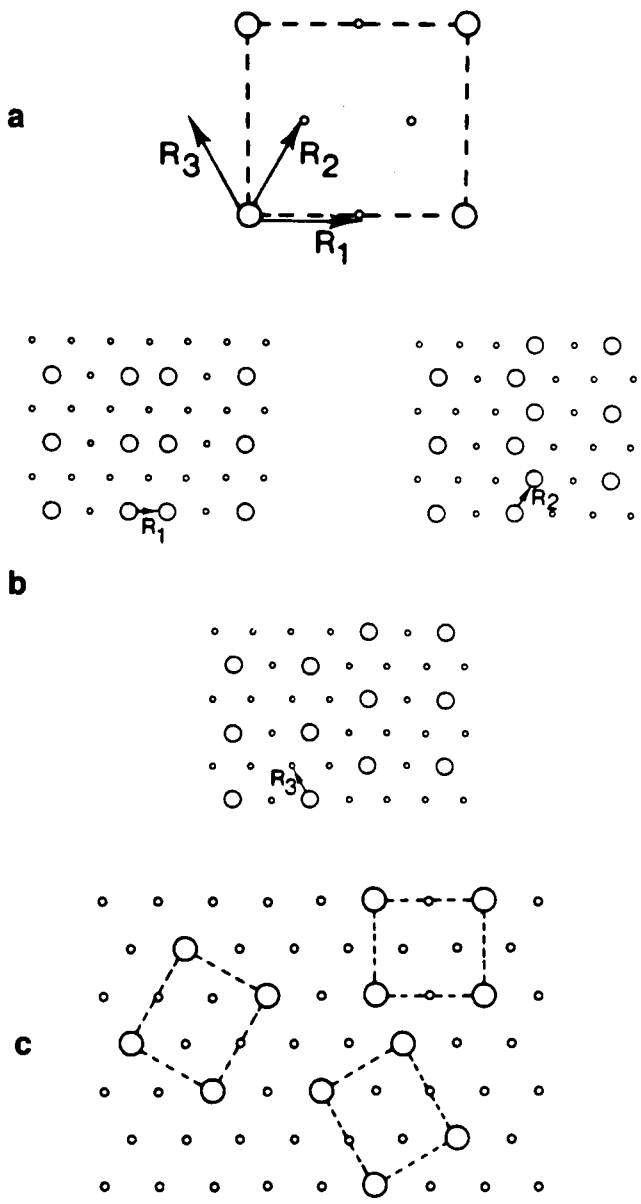


Figure II-11. Domain boundaries in ordered Ni_3Mo. a) Displacement vectors for antiphase boundaries (APB's); b) Configuration of APB's; c) Twin variants of domains.

Source: G. Van Tendeloo, P. Delavignette, R. Gevers and S. Amelinckx, "A Study of Dissociated Antiphase Boundaries in Ni_3Mo," Phys. Stat. Sol. (a), 18, 85-97 (1973).

in orientation of the twinned domains (120). Besides, the above types of domain interfaces, a periodic array of non-conservative anti-phase boundaries with a local excess of Ni atoms characteristic of a long period superstructure, $Ni_{3.4}Mo$, has also been observed during the formation of Ni_3Mo. On continued aging, these periodic APB's coalesce in groups of four to form the APB's characteristic of Ni_3Mo (122,123).

Reciprocal lattice and electron diffraction pattern. The reciprocal lattice sections corresponding to the three orthogonal directions of the orthorhombic Ni_3Mo are illustrated in Figure II-12a. If the electron beam impinges on a single Ni_3Mo variant, and is parallel to either the [001], [100] or [010] Ni_3Mo directions, then the expected diffraction pattern is as shown in Figure II-12a. When all three variants of Ni_3Mo are present, Figure II-12b is the expected diffraction pattern. The large circles denote the fundamental spots, and the closed and open circles respectively denote the Ni_3Mo superlattice and double diffraction spots. Because of double diffraction, the extinction rule that reflections of type (hol) for which $h + 1 = 2n + 1$ be absent, is violated. In the presence of APB's, both fundamental and superlattice spots may show a fine structure in the form of streaking. If more than one twin variant of Ni_3Mo is present, then the fundamental spots will show splitting due to deviations from the hexagonal symmetry (120).

The ordering of Ni_3Mo is quite complicated and takes place in several steps. Metastable phases such as Ni_2Mo (124-129), DO_{22} (127-129), and a long period superstructure, $Ni_{3.4}Mo$ (122,123,127-129)

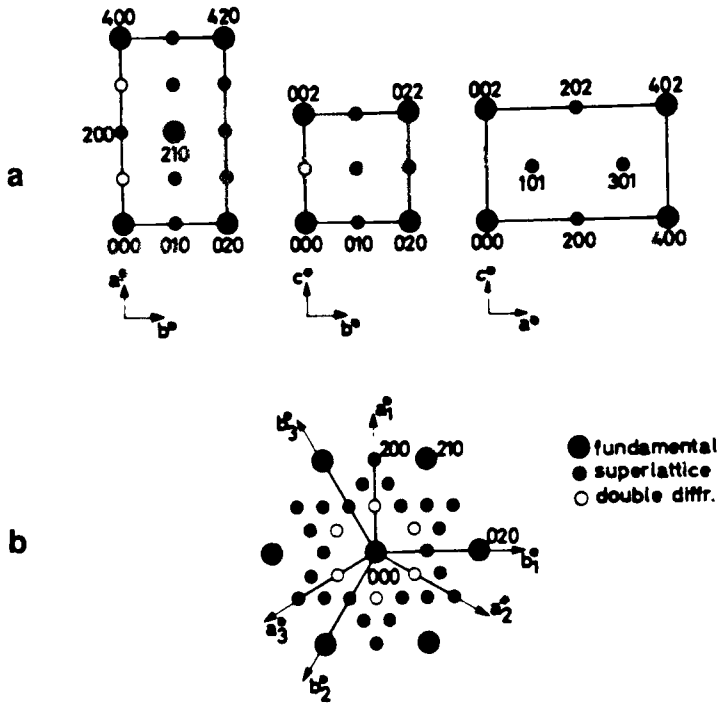


Figure II-12. Reciprocal lattice sections of fully ordered Ni_3Mo. a) (001), (100) and (010) sections; b) (001) section of a region containing three twin variants.

Source: E. Ruedl and S. Amelinckx, "The Substructure of Ni_3Mo due to ordering," Mat. Res. Bull., 4, 361-368 (1969).

have been observed during various stages of the transformation. A short description of these phases is presented later.

δ phase--NiMo

The structure of delta phase was determined by Shoemaker and Shoemaker (130,131) as being orthorhombic with a tetragonal symmetry. Its lattice dimensions are a = b = 0.9108 nm, c = 0.8852 nm. The atomic arrangement of this phase is quite complicated. There are 56 atoms per unit cell and over 600 reflections in the x-ray diffraction pattern (130,131). Very little research has been done on this phase. Guthrie and Stansbury (7) showed that near the α-NiMo phase boundary, the NiMo develops as a precipitation outlining the original α grains, whereas within the two-phase α + NiMo region Ruedl and Amelinckx (120) stated that the NiMo forms as thin platelets parallel to {111} fcc planes. Van Tendeloo and Amelinckx (128,132) studied the domain structure of ordered NiMo using electron diffraction and electron microscopy and observed a remarkable structure consisting of antiphase boundaries, inversion boundaries and permutation twins.

The Metastable Ordered Ni_2Mo Phase

The ordered Ni_2Mo phase is not an equilibrium phase in the nickel-molybdenum system. Its presence was first established by Yamamoto and co-workers (124,125) as a metastable phase during the ordering of Ni_3Mo in quenched Ni-22.7 and 24.4 at pct Mo alloys. This phase has been described as an isotype of ordered Pt_2Mo, having the space group D_{25}^{2h}-Immm and a body centered orthorhombic structure. The exact lattice parameters have not been determined, but can be derived

from the basic fcc unit cell because the Pt_2Mo can be considered as a direct superlattice (126,128,133). These are: $a = a_{fcc}/\sqrt{2}$, $b = 3a_{fcc}/\sqrt{2}$ and $c = a_{fcc}$. The body centered orthorhombic cell is shown by solid lines in Figure II-13a; the dashed lines outline the fcc cell.

Das and Thomas (126) have described this structure by stacking of atoms on either the {420} or {220} fcc planes, where every third plane contains only molybdenum atoms, the intervening two only nickel atoms. This is illustrated in Figure II-13b by the projection of atoms on the (001) plane; the dashed lines outline the orthorhombic Ni_2Mo lattice and the open circles represent the projection of atoms on the a/2 layer. The reciprocal lattice of the structure can be constructed from the original fcc lattice, where the superlattice reflections will appear at every 1/3<220> or 1/3<420> reciprocal lattice vectors. This gives rise to six orientational variants corresponding to six variants of {220} or {420}. A (001) section of the reciprocal lattice is shown in Figure II-13c. The large circles represent the fundamental reflections, whereas the small open and closed circles denote two variants of Ni_2Mo superlattice spots.

The Metastable Ordered DO_{22} Phase

The ordered DO_{22} phase is not a stable phase in the nickel-molybdenum system. This structure was first proposed by Okamoto and Thomas (92,116) to explain the diffraction effects associated with microdomains in the SRO state in nickel-molybdenum alloys. The first experimental evidence for this phase was obtained by Van Tendeloo et al. (127) in an investigation of ordering in the Ni_3Mo composition

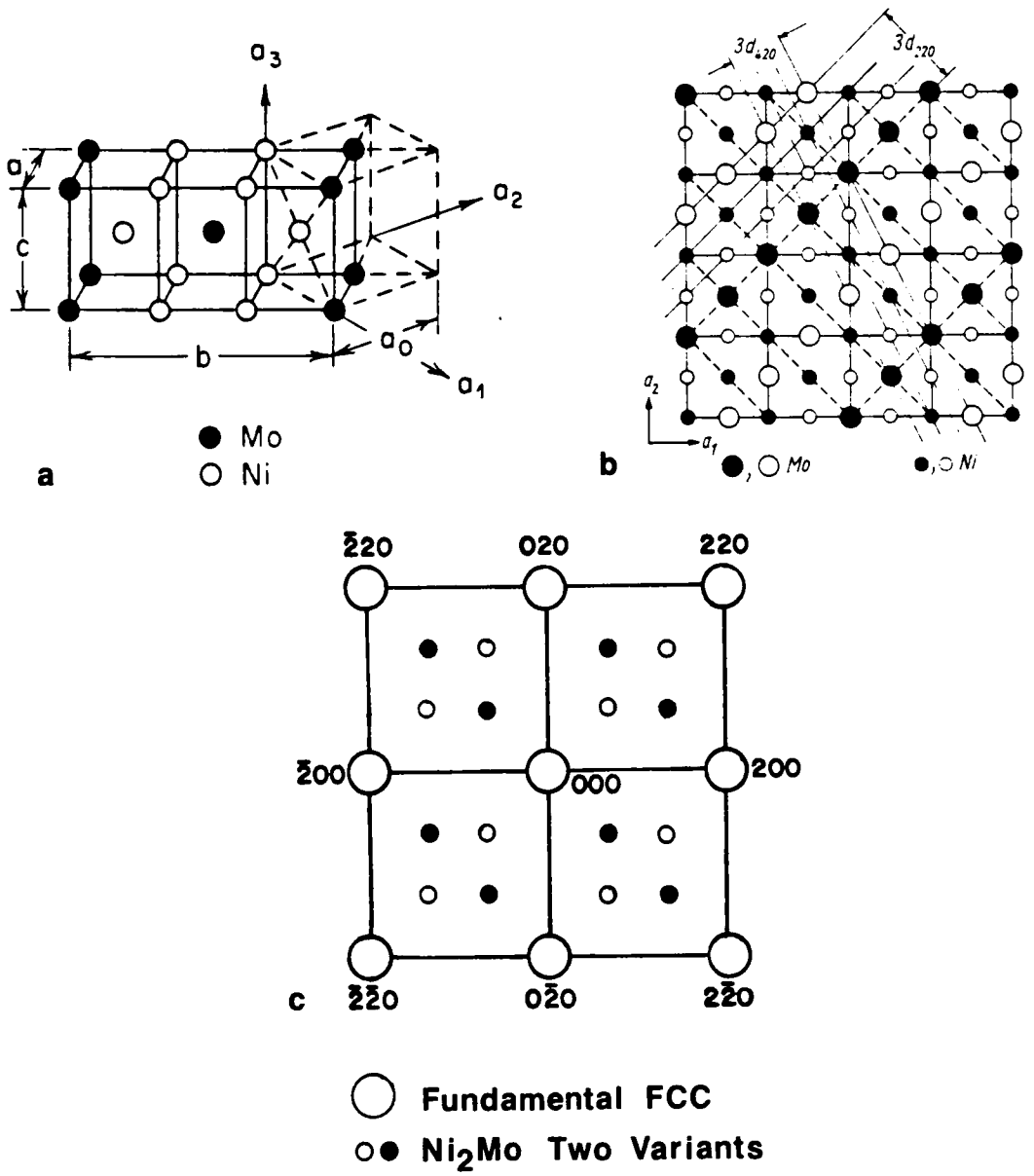


Figure II-13. Crystal structure of ordered Ni_2Mo. a) Orthorhombic unit cell; b) Atomic arrangement in the (001) plane; c) (001) reciprocal lattice section.

Source: S. K. Das and G. Thomas, "The Metastable Phase Ni_2Mo and the Initial Stages of Ordering in Ni-Mo Alloys," Phys. Stat. Sol. (a), 21, 177-190 (1974).

alloy. This phase was observed only under special experimental conditions and was generated immediately from the quenched SRO. Subsequently, the DO_{22} transforms to Ni_4Mo and Ni_2Mo. The DO_{22} is a tetragonal superstructure based on the fcc basic structure, having the composition Ni_3Mo and a cubic stacking of the close packed planes. The unit cell of this structure is illustrated in Figure II-14a, where the large circles represent molybdenum atoms, the small ones nickel.

The structure can be further described in a manner similar to that of Ni_4Mo and Ni_2Mo, by the periodic stacking of pure nickel and pure molybdenum atoms on {420} planes. As pointed out earlier, in Ni_4Mo and Ni_2Mo, respectively four and two nickel planes are followed by a molybdenum plane. In DO_{22}, three nickel planes are followed by a molybdenum plane (92,116,127). This feature can be visualized in Figure II-14b by looking at the atomic arrangement on the (010) fcc plane. The presence of the DO_{22} phase in the microstructure can be easily established by electron diffraction by examining the (001) reciprocal lattice section shown in Figure II-14c. In Figure II-14c, the large circles at the corners are the fundamental fcc spots, whereas the smaller circles at the {100}, {1 1/2 0}, and {110} positions represent the DO_{22} superlattice spots. There are three variants of DO_{22} spots present in this orientation, as indicated. It should be noted that the {1 1/2 0} is also the position of intensity for short range order (33,117,118). Therefore, better discrimination results by examining other orientations in reciprocal space for which reflections from one or more structures are absent, such as the [011]; the SRO and Ni_4Mo reflections are absent for this orientation.

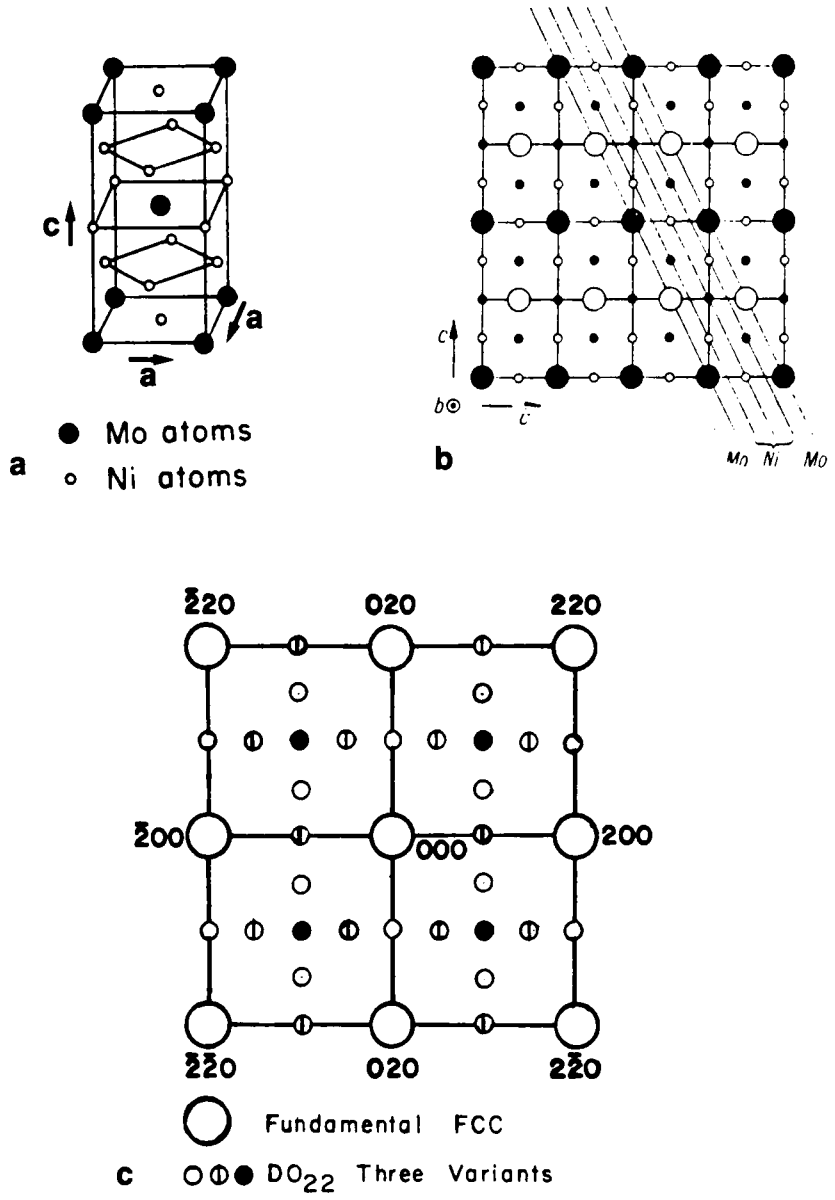


Figure II-14. Crystal structure of the ordered DO_{22} structure. a) Bct unit cell; b) Atomic arrangement in the (010) plane; c) (001) reciprocal lattice section.

Source: G. Van Tendeloo, R. De Ridder and S. Amelinckx, "The DO_{22} Intermediate Structure in the Ni-Mo System," Phys. Stat. Sol. (a), 27, 457-468 (1975).

The Metastable Long Period Superstructure $Ni_{3.4}Mo$ (LPAPB)

Van Tendeloo et al. (122,123) first reported the formation of this phase during the intermediate stages of ordering of Ni_3Mo. The LPAPB structure is characterized by a dense array of periodic non-conservative antiphase boundaries of mean spacing 1.39 nm (122) and composition $Ni_{3.4}Mo$ (123) and forms as an intermediate step to accommodate the shear change from the fcc stacking to the hcp stacking in Ni_3Mo (122,123,127-129). An atomic model on the close packed (010) plane of this structure resulting from the latest research of Schryvers et al. is represented in Figure II-15. The lattice parameters for this superstructure are $a' = 2.78$ nm = 5.5a-Ni_3Mo, $b' = 0.422$ nm = b-Ni_3Mo and $c' = 0.448$ nm = c-Ni_3Mo. Coalescence of the LPAPB's in groups of four, by a hairpin mechanism leads to the equilibrium Ni_3Mo structure (122,123,127-129).

The Ordered Ni_8Mo Phase

Very recently, Mayer and Urban (134) reported a new ordered Ni_8Mo phase in a Ni-11.1 at pct Mo alloy. This ordered phase develops under 1 Mev electron irradiation from the α solid solution and has a critical ordering temperature of $282\pm10^{o}C$ ($555\pm10^{o}K$). The unit cell, which is shown in Figure II-16a, is body-centered tetragonal, contains 16 nickel and 2 molybdenum atoms, and has cell dimensions $a = b = 3a_o/\sqrt{2}$ and $c = a_o$, where a_o is the lattice parameter of the fcc cell. In this unit cell, Figure II-16a, large circles represent molybdenum atoms and the small ones nickel. The atomic arrangement on the (001) fcc plane is shown in Figure II-16b, where the large circles once

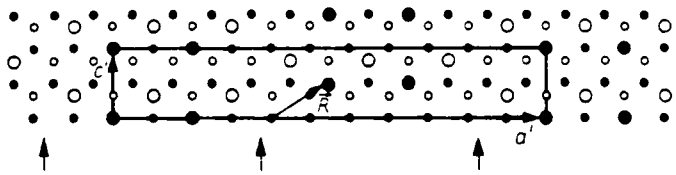


Figure II-15. Atomic model in the (010) plane of the long-period superstructure $Ni_{3.4}Mo$. R = 3/4[102]; a' = 1.39 nm.

Source: D. Schryvers, G. Van Tendeloo and S. Amelinckx, "On the Ordering Mechanism of Ni_3Mo: A High Resolution Electron Microscopy Study," Phys. Stat. Sol. (a), 87, 401-415 (1985).

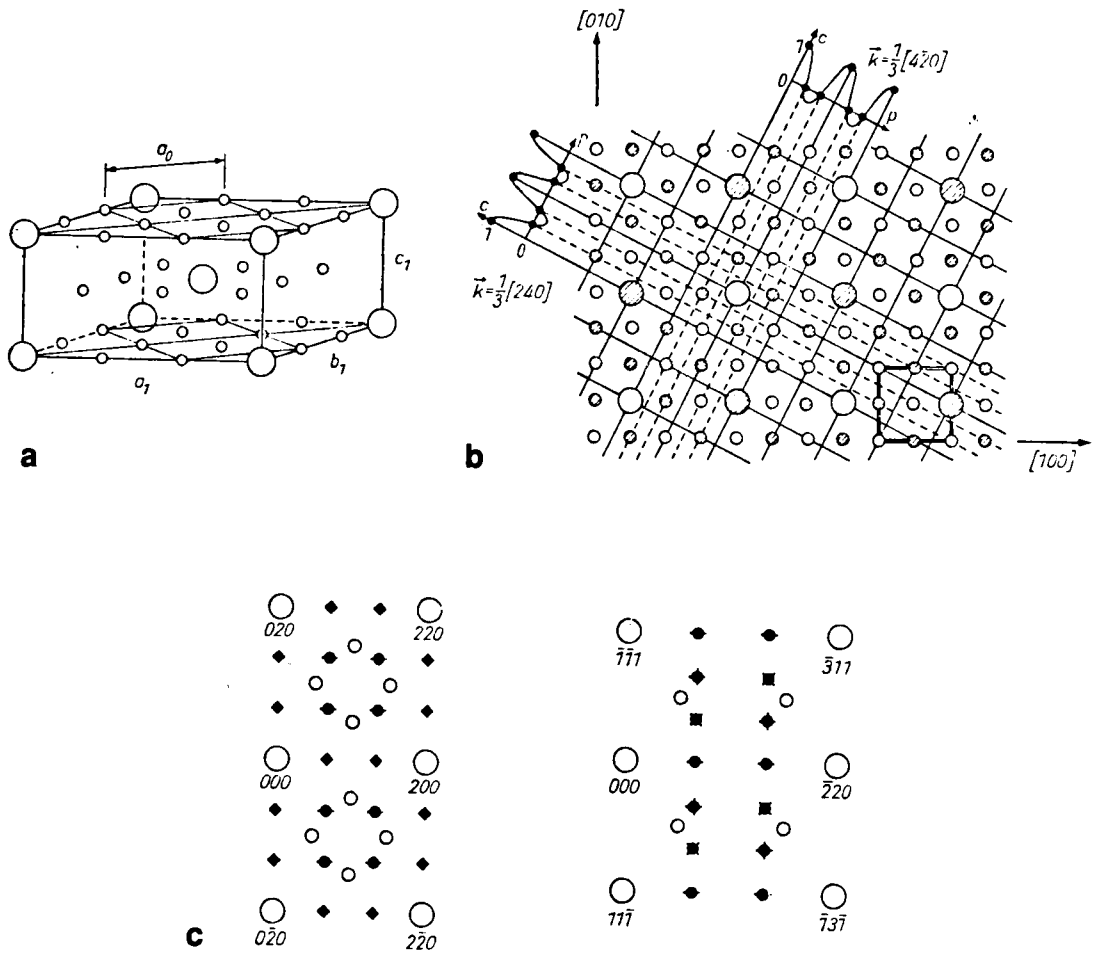


Figure II-16. Crystal structure of ordered Ni_8Mo. a) Bct unit cell; large circles are Mo atoms, small ones nickel; b) Atomic arrangement in the (001) plane; small circles denote Ni atoms, large circles Mo and shaded circles atoms at c/2; the fcc unit cell is shown at right corner; c) (001) and (112) reciprocal lattice sections; large and small open circles respectively denote fundamental and SRO spots; filled circles and squares respectively denote 1/3{420} and 1/3{200} Ni_8Mo spots; three variants of 1/3{420} spots are shown: [001] by dash, [010] by vertical dash, and [100] by inclined cross.

Source: J. Mayer and K. Urban, "Observation of Ni_8Mo Ordered Phase in Ni-Mo Alloys," Phys. Stat. Sol. (a), 90, 469-475 (1985).

again represent molybdenum atoms, the small ones nickel and the shaded circles atoms at the c/2 level. The structure can be further described, in a manner similar to Ni_4Mo, DO_{22} and Ni_2Mo, by the successive stacking of nickel and molybdenum atoms on {420} fcc planes. In contrast, some of the {420} planes contain both nickel and molybdenum atoms (Figure II-16b).

The electron diffraction pattern is characterized by superlattice spots at the 1/3{420} and 1/3{200} positions (Figure II-16c) and high resolution dark field images from the superlattice spots revealed domains with a mean diameter of 10 nm. By regarding the atomic stacking as concentration waves with wave vectors of the type 1/3{420}, and modulating two such waves (0 and 1 in Figure II-16b), they showed that this leads to additional (100) and (010) periodicities, which, in turn, gives rise to three orientational variants for ordered domains. Superlattice spots corresponding to these three variants, together with the {1 1/2 0} SRO reflections, are also indicated in the (001) and (112) reciprocal lattice sections in Figure II-16c. It should be noted in Figure II-16c that the 1/3{420} is also the position for Ni_2Mo reflections.

Mayer and Urban (134) explained these results on the basis of radiation-enhanced ordering and argued that ordered Ni_8Mo was an equilibrium phase. They further stated that since this phase is stable over a temperature range ($<282^{o}C$) too low for thermal heat treatments, the production of non-equilibrium defects by irradiation are required to accelerate the atomic diffusion necessary for formation. They also argued that radiation-induced phase formation depends critically on

defect production rates, since the substantial deviations from equilibrium, which can be caused only by high defect production rates, are counteracted by a thermodynamic driving force. Since the critical temperature for ordering remained unaffected over a wide range of defect production rates, they concluded that the system was at equilibrium. Furthermore, the abrupt appearance of sharp and intense superlattice reflections coupled with simultaneous formation of ordered domains, on cooling below T_c, was taken as evidence for a first order, that is, a nuleation and growth transition.

In light of these results (134), whether the nickel-molybdenum phase diagram warrants reevaluations in the low-temperature, low-molybdenum regime depends on establishing positively by other means that the ordered Ni_8Mo is an equilibrium phase.

Short Range Ordered α Phase

The α phase is a nickel-rich terminal solid solution with a face centered cubic (fcc) structure having a lattice expansion of 0.00033 nm per wt pct Mo (7). The lattice parameter of the Ni_4Mo composition alloy is 0.3608 nm. This phase manifests a temperature-dependent SRO, similar to many nickel base solid solution systems such as nickel-chromium, nickel-vanadium and nickel-tungsten. This phase also exhibits a resistivity anomaly known as the "K-State".

The K-state effect. The K-State was first proposed by Thomas (135), who studied alloys of nickel-chromium, nickel-copper, nickel-aluminum etc. Upon annealing previously cold worked specimens, he found an anomalous increase in resistivity over a certain

temperature range. Also specimens which had been well annealed to develop the K-State, showed a decrease in resistivity on subsequent cold working. These effects are opposite to those found in normal alloys.

Besides resistivity, other properties such as elastic modulus, tensile strength (136), hardness (137), thermal expansion (138), and specific heat (139), have been shown to behave anomalously with the formation of a K-State.

The K-State has been investigated by resistivity measurements by Baer (140), Lampe (141) and Chang (63). They observed changes in resistivity near 500^{o}C. These changes were very much heating rate dependent; higher the heating rate, lower was the resistivity (63). Stansbury et al. (139) in calorimetric experiments on a Ni-14 at pct Mo alloy, found anomalous behavior in specific heat at 500^{o}C. Lefevre et al. (142) investigated nickel-molybdenum alloys containing 10.5 and 14 at pct Mo and on the basis of x-ray and resistivity measurements concluded that the K-State was dependent on the degree of SRO in water-quenched alloys. Lei (8), Vasudevan (9) and Lei et al. (11) found that resistivity in Ni_4Mo alloys, decreases with an increase in cold work as shown in Figure II-17. Also alloys containing iron and chromium had lower values of resistivity than the binary Ni_4Mo. In addition, Vasudevan (9) and Lei et al. (11) observed that cold work beyond 68% RA resulted in an increase in resistivity (Figure II-17).

The explanations of the K-State phenomenon vary and depend on the particular alloy. Several theories have been advanced to explain the decrease in resistivity with cold work on the basis of changes in

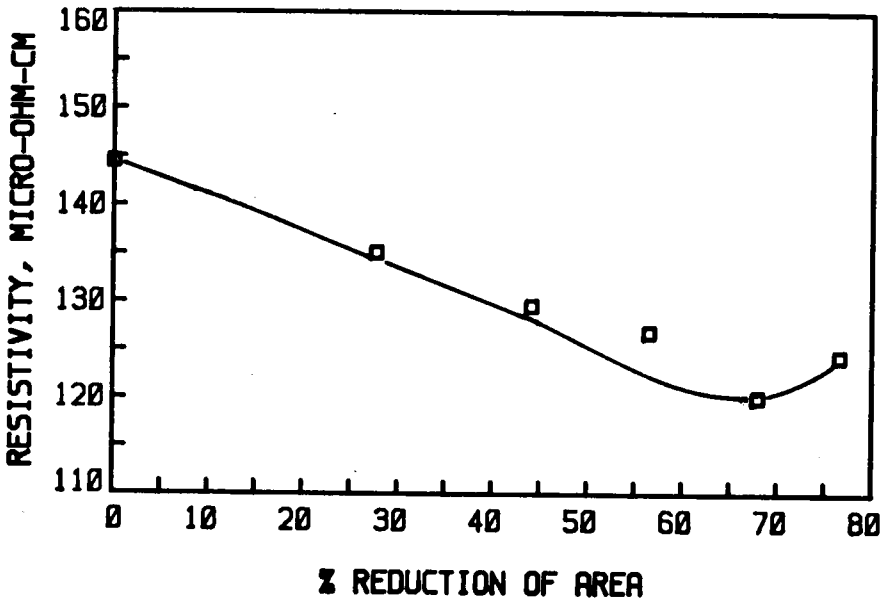


Figure II-17. Variation of resistivity with cold work in as-quenched Ni_4Mo alloys.

Source: K. Vasudevan, "The Effect of 0-4 Wt Pct Chromium on Transformations of Alpha Phase Ni-Mo-Cr Alloys with Ni:Mo Atom Ratio Equal to 4:1," M.S. Thesis, University of Tennessee (1982).

the electronic configuration of the alloy as a result of lattice distortions (143,144). It is generally agreed (8,9,11,63,142), that in nickel-molybdenum alloys the decrease in resistivity with cold work is due to a decrease in SRO in cold worked alloys. Also the further decrease in resistivity in non-LRO alloys of 4Ni:Mo ratio, but containing iron was explained by Lei (8) to be due to decreased SRO existing in alloys containing iron. The same explanation was given by Vasudevan (9) for the effect of chromium. The increase in resistivity beyond 68% RA in Ni_4Mo and in alloys containing chromium was attributed to the increased defect concentration becoming more effective in increasing the resistivity than the decrease in the degree of SRO is in decreasing it (9,11).

Although it is widely agreed that SRO is responsible for the K-State, it is not clear how this might increase resisitivity. Since most of the K-State alloys contain at least one transition element, significance has been frequently attached to the presence of an unfilled d-shell (135,145). Others have explained the increase in resistivity by picturing the SRO as microdomains (146), or at least non-random atom configurations providing more effective electron scattering than for the random solid solution. These explanations, however, are complicated by the fact that SRO increases resistivity in some systems (147), but decreases it in others (148).

The nature of SRO in Ni-Mo alloys. The nature of SRO in nickel-molybdenum alloys has attracted widespread attention. Numerous techniques such as x-ray diffraction (33,62,149), transmission

electron microscopy (92,116-118,124-129,150-151), and field-ion microscopy (89,92,162-156) have been applied to understand the nature of the SRO state in nickel-molybdenum alloys. The road towards understanding the nature of the SRO state is long and tortuous. In the discussion that follows, an attempt is made to maintain a historical perspective by presenting, as far as possible, the chronological sequence of events leading to the ultimate description of the nature of the SRO state in nickel-molybdenum alloys.

Spruiell and Stansbury (33,62) were the first to study local atomic arrangements in the SRO state by measuring the diffuse intensity in the $(h_1,h_2,0)$ plane of reciprocal space for single crystals of nickel-rich alloys containing 10.7 and 20 at pct Mo after varied thermal history. As shown in Figure II-18a, they observed diffuse intensity maxima at the {1 1/2 0} positions in reciprocal space, which was taken as evidence for SRO. This was observed in both alloys quenched from 900°C and 1000°C. Also, the degree of SRO, as deduced from the intensity data, was greater in samples quenched from 900°C.

Reheating the Ni-10.7 at pct Mo alloy near 479°C after quenching from 1000°C resulted in a sharpening of the diffuse intensity distribution corresponding to an increase in the degree of order. A 30 minute heat treatment of the Ni-20 at pct Mo alloy near 650°C caused the SRO peaks observed in the as-quenched samples to split into peaks located near the positions of the superlattice reflections for the long range ordered Ni_4Mo (Figure II-18b). Atomic models for the SRO state having no Mo-Mo nearest neighbor tendency were constructed based

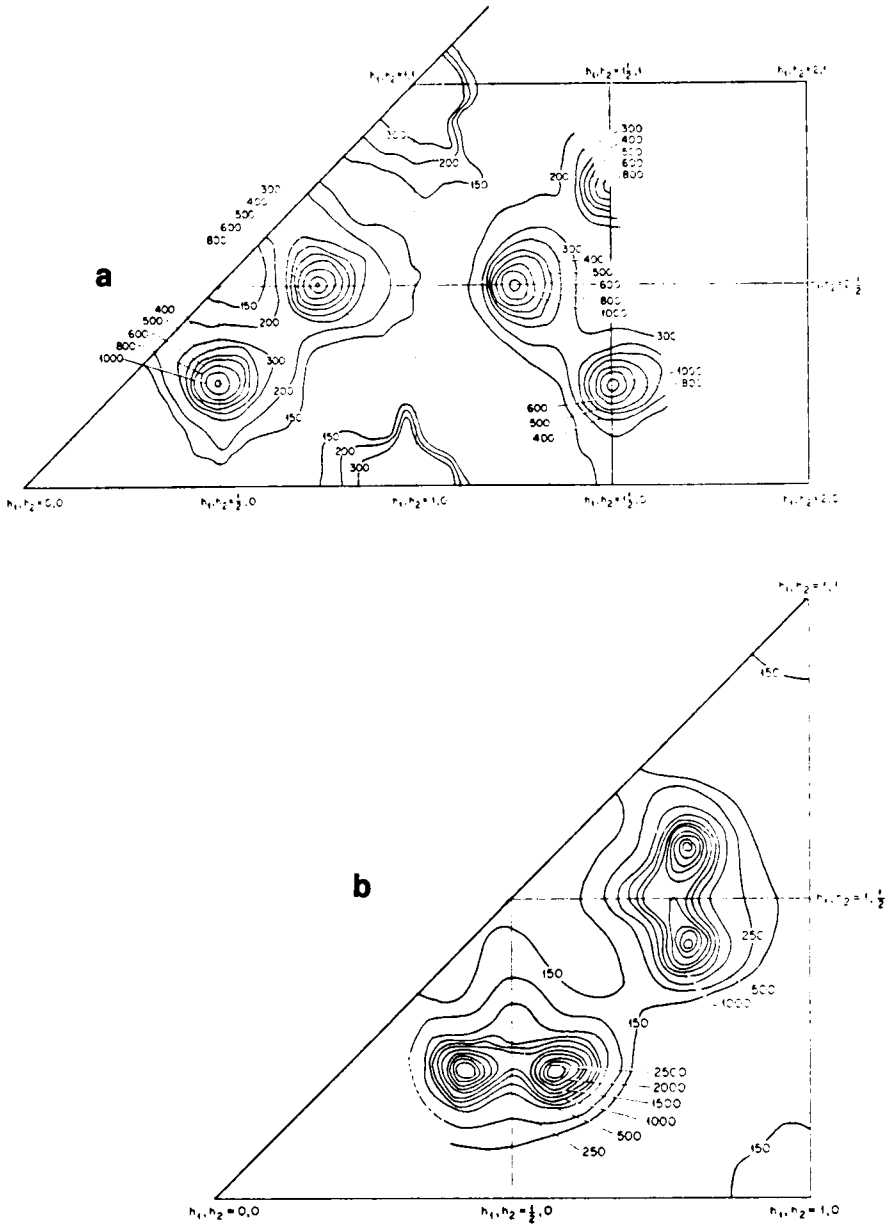


Figure II-18. Distribution of diffuse x-ray intensity at 86°K in the $(h_1,h_2,0)$ plane of reciprocal space for Ni_4Mo. a) Quenched from 1000°C; b) Quenched from 1000°C and aged for 1 hr at 653°C.

Source: J. E. Spruiell and E. E. Stansbury, "X-ray Study of Short-Range Order in Nickel Alloys Containing 10.7 and 20.0 At.% Molybdenum," J. Chem. Phys. Solids, 26, 811-822 (1965).

on the LRO Ni_4Mo structure, from which a set of SRO parameters was calculated. Based on a comparison of these calculated values to those determined experimentally, they (33) suggested that local atomic arrangements could be similar to those in long range ordered Ni_4Mo. The critical size of the domains necessary to cause the observed splitting was estimated to be of the order of $10a_o$ which is about 3.6 nm. Few years later, Ruedl et al. (117,118) published electron diffraction patterns of quenched Ni_4Mo showing diffuse intensity at {1 1/2 0} positions confirming the x-ray observations of Spruiell and Stansbury (33,62). A dark field electron micrograph obtained from a {1 1/2 0} spot of as-quenched Ni_4Mo exhibited a high density of tiny bright spots, which they (117,118) interpreted as direct evidence of a microdomain structure. Field ion microscopy has also been used to provide insight into the SRO state. Chakravarti et al. (13) did not observe ordered domains in the as-quenched state, whereas Lefevre et al. (162) observed a microdomain structure in field ion micrographs of as-quenched Ni_4Mo aged for very short times. Both the {1 1/2 0} intensity and the dark field images are considered as general confirmation of the basic characteristic of the SRO state. Depending on the author, and the time, the dark field image of the SRO state in nickel-molybdenum alloys has been described as "dotted" (117,118), "mottled" (12,13) or "speckled" (156-158).

Since the early research of Spruiell and Stansbury (33,62) and Ruedl et al. (117,118), the true nature of SRO in nickel-molybdenum alloys became a subject of intense debate. Several schools of thought, representing different models for the description of SRO, have emerged. These are described in the following.

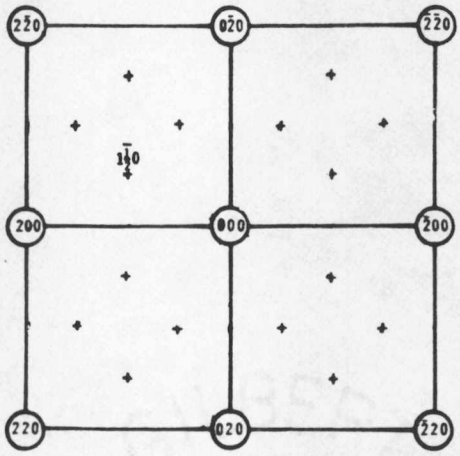
Clapp-Moss model. Clapp and Moss (167-169) used a statistical-mechanical treatment involving pairwise atom interaction potentials to obtain an expression for the intensity of diffuse scattering, $\alpha(k)$ as a function of V(k), the Fourier transform of the pairwise interatomic potential, v(r). From this expression, it was deduced that the maxima in diffuse intensity should occur at points in reciprocal space where V(K) is a minimum. Thus, they were able to account for the SRO diffuse intensity peaks at the {1 1/2 0} positions in Ni_4Mo without taking recourse to any structural descriptions for the SRO state. On the basis that these positions did not coincide with the positions of diffracted intensity for the equilibrium long range ordered Ni_4Mo, they rejected the microdomain concept.

Although the validity of structural models for describing SRO were seriously questioned by Clapp and Moss (167-169), Cowley (170) justified the microdomain concept of SRO from physical arguments. He (170) suggested two conditions which must be satisfied in order that a microdomain model be valid: 1) the microdomains can be described in terms of a chemically reasonable ordered structure, and 2) the structure must produce superlattice reflections which coincide with the positions of the diffuse SRO peaks corresponding to a minimum of the V(K) function. In the case of Ni_4Mo, however, the superlattice reflections do not coincide with the {1 1/2 0} SRO positions, which would appear to rule out the microdomain description of SRO.

Microdomain model. Although the concept of microdomains was first introduced by Spruiell and Stansbury (33,62) and Ruedl et al. (117,118), the evolution of a specific model describing the nature of

microdomains is generally credited to Thomas and co-workers (92,116,126,151-153). Okamoto and Thomas (92,116) using electron diffraction and field ion microscopy argued that the microdomain concept was not necessarily incompatible with the Clapp-Moss model (167-169). In their microdomain model (92,116), the SRO state in as-quenched Ni_4Mo was proposed to consist of an assembly of ordered microdomains. A (001) section of the reciprocal lattice for quenched Ni_4Mo along with the corresponding diffraction pattern is shown in Figures II-19a and -19b. The presence of microdomains was inferred from the diffraction evidence that samples of as-quenched Ni_4Mo showed heretofore unreported, weak scattering near the superlattice positions coexisting with much stronger {1 1/2 0} peaks. They (92,116) concluded that the occurrence of imperfect DO_{22} microdomains in regions of impinging non-conservative antiphase boundaries was responsible for this diffraction effect.

In a series of subsequent papers, Das, Thomas and co-workers (126,151-153) examined in further detail the relationship between the distribution of diffuse intensity and the {420} stacking sequences of nickel and molybdenum atoms which result in the Ni_2Mo, DO_{22} and Ni_4Mo structures. They corroborated the microdomain model of Okamoto and Thomas (92,116) and further reported diffuse intensity at the Ni_2Mo and Ni_4Mo positions in the electron diffraction patterns. This led to their proposal of a multi-microdomain model consisting of a dispersion of these structures in a disordered matrix. It was postulated that the diffuseness was associated with microdomains of small size and imperfect order, so that, in their view, the {1 1/2 0} and associated



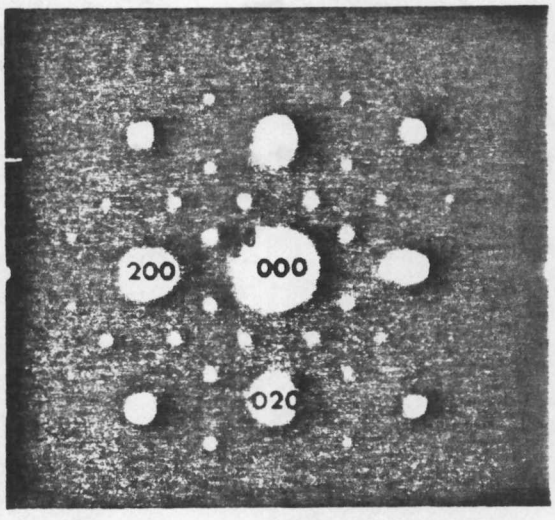


Figure II-19. (001) reciprocal lattice section and corresponding diffraction pattern of as-quenched Ni_4Mo. The plus marks at {1 1/2 0} positions indicate short range order.

Source: P. R. Okamoto and G. Thomas, "On Short-Range Order and Microdomains in the Ni_4Mo System," Acta Met., 19, 825-841 (1971).

diffuse intensity is attributed to the occurrence of imperfect DO_{22}, Ni_2Mo and Ni_4Mo domains delineated by non-conservative antiphase boundaries.

Chakravarti et al. (149) measured x-ray diffuse intensity in a larger volume of reciprocal space and concluded that overlap from adjacent {1 1/2 0} peaks gave rise to local intensity that could be interpreted as Ni_2Mo and Ni_4Mo in the as-quenched state. From SRO parameters derived from x-ray data, they (149) constructed a computer-based distribution of nickel and molybdenum atoms. Although groups of atoms tending to have a property of no Mo-Mo nearest neighbors was observed in the computer generated array, they (149) concluded that there is no evidence for LRO microdomains. Nesbit and Laughlin (81) also rejected the concept of microdomains and instead supported the Clapp-Moss model (167-169) for the physical interpretation of the SRO structure based on the sphericity of the SRO reflections, the lack of streaks in the <420> directions in the as-quenched state, and the absence of particles in dark field from the SRO spots.

The controversy over the nature of SRO in quenched Ni_4Mo was particularly highlighted by two groups, namely, Chevalier and Stobbs (C-S) (155-158) and Thomas-Sinclair (T-S) (153). C-S (155) examined the diffuse intensity in electron diffraction patterns in several planes of reciprocal space and explained the diffuse streaking reported by Thomas and co-workers (92,116,126,151,152) in terms of "the three dimensional superposition of SRO peaks" and stated that "there is no evidence in the fast quenched state for the sort of

streaking associated with the early stages of ordering." They (155) argued that SRO in Ni_4Mo could be explained by {1 1/2 0} scattering alone without taking recourse to structural considerations and concluded that their results precluded any possibility for microdomains of DO_{22}, Ni_2Mo or Ni_4Mo. In response, T-S (153) maintained that the multimicrodomain model of SRO in Ni_4Mo was the correct description and criticized the unnecessary use of thicker foils by C-S which obscured the weak diffraction effects observed by T-S. In later papers (156-158), C-S reaffirmed that the description of SRO in Ni_4Mo as microdomains was physically misleading and ascribed a unique structure for the SRO state in quenched Ni_4Mo characterized by "speckled" dark field images, which was a response to "fluctuations in the scattering potential." They proposed that the SRO state in quenched Ni_4Mo was better described as unbounded "Static Concentration Wave Packets" (SCWP) rather than bounded microdomains. This model of SRO is described later. Later, Thomas and Goringe (154) in discussing current ideas of SRO conceded that the microdomain concept for SRO, although applicable to other systems, may not be the correct description in nickel-molybdenum alloys

In a recent review, Stansbury (171) has pointed out the importance of cooling rate employed to retain the SRO state in deciding the true nature of the SRO state. It is significant that Chevalier and Stobbs (155) utilized the fastest cooling rate ($500^{o}C$/sec) which could be one of the factors contributing to their conclusions in difference to previous reports (92,116,151,152). Thus, according to Stansbury (171), "subsequent transformation occurs from a

limiting as-quenched state in the sense of Chevalier and Stobbs (155-157) or from some pre-nucleated state containing nuclei of Ni_4Mo, DO_{22} and/or Ni_2Mo (92,151-153) depending on the exact pre-transformation time-temperature history."

Cluster model. This model was used by De Ridder et al. (172) to explain the nature of diffuse scattering during the transition from SRO to LRO in various systems, including nickel-molybdenum alloys, rather than to explain the nature of SRO. Nevertheless, it is included here for purposes of discussion. De Ridder et al. (172) found that the nature of the diffuse intensity in electron diffraction patterns was a sensitive function of cooling rate used to retain the quenched state. Very fast cooling rates were required to restrict the SRO diffuse intensity to the {1 1/2 0} positions (127,128,172). Slower cooling rates gave rise to diffuse intensity in the form of pseudo circles connecting future LRO positions and weak lines extending from the {1 1/2 0} positions to the {100} positions. They (172) attributed the former to the formation of five member planar clusters and the latter to five point pyramidal clusters in the SRO state and pointed out that grouping of the latter type of cluster was in agreement with the rod-like development of Mo atoms in the <100> directions observed by Chakravarti et al. (149). They (172) also emphasized that the presence of microdomains was a characteristic of the transition state rather than that of the true SRO state.

Static concentration wave model. The static concentration wave (SCW) approach is based on the Landau and Lifshitz (71) and Khachaturyan (57,173) theories of second order phase transitions. The

basis of this theory lies in describing the probability of finding a particular atomic species at a given lattice by means of a superposition of static concentration waves. DeFontaine (174) building on this framework has applied this theory to the order-disorder transformation in Ni_4Mo.

In his mean field theory (174), the free energy of mixing is expressed in terms of SCW's (representing concentration) and then expanded in a Taylor series. To determine the equilibrium configuration at any given temperature and composition, he uses Fourier transform techniques instead of defining sublattices as in the Bragg-Williams theory (60). On replacing the terms for the concentration deviations in the free energy expression by their Fourier transforms in real and reciprocal space, he establishes the expression for the "k-space" configurational free energy of mixing in terms of atom pair interaction parameters as:

$$\Delta F = A(k)\eta^2 + B(k)\eta^3 + C(k)\eta^4 \qquad \text{(II-9)}$$

where A, B and C are dependent on temperature, wave vector and concentration and η is the generalized long range order parameter which is proportional to the amplitude of the SCW's.

By neglecting terms higher than second order for small concentration wave amplitudes (that is, close to the disordered state), he (174) then shows that the configurational free energy is minimized by the wave vector for which the coefficient of the second order term, A(k), takes a minimum value. A(k) is given by

$$A(k) = N_v[2V(k) + k_BT/C_AC_B] \qquad \text{(II-10)}$$

where, N_v denotes the number of atoms per unit volume, k_B is the

Boltzmann constant, T is the temperature, C_A, C_B are the atom fractions of the two atomic species and V(k) is N_v times the Fourier transform of the atom pair interaction function, v(r) given by

$$v(r) = [v_{AA}(r) + v_{BB}(r) - 2v_{AB}(r)]/2 \qquad \text{(II-11)}$$

In this expression, v_{ij} is the interaction energy of an (ij) atom pair with pair numbers separated by the lattice vector r.

He (174) then argues that the points in reciprocal space of importance are those at which the function V(k) takes a minimum value, since according to equations II-9 and -10, the corresponding wave vector, k^*, minimizes the harmonic part of the free energy. These points are called special points and by symmetry requirements alone satisfy the condition of minimum V(k). There are four special points in the first Brillouin zone for fcc-based structures one of which, the <1 1/2 0> point, is of special significance in the nickel-molybdenum system. By confining atom interactions to the third coordination shell, DeFontaine (174) shows that the absolute minimum of the "k-space" potential occurs at the special points.

Several major conclusions follow on application of his theory (174) to the (420) structures in nickel-molybdenum alloys:

1). The SRO diffuse intensity is predicted at the {1 1/2 0} special position, as observed experimentally.

2). The SRO diffuse intensity contours are predicted to be spherical, as observed in the diffraction patterns.

3). The slight streaking of the {1 1/2 0} intensity contours along the [210] direction is postulated to be due to "softening" of V(k) in that direction.

4). The (420) stacking can be described by their equivalent concentration wave. For each structure $N_{X-1}M$, there are exactly X (= 2,3,4,5) Fourier waves of same amplitude. The corresponding k-vectors when plotted along the [210] direction in reciprocal space mark the positions of $N_{X-1}M$ (X = 2,3,4,5) spots.

5). Of particular significance relating to the transformation behavior on Ni_4Mo is the conclusion that the stability of the ordered structures, $N_{X-1}M$ (X=2,3,4,5) is governed <u>not</u> by a minimum of V(k), but by the existence of non-vanishing third order terms with negative coefficients in the free energy expression, which leads to the conclusion that "all reactions of the (420) series <u>must</u> occur at equilibrium by nucleation and growth."

6). DeFontaine (174) introduces and develops the concept of "Spinodal Ordering." He defines a "spinodal ordering temperature," T_o, as the temperature at which the second order term in the free energy expression changes from positive to negative values for infinitesimally small concentrations. At T_o, the second derivative of free energy with respect to η (that is, the concentration) is zero, which yields

$$T_o(k) = -2V(k)C_AC_B/k_B \qquad \text{(II-12)}$$

where the parameters on the right hand side are as defined previously. For each wave vector k, this equation describes a spinodal line in the temperature-composition diagram. Thus, at temperatures $T<T_o$ the disordered material is unstable with respect to infinitesimal concentration fluctuations of type k. From the above expression, it can also be deduced that the concentration wave having the lowest V(k)

will exhibit the highest T_o value. According to DeFontaine (174), the T_o for the <1 1/2 0> and the 1/5<420> spinodals are respectively higher and lower than the critical temperature for the SRO to LRO transformation in Ni_4Mo. The value for the 1/5<420> spinodal was determined by Banerjee et al. (159,160) to be around 577°C (800°K), whereas that for the <1 1/2 0> spinodal was placed at around 877°C (1140°K) by Mayer and Urban (161).

To explain the diffraction effects during the very early stages of aging the quenched-in structure, DeFontaine (174) assumes that the behavior can be approximated by a linear diffusion equation derived from the harmonic portion of the free energy, with the restriction that the quenched-in concentration amplitudes, X_o, are small. The resulting kinetic law is obtained as:

$$X(k,t) = X^o(k)\exp[\alpha(k)t] \qquad \text{(II-13)}$$

where, t is the time and $\alpha(k)$ is the amplification rate given by

$$\alpha(k) = -M\,\beta(k)\,A(k) \qquad \text{(II-14)}$$

in which M is a (positive) atomic mobility, $\beta(k)$ is a geometrical factor defined as a sum over nearest neighbors and A(k) is the coefficient of the second order term in the free energy expression (equation II-9). In his theory (174), $\alpha(k)$ is the ordering analogue of the amplification rate $R(\beta)$ in Cahn's (106) theory of spinodal decomposition.

By choosing appropriate values for the pair interaction energy ratios, V_2/V_1 and V_3/V_1, DeFontaine (174) calculates the amplification rate, $\alpha(k)$. Plotting the amplification rate along the [h h/2 0] direction yielded maxima at the {1 1/2 0} position, thus indicating

preferential amplification of these waves. This was taken as the explanation for the appearance of {1 1/2 0} SRO diffuse intensity maxima.

In his spinodal ordering theory (174), it is assumed that a) the material is quenched rapidly through the temperature range between T_c and T_o to prevent nucleation of LRO Ni_4Mo and b) the temperature is held below T_o, the spinodal temperature, but above that at which the 1/5<420> waves of the Ni_4Mo superlattice become unstable. On this basis, he concludes that on rapid quenching from the disordered region, waves corresponding to the maximum of the amplification rate would be preferentially amplified because of the primary influence of the harmonic terms of the free energy. This is, in turn, manifested by the intensification of the SRO spots prior to long range ordering, as observed experimentally. While Okamoto and Thomas (92) suggested that the presence of the <1 1/2 0> wave is due to imperfectly ordered DO_{22} microdomains, DeFontaine's (174) interpretation is rather that the minimization of V(k) leads to the <1 1/2 0> wave, which, in turn, can be considered as creating imperfectly ordered "average" clusters.

Static Concentration Wave Packet model. The static concentration wave packet (SCWP) model for describing SRO in nickel-molybdenum alloys was introduced by Chevalier and Stobbs (156,157). It is essentially an extension of the SCW model of DeFontaine (174), but with the additional suggestion of Cook (175) that the SCW can be limited in space, thus forming a "packet."

According to Chevalier and Stobbs (156,157), the SCWP is created by attenuation of the SCW in real space by a exponential decay

function. To interpret the scattering behavior in terms of the SCWP model, they (157) compared the measured SRO parameters (149) with those predicted by the model and obtained, in their words, "a good fit." Interpretation of the dark field "speckled" image in terms SCWP's was less certain. They (156,157) stated that the presence of microdomains can be demonstrated only if a stereo pair of dark field images can be produced. If such a stereo correlation does not exist, as observed by them in as-quenched Ni_4Mo, then the SRO can be best described as SCWP's. "A SCWP has no crystal superstructure and is strictly unbounded," in contrast to microdomains which are uniform and bounded. They argued that the SCWP can form on all {420} planes as opposed to microdomains which are bounded by specific pairs of {420} planes, and conceptually two or more SCWP's of continuously varying composition can interpenetrate and lead to the "speckled" image.

Rationalization of models for SRO in Ni-Mo alloys based on latest experimental evidence. A recent publication by Banerjee et al. (160) reporting the effects of electron irradiation in the TEM has provided significant new insight toward establishing the correct model for the description of SRO and toward understanding the transiton from SRO to LRO in Ni_4Mo. The starting structures on which radiation was imposed in their study were: 1) a completely SRO state obtained by water-quenching samples contained in He-filled silica capsules from 1102^{o}C, and 2) a completely LRO state produced by reheating the SRO samples in "1" to 802^{o}C for 96 hours. They reported the effects of temperature at which radiation was imposed and time of radiation as

variables applied to the initial states. Their results (160) are summarized here to provide a framework for subsequent discussion on the nature of SRO and on the mechanisms of the SRO to LRO transformation in Ni_4Mo.

Low temperature range: $50^oK<T<200^oK$ ($-223^oC<T<-73^oC$)

Initial SRO and LRO states completely destroyed by radiation.

Intermediate temperature range: $200^oK<T<550^oK$ ($-73^oC<T<277^oC$)

1. Initial LRO state: a) At $T<450^oK$ (177^oC), SRO develops only from a highly disordered state, that is, only after LRO is destroyed. b) At $T>450^oK$, LRO cannot be destroyed and SRO does not form from LRO; however, if LRO is destroyed by radiation at low temperatures, then SRO can form above 450^oK. c) LRO does not form from SRO, since rapid increase in SRO occurred on radiation of an intermediate state consisting of SRO and LRO.

2. Initial SRO state: Intensity of SRO peaks decreased until a stationary value was reached, but there was no tendency for LRO formation.

High temperature range: $550^oK<T<1000^oK$ ($277^oC<T<727^oC$)

1. Initial LRO state: Virtually unchanged.

2. Initial SRO state: a) In the temperature range between 550 (277^oC) and 720^oK (447^oC), there was simultaneous presence of SRO and LRO with continuous shift of diffraction intensity from SRO to LRO reflections linked by diffuse intensity. No $D1_a$ microdomains were observed, thus indicating that the alloy was in a single-phased transitional state. b) At 770^oK (497^oC), SRO to LRO transition was continuous and SRO disappears when the LRO parameter attained a value of 0.75. Intensity of LRO reflections increased till S = 0.85 and $D1_a$ microdomains were observed at this stage. c) At 820^oK (547^oC), SRO intensity disappears discontinuously accompanied by rapid formation of LRO, indicating existence of a two-phase region.

Banerjee et al. (160) relate their observations to arguments posed over the correct model for description of SRO and on mechanisms

for the transformation from SRO to LRO in Ni_4Mo. In this section, only the conclusions relating to the former are presented; those relating to the latter are covered later.

Banerjee et al. (160) rejected the microdomain model for SRO on the basis that in the intermediate temperature range ($200^oK<T<450^oK$) SRO develops from the completely disordered state and not from the initial LRO state. The inference is that if the microdomain model were operative, the LRO to SRO transformation would be accomplished by fragmentation of the LRO domains accompanied by disordering at the domain boundaries and formation of non-conservative APB's and it would not be necessary to go through the completely disordered state. They also argued that LRO is completely destroyed by radiation whereas SRO is not and if indeed the SRO were derived from the LRO by the introduction of non-conservvative APB's, then SRO should also not survive under the disruptive influence of radiation.

Banerjee et al. (160) and later Mayer and Urban (161) supported the static concentration wave and spinodal ordering model of DeFontaine (174). They (160,161) base their arguments on the grounds that small concentration waves with a high amplification rate can survive the disordering influence of radiation. Since for low amplitude concentration waves the amplification rate for the <1 1/2 0> SRO wave is higher than that of the 1/5<420> LRO waves (174), they (160) argued that the SRO state is stable relative to the disordered state and hence the system passes through the disordered state to accomplish the LRO to SRO transformation.

With respect to the static concentration wave packet (SCWP) model of SRO of Chevalier and Stobbs (156,157), Banerjee et al. (160) point out that the bridges of diffuse intensity linking SRO and LRO positions in the high temperature range indicates the simultaneous presence of waves with wave vectors ranging from <1 1/2 0> to 1/5<420>, which could allow formation of SCWP's. For this to be true--they (160) point out--waves having varying wave vectors must be locally coherent. Since they (160) did not report dark field "speckle" images obtained from the bridges of diffuse intensity between SRO and LRO positions establishing the absence of coherency between the SCWP's, the SCWP model (156,157) cannot be rejected.

As a final note therefore, the static concentration wave model of DeFontaine (174) has gained--the widest acceptance--and is considered as--the best description--for the SRO state in nickel-molybdenum alloys.

The SRO to LRO Transformation in Ni_4Mo

Continuous heating and cooling kinetics. Lei (8) and Vasudevan (9) extensively studied the order-disorder changes in Ni_4Mo on continuous heating and cooling. Vasudevan's (9) results of resistivity measurements on continuous heating and cooling of Ni_4Mo are shown in Figure II-20. The symbols H, C and I in Figure II-20 stand for heating, cooling and isothermal measurements; the numbers 1, 2 etc. denote the sequence of runs.

In Figure II-20, curve 1H, resulting from heating the initially 77% RA cold swaged Ni_4Mo alloy, shows that the resistivity increases

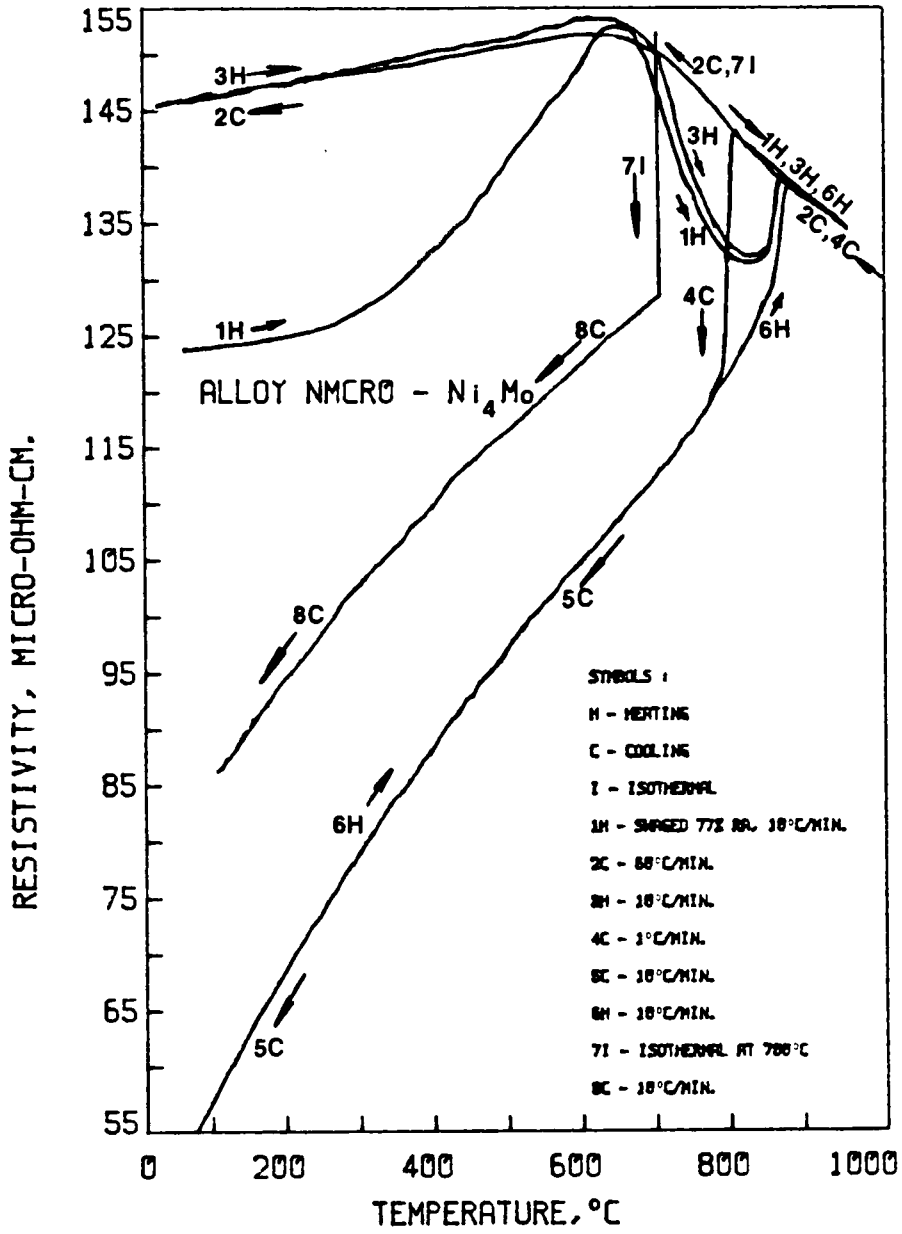


Figure II-20. Variation of resistivity with temperature on continuous heating and cooling in Ni_4Mo.

Source: K. Vasudevan, "The Effect of 0-4 Wt Pct Chromium on Transformations of Alpha Phase Ni-Mo-Cr Alloys with Ni:Mo Atom Ratio Equal to 4:1," M.S. Thesis, University of Tennessee (1982).

linearly to about 300°C with a slope of 0.021 micro ohm cm/°C due to increasing thermal scattering of electrons. This is followed by a non-linear rapid increase in resistivity to 650°C due to progressive return of SRO which had been destroyed by plastic deformation. If the linear portion of the curve is interpolated, the SRO contribution to the resistivity above 300°C can be estimated. Above 650°C, the onset of long range order leads to rapid decrease in resistivity. Near 850°C, LRO resistivity attains its equilibrium value and then rises sharply as the ordering temperature (868°C) is approached. Above 870°C, the resistivity again decreases as the degree of SRO decreases with increasing temperature. Thus, it is evident that the decrease in SRO is more effective in decreasing the resistivity than the increase in temperature is in increasing it. These results are in excellent agreement with those of Lei (8) and Chang (63). It should be noted that measurements have not been made at higher temperatures to determine if the rate of decrease of SRO continues to decrease the resistivity by overcompensating the increase due to thermal scattering for temperatures to the melting point.

Curve 2C in Figure II-20 represents data for a sample cooled from above 950°C at about 60°C/min. On cooling, the resistivity initially increases to about 152 micro ohm cm at 650°C and then slowly decreases to a value of 146 micro ohm cm at room temperature with a temperature coefficient of resistivity, α, equal to 0.011 micro ohm cm/°C. The initial increase is due to increase in SRO which continues down to about 650°C, below which the amount of SRO is effectively "frozen-in" due to insufficient atom mobilities.

The following heating curve, 3H, shows that the resistivity coincides with the previous curve 2C, to 300°C, and then has a higher resistivity to 650°C due to additional SRO which occurs by virtue of adequate atom mobility. Above 650°C, the behavior is similar to that of curve 1H. Curve 4C results from slow cooling with a rate of 1°C/min from 950°C to 700°C. The resistivity increases initially on cooling to about 800°C, and then rapidly drops in the temperature range 800-775°C with the initiation of long range order. This cooling rate is sufficiently slow to allow complete transformation to the long range ordered state. Curve 5C is a continuation of curve 4C from 700°C to room temperature at a cooling rate of 10°C/min. At room temperature, the LRO value of resistivity is 48 micro ohm cm which contrasts markedly with the "water-quenched-in" SRO state value of 144 micro ohm cm, the state resulting from cooling at 60°C/min value of 146 micro ohm cm and the cold worked state value of 124 micro ohm cm.

The resistivity-temperature relationship on reheating the long range ordered Ni_4Mo alloy is represented by curve 6H. The resistivity values are essentially similar to 775°C with curve 5C. Beyond 775°C, the resistivity increases with a higher gradient to 850°C, after which there is a more rapid increase as the ordering temperature is approached. Above the ordering temperature, the curve is reproducibly similar to curves 1H and 3H. The long range short range order transformation occurs at 868±2°C which is in exact agreement with the results of Guthrie and Stansbury (7) and Lei (8).

The following curve 7I represents an isothermal anneal at 700°C. The sample was initially held for 5 minutes at 950°C, to obtain a

fully α matrix and then rapidly cooled to 700^{o}C. At the end of 3 hours at 700^{o}C, the resistivity drops from about 150 micro ohm cm at the start of the hold to 129 micro ohm cm, after which the sample was medium cooled to room temperature (curve 8C).

Reference to curve 6H in Figure II-20 shows that the equilibrium value of the long range ordered state at 700^{o}C is 110 micro ohm cm. The fact that 3 hours holding at 700^{o}C results in a resistivity of 129 micro ohm cm, is indicative of a partially ordered state. Much longer holding times should result in a resistivity corresponding to the equilibrium value. One aspect of the resistivity-temperature relationship is particularly noteworthy. In the heating curve 6H, it is noticed that at 868^{o}C the resistivity rises sharply from 130 to 140 micro ohm cm and then decreases. This marks the transition from long range to short range order. Although there are data points shown in the steeply increasing section, there is no basis for the resistivity of the LRO state to have the same value as the SRO state at T_c. Rather, a discontinuous, that is, first order change would be expected at 868^{o}C. In fact, curve 2C represents the SRO state. The difference between the two curves at any temperature is the difference in resistivity of the two states. The two states may exist in equilibrium at 868^{o}C. At lower temperatures, the SRO state should transform to LRO and is in fact observed (curve 4C). In a second order transition, the change would occur over a range of temperatures on continuous cooling. In this case, the change is almost isothermal due to a, by chance, balance between heat evolved by the transformation and heat losses from the specimen. In any case, the resistivity is very sensitive in

this temperature range to heating and cooling rate, resulting in a thermal hysteresis.

Lariko et al. (176) have pointed out that ordering is a phase transformation of the first kind if with a slow heating rate, the ordering of the alloy takes place reversibly, but with a marked hysteresis and also qualitatively if the high temperature disordered phase can be retained by rapid cooling. They also pointed out that systems in which the disordered phase could be retained by rapid cooling were face centered cubic. The resistivity-temperature response in Ni_4Mo alloys as shown in Figure II-20 displays this behavior. Moreover, the short range ordered phase has a face centered cubic structure. These features concur with the hypothesis of Lariko et al. (176) and strengthen the arguments adduced in the preceding paragraph that, ordering in Ni_4Mo on continuous cooling is a phase transformation of the first kind, that is, a nucleation and growth process.

In Figure II-20, first, comparison between curves 5C and 8C evinces that the difference in resistivity between the completely ordered and partially ordered states becomes larger the lower the temperature. This is because the long range ordered state has a higher temperature coefficient of resistivity than the short range ordered state. Second, there is a negative deviation of resistivity in the long range ordered state above about $325^{o}C$. This is not properly understood. The SRO resistivity of both Cu_3Au (148) and Ni_4Mo decreases with an increase in temperature. However, in the long range ordered state, Cu_3Au displays a positive deviation in resistivity on

heating (60) whereas Ni_4Mo shows a negative deviation in the temperature range of 325 to about 650°C followed by a positive deviation in resistivity from about 650 to 868°C. In the case of Cu_3Au, a positive deviation in resistivity could possibly arise due a change from a state of perfectly ordered to imperfectly ordered domains, that is, the LRO parameter, $S < 1$. Since such an occurrence cannot be overruled in the case of Ni_4Mo, it is difficult to explain the negative deviation in resistivity.

Very little microstructural work has been done on continuously cooled Ni_4Mo. Irani et al. (177) reported a foam structure in continuously cooled samples. They also observed that an increase in cooling rate from 3 to 5°C/min, resulted in a decrease in average domain size and also that the domains became oriented along certain crystallographic directions.

Temperature dependence of structural changes during isothermal annealing. The structural changes that occur on isothermal aging of Ni_4Mo at 600, 700, 800 and 850°C for times to 4500 hours were reported by Lei (8) and Stansbury et al. (10). Their results of resistivity and microhardness are presented in Figures II-21a and -21b, respectively.

From Figure II-21a, the resistivity after 10 hours at 850 and 800°C drops to about 50 micro ohm cm from the water-quenched value of 144 micro ohm cm and remains essentially unchanged for longer annealing times. At the lower temperatures, the transformation is slower, being complete only after 192 hours at 700°C and after 4500 hours at 600°C. The final resistivity after annealing at each

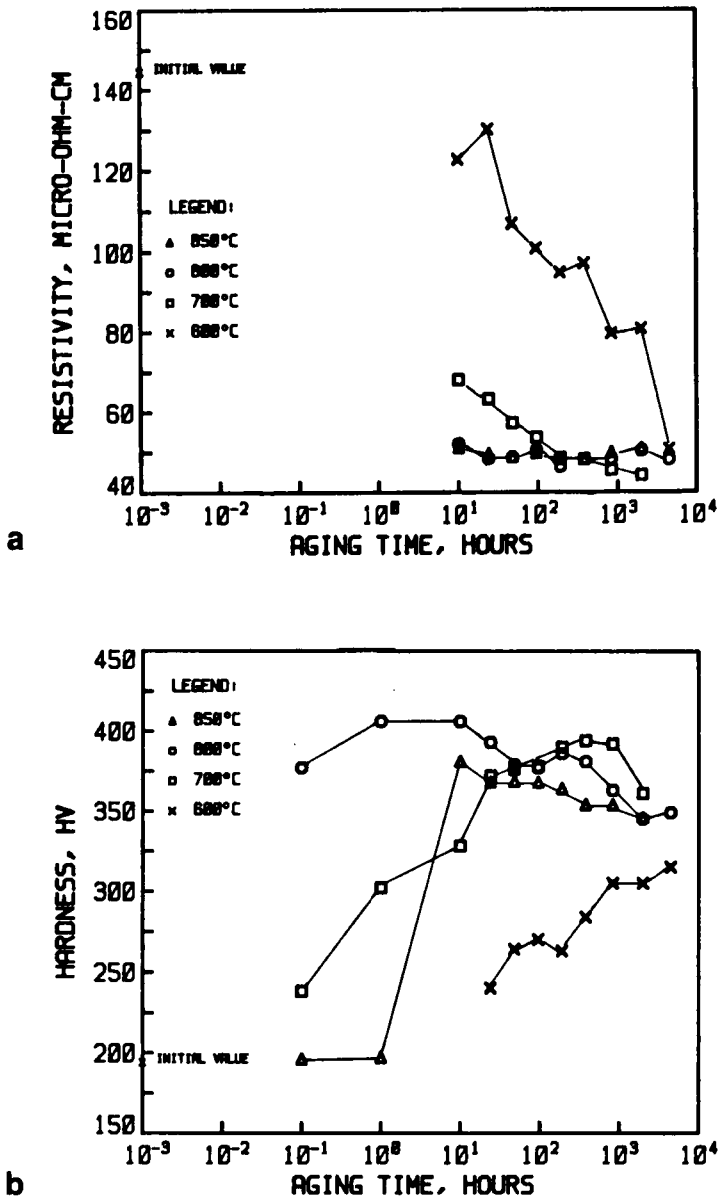


Figure II-21. Resistivity (a) and microhardness (b) as a function of aging time for Ni_4Mo. Aged at 600, 700, 800 and 850°C.

Source: T. S. Lei, "The Effect of 0-8 Wt.% Iron on Transformations of Alpha Phase Ni-Mo-Fe alloys with Ni:Mo Ratio Equal to 4:1," Ph.D. Dissertation, University of Tennessee (1979).

temperature converges to the same value of 48±3 micro ohm cm. Thus, the value of 48 micro ohm cm is taken as representative of the resistivity of fully LRO Ni_4Mo at room temperature.

Figure II-21b shows that the hardness has increased from the water-quenched value of 195 HV to 375 HV within only 6 minutes at 800°C and only slightly at 850 and 700°C. The hardness continues to increase at each of the three higher temperatures, with some indications of overaging, that is, maximum in the curve, and then converges to essentially the same value after 2000 hours. This maximum occurs after 1 hour at 800°C with a value of 410 HV, at 10 hours with a value of 381 HV at 850°C, and at 192 hours with a value of 390 HV at 700°C. At 600°C, there is a continuous increase in hardness over the time period of 4500 hours, with the final value still below that attained at the higher temperatures.

The hardness and electrical resistivity measurements complement each other and are consistent with classical nucleation and growth behavior (10). The low and constant resistivity attained at the later stages of aging indicates a limiting degree of long range order. The initial increase in hardness is due to increase in the extent of ordering, the degree of order within domains, domain size and microstrains (178). Widely different heat treatments result in approximately the same peak hardness, an observation also made by Irani et al. (177). Approximately constant domain sizes after long annealing times was suggested to be responsible for this. Stoloff and Davies (55,179) have pointed out that the peak in the hardness corresponds to a critical mixture of LRO and SRO, whereupon a

transition in deformation mode from single (in SRO) to paired (in LRO) dislocations leads to a higher strength than that attainable for either fully ordered or fully disordered states. Also, the peak corresponded to a critical domain size, a size at which domains came into contact (55). Stansbury et al. (10) observed that the peak in hardness, which occurs at different times at different temperatures, clearly corresponds to different domain sizes. Based on this observation, they (10) argued that the high, and nearly constant hardness, was governed primarily by the high degree of order within the domains and to a lesser extent by domain size. The slight decrease in hardness beyond the maximum was attributed to domain growth permitting longer glide lengths for dislocations. This decrease in hardness is less pronounced than that in other tetragonal (180) and non-tetragonal ordering systems (181), and was attributed to a high coherency between adjacent domains.

Based on isothermal resistivity measurements, Lei (8) reported that the TTT curves of Ni_4Mo, as shown in Figure II-22, are "C-Shaped," with the nose occurring at 775^{o}C and 20 seconds. The beginning curve in Figure II-22, denotes a 0.5 micro ohm cm change in resistivity; the curve to the right represents 75% of the total change (about 20 micro ohm cm at 800^{o}C and 40 micro ohm cm at 600^{o}C). There is some evidence of an inflection (that is, a time displacement) in the C-curve near 735^{o}C implying a change in tranformation mechanism, but this has not been positively established. The peak in the C-curve at 775^{o}C corresponding to maximum rate of ordering also corresponds to maximum microhardness as confirmed by the earlier report of Snyder and Brooks (12).

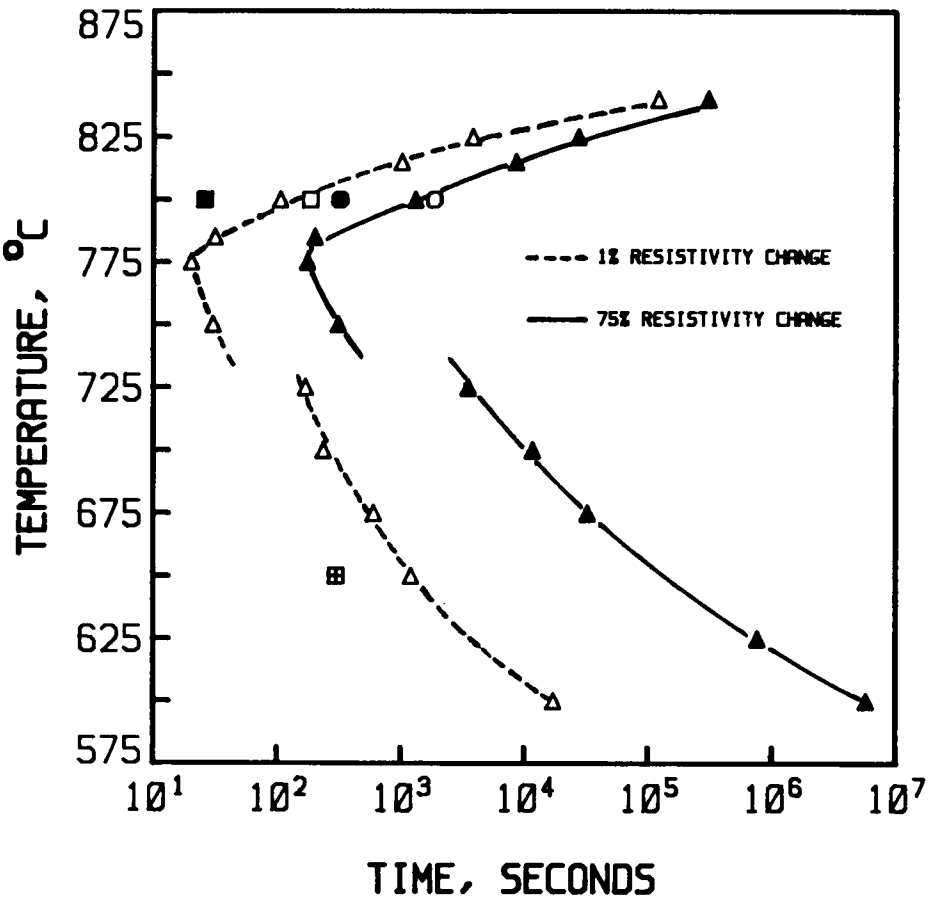


Figure II-22. Isothermal time-temperature-transformation behavior of Ni_4Mo based on resistivity measurements.

Source: T. S. Lei, "The Effect of 0-8 Wt.% Iron on Transformations of Alpha Phase Ni-Mo-Fe alloys with Ni:Mo Ratio Equal to 4:1," Ph.D. Dissertation, University of Tennessee (1979).

Effect of cold work on ordering kinetics. There have been limited studies on the influence of prior cold work of the as-quenched state on the kinetics of long range ordering of Ni_4Mo. Ling et al. (182) using x-ray diffraction and microhardness techniques reported that a 60% cold worked sample aged at 650 and 700°C displayed considerable enhancement in the rate of ordering compared to a non-cold worked sample. They (182) also reported that the maximum in the hardness curve was attained at shorter times in the prior cold worked sample, although the percent increase in hardness was higher in the non-cold worked sample. The cold worked sample also evinced a more pronounced overageing effect, which they attributed to the larger, but uniform domain size prevailing in these samples.

Vasudevan (9) also observed that cold working prior to isothermal aging at 700°C, enhanced the kinetics of ordering. In specimens of an Ni_4Mo + 0.41 wt.% Cr, cold worked to 0, 28, 68 and 77% reduction in area (RA), he observed that the time of initiation of ordering, indicated by the first fall in resistivity, was about the same. The 77% RA cold work specimen showed substantially higher ordering rates than those containing cold work less than this. As pointed out earlier (page 63), about 68% RA was sufficient to remove the SRO existing in water quenched alloys. Cold work beyond this increased the resistivity due to an increase in defect concentration. The fact that the 77% RA cold work specimen showed high rates of ordering was interpreted as arising due to accelerated heterogeneous nucleation in a defect-enriched matrix. In the other specimens, the ordering rates were quite similar in the initial stages, and in the later stages was higher, the greater the degree of cold work.

Moreover, it was observed that some SRO, indicated by an increase in resistivity during the isothermal hold, had to be recovered initially before substantial rates of ordering could be realized.

Transformation mechanisms. The question of whether ordering in Ni_4Mo is a first order (nucleation and growth) or second order (homogeneous or continuous) transformation has attracted a fair amount of attention. The evidence for a nucleation and growth mechanism at the higher temperatures, above 750°C, is quite positive. Saburi et al. (150) from TEM observations concluded that the transition to LRO at 800°C took place by a nucleation and growth process. Partially ordered nucleii were observed under TEM after 5 minutes aging and domains impinged on each other after 30 minutes. The same conclusion was reached by Chevalier and Stobbs (157) who reported the existence of a two-phase region consisting of single Ni_4Mo domains with a "pronounced tetragonal prism shape" in a SRO matrix, during the initial stages of aging at 750 and 800°C. Similar shaped domains were also reported by Lei (8) in samples transformed for 1 hour at 850°C, a temperature higher than that in previous studies. Besides, examining single LRO Ni_4Mo domains in a SRO matrix, Lei (8) developed etching techniques which enabled observations of individual domains optically.

The mechanism of transformation at lower temperatures, below 750°C, is less certain. Chakravarti et al. (13) did not observe single Ni_4Mo domains in a SRO matrix at 700°C using field ion microscopy but rather a structure consisting of contiguous Ni_4Mo domains which grow towards perfection with time. They (13) concluded that at 700°C

ordering proceeded homogeneously and proposed that this may be because "at low temperatures, the frequency of nucleation is so high and the nucleii so small that the material is homogeneous, that is, impingement between domains is instantaneous and there is essentially no "two-phase" region between ordered nucleii and disordered matrix." Ling and Starke (178) also concluded that at 700°C ordering proceeds homogeneously because of the gradual broadening and splitting of fundamental (420) lines into superlattice lines. The degree of order increases homogeneously inside the domains and the LRO parameter follows a relation S = 1-exp(-kt), (t=annealing time and k=constant), before reaching a value of 0.7. After S=0.8, increase in domain size occurs linearly and was attributed to elimination of domain boundaries due to domain growth. They also proposed that the rate of domain growth was analogous to rate of grain growth and satisfies the relation $D^n - D_o^n = kt$, where n = 2.9.

Some evidence for a change in reaction mechanism at about 735°C is evident in the isothermal TTT curves of Lei (Figure II-22). Although the data are somewhat limited in the vicinity of this temperature, the curves show a displacement in time between 725 and 750°C, suggesting a change in mechanism. This is also supported by the observations of Chakravarti et al. (13) and Ling and Starke (178). In addition, Chevalier and Stobbs (157) did not exclude the possibility of continuous ordering below 750°C, although a first order transformation was prevalent above this temperature. Banerjee et al. (160), on the other hand, conclude from their radiation experiments that the transformation proceeds by nucleation and growth as low as

527°C, and that a continuous ordering mechanism is operative only below this temperature.

Correlation with theoretical predictions. A shift in the transformation mechanism from distinct nucleation and growth to relatively homogeneous or continuous ordering has a rational basis in the theory developed by DeFontaine (174) and described at length in reference to the nature of SRO in Ni_4Mo (pages 75-79). Of particular significance relating to the time-temperature-transformation behavior in Ni_4Mo is his conclusion that the stability of ordered structures, N_XM (X=1,2,3,4), is governed not by a minimum of V(k), but by the existence of non-vanishing third order terms with negative coefficients in the k-space configurational free energy of mixing expression (equation II-9, page 75). This leads to the conclusion that "all ordering reactions of the (420) series must occur at equilibrium by nucleation and growth." The inference is that the occurrence of any other mechanism must not be of thermodynamic origin, but due to kinetic factors.

As discussed earlier (page 77), DeFontaine (174) developed the concept of the "spinodal ordering temperature," T_o, below which the alloy is unstable with respect to infinitesimal concentration fluctuations. Between T_c, the critical ordering temperature for Ni_4Mo and T_o for 1/5<420> concentration waves, the reaction must proceed by nucleation and growth. Below the spinodal ordering temperature, T_o for Ni_4Mo, the alloy becomes unstable with respect to 1/5<420> concentration fluctuations, the nucleation barrier disappears and the transformation proceeds in a continuous fashion.

Banerjee et al. (160) based their conclusions on this theory (174). The rapid appearance of distinct 1/5{420} Ni_4Mo reflections above 800^oK (527^oC) and the formation of Ni_4Mo domains led to the conclusion that a nucleation and growth process was operative above this temperature, whereas a continuous ordering mechanism was prevalent below this temperature as indicated by the shift of diffuse intensity from the {1 1/2 0} SRO positions to the 1/5{420} LRO positions and the absence of microdomains. Banerjee et al. (160) also proposed a diagram to describe the alloy steady state under irradiation combined with an ordering mechanism map. This is shown in Figure II-23. The diagram consists of two parts, one for LRO (Figure II-23a) and one for SRO (Figure II-23b). Curve (1) in Figure II-23a represents calculations for the variation in the degree of long range order with temperature based on the Bragg-Williams (60) model. Curve (2) is derived based on Dienes's (68) theory and represents the value of S under steady-state conditions when initially LRO sample are irradiated. Curve (3) gives the experimentally determined values of S when initially SRO samples are irradiated, while Curve (4) denotes the experimentally determined SRO reflection intensity, R. The various regions identified in Figure II-23 are characterized as follows:

Region A = Destruction of LRO

Region B = No significant change if initial state corresponds to S = 1 or S = 0.

Region C = Continuous ordering by decay of the SRO waves and simultaneous amplification of LRO waves.

Region D = Initially as in Region C; after SRO is destroyed completely the degree of LRO increases further by domains formation and growth.

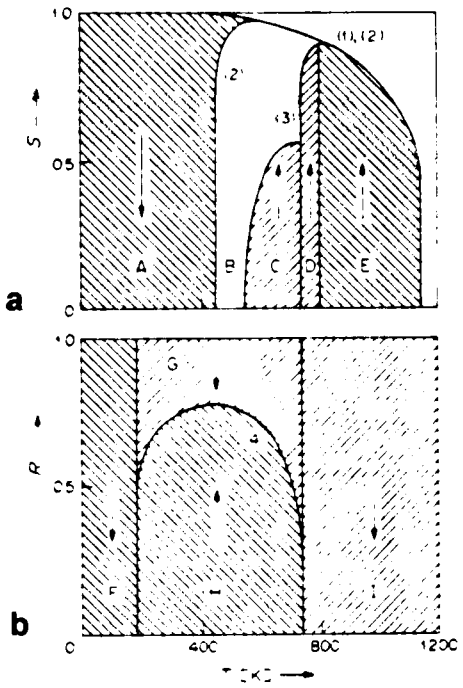


Figure II-23. Diagram of the alloy state and ordering mechanism map in Ni_4Mo. a) LRO; b) SRO.

Source: S. Banerjee, K. Urban and M. Wilkens, "Order-Disorder Transformation in Ni_4Mo Under Electron Irradiation in a High-Voltage Electron Microscope," Acta Met., 32, 299-311 (1984).

Region E = Nucleation and growth of Ni_4Mo domains.

Region F = Destruction of SRO.

Region G = Reduction of the degree of SRO and at T>550^{o}K transition to LRO.

Region H = Development of SRO.

Region I = Destruction of SRO and transition to LRO.

It should be noted in Figure II-23 that Banerjee et al. (160) indicate that the change in ordering mechanism of Ni_4Mo from nucleation and growth to continuous ordering occurs at 527^{o}C, whereas all the other reports (8,13,157,171,178) place this temperature much higher, namely at around 750^{o}C. Vasudevan's (9) results on the effect of prior cold work show that even in samples in which the SRO was completely destroyed by cold work, some SRO forms initially (as indicated by increase in resistivity) prior to LRO formation on aging at 700^{o}C. This demonstrates intensification of the SRO <1 1/2 0> waves prior to long range ordering and provides justification for the prevalence of the spinodal (continuous or homogeneous) ordering mechanism below about 750^{o}C (8,13,157,171,178) rather than below 527^{o}C as reported by Banerjee et al. (160). DeFontaine's (174) conclusion that the ordering of Ni_4Mo must proceed at equilibrium by nucleation and growth at all temperatures implies that departures from such behavior are due to kinetic factors. Thus, the discrepency in the placement of the temperature for the change in ordering mechanism is probably related to differences in the kinetics of ordering when induced by radiation as opposed to purely thermal treatments. It is not inconceivable that the density of defects produced by irradiation

far surpass that by cold work, so that the more accelerated diffusion in the former enables formation of discrete LRO nucleii and the transformation continues to be first order to much lower temperatures.

Finally, while it is quite clear that the SRO <1 1/2 0> waves play a critical role as precursors of the 1/5<420> LRO waves in the continuous ordering case, and the transformation occurs by increasing accumulation of molybdenum atoms into every fifth (420) plane as evidenced by the continuous transfer of diffracted intensity from SRO to LRO positions, the question of how distinct LRO domains of Ni_4Mo evolve in the nucleation and growth regime remains uncertain. Particularly, it is not clear whether the SRO state plays a role at all in nucleating the ordered Ni_4Mo. This question has been partially answered by Chevalier and Stobbs (157) who state that the SRO SCWP's "cannot" nucleate the Ni_4Mo equilibrium structure. They gather support for this conclusion on the observation that during the early stages of ordering, the intensity of the SRO reflections increases and then attains a stationary value while simultaneously distinct LRO Ni_4Mo reflections appear. The implication is that the Ni_4Mo domains form by an independent mechanism unrelated to the SRO state.

Ordering in Nickel-Molybdenum Alloys Containing Less than 20 at pct Mo

Spruiell et al. (183) used TEM to study the formation of Ni_4Mo in nickel-molybdenum alloys containing 23.4 and 25.8 at pct Mo in the temperature range 600-775°C. They observed particles of Ni_4Mo on aging and believed these to have formed by a homogeneous nucleation and

growth process and then coarsened to a cube shaped, modulated morphology. This modulated morphology was concluded to have resulted from the strain field surrounding the particles and seemed to be enhanced by conditions which resulted in greater coarsening. The cube-shaped particles were found to possess a habit in which the cube faces were parallel to the {100} planes of the fcc α matrix. This has also been reported by Goodrum and Lefevre (184) and Nesbit and Laughlin (81) who observed that the Ni_4Mo precipitates became facetted on the {100} planes and aligned in the <100> directions of the matrix. The particle sizes determined by Spruiell et al. (183) were found to be directly proportional to the cube root of time, that is, $D^3 - D_o^3 = kT$. This cube root relationship between particle size and time was confirmed by Goodrum and Lefevre (184) in a Ni-17 at pct Mo alloy aged at 700°C for 50 hours.

Nesbit and Laughlin (81) studied ordering in an Ni-16.7 at pct Mo alloy at 700 and 750°C using TEM. Prolonged aging at 700°C resulted in the precipitation of Ni_4Mo, facetted along the (100) and (010) planes. They (81) concluded that at 750°C, a heterogeneous transformation occurs by a mechanism of homogeneous nucleation, whereas at 700°C a homogeneous transformation occurs by the mechanism of spinodal ordering.

Microstructural Features of Ordered Ni_4Mo

General features. One outstanding aspect which characterizes the optical microstructure of the ordered Ni_4Mo phase is the presence of a thin, striated, Widmanstatten type structure. Grube and Schlecht

(109) observed these in a Ni-25 wt pct Mo alloy and proposed that they were slip lines arising from stresses associated with the crystal structure change. Guthrie and Stansbury (7) reported the appearance of these striations and presumed they were parallel to the {100} planes of the fcc α phase. However, Spruiell (33) used a two-surface trace analysis to show that at least in one set, these striations were parallel to the traces of annealing twin planes, which are {111} planes in the fcc α phase. On the other hand, Irani et al. (177) reported wider striations parallel to {101} fcc planes and proposed that these striations were a form of stress-relief to release some of the stresses associated with the change in crystal symmetry from cubic to non-cubic. They coined the term "Order Twin" for these striations. In agreement with Irani et al. (177), Saburi et al. (185) using a two-surface trace analysis also showed that these wider striations were parallel to {110} fcc planes. Based on TEM observations, they attributed this optical Widmanstatten structure to groups of APT-related domains with aligned perpendicular twin boundaries as the boundary of the striations.

Lei (8), Vasudevan (9) and Stansbury et al. (10) conducted a detailed examination of the optical microstructure and concluded that two different types of striations form in ordered Ni_4Mo. The first type, called the {111} fcc striations, forms as straight lines parallel to annealing twin boundaries. Since these striations form within a single grain in three or four orientations parallel to annealing twin boundaries, which are traces of {111} fcc planes, they (8-10) argued that the striations must be parallel to {111} fcc

planes. Similar striations have also been reported by Saburi et al. (15) in samples of ordered Ni_4Mo deformed by compression. The second type, referred to as the {110} fcc striations, forms as tapered bands not parallel to annealing twin boundaries. Both types of striations are shown in the optical micrographs in Figure II-24a and -25a for the Ni_4Mo alloy aged for 10 hours at 850 and 800°C respectively.

With continued aging, the {111} striations were observed to decrease in number and the {110} striations tend to become straight, developing parallel interfaces (Figures II-24b and II-25b). Also, the contrast between domains across the {110} striations diminishes with domain growth. Another characteristic of the {111} striations is also evident in Figure II-24a and -25a where the striations may cross over many domains, spanning the entire grain.

Besides the {111} and {110} fcc striations, Lei (8), Vasudevan (9) and Stansbury et al. (10) also reported the appearance on long time aging of a third morphology consisting of large irregularly-bounded, patchy regions. This is shown in Figures II-24b and -25b for the Ni_4Mo alloy aged for 2000 hours at 850°C and 4500 hours at 800°C, respectively. Each patchy region represents a single LRO domain of Ni_4Mo. These domains initially appear as a fine mottled structure (Figures II-24a and -25a). At lower temperatures, namely 700 amd 600°C, individual domains of Ni_4Mo could not be resolved owing to their fineness. In contrast to the higher temperatures (800 and 850°C), aging at the lower temperatures produces extensive grain boundary migration as shown in Figures II-26a and -26b respectively for samples aged for 840 hours at 700°C and 4500 hours at 600°C.

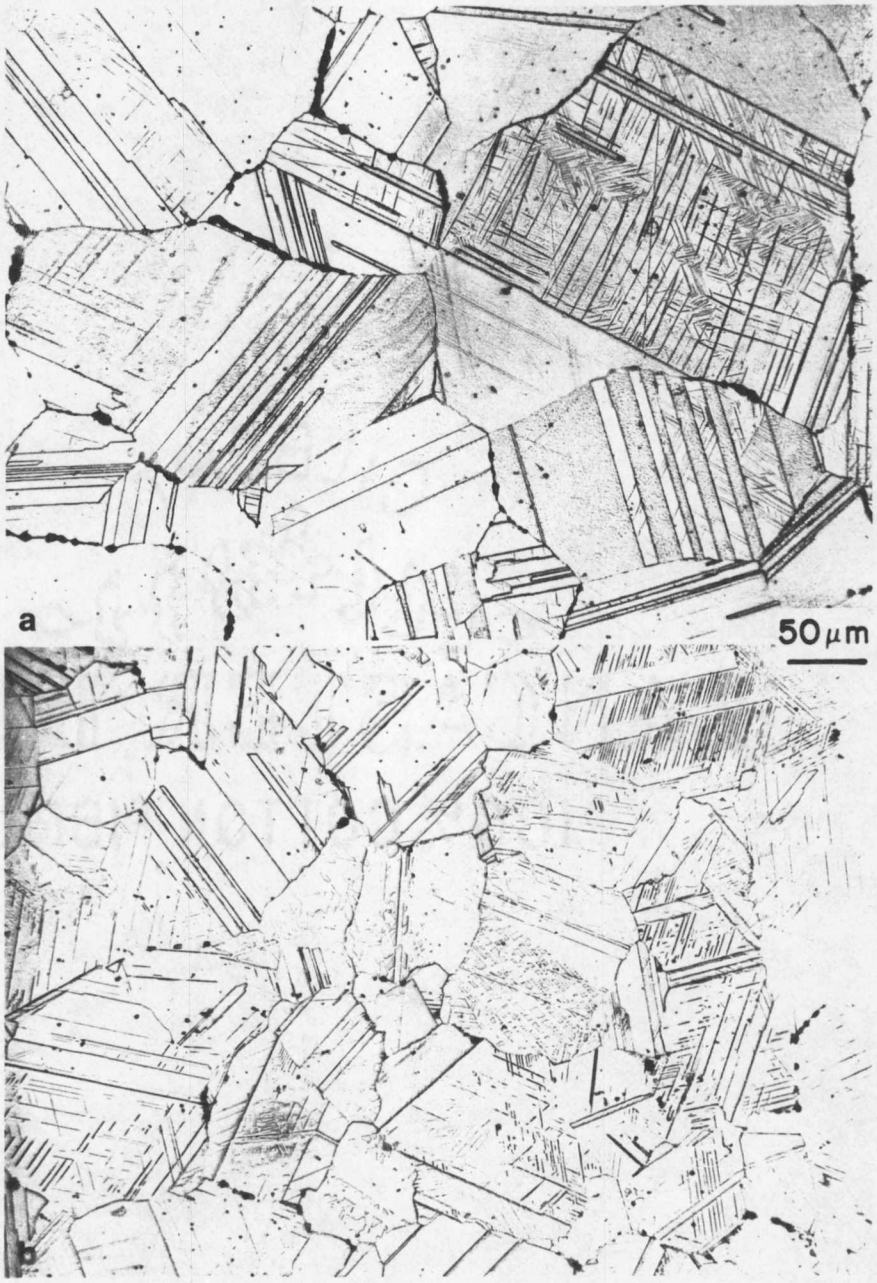


Figure II-24. Optical microstructures of ordered Ni_4Mo aged at 850°C. a) 10 hrs; b) 2000 hrs.

Source: T. S. Lei, "The Effect of 0-8 Wt.% Iron on Transformations of Alpha Phase Ni-Mo-Fe alloys with Ni:Mo Ratio Equal to 4:1," Ph.D. Dissertation, University of Tennessee (1979).

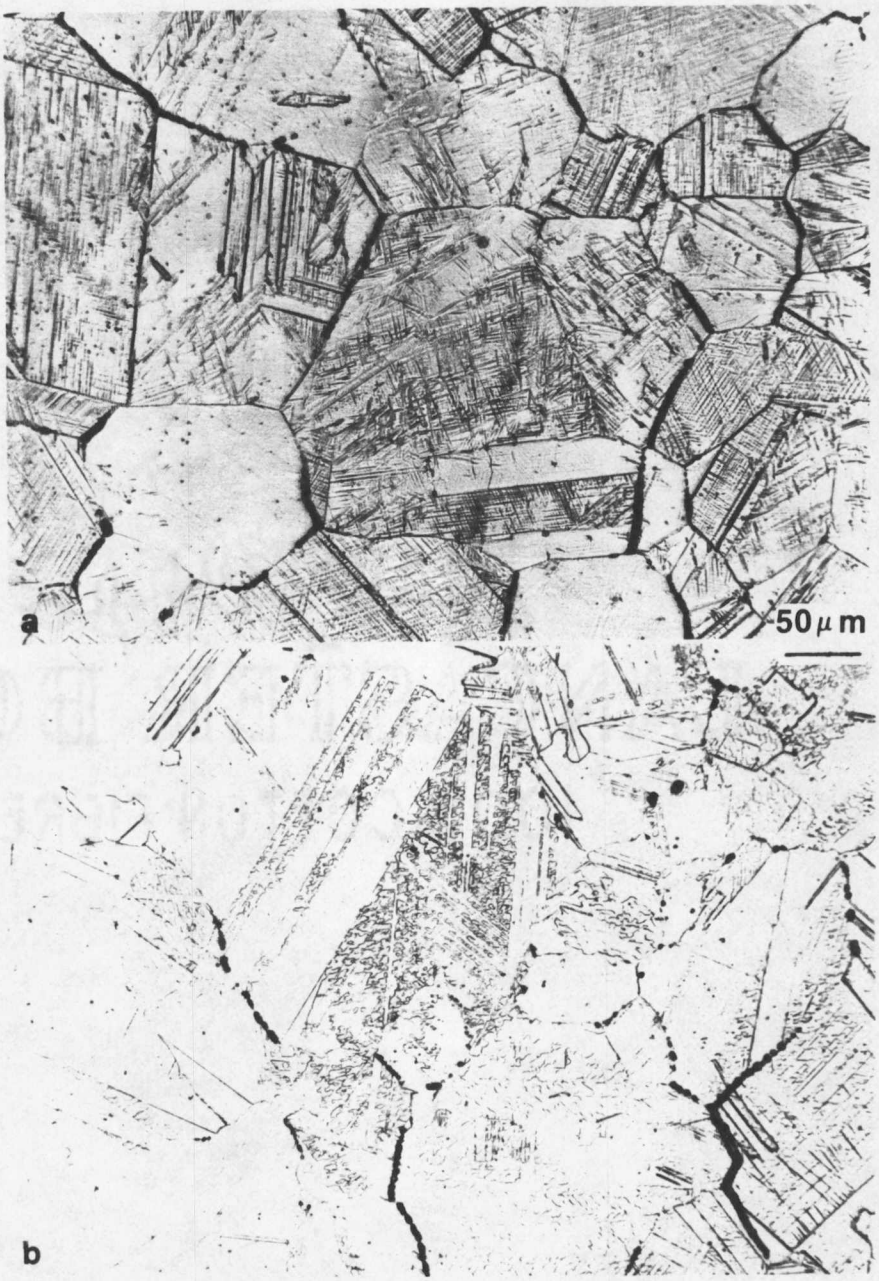


Figure II-25. Optical microstructures of ordered Ni_4Mo aged at 800°C. a) 10 hrs; b) 4500 hrs.

Source: T. S. Lei, "The Effect of 0-8 Wt.% Iron on Transformations of Alpha Phase Ni-Mo-Fe alloys with Ni:Mo Ratio Equal to 4:1," Ph.D. Dissertation, University of Tennessee (1979).

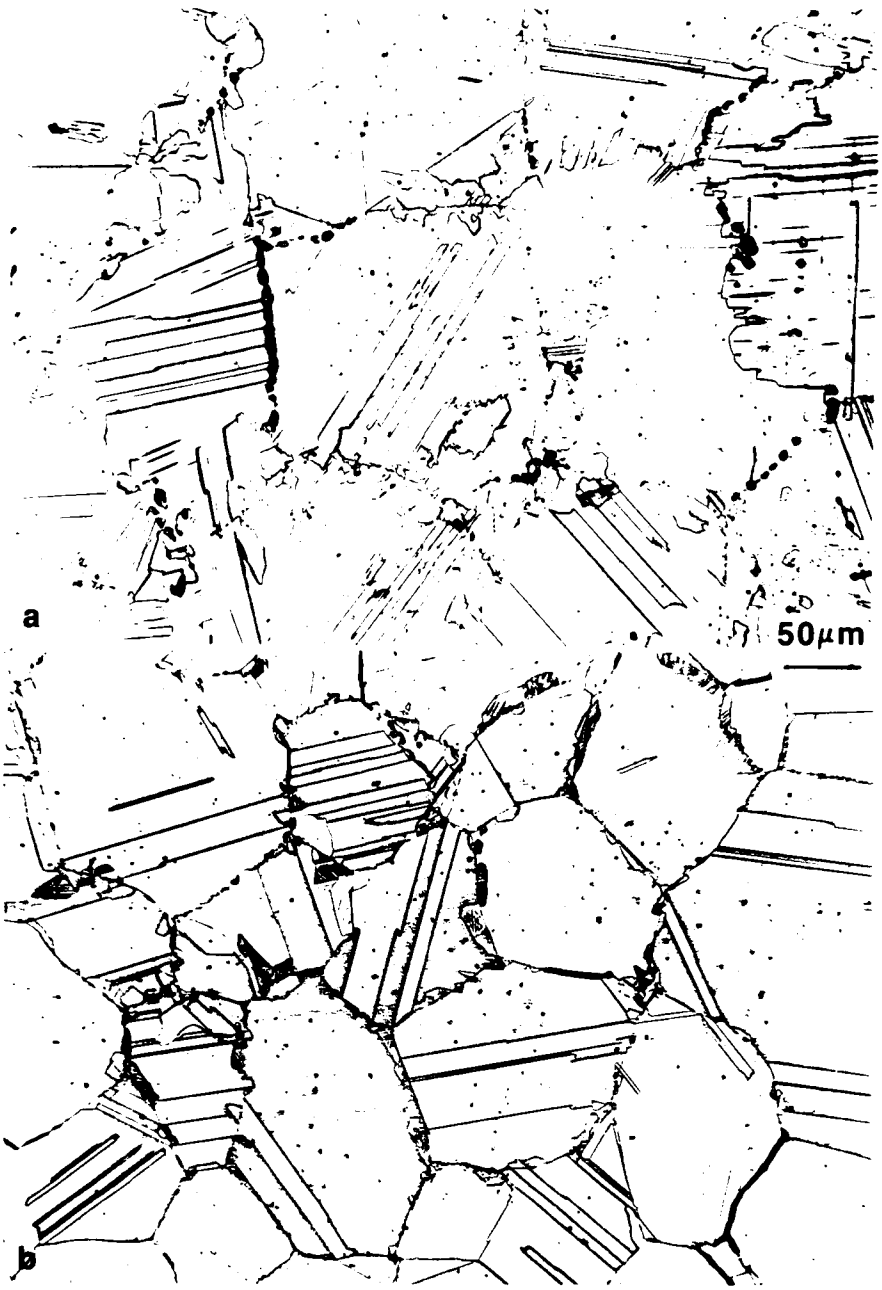


Figure II-26. Optical Microstructures of ordered Ni_4Mo aged at 700 and 600°C. a) 700°C, 840 hrs; b) 600°C, 4500 hrs.

Source: T. S. Lei, "The Effect of 0-8 Wt.% Iron on Transformations of Alpha Phase Ni-Mo-Fe alloys with Ni:Mo Ratio Equal to 4:1," Ph.D. Dissertation, University of Tennessee (1979).

Within the migrated zones, {111} striations characteristic of the microstructure at the higher temperatures are present. In addition, initial annealing twins show instabilities associated with domain boundary migration either from or into the region of the twin.

These microstructural features associated with ordering of Ni_4Mo were interpreted and discussed at length by Stansbury et al. (10). Specific topics addressed were:

1. The nature of the {111} fcc striations.
2. The nature of the {110} fcc striations.
3. Domain morphology, growth and contrast.
4. Boundary instabilities.

These are discussed in detail in the following.

The nature of the {111} fcc striations. The literature relevant to these striations has been cited earlier. Since the straight striations form parallel to annealing twins, traces of {111} fcc planes, they are referred to as the {111} fcc striations. The striations could not be parallel to {100} fcc planes since they were not parallel to the sides of square etch pits but rather to a diagonal drawn across the pits, these pits forming as a consequence of preferential attack along {100} fcc planes.

To determine if these striations arise from stresses due to water-quenching from the aging temperatures, a sample of Ni_4Mo was held for 16 hours at $800^{o}C$ and air cooled. The striations, although fewer in number, were still observed in this sample, thus implying that stresses generated by the water-quenching could partially contribute to their formation.

The tendency to form striations varies considerably. At short times (to 1 hour), ordering occurs in relatively small regions and the striations are confined to these regions. When ordering occurs throughout the grain, at intermediate times, the striations traverse the grains. When extensive domain growth has occurred at 850 and 800^{o}C, the number of striations decrease (Figures II-24b and -25b). The striations result from an intense local etching effect, producing grooves which extend over many domains and show no features which can be related to individual domains. The only structural feature common to all of the domains is that the {111} fcc planes of the initially unordered α, which are common to all of the ordered variants, are also the slip planes along which any strain will have introduced dislocations. It is difficult, however, to associate the etching effect with dislocations on these planes since the grooves are very large in both length and width relative to either dislocations or dislocation arrays. However, when specimens are etched carefully, serrations are sometimes observable on the surfaces of the grooves which give the appearance of rows of etch pits, thus indicating a relationship with dislocations.

Since the striations formed before a hardness maximum, it was proposed that they were mechanical twins in an ordered lattice forming to accommodate both quenching stresses and stresses generated by the tetragonality of the ordered phase. Saburi et al. (15) and Nesbit and Laughlin (186) have also reported mechanical twins in ordered Ni_4Mo deformed by compression. In addition, Nesbit and Laughlin (186) concluded that the mechanical twins were created by overlapping

intrinsic stacking faults. At later stages of ordering, a second mode of relief via intergranular cracking sets in, an observation previously made not only in Ni_4Mo (13,111,177), but also in CuAu (180) and CuPt (181).

The nature of the {110} fcc striations. The second type of striations observed in their study (10) is the presence of tapered bands. The habit plane of these striations has been reported as {110} (177,185) and was confirmed (10) by a single surface trace analysis of the center grain in Figure II-25a (800°C, 10 hours). The trace analysis, based on known orientations of the four annealing twin boundaries within this grain, yielded a grain orientation of $[\bar{1}\ 5\ 10]$ which is 4° from a [012] pole. Based on this orientation, the traces of the four tapered striations in this grain coincided with the traces of {110} planes.

The morphology of these tapered bands is that of groups of irregular domains limited by the boundaries of the tapered region. Based on reported TEM studies (185), the etching of these boundaries is attributed to aligned perpendicular twin boundaries. This explanation was strengthened in this research by the observation that after prolonged aging at 850 and 800°C, the striations consist of rows of domains (Figures II-24b, -25b), and the boundaries tend to be parallel developing a "twin-like" appearance. There is also a marked contrast in the response to etching of domains within and outside the striation. Whether each striation consists of APT-related domains (185) could not be ascertained. Nevertheless, the observation that the

interfaces separating the domains were only slightly curved implied that the striations consisted of APT-related domains (10).

Domain morphology, growth, and contrast. In the initial stages of ordering, the Ni_4Mo domains appear as a fine mottled structure (lower grain in Figure II-24a). Observation at higher magnifications reveals that this structure consists of domains aligned in certain fcc crystallographic directions. The traces of the domain interfaces have been observed to be parallel to {110} fcc planes by Nosova and Polyakova (18) and Tyapkin et al. (187), and confirmed optically by Lei (8) in an $Ni_{4.37}Mo$ + 0.73 wt pct Fe alloy, and by Vasudevan (9) in an Ni_4Mo + 0.41 wt pct Cr alloy.

At 850 and 800°C, the ordering proceeds heterogeneously, since domains form initially in isolated regions, whereas at 700, and possibly 600°C, a heterogeneous mechanism is not apparent. This may be due to the fact that at the lower temperatures, "the frequency of nucleation is so high, and the nucleii so small, that the transformation appears homogeneous," an observation already made elsewhere (13,178).

Following nucleation, the domains enter a growth period and the result of this at 850 and 800°C is the formation of large, patchy regions with irregular boundaries (Figures II-24b, -25b), each region being an individual domain of LRO Ni_4Mo. At 700°C, the domains are still fine, and cannot be observed optically even after 4500 hours at 600°C. This decrease in domain size with undercooling is consistent with classical nucleation and growth behavior.

The sequence of events in the ordering of Ni_4Mo were summarized as follows: At each of the three higher temperatures, the reaction initially involves the formation of PT-related domains (APB's and APTB's may be present but cannot be discerned). The elastic stresses are a minimum for the PT configuration (188) and optically these appear as the {110} fcc striations (185). With the onset of domain growth at the later stages of aging, the {110} striations are gradually consumed (resulting in loss of contrast) by the large, patchy domains. The wavy and irregular nature of these boundaries indicates that they are APB's. The driving force for this reaction must be associated with the lower energy of the APB's and the reduction in domain boundary area. Thus, the APD's and probably APT's are likely to be predominant after long aging times. Kiriyenko and Potapov (189) have however, concluded the reverse, that is, the APD's and APT's form initially and are replaced by PT's. This disagreement may be due to the fact that unlike their study (10), Kiriyenko and Potapov (189) did not carry out aging treatments beyond 16 hours, and therefore did not observe the changing morphology. Obviously TEM investigations would be required to confirm these aspects.

Boundary instabilities. The grain boundary reaction and concomitant migration has been reported previously in Ni_4Mo (12,13,126,190), in other systems involving a cubic to tetragonal transition as in CuAu (180) and Ni_3V (191), in systems involving a cubic to rhombohedral change as in CuPt (181), and in systems involving a cubic to orthorhombic transition as in Ni_2V (106,133). A

closer inspection of the grain boundary reaction, particularly at 700 (Figure II-26a) and 600°C (Figure II-26b), reveals that the migrating boundary is coherent with one grain and incoherent with the adjacent one into which it advances. This type of behavior has been attributed to a coherent allotriomorph in Ni_2V by Tanner (106,133), and to recrystallization by stress-induced boundary migration in CuAu, Ni_4Mo, and CuPt by Arunachalam and Cahn (180), Snyder and Brooks (12), and Irani and Cahn (181) respectively. The latter explanation seems to be appropriate in Ni_4Mo (10).

At 850 and 800°C, stresses associated with transformation to LRO are relieved by intergranular cracking, whereas at 700 and 600°C, grain boundary cracking is not observed. The difference was attributed to the greater cohesiveness of the boundaries at the lower temperatures and hence the stresses are relieved by severe boundary migration (10). Similar observations of this temperature dependence of the stress-relief mechanisms operative during ordering have been made in other systems (180,181).

The instabilities occurring at twin boundaries (Figures II-26a and -26b) and the resultant breakdown of these normally low energy coherent boundaries, results in additional interfaces. Whether this increase in twin interface area is counteracted by decrease in domain boundary area by domain growth could only be speculated upon. In any case, the net result was postulated to represent a lower energy state (10).

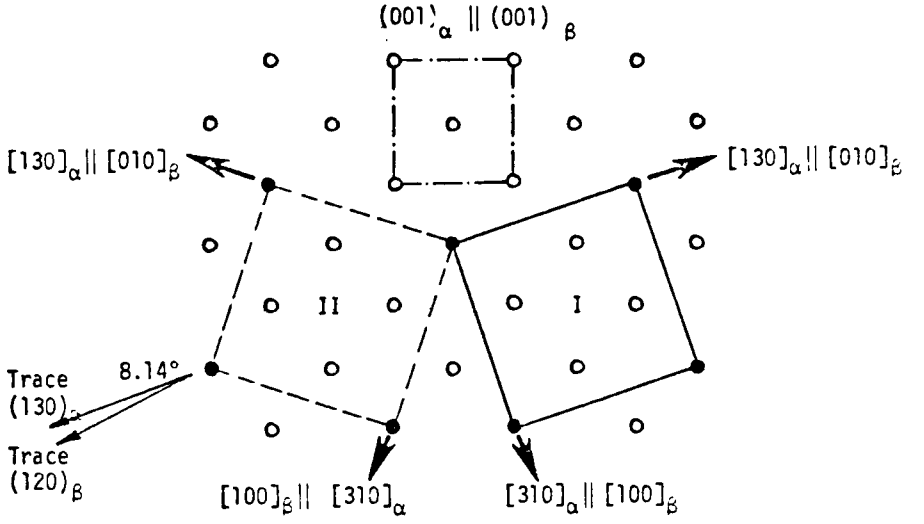
Morphology of single ordered Ni_4Mo domains. The ordering process in Ni_4Mo gives rise to six different orientational variants. Saburi et al. (150) using dark and bright field electron microscopy reported that in samples aged at 800°C, the Ni_4Mo domains were spherical in shape. In an earlier paper (125), they proposed that the orientation relationship between Ni_4Mo domains and the fcc α matrix was: $[\bar{3}10]_\alpha//[100]_\beta$, $[130]_\alpha//[010]_\beta$ and $[001]_\alpha//[001]_\beta$. Chevalier and Stobbs (157) also reported single Ni_4Mo domains at 750 and 800°C having a "pronounced tetragonal prism shape." Similar shaped domains were reported by Lei (8) and Stansbury (171).

Nesbit and Laughlin (81) also reported a morphology of LRO Ni_4Mo domains in a Ni-16.7 at pct Mo alloy after aging for 1000 minutes at 700°C. They (81) proposed an oval shape for the domains when viewed in a direction normal to the c-axis, and a square shape when viewed along the c-axis (the $[001]_\beta$ direction). The habit planes of their model were: $(100)_\alpha//(310)_\beta$ and $(010)_\alpha//(\bar{1}30)_\beta$. They also reported a 2:1 ratio for the dimensions of the domain for the $[001]_\beta$ to the perpendicular direction.

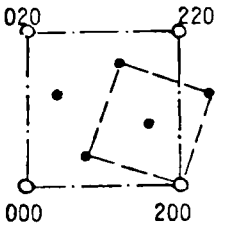
Lei (8) examined in detail the morphology of individual Ni_4Mo domains produced by aging at 850°C for 1 hour, a temperature higher than that in other reports (81,150,157). Besides observing single domains by TEM, he (8) developed etching techniques which permitted observation by optical microscopy. Two variants of ordered Ni_4Mo in real and reciprocal space are shown schematically in Figure II-27 for purposes of discussion. Lei (8), in agreement with the results of Nesbit and Laughlin (81) and Chevalier and Stobbs (157), observed that

the domains were square shaped when viewed in a direction normal to the c-plane of the domain (Figure II-28a), and were "pillow" shaped when the c-axis lies in the plane of observation (Figure II-28b). Based on the SADP, the square domain was shown to be Variant II according to the assignment in Figure II-27. These observations led to the proposal (8) that the boundaries of the Ni_4Mo domain were: $(210)_\alpha//(110)_\beta$ and $(\bar{1}20)_\alpha//(1\bar{1}0)_\beta$. This orientation relationship is identical to that proposed by Chevalier and Stobbs (157), but different from the assignment made by Nesbit and Laughlin (81).

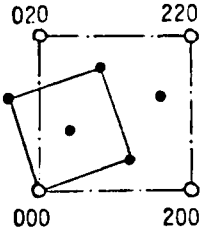
Lei (8) emphasized that in order to properly assign indices to the habit plane between the LRO domain lattice and the fcc lattice, it is necessary to consider LRO diffraction spots from that particular domain. He argued that, if this is not considered, then the interface plane between the Ni_4Mo domain and the matrix could be incorrectly assigned to $(1\bar{3}0)_\alpha//(010)_\beta$ of Variant I instead of the correct assignment of $(\bar{1}20)_\alpha//(1\bar{1}0)_\beta$ of Variant II. He (8) proposed an ideal three dimensional model for the Ni_4Mo domain. This model and perspective sections are shown in Figure II-29. The proposed habit planes were: $(210)_\alpha//(110)_\beta$, $(\bar{1}20)_\alpha//(1\bar{1}0)_\beta$ and $(001)_\alpha//(001)_\beta$. The relative dimensions of the domains were 2:2:1, a ratio reverse to the one proposed by Nesbit and Laughlin (81), but in exact agreement with that of Chevalier and Stobbs (157). Lei (8) and Stansbury (171) point out that in view of the 1.16% contraction along the c-axis and 0.4% expansion along the a- and b-axes, the domains should grow faster in the (001) plane as indicated in Figure II-29. It is conceivable that both alloy composition and different aging temperatures could produce different domain morphologies.



a) —·— Face-centered cubic cell.
—— } I Two possible variants of the β lattice for
– – } II $(001)_\alpha \| (001)_\beta$



b) Reciprocal cell of f.c.c and Variant II of β corresponding to (a).



c) Reciprocal cell of f.c.c. and Variant I of β corresponding to (a).

Figure II-27. The relationship between anti-parallel twins in real space and reciprocal space in Ni_4Mo. $(001)_\alpha//(001)_\beta$.

Source: T. S. Lei, "The Effect of 0-8 Wt.% Iron on Transformations of Alpha Phase Ni-Mo-Fe alloys with Ni:Mo Ratio Equal to 4:1," Ph.D. Dissertation, University of Tennessee (1979).

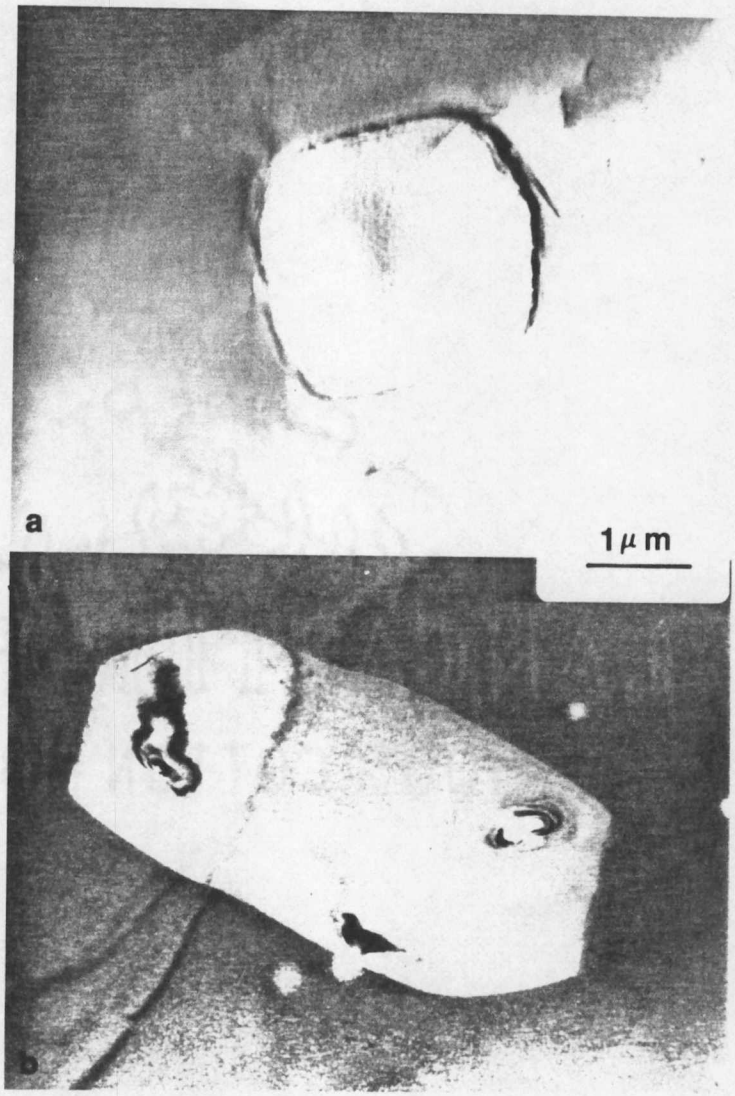
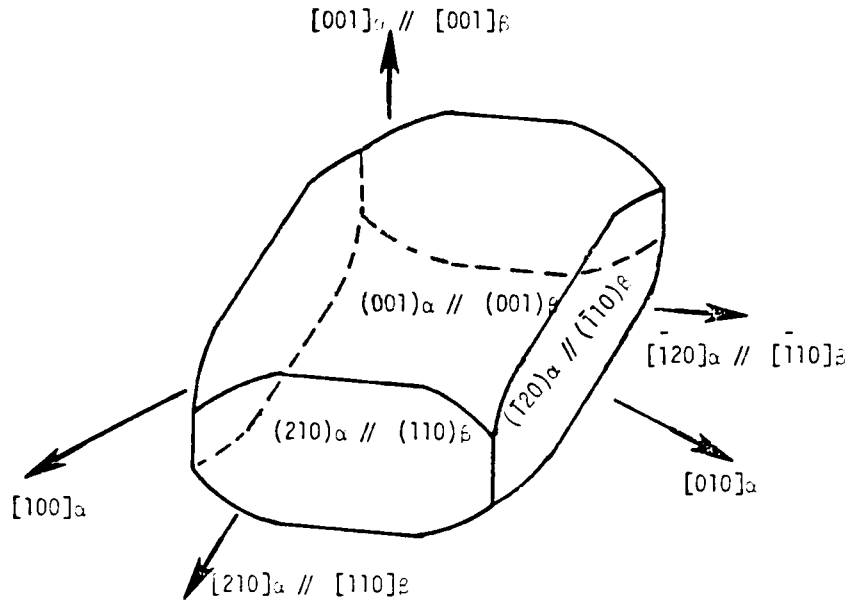
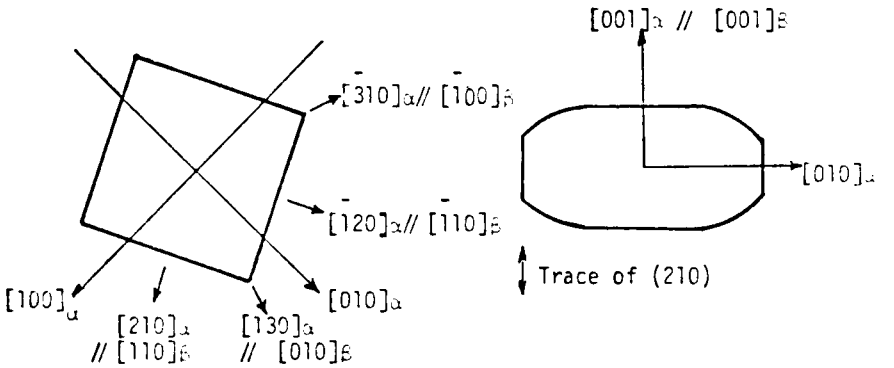


Figure II-28. Bright field micrographs of single Ni_4Mo domains. a) Square domain; b) Rectangular domain.

Source: T. S. Lei, "The Effect of 0-8 Wt.% Iron on Transformations of Alpha Phase Ni-Mo-Fe alloys with Ni:Mo Ratio Equal to 4:1," Ph.D. Dissertation, University of Tennessee (1979).



(a) Ideal three dimensional model of β domains.



(b) Section // (001)β. (c) Section // (100)α.

Figure II-29. Ideal three-dimensional model of Ni_4Mo domains with habit planes and perspective sections.

Source: T. S. Lei, "The Effect of 0-8 Wt.% Iron on Transformations of Alpha Phase Ni-Mo-Fe alloys with Ni:Mo Ratio Equal to 4:1," Ph.D. Dissertation, University of Tennessee (1979).

Lei (8) also followed optically the mechanism by which individual domains and strings of domains agglomerate into "walls." Representative optical micrographs describing this are shown in Figures II-30a and -30b. Generally, the "wall" forms along {100} fcc planes which is confirmed by their being parallel to the edges of square etch pits which develop {100} plane faces. The walls thicken by nucleation and growth of domains over a distance of several domain thicknesses along the wall faces, as implied by the presence of isolated domains near the "wall" faces. The intervening space subsequently transforms allowing the "wall" face to grow. Individual domains and strings of domains some of which have begun to agglomerate are shown in Figure II-30b. Within the agglomerated regions, individual domain boundaries are still resolvable to some extent. The strings are composed mostly of pairs of square domains, many in the antiparallel twin orientation corresponding to the two twin variants of Ni_4Mo in Figure II-27. In addition to the square domains, many elongated domains are also observed (Figure II-30b) both along the strings and isolated in the SRO matrix. These are domains with c-axes in the plane of the surface and hence the thin dimension is observed. Within the "walls" of domains in Figure II-30a, the {111} fcc striations characteristic of ordered Ni_4Mo can also be seen.

The SRO to LRO Transformation in Ni_3Mo

The ordering of Ni_3Mo is quite complex and takes place in several steps. It has been shown that quenched Ni_3Mo displays a SRO similar to that on Ni_4Mo (124-126). During the early stages of the



Figure II-30. Optical microstructures of domain morphology at 850°C. Aged 1 hr. a) Walls formed by agglomeration of single domains in SRO matrix; b) Single, stringers and agglomeration of domains in SRO matrix.

Source: T. S. Lei, "The Effect of 0-8 Wt.% Iron on Transformations of Alpha Phase Ni-Mo-Fe alloys with Ni:Mo Ratio Equal to 4:1," Ph.D. Dissertation, University of Tennessee (1979).

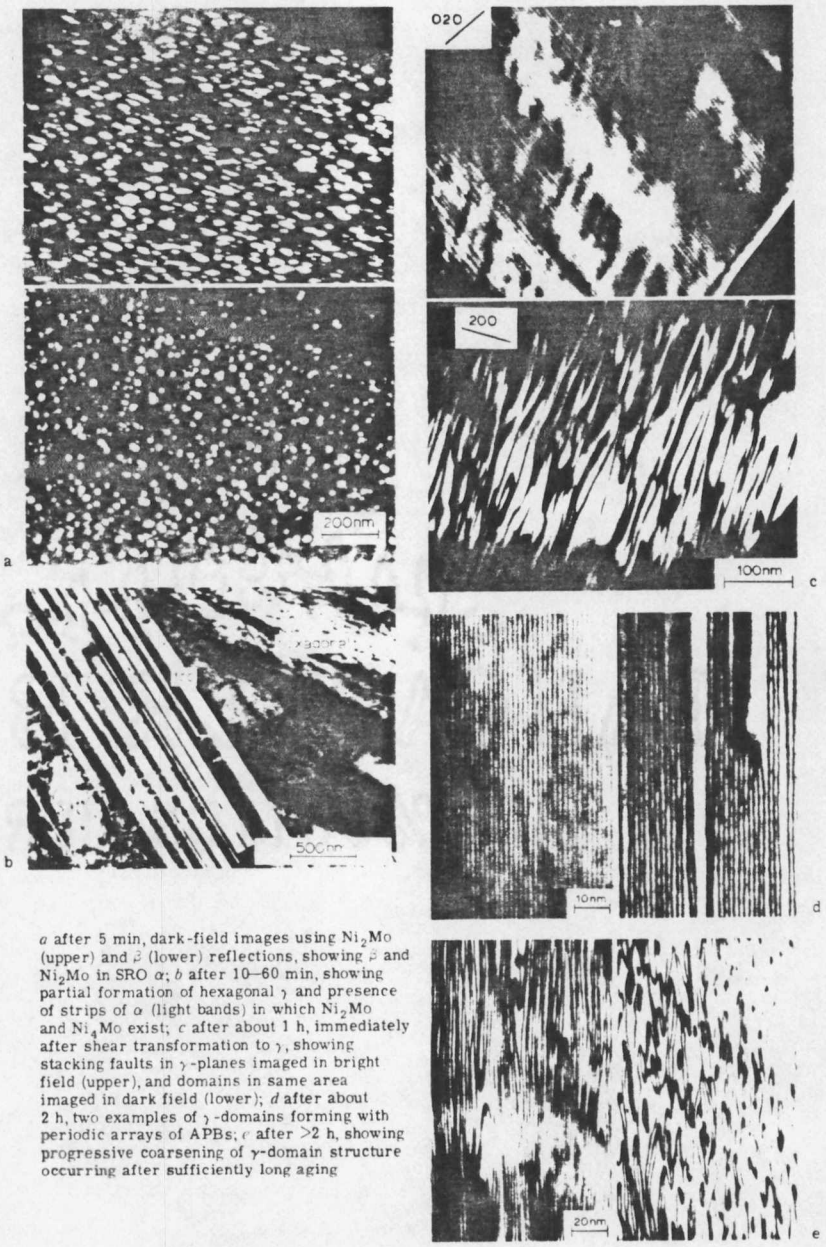
transformation at 860°C, Yamamoto and co-workers (124,125) first reported the formation of Ni_2Mo as a metastable phase. This has been confirmed by several researchers (122,123,126-129). According to Yamamoto et al. (125), the transformation from α to ordered Ni_3Mo takes place in four stages: 1) decompositon of α to Ni_4Mo and Ni_2Mo, 2) growth of Ni_4Mo domains and coagulation of Ni_2Mo along Ni_4Mo domain boundaries, 3) nucleation of Ni_3Mo at grain boundaries, and 4) growth of Ni_3Mo to consume previous Ni_4Mo and Ni_2Mo.

Van Tendeloo et al. (122,123), in studying structural changes in Ni_3Mo at 820°C, also reported, a very dense one-dimensional array of two-dimensional defects during the early stages. These defects were established to be a long period superstructure characterized by periodic non-conservative antiphase boundaries of mean spacing 1.39 nm (122) and composition $Ni_{3.4}Mo$ (123). The spacing between the LPAPB's was determined from TEM images and from the separation of spots in the diffraction patterns, and the composition of the superstructure (having a local excess of nickel atoms) was determined by x-ray microanalysis. These APB's formed parallel to the (100) Ni_3Mo planes and were characterized by a displacement vector, $R = (2n + 1)[102]/4$. The unit cell dimensions and atomic arrangement on the close packed plane for this structure were described earlier (pages 58-59). This periodic array of APB's forms as a consequence of a shear transformation that is required to transform the fcc stacking to hcp stacking in Ni_3Mo. In a subsequent report, Van Tendeloo et al. (127) argued that from theoretical considerations the DO_{22} phase is expected to form in nickel-molybdenum alloys, and also obtained evidence for

this phase during the very early stages of ordering of Ni_3Mo (127,128). This structure was produced only under specially executed experimental conditions and was generated immediately from the SRO state. Subsequent aging produced Ni_4Mo and Ni_2Mo in a fcc matrix, which was then sheared into the Ni_3Mo structure, with the LPAPB as an intermediate step (127,128). The microstructural development of the different intermediate structures during the various stages of ordering of Ni_3Mo is illustrated in Figure II-31.

A recent publication by Schryvers, Van Tendeloo and Amelinckx (129) has provided significant insight into the rather complicated mechanism of ordering of Ni_3Mo. Using high resolution electron microscopy (HREM), they were able to establish the correct sequence of steps involved during the ordering of Ni_3Mo as a function of temperature. They also determined an unambiguous value for the factor n in the expression for the displacement vector ($R = (2n + 1)[102]/4$) of the LPAPB's, which was important for arriving at the correct atomic model for the long period superstructure. Based on computer calculations of the high resolution (HR) images of the atomic configuration of the LPAPB structure, the value of n was determined as 1, thus establishing the displacement vector, R as $3[102]/4$. This value of R is one fourth that for the APB's in the equilibrium Ni_3Mo superlattice. The resulting atomic model for the LPAPB is illustrated in Figure II-15 (page 59).

The transformation of the high temperature fcc α phase to ordered Ni_3Mo is dependent on temperature and takes place in the manner illustrated in Figure II-32. When the high-temperature fcc



a after 5 min, dark-field images using Ni_2Mo (upper) and β (lower) reflections, showing β and Ni_2Mo in SRO α; *b* after 10—60 min, showing partial formation of hexagonal γ and presence of strips of α (light bands) in which Ni_2Mo and Ni_4Mo exist; *c* after about 1 h, immediately after shear transformation to γ, showing stacking faults in γ-planes imaged in bright field (upper), and domains in same area imaged in dark field (lower); *d* after about 2 h, two examples of γ-domains forming with periodic arrays of APBs; *e* after >2 h, showing progressive coarsening of γ-domain structure occurring after sufficiently long aging

Figure II-31. TEM micrographs showing the sequential development of intermediate structures during ordering of Ni_3Mo. Aged at $800^{o}C$.

Source: After ref. 34 in C. R. Brooks, J. E. Spruiell and E. E. Stansbury, "Physical Metallurgy of Nickel-Molybdenum Alloys," Inter. Met. Rev., 29, 210-248 (1984).

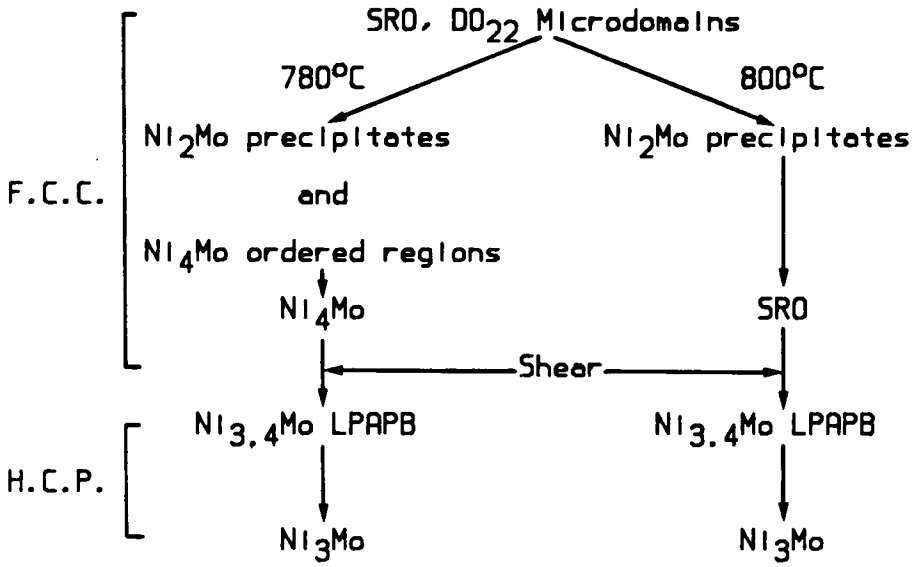


Figure II-32. Mechanism of ordering of Ni_3Mo.

Source: D. Schryvers, G. Van Tendeloo and S. Amelinckx, "On the Ordering Mechanism of Ni_3Mo: A High Resolution Electron Microscopy Study," Phys. Stat. Sol. (a), 87, 401-415 (1985).

phase is rapidly quenched by direct contact with water, only SRO reflections at the {1 1/2 0} positions were observed. On the other hand, in material quenched slowly in quartz tubes, intensity in the form of diffuse rings passing through the SRO spots, together with faint segments at the {100} positions were observed. These diffraction effects and accompanying dark field images established the presence of DO_{22} microdomains distributed sparsely in the SRO matrix. Short annealing (to 5 minutes) produced Ni_2Mo at 800°C, whereas at 770°C ordered regions of Ni_4Mo and Ni_2Mo precipitates appeared simultaneously. The DO_{22} microdomains served as the nucleation sites for the Ni_2Mo at 800°C. At 770°C, the Ni_4Mo domains were observed to form along the {110} Ni_2Mo planes and subsequent growth of these eliminated the fcc SRO matrix and the Ni_2Mo precipitates. At 800°C, no Ni_4Mo was observed, which is contrary to the reports of Yamamoto and co-workers at 860°C (124,125).

On continued aging at 800°C, the Ni_2Mo precipitates were initially replaced by the fcc SRO and the transformation progressed by the formation of bands of LPAPB in hcp stacking separated by bands of fcc stacking and limited by close packed planes $(0001)_{hcp}$ // $(111)_{fcc}$. Schyvers et al. (129) argued that the Ni_2Mo precipitates produce large accommodation strains in the fcc matrix and hence have to disappear in order to accomplish the shear transformation. On the other hand, continued aging at 700°C produced fcc bands containing only ordered Ni_4Mo domains; neither Ni_2Mo precipitates nor SRO were present, a situation different from that at 800°C. Thus, in this case, the Ni_4Mo is sheared into the hcp-stacked LPAPB structure. Along the contact

plane $(111)_{fcc}$ // $(0001)_{hcp}$ or (010) Ni_3Mo, the planes parallel with the ones on which the shear takes place, two ordered phases meet, Ni_4Mo on the fcc side and Ni_3Mo on the hcp side.

The close packed planes for Ni_4Mo are the (111) fcc planes, whereas that for the LPAPB and the Ni_3Mo are the (010) Ni_3Mo planes. To support the experimental results, Schryvers et al. conducted a detailed examination of the atomic arrangement on the close packed planes of the Ni_4Mo, the LPAPB and the Ni_3Mo, and argued that the Ni_4Mo (Figure II-33a) can be sheared into the hcp-stacked Ni_3Mo (Figure II-33c) only by taking-up the intermediate LPAPB configuration (Figure II-33b). The process, they stated, cannot be one of pure shear, since shear conserves the atomic configurations--which is clearly not the case--and must involve a combination of shear and diffusional rearrangement of atoms. This diffusional process, they pointed out, could be envisaged alternatively as the periodic insertion of two different kinds of APB's perpendicular to the shear plane (parallel to the future (100) Ni_3Mo planes) with displacement vectors, R_1 = [102]/4 and R_2 = [100]/2 referred to the stable Ni_3Mo structure.

Eventual coarsening of the periodic APB's in groups of four, by a hairpin mechanism, produces the APB's characteristic of the stable, equilibrium Ni_3Mo (122,123,127-129).

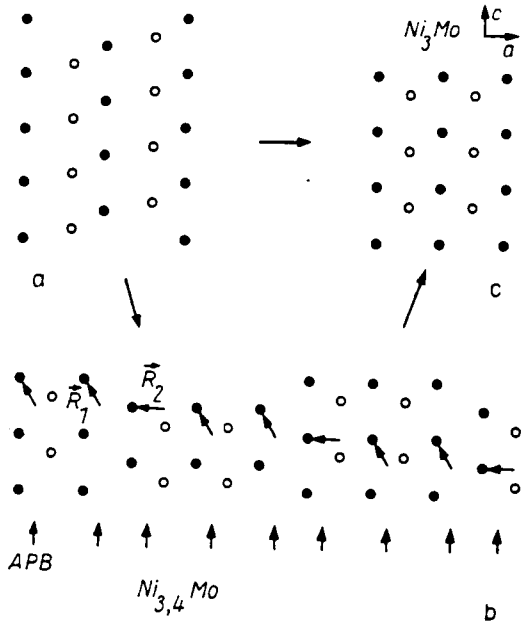


Figure II-33. Possible sequence for the shearing mechanism from Ni_4Mo to Ni_3Mo. The shearing from Ni_4Mo (a) is accompanied by the introduction of APB's normal to the shear plane to form the LPAPB structure (b), which coarsens into the stable Ni_3Mo (c).

Source: D. Schryvers, G. Van Tendeloo and S. Amelinckx, "On the Ordering Mechanism of Ni_3Mo: A High Resolution Electron Microscopy Study," Phys. Stat. Sol. (a), 87, 401-415 (1985).

Ordering in Nickel-Molybdenum Ternary Alloys

The Ni-Mo-Fe System

Norem and Stansbury (20) investigated the phase relationships in the ternary Ni-Mo-Fe system. Their proposed isothermal section for 890, 860, 800 and 700°C are shown in Figures II-34a-d. A schematic phase diagram of the nickel-rich portion constructed by Lei (8) from the results of this work (20) is depicted in Figure II-35. It should be remembered that these ternary sections are not necessarily identical to the equilibrium phase diagram for this system. There are significant differences between alloys of the same composition treated for 1000 hours and 3400 hours and hence there is no reason to assume that the 3400 hour sample represents the equilibrium state. However, if the microstructure of the alloy does not show any changes other then coarsening of existing reaction products after being held for a sufficiently long time at a particular temperature, then it can be reasonably assumed that the system has attained equilibrium.

It was found in this investigation (20) that addition of small amounts of iron rapidly suppresses the formation of the Ni_4Mo phase. In fact, an alloy containing 4 wt pct Fe showed no Ni_4Mo at any temperature. Earlier work done by Stansbury (192) at the University of Tennessee, indicated that the solubility of iron in Ni_4Mo is about 3 wt pct at 700°C, 2.5 wt pct at 800°C and less than 2.5 wt pct at 850°C. Lei (8) in slight contrast to this, reported the solubility of iron in the Ni_4Mo phase as 4.5, 3.2, 1.3 and 0.3 wt pct at 600, 700, 800 and 850°C respectively.

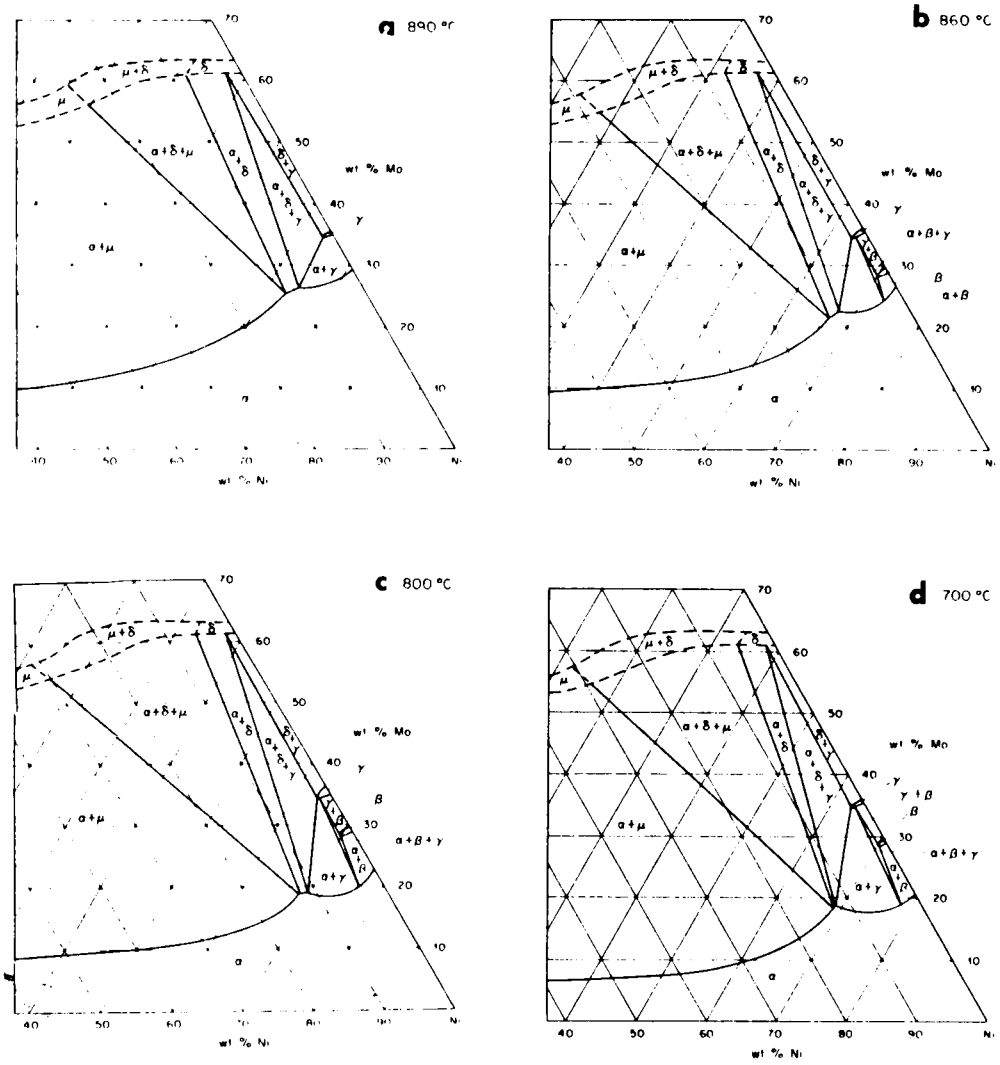


Figure II-34. Isothermal sections of the Ni-Mo-Fe ternary phase diagram. a) 890°C; b) 860°C; c) 800°C; d) 700°C.

Source: W. E. Norem and E. E. Stansbury, "An Investigation of Nickel-Rich Alloys Containing Molybdenum and Iron," Report to Union Carbide, Oak Ridge National Laboratory, Oak Ridge, TN (1963).

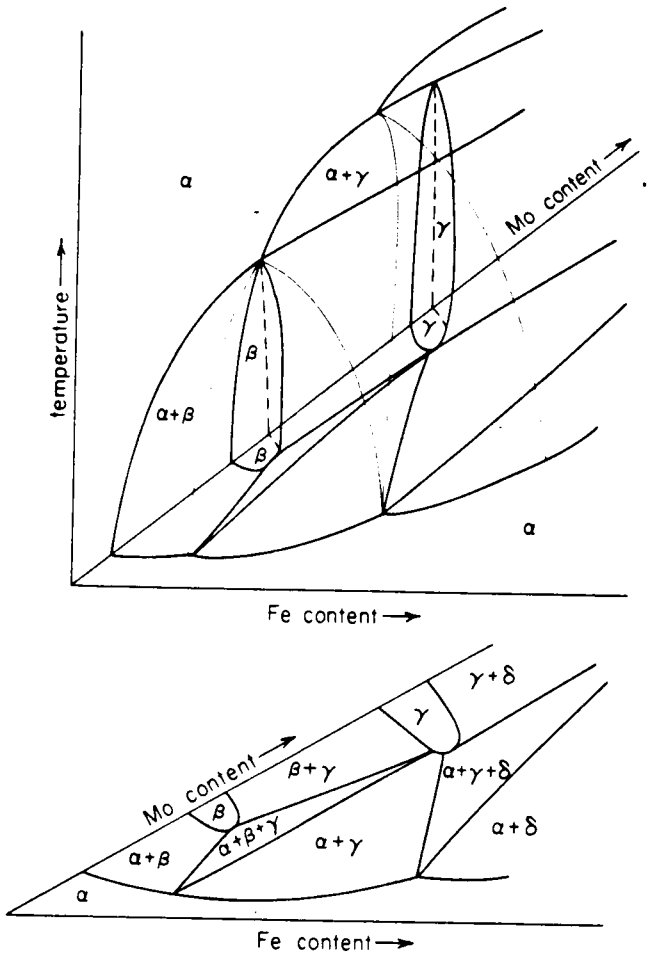


Figure II-35. Schematic depiction of the Ni-rich region of the Ni-Mo-Fe phase diagram. The isothermal section at the base of the upper figure is shown in more detail in lower figure.

Source: T. S. Lei, "The Effect of 0-8 Wt.% Iron on Transformations of Alpha Phase Ni-Mo-Fe alloys with Ni:Mo Ratio Equal to 4:1," Ph.D. Dissertation, University of Tennessee (1979).

A two phase α and Ni_3Mo (γ) field was found to exist between 868 and 910°C (Figures II-34a,-34b). This field varies only slightly with temperature. At temperatures below 868°C, the critical LRO temperature for Ni_4Mo, a three phase $\alpha + \beta + \gamma$ field exists (Figures II-34c,-34d). In alloys containing higher amounts of iron, a three phase $\alpha + \gamma + \delta$ field was found to exist (Figures II-34a-d).

Continuous Heating and Cooling Kinetics in Ni-Mo-Fe and Ni-Mo-Cr Alloys

Lei (8) investigated the kinetics of ordering in Ni_4Mo-based alloys containing 0 to 8 wt pct Fe on continuous heating and cooling using electrical resistivity measurements. Vasudevan (9) carried out similar studies in Ni_4Mo alloys with chromium in the range 0 to 4 wt pct. His results (9,21) are presented here in some detail and compared, where appropriate, to those of the effect of iron (8). The difference in transformation behavior between Ni_4Mo and alloys containing chromium is shown by comparing their resistivity values under the following conditions:

1. As cold reduced 68% RA.
2. Water quenched from 950°C
3. Rapidly cooled from 950°C to 25°C at 60°C/min.
4. Slow cooled from 950°C to 25°C at 1°C/min.

In addition, the temperature dependence of structural changes is inferred by analyses of changes in slope of the resistivity-temperature curve occuring on heating and cooling. These results are summarized in Table II-1 and Figures II-36 and -37. Several consistent changes in resistivity as a function of chromium content are evident.

First, the resistivity in the SRO state decreases with an increase in chromium content (Figure II-36), and since SRO increases resistivity over that for the random state in this system, this suggests that decreased SRO in chromium-containing Ni_4Mo alloys more than compensates for the normal increase expected on additional solid solution alloying. Second, irrespective of the cooling rate employed to retain SRO, or the extent of cold work, the slopes of the lines representing the effect of chromium are the same (Figure II-36). This implies that regardless of the degree of SRO, as represented by the resistivity, the effect of chromium is independent of either cooling rate or cold working.

It is also evident from the resistivity values in Figure II-36 that the degree of SRO after cooling at $60^{o}C$/min in vacuum is higher than that following water-quenching. This higher resistivity on slower cooling correlates with the longer time available to increase the degree of SRO on cooling than that available on water-quenching. This result is corroborated by the observation of De Ridder et al. (172) that the intensity of the {1 1/2 0} diffuse peaks in the diffraction pattern associated with SRO increases with a decrease in cooling rate.

A third influence of chromium, shown in Table II-1 and Figure II-37 for alloys slowly cooled at $1^{o}C$/min from $950^{o}C$, is the increase in room temperature resistivity with an increase in chromium content. The increase in resistivity is small to 0.74 wt pct Cr, beyond which there is a sharper rise. The high value for the 3.84 wt pct Cr alloy indicates complete suppression of LRO for cooling rates exceeding $1^{o}C$/min from above the ordering temperture. In Ni_4Mo + Fe alloys under

TABLE II-1

Typical Values of Resistivity* of Ni-Mo-Cr Alloys

Alloy	NMCR0	NMCR6	NMCR3	NMCR1	NMCR2	NMCR4	NMCR5
Conditions	Ni_4Mo	0.41% Cr	0.54% Cr	0.74% Cr	2.08% Cr	2.97% Cr	3.84% Cr
W.Q. from 950°C	140.6	135.0	139.5	136.2	136.4	133.3	134.2
Cold reduced 68% RA	120.1	119.2	118.5	118.0	117.7	116.7	115.8
Cooled 60°C/min. from 950°C	146.4	144.5	144.0	145.0	145.0	142.5	142.5
Cooled 1°C/min. from 950°C	50.0	53.0	58.5	61.0	84.0	132.5	144.5
Ordering Temperature							
On heating, °C	868	865	860	855	825	—	—
On cooling, °C	800	800	785	770	725	—	—

*Resistivity in micro-ohm-cm. at room temperature.

Source: K. Vasudevan, "The Effect of 0-4 Wt Pct Chromium on Transformations of Alpha Phase Ni-Mo-Cr Alloys with Ni:Mo Atom Ratio Equal to 4:1," M.S. Thesis, University of Tennessee (1982).

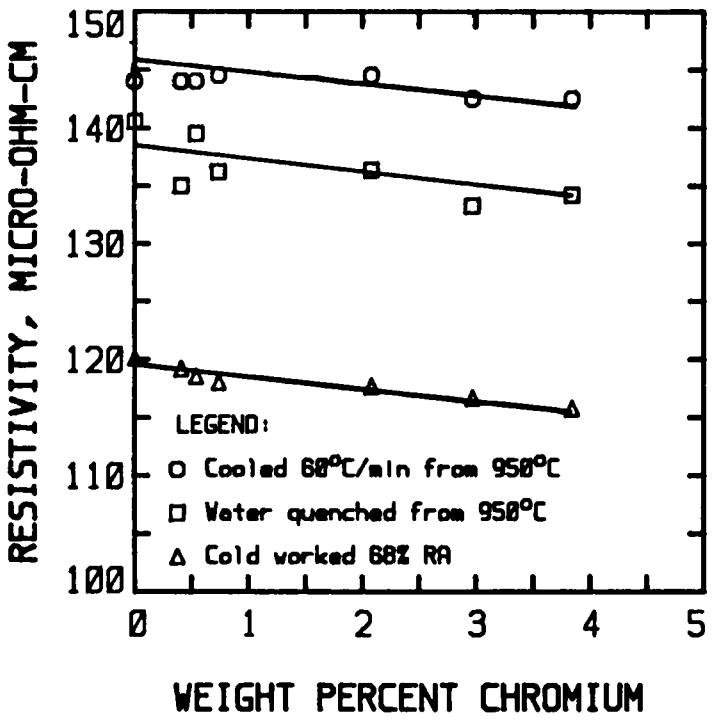


Figure II-36. Variation of SRO resistivity at 25°C of Ni-Mo-Cr alloys.

Source: K. Vasudevan and E. E. Stansbury, "Influence of Chromium on Ordering of Ni_4Mo," Scripta Met., 19, 1101-1106 (1985).

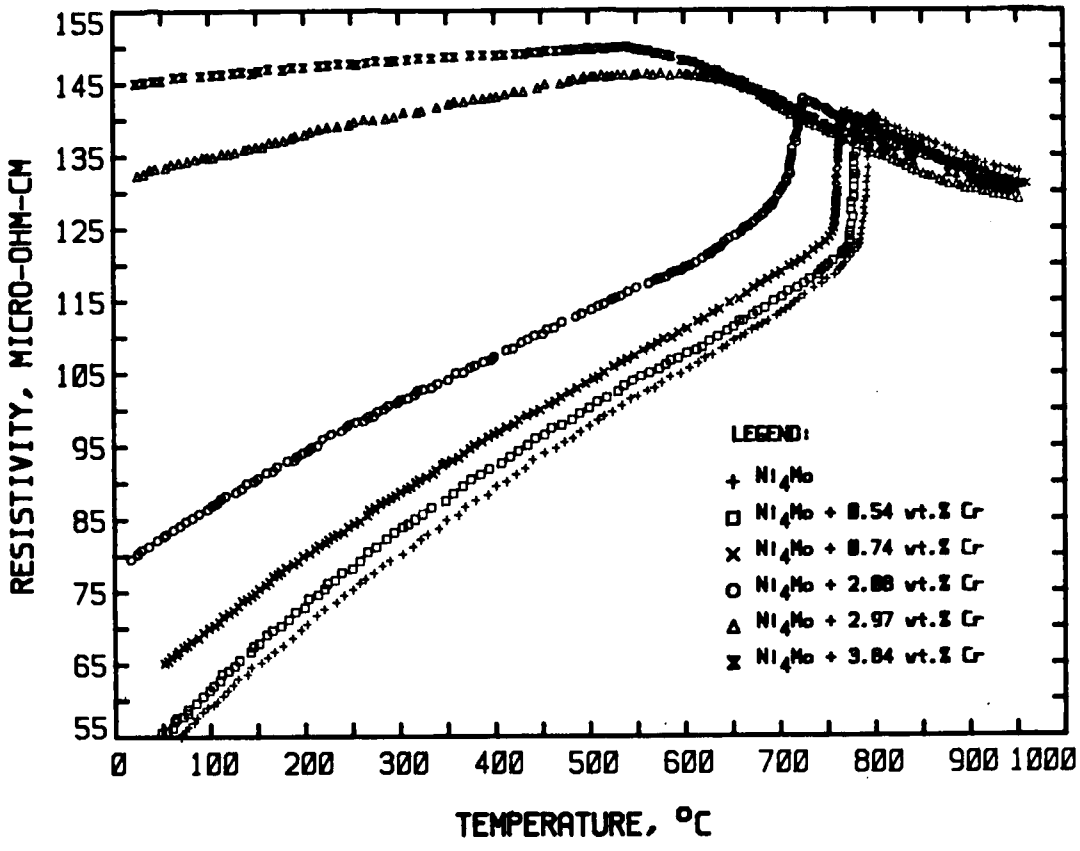


Figure II-37. Variation of resistivity of Ni-Mo-Cr alloys with temperature on slow cooling. Cooled at $1^{o}C$/min from $950^{o}C$.

Source: K. Vasudevan and E. E. Stansbury, "Influence of Chromium on Ordering of Ni_4Mo," Scripta Met., 19, 1101-1106 (1985).

the same conditions, complete suppression of LRO occurs above 4.4 wt pct Fe (8), indicating that chromium is somewhat more effective than iron in slowing the kinetics of ordering of Ni_4Mo.

It is not clear whether chromium increases the resistivity by enhancing electron scattering in the LRO state just as foreign atoms do and/or decrease the degree of LRO, or that the transformation is incomplete within the time range of cooling. At least in alloys containing to 0.74 wt pct Cr the increase appears to be solely due to increased electron scattering, whereas in those containing 2.08 wt pct Cr and above, both increased scattering and decreased degree of long range order are contributory.

A final feature observable in Table II-1 is the lowering of the LRO-SRO transformation temperature with addition of chromium in the range 0-2.08 wt pct on heating at $10^{o}C$/min and cooling at $1^{o}C$/min. The transformation temperatures for the 2.97 wt pct and 3.84 wt pct Cr alloys were indistinct, because of the sluggish kinetics. The disordering temperature is relatively insensitive to the heating rate, and from observations on the binary alloy, is near the value for equilibrium. However, on cooling at $1^{o}C$/min, the ordering temperature is progressively decreased with increasing chromium content. This effect of chromium on the ordering temperature was shown to be consistent with microhardness, resistivity and microstructural observations of long-time isothermally aged alloys (9).

Isothermal Kinetics of Ordering in Ni_4Mo-Based Ternary Alloys

Studies on the influence of a wide variety of alloying elements on the transformation behavior of Ni_4Mo alloys are limited. There have

been reports both on structural changes in alloys containing vanadium (23,24), niobium (23,24), iron (8) and chromium (9) and in commercial alloys (26,27,29-32). Other than the studies of Norem and Stansbury (20) and Lei (8) on the effect of iron and that of Vasudevan on chromium, there have been limited systematic attempts at establishing changes in the microstructure and properties over a wide range of temperatures and times. The role of third elements in the commercial alloys Hastelloy B and Hastelloy B-2 cannot be overlooked. These alloys are based on the Ni_4Mo composition and can undergo substantial structural changes in the form of one or more ordered phases when subjected to certain ranges of temperature during service (26,27,29-32), which can lead to premature failure. Although these alloys are not used at high temperatures, the possibility of such an occurrence should not be discounted. In this section, the results of the literature cited above as they pertain to structural and property changes, are described.

Effect of Vanadium and Niobium. Kiriyenko et al. (23) examined the influence of 2.09-2.39 at pct V and 1.34 at pct Nb on ordering kinetics in a Ni-19 at pct Mo alloy at 700 and 800°C. They (23) found that addition of V slowed down the ordering at 700°C and takes more than 100 hours. At 800°C, the reaction was slowed down initially, but after 7 hours a rapid increase in hardness was observed due to the formation of Ni_3Mo. This phase was not observed at 700°C. The effect of Niobium on moderating the ordering process was less marked. This is probably associated with smaller amounts of this addition. Some Ni_3Mo was observed at 800°C; only Ni_4Mo was present at 700°C.

Kiriyenko et al. (23) suggested that ordering becomes slow in these ternary alloys at high temperatures because diffusion of molybdenum atoms was reduced due to the development of vacancy complexes around vanadium atoms, as a result of which there is a change in the number of migrations which molybdenum atoms can make over the distances required for the formation of an ordered nucleus. They pointed out that the capacity of vanadium for formation of such complexes may be less marked at lower temperatures. Addition of vanadium to Ni_4Mo was proposed to alter the phase diagram, in particular, depressing the ordering temperature and perhaps expanding the α + Ni_3Mo region. The increased probability of stacking faults in ternary alloys, they claimed, could under certain circumstances act as basis for formation of Ni_3Mo.

Vlasova et al. (24) in their study of a $Ni_{78.6}Mo_{19}V_{2.4}$ alloy, in contradiction to the results of Kiriyenko et al. (23), did not observe any changes in the initially quenched SRO state at 800°C. Neither Ni_4Mo nor Ni_3Mo were reported. This is probably because the aging times used by them (24) were shorter (3 hours). At 700°C, however, again in contrast to the results of Kiriyenko et al. (23), initial aging produced Ni_4Mo which was then followed by the formation of DO_{22} and Ni_2Mo. The latter two phases did not show any tendency to disappear, but instead persisted till 500 hours.

Effect of iron and chromium. Lei (8) studied the ordering kinetics in Ni_4Mo-Fe alloys at 600, 700, 800 and 850°C using resistivity and hardness measurements. He found that the resistivity

increases and hardness decreases with an increase in iron content over the composition limits and at temperatures and times for which the Ni_4Mo phase is indicated as present in Figure II-38. Kinetically iron slows down the ordering as is evident from the TTT curve in Figure II-39.

With increasing iron contents, the microstructure changes progressively from β to $\alpha + \beta + \gamma$, $\alpha + \gamma$, $\alpha + \gamma + \delta$ and $\alpha + \delta$ as evident from Figure II-38. Initial increase in resistivity for compositions to 0.74 wt pct Fe, was associated with partial decomposition of β to $\alpha + \gamma$. At 1.94 wt pct Fe, the microstructure is $\alpha + \gamma$ at 850°C and the high resistivity was associated with the predominant influence of the SRO α phase. In alloys containing still higher iron contents, a discontinuous precipitation of δ phase was observed at the higher temperatures. For the reactions occurring at temperatures below 850°C (Figure II-38), similar correlations were drawn between the behavior of the resistivity and observed phases as they changed with iron content (8).

Vasudevan (9) studied the ordering kinetics in Ni_4Mo-Cr alloys containing chromium in the range 0 to 4 wt pct at 600, 700, 800 and 850°C for times upto 4500 hours using resistivity, microhardness, optical and scanning electron microscopy (SEM). To determine the local identity of phases, energy dispersive analysis of x-rays (EDAX) in the SEM was employed. His results substantiate the results of Lei (8) in that, addition of a third element slows down the kinetics of ordering of Ni_4Mo. The effect of chromium though, was greater. Vasudevan's (9) results on the resistivity, hardness and the phases present at the end

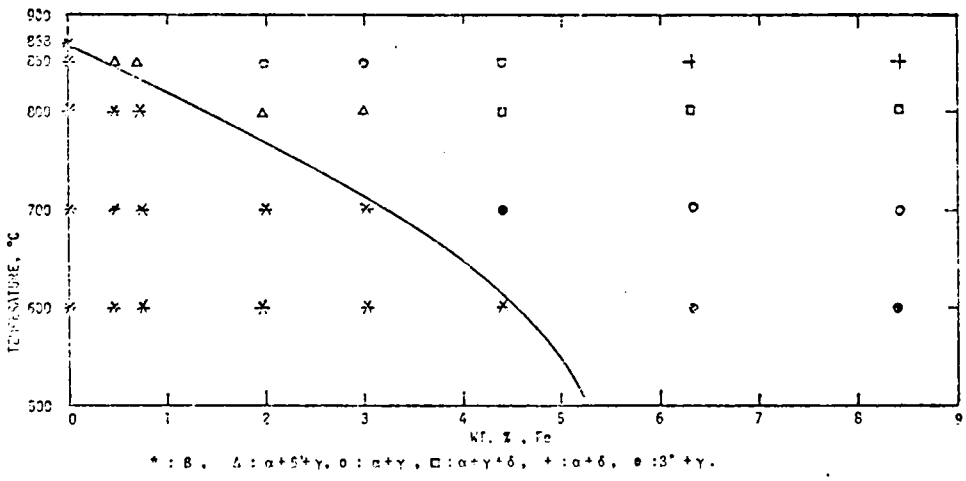


Figure II-38. Phases present in Ni-Mo-Fe alloys after aging 4500 hrs at 600 and 800°C and 2000 hrs at 700 and 850°C.

Source: T. S. Lei, "The Effect of 0-8 Wt.% Iron on Transformations of Alpha Phase Ni-Mo-Fe alloys with Ni:Mo Ratio Equal to 4:1," Ph.D. Dissertation, University of Tennessee (1979).

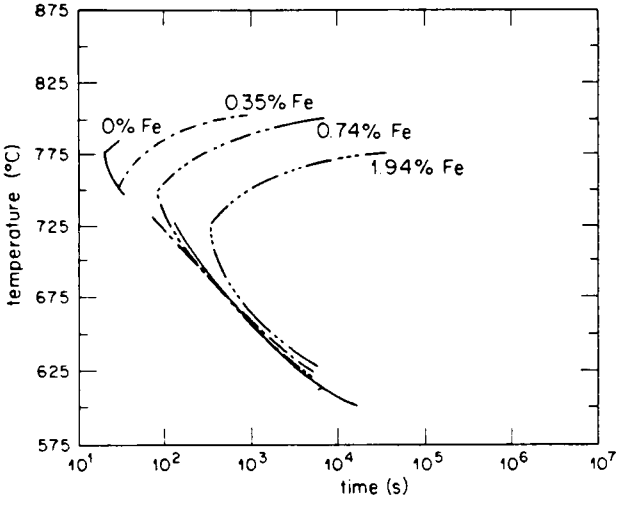


Figure II-39. Effect of iron on kinetics of α-phase transformation in Ni_4Mo-based alloys.

Source: T. S. Lei, "The Effect of 0-8 Wt.% Iron on Transformations of Alpha Phase Ni-Mo-Fe alloys with Ni:Mo Ratio Equal to 4:1," Ph.D. Dissertation, University of Tennessee (1979).

of 4500 hours at each of the above four temperatures are summarized in Figures II-40a, -40b and -41, respectively.

Effect of chromium at 850°C. With increasing chromium contents, the microstructure progressively changes from β phase to α + β + γ, α + γ and α + γ + δ as seen in Figure II-41. The initial increase in resistivity (Figure II-40a) in the range 0 to 0.74 wt pct Cr is due to partial decomposition of the β to α and γ. The rapid increase at compositions of 2.08 wt pct Cr and above is due to large amounts of the SRO α phase. In the higher chromium alloys (2.97 and 3.84 wt pct), a discontinuous precipitation of α and δ phases was observed. This reaction has also been reported by Tawancy (30) in Hastelloy B-2 aged at 900 and 955°C.

Effect of chromium at 800°C. As shown in Figure II-41, with increasing chromium contents, the phase relationships change from β→ α + β + γ → α + β + γ. The increase in resistivity with increasing chromium (Figure II-40a) is associated with the appearance of increasing amounts of α. A discontinuous precipitation of α and δ was also observed at this temperature in the 2.97 and 3.84 wt pct Cr alloys.

Effect of chromium at 700°C. The phase relationships are more complicated at this temperature. With increasing chromium, the phases change in the sequence β → α + β + γ → α + β + γ + δ. The small increase in resistivity (Figure II-40a) for chromium contents to 0.74 wt pct is due to partial decomposition of β to α + γ at the grain boundaries. Subsequent increase in resistivity at the higher chromium levels is associated with larger amounts of α within the matrix.

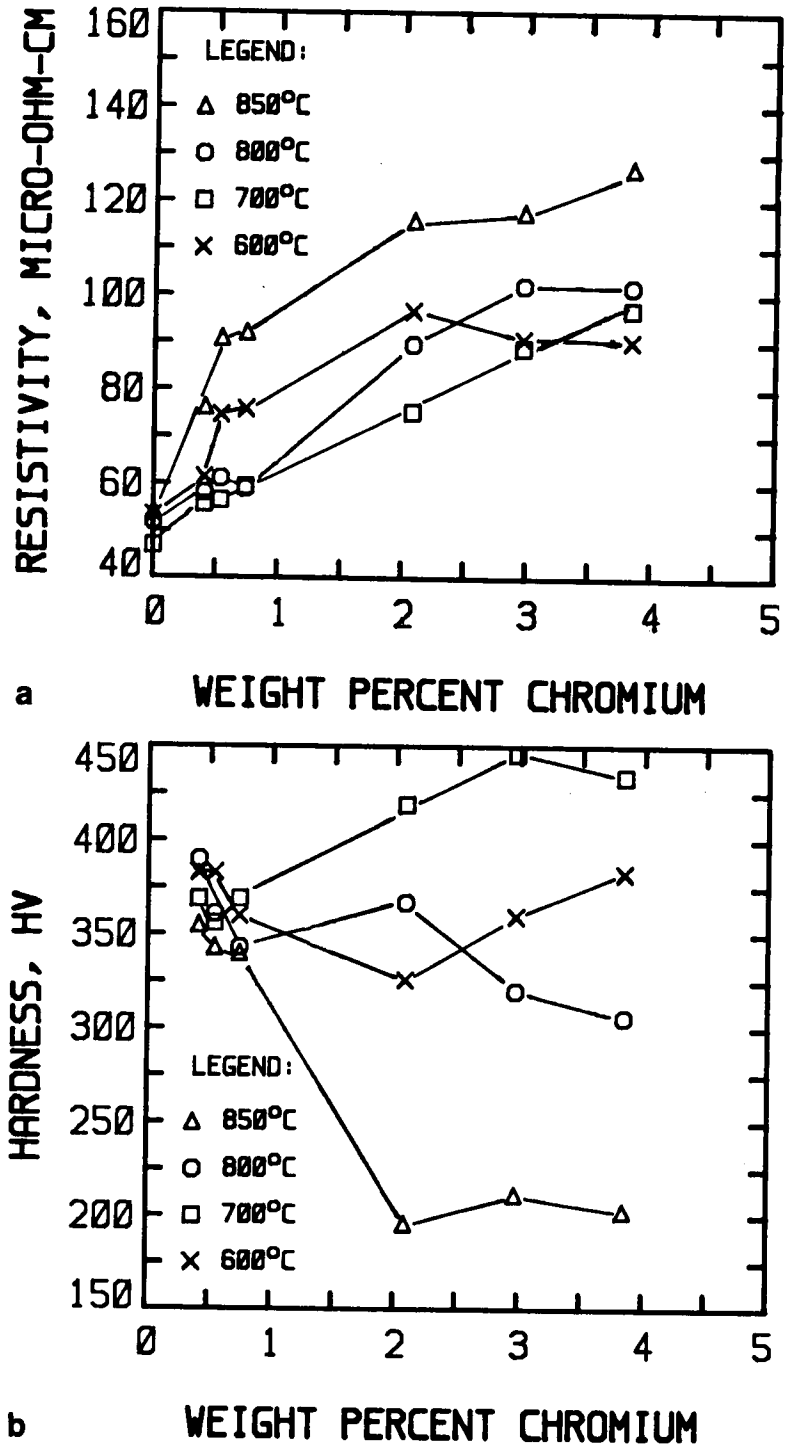


Figure II-40. Resistivity (a) and microhardness (b) as a function of chromium content in Ni_4Mo alloys. Aged 4500 hrs at the indicated temperatures.

Source: K. Vasudevan, "The Effect of 0-4 Wt Pct Chromium on Transformations of Alpha Phase Ni-Mo-Cr Alloys with Ni:Mo Atom Ratio Equal to 4:1," M.S. Thesis, University of Tennessee (1982).

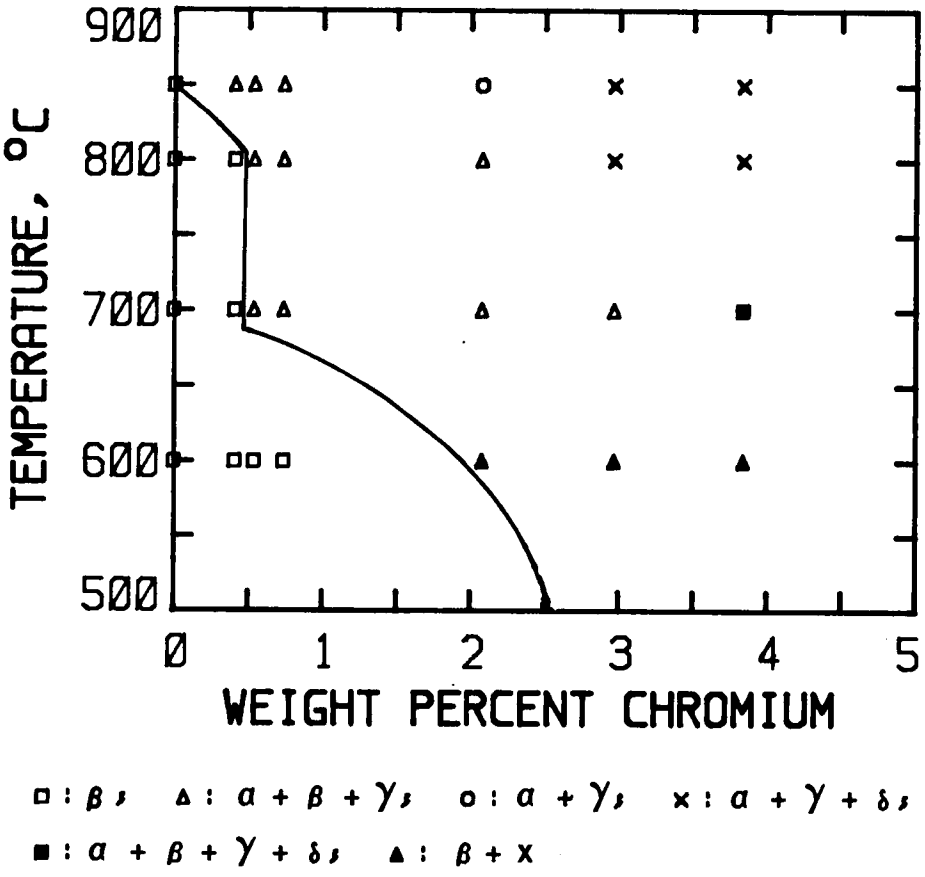


Figure II-41. Phases present in Ni-Mo-Cr alloys after aging 4500 hrs at 600, 700, 800 and 850°C.

Source: K. Vasudevan, "The Effect of 0-4 Wt Pct Chromium on Transformations of Alpha Phase Ni-Mo-Cr Alloys with Ni:Mo Atom Ratio Equal to 4:1," M.S. Thesis, University of Tennessee (1982).

Effect of chromium at 600°C. In this case, the microstructural features were too fine to enable resolution by optical microscopy. For chromium levels to 0.74 wt pct, only β was observed. At 2.08 wt pct Cr and above, besides β, distinct precipitates of an unidentified X phase were observed. The increase in resistivity in Figure II-40 at this temperature to 0.74 wt pct Cr was attributed to increased electron scattering by chromium. At the higher chromium levels, the resistivity was associated with increased electron scattering caused by chromium in solid solution and imperfectly ordered domains.

Based on these observations and from Figure II-41, Vasudevan (9) concluded that the solubility of chromium in the Ni_4Mo phase is less than 0.54 wt pct at 850, 800 and 700°C and less than 2.08 wt pct at 600°C.

Effect of iron and chromium on the microstructure. Addition of iron (8) and chromium (9) to Ni_4Mo gradually changes the microstructure. Representative optical micrographs for alloys containing 2.08 and 3.84 wt pct Cr are shown in Figures II-42 and -43a-d. In alloys containing as little as 0.41 wt pct Cr, Vasudevan (9) observed the formation of Ni_3Mo at grain boundaries on aging for 4500 hours at 850°C. At compositions between 0.41 and 0.74 wt pct Cr, the amount of grain boundary Ni_3Mo increased in proportion. Regions in the microstructure adjacent to the Ni_3Mo were α. Also, thin, multiple striations of Ni_3Mo were observed to emanate from the grain boundaries. The grain interiors revealed lenticular shaped domains of Ni_4Mo characteristically different from the large, patchy domains in the binary Ni_4Mo (8-10). The microstructure of the 2.08 wt pct Cr

alloy at 850°C revealed only large plates of Ni_3Mo in a α matrix (Figure II-42a). In alloys containing 2.97 wt pct Cr and above, a discontinuous precipitation of α and NiMo phases occurred at the grain boundaries and progressed into the grain interiors with time (Figure II-43a). A similar reaction also occurs in alloys containing over 4.41 wt pct Fe (8) and in Hastelloy B-2 (30).

At 800°C, the formation of Ni_3Mo alloys was seen in alloys containing over 0.41 wt pct Cr. Higher levels of chromium tend to further stabilize the Ni_3Mo. The Ni_3Mo forms in two morphologies, namely, thin Widmanstatten striations parallel to {111} fcc planes (as judged by their being parallel to annealing twin boundaries) and massive, lamellar plates. Large amounts of both morphologies of Ni_3Mo were observed on aging alloys containing over 2 wt pct Cr. This is shown in Figures II-42b and -43a for the 2.08 and 3.84 wt pct Cr alloys aged for 4500 hours at 800°C. The microstructure in Figure II-42b consists of wavy Ni_4Mo domains with numerous massive, lamellar Ni_3Mo plates around the grain boundaries. Thin, long Widmanstatten striations of Ni_3Mo can also be observed in the center grain. On the other hand, the microstructure of the 3.84 wt pct Cr alloy, in Figure II-43b, shows numerous such striations within the grains and massive gamma plates at the grain boundaries all in a matrix of α; no Ni_4Mo is present. Also, small Widmanstatten precipitates of the NiMo phase are present in this microstructure (Figure II-43b). These precipitates form parallel to both the thin striations of Ni_3Mo and initial annealing twins, thus indicating the adoption of a {111} habit. This feature is in agreement with the results of Ruedl and Amelinckx (120)

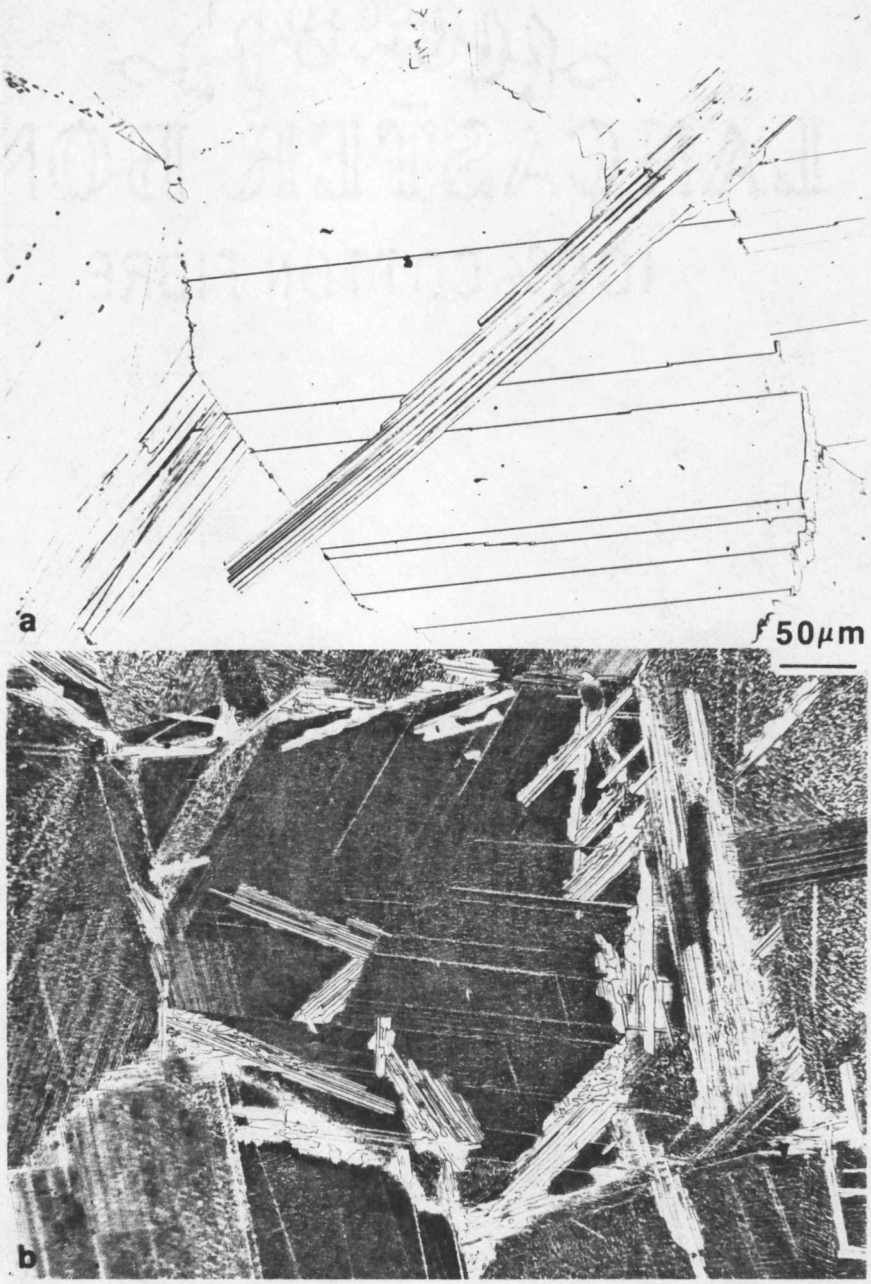


Figure II-42. Optical microstructures of the 2.08 wt pct Cr alloy. Aged 4500 hrs at a) 850°C, and b) 800°C.

Source: K. Vasudevan, "The Effect of 0-4 Wt Pct Chromium on Transformations of Alpha Phase Ni-Mo-Cr Alloys with Ni:Mo Atom Ratio Equal to 4:1," M.S. Thesis, University of Tennessee (1982).

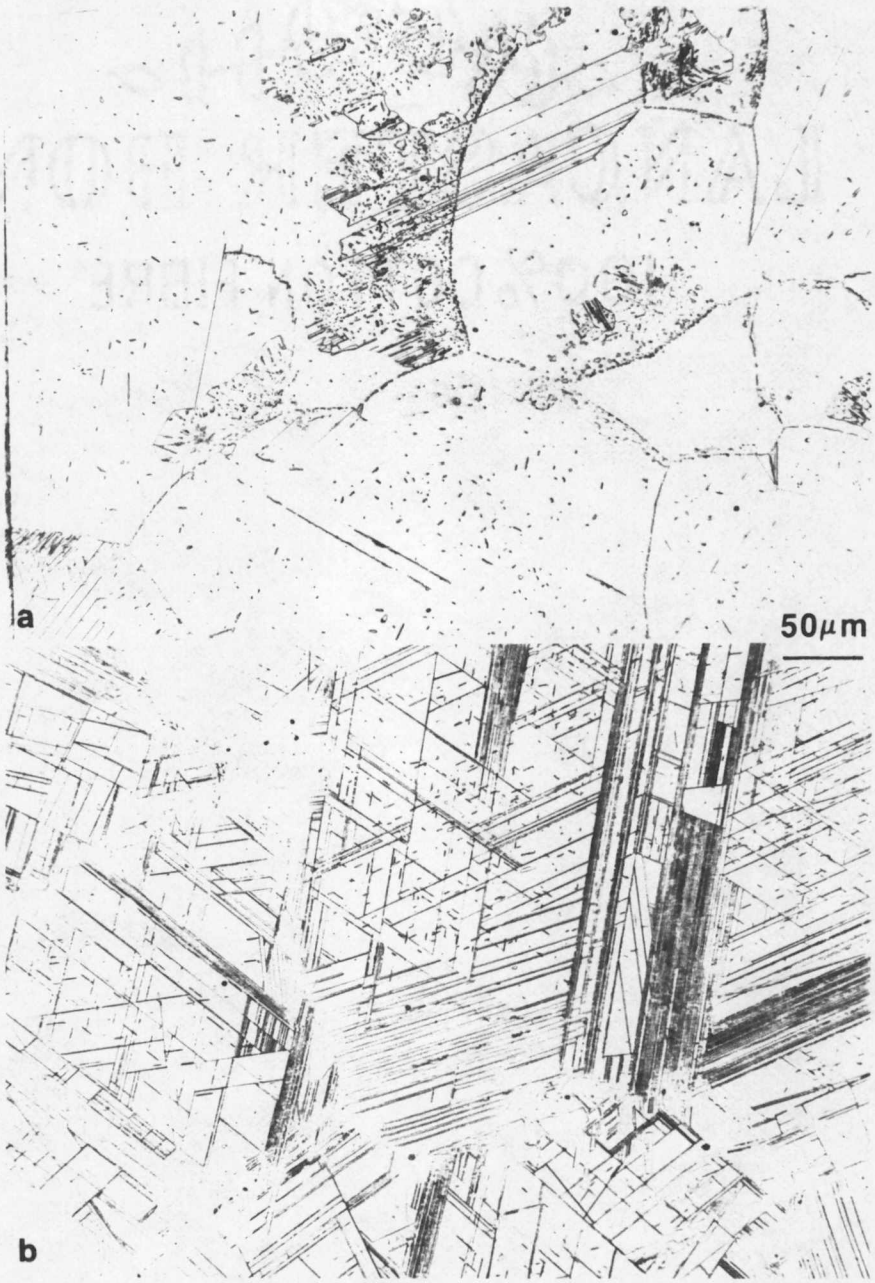


Figure II-43. Optical microstructures of the 3.84 wt pct Cr alloy. Aged 4500 hrs at a) 850°C, b) 800°C, c) 700°C, and d) 600°C.

Source: K. Vasudevan, "The Effect of 0-4 Wt Pct Chromium on Transformations of Alpha Phase Ni-Mo-Cr Alloys with Ni:Mo Atom Ratio Equal to 4:1," M.S. Thesis, University of Tennessee (1982).

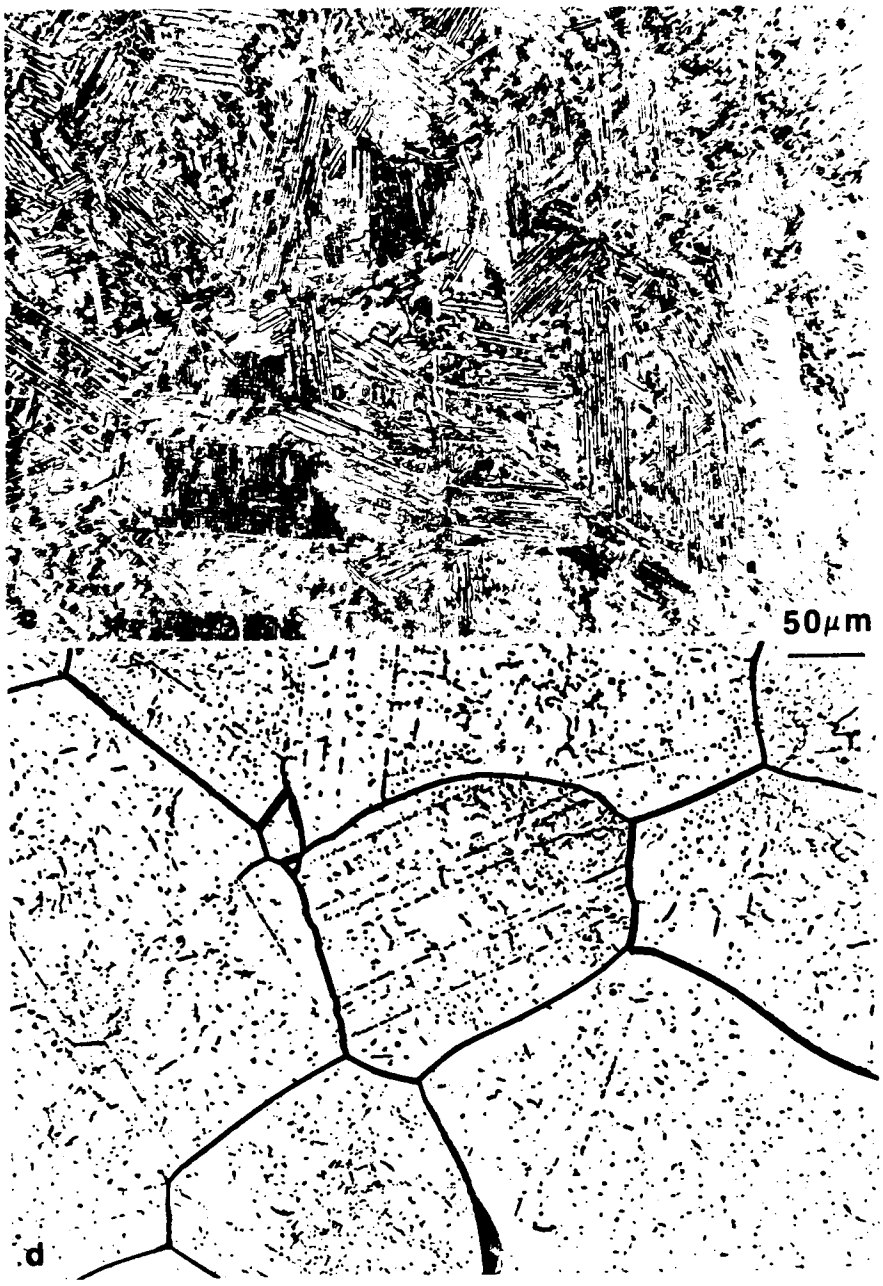


Figure II-43. (Continued).

who reported that in the two-phase α + NiMo region, the NiMo forms parallel to {111} fcc planes.

At 700°C, in alloys with chromium levels in the range 0.54 to 2.08 wt pct, the Ni_4Mo decomposed into α and Ni_3Mo at the grain boundaries. The changes in the microstructure were more complicated in alloys with 2.97 and 3.84 wt pct Cr. A variety of Widmanstatten precipitates, which remained unidentified, evolved during the initial stages of annealing (to 100 hours). These changes were accompanied by a rapid increase in the microhardness. Prolonged aging to 4500 hours (Figure II-43c), produced substantial amounts of Ni_3Mo with the same two morphologies as those at 800°C. The microstructure in Figure II-43c also reveals small amounts of Ni_4Mo. The intervening spaces between adjacent Ni_3Mo plates contained much lower concentrations of molybdenum and were identified as α. These features could be seen clearly in SEM micrographs. In addition, Widmanstatten precipitates of NiMo were also observed at higher magnifications under the SEM. The formation of the massive, plate-type morphology of the Ni_3Mo phase was observed to be accompanied by a further increase in hardness.

At 600°C, the microstructure of the lower chromium alloys (to 0.74 wt pct) did not show any discernible changes, although the microhardness and resistivity data indicated that ordering processes were taking place, albeit with less vigor than that at the higher temperatures. In alloys in the higher 2.08 to 3.84 wt pct range, fine precipitates (Figure 45d) could be discerned after annealing for extended periods of time (to 4500 hours). Since the response to etching and the microhardness and resistivity behavior of alloys in

this chromium range were measureably different, it was concluded that the microstructure consisted of secondary precipitates distributed in a Ni_4Mo matrix. The nature of the precipitates however, could not be ascertained. The reported data for the binary Ni_4Mo alloy at 600 and 650°C (8,126) indicates that these precipitates are Ni_2Mo.

In this research (9), preliminary phase identification was carried out by SEM-EDAX. Although this technique allows determination of the composition of phases in a multi-phase microstructure, neither the technique nor extent of its use led to conclusive identification of the phases in the alloys under study. One uncertainty was related to the composition of the Mo-rich phase observed at the grain boundaries at 850 and 800°C and within the grains at 700°C in the higher chromium alloys. Although it was interpreted as NiMo, the observed variations in composition from very high to moderately high in molybdenum indicated the possible presence of the metastable phase Ni_2Mo. Also, the presence of other metastable phases such as the DO_{22}, reported in ternary Ni_4Mo alloys containing vanadium (28) and in commercial alloys Hastelloy B (29) and Hastelloy B-2 (31), could not be precluded. Several Widmanstatten precipitates which appeared at the earlier stages of annealing in the higher chromium alloys at 800 and 700°C as probable precursors of later structures, also remained unidentified.

Major problems arise in determining or even estimating the phases in the Ni_4Mo alloys containing chromium. Although some estimate of the phases that will be present at equilibrium can be obtained by following changes in the microstructure with time, sufficiently

accurate compositions of the various phases, which are required to map out the phase diagram, cannot be determined by SEM-EDAX. As a result, Vasudevan (9) was unable to positively identify the observed phases and to establish a ternary Ni-Mo-Cr phase diagram. In contrast, thin film EDAX in the TEM is capable of determining phase compositions within a percent; this technique can be used to advantage for establishing the ternary phase diagram.

Changes in structure and properties in commercial Ni_4Mo-based alloys. Hastelloy B and B-2 are commercial alloys which can considered closely related to the Ni_4Mo composition. Alloy B has a nominal composition (in wt pct) of: Mo-28, Fe-5, Co-2.5, Cr-<1.0 ,C-<0.05, Si-<1.0, and balance Ni, whereas that of alloy B-2 is: Mo-26 to 30, Fe-<2.0, Cr-<1, Co-<1.0, C-<0.015, Si-<0.1, and balance Ni. Both these alloys have excellent corrosion resistance and mechanical properties and are well suited for equipment handling hydrochloric acid over a wide range of temperatures and concentrations (25).

Information available on the mechanical properties and physical metallurgy of Hastelloy B and B-2 have recently been reviewed by Brooks et al. (19). The interested reader is referred to this paper for comparison of mechanical property data for these alloys relating to specific temperatures and times of heat treatment. Alloy B has an fcc structure in the solution treated condition and undergoes structural changes on aging below the ordering temperature. Aging results in increase in tensile strength, yield strength and hardness, low creep rate, high stress rupture properties but a decrease in ductility (19,26,27).

Clausing et al. (26) and Roan and Brooks (27) studied the mechanical properties and aging characteristics of Hastelloy B in the temperature range 700 to 900°C. A feather-like precipitate was observed at 900 and 815°C, which resulted in a slight increase in strength but extensive decrease in ductility. This precipitate was postulated to be Ni_3Mo (27). At 705 and 765°C, a Widsmanstatten structure, presumably Ni_4Mo + Ni_3Mo predominated. Although the strength obtainable at these temperatures was much higher than that at the higher temperatures, the accompanying decrease in ductility was about the same (27). Lei (8) has reported the occurrence of the NiMo phase in Ni_4Mo alloys containing over 4.41 wt pct Fe. The feather-like needle precipitates observed by Roan and Brooks (27) at 815 and 900°C do not have the characteristic massive plate-like appearance of the Ni_3Mo phase (8,9,125). However, they bear a remarkable resemblence to the needle-like NiMo precipitates observed by Guthrie and Stansbury (7) in the two-phase α + NiMo region. The NiMo phase has also been reported by Vasudevan (9)in Ni_4Mo alloys containing 2.97 wt pct Cr and above and Tawancy (30) in Hastelloy B-2 aged at 900 and 955°C. Based on these observations, it appears that the precipitates observed at the higher temperatures by Roan and Brooks (27) are NiMo.

Ruedl (29) made attempts at understanding the nature of structural changes on aging Hastelloy B in the temperature range 600 to 800°C using TEM. He observed the formation of the DO_{22} intermediate phase. Aging for about 10 hours at 600°C, initially led to the formation of the DO_{22} phase followed by complete transformation of this structure to Ni_4Mo at 200 hours. Annealing for an additional 100

hours resulted in partial transformation to Ni_3Mo. At 700°C, there were no detectable changes from the SRO state to 100 hours. Further annealing to 330 hours produced a high density of bands parallel to {111} fcc planes containing DO_{22} and Ni_3Mo. The intervening spaces between these bands were fcc. No evidence was found for the formation of Ni_4Mo, Ni_2Mo and the LPAPB structure as observed in the binary Ni_3Mo. This observation was taken as evidence for a direct transformation from the the DO_{22} to Ni_3Mo. The absence of the Ni_2Mo phase was postulated to be due to changes in neighbor interaction energies caused by the presence of alloying elements other than nickel and molybdenum.

There have been fewer studies on the aging characteristics of Hastelloy B-2 (30-32,193). The high-temperature as-quenched structure is fcc and short range ordered (31,32). Aging in the temperature range 600 to 800°C produces an appreciable increase in the hardness (19,193), tensile and yield strength, but substantial reduction in ductility (32). At 850°C, there is little or no change in the hardness from that of the as-quenched state (19,193). The structural changes occurring with time at 600 and 700°C have been followed by TEM by Tawancy (31,32). At 600°C, initial annealing produced DO_{22} domains; further annealing led to complete transformation of this structure to Ni_4Mo. At 700 and 765°C (32), no DO_{22} was reported. Instead, Ni_4Mo domains developed in the initial stages and coarsened into "twin-related platelets" on continued aging. The continuous development of this platelet morphology of Ni_4Mo domains was related to progressive degradation of the tensile ductility and the aqueous

corrosion resistance (32). Tawancy (30) also reported that thermal treatments at high temperatures, namely 900 and 955^{o}C, lead to precipitation of NiMo at the grain boundaries.

A final note relating to the phase equilibria and corrosion properties of commercial alloys is the role of carbon. Molybdenum is the vital element responsible for the good corrosion resistance of Hastelloy B and B-2 (5,26). Since molybdenum is a strong carbide former, precipitation of Mo-rich carbides such as Mo_2C or Mo_6C at the grain boundaries causes depletion of molybdenum, which can lead to intergranular corrosion and failure (5,26). Fraker and Stadelmeier (194) investigated carbide formation in the Mo-Ni-C system. In the vicinity of the Ni_4Mo composition and at 1000^{o}C, three different carbides can form, namely: Mo_2C, M_6C and $M_{12}C$; M denotes different proportions of Mo and Ni adding to 6 or 12 whichever is the case. The latter two fall under the category of eta-carbides. The type of carbide formed depends on the composition: high molybdenum and low carbon favors $M_{12}C$, the reverse favors M_6C and Mo_2C. Their (194) results are in general agreement with the more detailed diffusion-couple studies of Heijwegen and Reick (195) covering a wider temperature range of 900 to 1300^{o}C. The $M_{12}C$ was not detected below 900^{o}C in this study (195). Ruedl (29) has reported M_6C carbides in Hastelloy B solution annealed at 1000^{o}C. Tawancy (196) identified the eta-carbide of type $M_{12}C$ at the grain boundaries in Hastelloy B-2 containing less than 0.002 wt pct C, aged at 800^{o}C for 1 to 100 hours. He concluded that since NiMo had been identified in this alloy, the eta-carbide and NiMo may coexist. Stansbury et al. (10) also confirmed

the presence of grain boundary eta-carbides of type $M_{12}C$ in Ni_4Mo based on their response to etching by Murakami's reagent.

Order Strengthening in Ni_4Mo

It was first pointed out by Koehler and Seitz (197) that an ordinary unit dislocation moving in an ordered lattice will not recreate the ordered structure in its wake, and disorder in the form of an antiphase boundary (APB), will result. The extra energy required to create the APB can be eliminated, however, by motion of dislocations in groups, connected by a strip of APB, such that no net change in order occurs behind the dislocations. These groups, which consist of two or more unit dislocations of like sign connected by a strip of APB or other planar fault, are known as "superdislocations." The presence of superdislocations has been positively established in a variety of ordered alloys such as Cu_3Au (198,199), Ni_3Mn (57,200), Fe_3Al (201), FeCo (202) and, Ni_3Mo (120) to name a few. In Ni_4Mo, in contrast, superdislocations are observed very rarely at room temperature (12,186).

Stoloff and co-workers (55,59,179,203) have pointed out that the mechanical behavior of ordered alloys is primarily controlled by the motion of single and superlattice dislocations and their interactions with each other and with obstacles such as grain boundaries, precipitate particles, and planar defects such as APB's and stacking faults. Furthermore, the stacking fault energy also plays a role in governing the dislocation fine structure and hence the deformation behavior, since each unit dislocation within the superdislocation may dissociate into its constituent partial dislocations (59,203).

Ruedl et al. (118) have shown that superdislocations in Ni_4Mo are comprised of pairs of either two, three or five unit dislocations having burgers vectors of type a<110>/2. They also postulated that the superdislocations can dissociate into four-fold, six-fold or ten-fold partials connected by stacking faults or APB's. The burgers vector of the partials are of type $a[11\bar{2}]/6$, $a[\bar{2}11]/6$ or $a[1\bar{2}1]/6$ when referred to the basic fcc lattice. The glide planes of either the ordered or the disordered alloy are the {111} fcc planes. Even if the stacking fault energy of the ordered alloy is too high to permit dissociation into partials, splitting of superdislocations can still occur into either two, three or five connected by one, two or four APB's. The faults created by the dissociation are stacking faults when referred to the basic fcc lattice and simultaneously APB's when referred to the superlattice (118).

The equilibrium distance between unit dislocations within a superdislocation is determined by the energy balance between the mutual repulsive force between dislocations of like sign and the surface tension (attractive force) of the antiphase boundary which binds the individual dislocations together (55,204). Chakravarti et al. (13) calculated the APB energy following the method outlined by Flinn (204) and incorporating certain assumptions related to the nature of near-neighbor bonds in Ni_4Mo. They (13) found that the fcc planes of least APB energy were the {110}, whereas those of highest energy were the {310}. Chakravarti et al. (13) also calculated the separation between unit dislocations in a superdislocation in the most favorable "edge" configuration for varying degrees of long range order

(that is, S value) and found that the separation distance becomes smaller as the S value increases towards 1. Since in all cases, except for S<0.2, the separation was less than the corresponding domain size, they concluded that there should exist a high probability for the occurrence of superdislocations in ordered Ni_4Mo. However, in practice, superdislocations in Ni_4Mo are observed only rarely (12,186). A possible reason for this is forwarded later.

Strengthening due to ordering in Ni_4Mo has been observed by a number of researchers (8-10,12-18,177,178,184,186). This is generally manifested by an increase in hardness (8-10,177,178), strain-hardening coefficient, tensile and yield strength, but a drastic reduction in ductility (12-18). Most of these reports have drawn a relation between degree of LRO, domain size, mechanical properties and fracture characteristics. Snyder and Brooks (12) found the 0.2% yield strength of Ni_4Mo to increase from 56,000 psi for the water-quenched fcc phase to 127,000 psi for material aged for 10 minutes at 775^{o}C. The domain size was found to increase to 15 nm from about 4 nm. At the end of 186 hours at the same temperature, the domain size increased to about 350 nm, but the yield strength dropped below that of the as-quenched state. The ordering was also associated with a change in fracture mode from transgranular to intergranular.

Chakravarti et al. (13) also reported results of tensile tests on the Ni_4Mo alloy heat treated for various times at 700^{o}C. Within 100 minutes the yield strength increased sharply to 95500 psi from the as-quenched value of 50000 psi. Further increase in the yield strength to 110000 psi and the work-hardening coefficient occurred in the time

period to 15 hours. These changes were simultaneously accompanied by drastic reduction in ductility from 60% to 3.2%, increase in the domain size and degree of order from 0 to 10.6 nm and 0 to 1, respectively, and a change in fracture morphology from transgranular to intergranular. These results are in general confirmation with the higher temperature results of Snyder and Brooks (12). Chakravarti et al. (13) attributed the strengthening mechanism at 700^{o}C to the increase in domain size, the degree of order and stresses induced due to the tetragonality of the ordered phase. The decrease in ductility was attributed to either the development of dislocations in coplanar arrays or concentrated slip in the heterogeneous structure observed at grain boundaries at longer aging times.

Ling and Starke (178) measured the strains produced by ordering and proposed that high strength occurred at the later stages of ordering mainly due to the high density of dislocations generated from the strained coherent interface. The early stage hardening was supposed to occur due to domain hardening and/or partial order. A region of constant hardness was also observed, and was explained by proposing that the strain generated by creation of new dislocations was counteracted by reduction in strain from the elimination of boundary during domain growth.

Chen et al. (14) measured mechanical properties in Ni_4Mo with and without an accompanying stress and observed that the degree of order, domain size, yield strength and work hardening coefficient increase faster with aging for the stress-ordered samples than for the stress-free ones. However, the stress-free ordered samples showed

higher maximum yield strength, work hardening coefficient, and more pronounced overageing.

Saburi et al. (15) carried out compression tests on Ni_4Mo aged for various times at 800°C and observed that the yield strength of the as-quenched alloy increased from 42500 psi to a maximum of 85000 psi at 10 minutes, followed by a decrease for longer annealing times to 160 hours. The strain-hardening coefficient continuously increased, almost levelling off at the end of this time range. Observation of the deformed samples by TEM and electron diffraction revealed arrays of slip bands prior to the maximum in yield strength; at, and beyond the maximum (occurring at 10 minutes aging), copious amounts of mechanical twins on {111} fcc planes appeared and progressively increased at longer annealing times. These mechanical twins have also been reported by Nesbit and Laughlin (186), using the same technique, in Ni_4Mo compressively deformed by rolling, who in addition, showed that the twins were created by the superposition (overlap) of stacking faults on closely-spaced {111} fcc planes.

Saburi et al. (15) associated the maximum in yield strength to a transition in deformation mode from slip to twinning. They attributed the initial increase in strength to the motion of a<110>/2 type dislocations, such slip occurring by the high energy process involving creation of APB's in two-thirds of the domains as the dislocations cut through them. They further argued that as ordering proceeds towards perfection, energetically twinning will be favored instead, since first near neighbor wrong bonds are created only in one-third of the domains as opposed to two-thirds in slip. As a consequence, the yield

strength decreases progressively as the proportion of twinning increases relative to slip. The continuous increase in the strain-hardening coefficient was proposed to be due to increasing twin-twin interactions as the domains grow in size and perfection.

Ordering in Ni_4Mo also results in an increase in hardness. The changes in hardness with aging time at temperatures below the critical ordering temperature (10) were described earlier (Figure II-21, page 90) and are reiterated here for purposes of discussion. At 700, 800 and 850^{o}C, the hardness initially increases, reaching a maximum, followed by a slight decrease. The changes are most rapid at 800^{o}C and slower at 700 and 850^{o}C, the maximum occurring between 0.1 to 1 hour, 192 hours and 10 hours at the respective temperatures. At 600^{o}C, the changes are much slower and are accompanied by a continuous increase in hardness with no indications of a maximum even after 4500 hours (10). The peak hardness at the three higher temperatures, as also reported by Irani et al. (177), are approximately the same.

Irani et al. (177) have attributed the initial increase in hardness to order twinning (not to be confused with mechanical twinning) and the approximately constant maximum hardness to constant domain sizes. Stoloff and Davies (55,179) explained that the peak in the yield strength (and hardenss) corresponds to a critical mixture of SRO and LRO, whereupon a transition in deformation mode from single (in SRO) to paired (in LRO) dislocations occurs, and interactions between single and paired dislocations lead to a higher strength than that attainable for either fully ordered or disordered states. Also, the peak corresponds to a critical domain size, a size at which

domains come into contact. Since paired, superdislocations are rarely observed in Ni_4Mo, this explanation for the peak in hardness and strength would not seem to be applicable to Ni_4Mo. The interpretation of Stansbury et al. (10) is rather that the high degree of order within the domains is the governing factor, since the domain sizes corresponding to the maxima at various temperatures are different. The slight decrease in hardness beyond the maximum was attributed to the longer glide lengths for dislocations permitted by domain growth (10).

An obvious implication from the occurrence of mechanical twins and stacking faults in ordered Ni_4Mo, induced by either tension (12) or compression (15,186) and their absence in the disordered state, is that ordering in Ni_4Mo leads to a decrease in the stacking fault energy. In the early stages of ordering, when domains lack perfection, slip can be induced by motion of single dislocations, but would still be resisted by the obstructing influence of increased domain boundary area, since simultaneously domains are small. As ordering becomes perfect, the stacking fault energy is lowered further, so that twinning is expected to be the major mode of deformation. Although superdislocations are expected to form easily in Ni_4Mo from structural considerations (13,118), their general absence in practice (12,186) is probably related to the lowering of the stacking fault energy by ordering, which would instead promote the formation of stacking faults and twins. In principle, therefore, if the grain boundaries are strengthened and the stacking fault energy raised appreciably by suitable alloy additions, it should be possible to induce sufficient ductility by slip in ordered Ni_4Mo, which coupled with the already

available high strength would make it a potential material for high temperature applications.

Major difficulties exist in the establishment of a consistent mechanism for the deformation behavior of Ni_4Mo. First, all the individual studies (12,13,15) have been conducted at different temperatures where the mechanisms of transformation, structural changes, changes in degree of order and domain size with time, are all different. Second, since the transformation behavior itself is dependent on temperature, changing from a nucleation and growth process at high temperatures to continuous ordering at lower temperatures (8,13,157,160,171,178), it is conceivable that the deformation behavior would also be influenced in some related manner. This aspect has not been given attention. Third, limited attention has been directed towards the influence of the two other types of domain interfaces that occur in Ni_4Mo, namely, APTB's and PTB's, on the deformation behavior. It would be enormously instructive to carry out detailed investigations over a broad range of temperatures and time, and study the deformation behavior in relation to the degree of order, domain size, type, and structure.

CHAPTER III

EXPERIMENTAL METHODS

Alloy Preparation

Seven Ni_4Mo-based alloys, containing 0 to 4 wt pct chromium were prepared in the earlier stages of research on Ni-Mo-Cr alloys (9). The alloy designations, corresponding compositions and nickel:molybdenum ratios are listed in Table III-1. The alloys were prepared from a nickel-molybdenum master alloy, with nickel corrections to obtain the Ni_4Mo composition and additions of chromium chips of 99.999 wt pct purity. Approximately 950 grams of each alloy were melted in a Balzers induction furnace under a refilled argon-hydrogen atmosphere at 45 cm pressure, degassed under vacuumn and poured into water-cooled copper molds to produce cylindrical ingots 20 mm (0.75 in.) in diameter and 63 mm (2.5 in.) long.

The cast alloys were homogenized at 1150°C for 100 hours in a high temperature furnace in dry hydrogen, furnace cooled, reheated to 950°C for 1 hour and then water-quenched to retain the high-temperature fcc α phase. Subsequent swaging with intermediate anneals in the range 950-1000°C were used to produce rods 4.75 mm (0.187 in.) and 3.25 mm (0.125 in.) in diameter. The larger rods were used for optical metallography and microhardness tests and the smaller ones for electrical resistivity and transmission electron microscopy.

TABLE III-1

Chemical Compositions of Alloys

	Alloys						
Composition*	NMCR0	NMCR6	NMCR3	NMCR1	NMCR2	NMCR4	NMCR5
Ni	70.94	70.48	70.18	69.86	68.49	67.36	68.16
Mo	28.77	28.70	28.67	28.68	28.29	28.29	28.07
Cr	0.10	0.41	0.54	0.74	2.08	2.97	3.84
Fe	0.10	0.10	0.10	0.10	0.10	0.10	0.10
Al	0.05	0.05	0.05	0.05	0.05	0.05	0.02
Co	0.10	0.10	0.10	0.10	0.10	0.10	0.10
Cu	0.03	0.03	0.03	0.03	0.02	0.02	0.02
Mg	0.01	0.01	0.01	0.01	0.01	0.01	0.01
Mn	0.10	0.10	0.10	0.10	0.10	0.10	0.10
Si	0.02	0.02	0.02	0.02	0.02	0.02	0.02
V	0.01	0.01	0.01	0.01	0.01	0.01	0.01
W	0.10	0.10	0.10	0.10	0.10	0.10	0.10
Zr	0.01	0.01	0.01	0.01	0.01	0.01	0.01
C	0.005	0.003	0.006	0.003	0.006	0.008	0.005
B	0.002	0.005	0.002	0.002	0.003	0.003	0.006
P	0.006	0.004	0.004	0.005	0.004	0.004	0.004
S	0.002	0.002	0.002	0.002	0.003	0.002	0.002
Ni : Mo	4.032	4.015	4.001	3.981	3.957	3.892	3.969

*Composition in weight percent.

Note : Actual compositions of Fe, Al, Co, Mg, Mn, Si, V, W, B, P and S are less than the amounts indicated.

Heat Treatments

Samples of both sizes, 100 mm (4 in.) long, were cut from the swaged rods and encapsulated in either vycor or quartz tubes under rough vacuum. The smaller rods were held at 950°C for 2 hours and the larger ones at 1250°C for the same time and water-quenched upon breaking the capsules to retain the fcc α phase; the grain sizes produced by these treatments were 0.1 and 0.5 mm respectively. To study the effect of grain size in the TEM, additional samples of the smaller size rods were also subjected to the 1250°C treatment. Smaller samples from the solution treated rods were sealed in vycor tubes under vacumn and aged in a four-in-one furnace assembly in sections maintained at 600, 700, 800 and 850°C. A 150 mm (6 in.) uniform temperature zone was established. The temperature which was periodically checked with a chromel-alumel thermocouple varied over time by ±4°C. Groups of specimens of each alloy were introduced into the isothermal zone of each furnace and after aging at each temperature for times to 4500 hours, the capsules were broken and the specimens water-quenched to arrest further transformation.

Optical Metallography, Hardness and Electrical Resistivity Measurements

The techniques used for the microhardness and electrical resistivity measurements have been described in detail in reference 9. Microhardness measurements were made on polished metallographic specimens in a Tukon tester with a 10 kg load. For optical metallography, an etchant consisting of 1 part CrO_3 and 3 parts HCl was used and the specimens etched by swabbing for 3 to 10 seconds.

Manual measurements of electrical resistivity were made by mechanically placing the alloy rod across a pair of calibrated knife edges and connecting the ends to a precisely controlled current source in series with a calibrated resistor. With a controlled current of 1 ampere passing, the voltage drop across the knife edges was measured and the resistivity calculated using the standard expression $\rho = 0.785Vd^2/IL$, where d = diameter, L = sample length between the knife edges along the rod axis, V = voltage drop across L, and I = current passed through the rod. A computer-controlled resistivity apparatus was designed and programmed for resistivity measurements at elevated temperatures over wide ranges of heating and cooling rates, or isothermally (8,9). Low temperature measurements were performed manually by immersing the specimens in either ice water, a dry ice and methanol mixture, liquid nitrogen, or liquid helium depending on the temperature range desired.

Transmission Electron Microscopy

Specimen Preparation

Basic considerations. Before describing the details pertaining to the preparation of specimens for this investigation, a brief discussion is presented of important factors to be considered for successful polishing of specimens for TEM examination. This overview is derived from the book by Tegart (205) and from the author's own limited experience. Tegart's book (205) on the underlying principles of electropolishing is a must for the beginner in the field.

The preparation of specimens for TEM is an intricate and arduous process, albeit the most important one. Initial sectioning from bulk material and production of discs for polishing constitutes the first step. Many standard techniques are covered in most books on electron microscopy (206-208). The main emphasis of the present discussion is on the polishing process.

There are basically five important factors that control the polishing process: 1) type of electrolyte, 2) temperature, 3) applied cell voltage, 4) applied current, and 5) flow rate. Typically, in most metals, the relationship between the current and applied voltage can be divided into three stages. In the first stage, there is a parabolic increase in current with voltage; this stage corresponds to etching. The second stage is characterized by a nearly constant current over a range of intermediate voltages. This stage corresponds to polishing and is the one the system should be placed in. The polishing action is achieved by the continuous formation and removal of a thin surface film and is accompanied by brightening of the surface (205). Ideally, it is desirable to have the right combinations of electrolyte, temperature and flow rate which provide sufficient latitude in this range so that the polishing can proceed unhindered by small fluctuations in the applied voltage. Certain electrolytes may produce acceptable brightening yet give rise to non-uniform or inadequate thinning by their tendency to rapidly attack asperities and defects on the surface. Therefore, a "good" polish is judged by the extent of brightening of the surface, while simultaneously providing uniformly thinned areas. The third stage occurs beyond the voltage levels of

polishing and is characterized by rapid increase in current. In this stage, gas evolution and pitting occurs. Although some pitting is tolerable as long as adequate thin areas are present, in general, this should be avoided, since, once pits are initiated, further concentrated attack will cause rapid through-thickness propagation of the pits, eventually leading to penetration without uniform thinning.

The effects of temperature are manifold and synergistic. Increase in temperature lowers the viscosity of the solution, which, in turn, increases the limiting current for polishing at a fixed range of voltages. As a result, polishing can be achieved in shorter times. Simultaneously, however, the voltage range for polishing may in some cases get compressed, with concomitant loss of flexibility in controlling the polishing process. Also, the increased kinetics will result in the inability to maintain the uniformly thin surface layer essential for polishing, and may frequently result in oxidation of the sample surface. Low temperatures produce more uniform attack and less oxidation and provide a greater measure of control. However, this is offset by decreased polishing currents, which, in turn, necessitates longer polishing times. At sufficiently low temperatures, the voltage required to initiate polishing may be so high as to surpass the practical limits of the polishing device. Ideally, the polishing solution chosen should be relatively insensitive to variations in temperature over a broad range, yet provide uniform polishing and thinning at increasing current levels--that is--at shorter times.

The effect of flow rate is to either concentrate or spread the attack. Low flow rates provide quiescent conditions which are

essential for uniform thinning. However, the passive film that is formed may continuously grow in thickness such that further polishing action is terminated prematurely. In some cases, the prevailing stagnant conditions can cause penetration sufficiently far away from the foil center as to render it inaccessible in the microscope. High flow rates restrict the attack to the foil center, which is clearly desirable. However, very high flow rates can result in mechanical damage of the thin areas, as well as one-sided polishing. It is obvious that these effects of the flow rate are relative and are dependent on the viscosity of the particular solution used.

It is evident from the brief discussion above that successful polishing can be achieved only by a compromise of several related factors. As a starting point, the recipes available for the particular alloy system under investigation should be consulted. In the absence of such information, some ideas on the types of solutions and the polishing conditions to be selected can be gained from information on related systems and that available on the pure metals constituting the alloy system. Availability of extensive information does not always guarantee immediate success, since the polishing parameters tend to vary somewhat with the type of equipment used for polishing. As a result, optimum polishing conditions are arrived at, unfortunately, only by painstaking trial and error procedures.

Ni-Mo-Cr alloys. The heat treated 3.25 mm (0.125 inch) diameter rods were first electrochemically machined in a 13% H_2SO_4-87% methanol solution to a diameter of about 3 mm so as to fit in the microscope

specimen holder. Disks approximately 0.3 mm (0.012 in.) thick were sliced from the heat treated and electrochemically machined 3 mm rods using a Gillings Hamco Thin Sectioning Machine. The undulations on the periphery of the discs caused by the cutting operation were removed by placing the discs under a rubber stopper and grinding on a 000 emery paper.

Final thinning of the cut and smoothened sections was directly carried out in a Struers "Tenupol," twin-jet polishing apparatus, equipped with a photocell to detect the light from the initial penetration of the specimen; the power to the cell is automatically cut-off thereupon.

In view of the aforementioned factors to be considered for obtaining optimum polishing, several solutions were tried. The best results for all the alloys, including the binary Ni_4Mo, were obtained with a polishing solution consisting of 640 ml orthophosphoric acid, 150 ml concentrated sulfuric acid, 35 ml concentrated hydrochloric acid and 210 ml distilled water. The hydrochloric acid is a vital ingredient for obtaining a bright polished finish. Without it, a tenacious oxide film persisted on the foil surface and could not be stripped-off even by cleaning solutions maintained at high temperatures ($<80^{o}C$). The optimum values for the polishing parameters such as temperature of electrolyte, flow rate, cell potential and current were determined by trial and error. The temperature was maintained at $12^{o}C$ and the flow rate was kept at a medium level (number 6 on the controlling dial). The applied cell voltage and the polishing current ranged from 20 to 30 volts and 0.8 to 1.4 amperes,

respectively. The exact values used were dependent on the alloy content and the thermal history; those at the higher end of the range were preferred for the higher chromium alloys. Polishing was carried out with the specimen in a 3 mm specimen holder until a small hole appeared, whence the photocell, located on one side of the cell detected the light from a light source positioned on the other end, and automatically switched off the polishing current and the pump and activated a buzzer. However, frequent malfunctioning of the photocell necessitated manual cut-off of the polishing by visually detecting the initial penetration, without the photocell in place. The quality of polishing and thinning were easily judged by optical microscopy, prior to actual observation in the TEM.

It was found that the electrochemical phenomena giving rise to the polishing were strongly dependent on the chromium content and the heat treated condition. In general, when high volumes of molybdenum-rich second phases were present, reasonable polishing was achieved only at the higher levels of applied voltage and current. In these cases, some etching of the foil surface was unavoidable. When highly molybdenum-rich second phases were present, the surrounding regions being depleted in molybdenum were preferentially attacked, thus leaving voids at positions where the particles were located. In such cases, polishing was carried out at lower currents to decelerate the attack and prevent particle "fall-out." However, since the particles themselves remained unattacked, they were too thick for electron transparency. To identify these second phases by electron diffraction, a few specimens, following jet-polishing, were either subjected to

further thinning by ion-milling for 5 to 10 minutes or observed at higher accelerating voltage.

The polished and penetrated specimens were carefully rinsed successively in distilled water and methanol and then laid out on a blotting paper. The foils dried in a few seconds and were then stored in plastic "beem" capsules prior to the TEM observations.

Observations of Thin Foils

Observations of thin foils were conducted in four transmission electron microscopes: Phillips EM300 operated at 100 KV, Philips EM400 operated at 100 KV, Philips EM430 operated at 300 KV,and a JEM-100CX operated at 120 KV; the latter three are located at the Oak Ridge National Laboratory (ORNL, P. O. Box X, Oak Ridge, Tennessee 37831, USA). The microscopes were calibrated for magnification, camera constant and rotation between image and diffraction pattern, utilizing standard procedures. The magnification calibration was performed with a carbon diffraction grating containing 2160 lines/mm. For the camera constant calibration, an aluminum diffraction standard of known d-spacings was used. The rotation calibration was achieved with the aid of a molybdenum oxide (MoO_3) standard. The standard was prepared by resistance heating a molybdenum wire and gathering the oxide vapors thence produced on a clean glass slide. The oxide was then floated off the slide onto the surface of a dish of water and collected from underneath on a formvar-coated 3mm copper grid held by means of a pair tweezers. After drying the grids for over 24 hours, a layer of carbon was deposited on them in an evaporater to fortify the thin formvar

film against the disruptive action of the electron beam. It is well known that MoO_3 forms with straight edges parallel to <100> directions. By measuring the angles between these edges in the bright field image with the corresponding <100> direction in the diffraction pattern, the rotation angle between the image and the diffraction pattern can be easily established as a function of magnification (206,207). Other details pertaining to the settings and conditions used for the various calibrations, as well as the actual calibrated values, are presented in Appendix A.

Bright field, dark field, and electron diffraction observations were utilized to obtain specific information pertaining to changes in structure. For second phases which were too small to enable individual identification by conventional electron diffraction, the convergent beam electron diffraction (CBED) technique in the EM400 mounted with a field emission gun (FEG) was used. This configuration for the gun provides more intense illumination than available from other sources such as the LaB_6 or the tungsten filament (86). The chemical compositions of the various phases present in the microstructure were determined by thin film x-ray microanalysis. The EM400 microscope equipped with the EDAX (energy dispersive analysis of x-rays) attachment and a smaller probe size was exclusively used for this purpose, although the JEM-100CX also has this capability.

Convergent beam electron diffraction (CBED). The basic principles of the CBED technique are illustrated in Figures III-1 and -2. The lens design is modified to produce a small convergent cone of

electrons (Figure III-1) instead of parallel illumination as in conventional microscopes. The electron diffraction pattern is always present in the back focal plane of the objective lens. For a converging beam, Bragg reflections from different planes image as discs instead of spots. This is a direct result of the angular range of electrons impinging on the sample. The size of the disks is controlled by the convergence angle, which, in turn, is directly proportional to the size of the aperture of the second condenser lens (85). Typically, apertures having sizes of 20, 70 amd 150 micrometers are used. The choice of aperture is governed by the type of information that is desired. When large apertures are used, individual discs overlap, creating the so-called Kossel patterns; smaller apertures enable clear resolution of individual discs and patterns produced therefrom are called Kossel-Mollenstedt patterns (86). This is the generally preferred working mode, unless specific information relating to the overall crystal symmetry, as obtainable from Kossel patterns, is desired (85,86).

Both conventional and convergent beam electron diffraction effects are best discussed in terms of the interactions between the Ewald's sphere and the reciprocal lattice (Figure III-2). Since the wavelength (λ) of high energy electrons is small (= 0.0037 nm for 100 KV electrons), the radius of curvature of the Ewald's sphere, $R = 1/\lambda$, is much greater than the spacing of reciprocal lattice points. Whenever a reciprocal lattice point lies on the Ewald's sphere, the condition for diffraction (Bragg's law) is met and reflections representing those particular planes will appear. If the electron beam

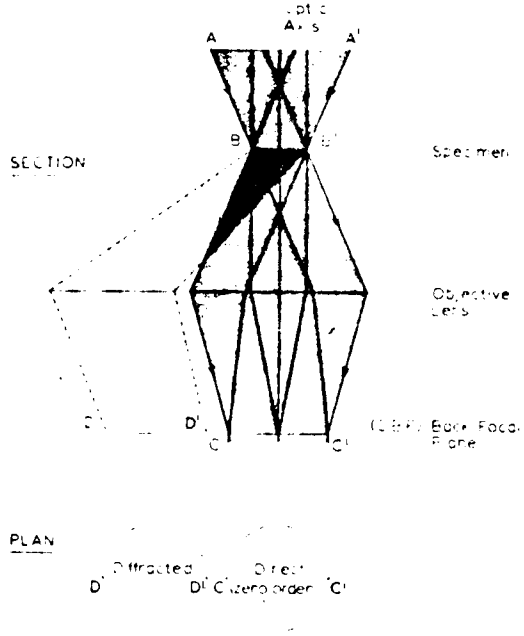


Figure III-1. Ray diagrams illustrating the formation of convergent beam patterns.

Source: J. W. Steeds, "Convergent Beam Electron Diffraction," in Introduction to Analytical Electron Microscopy, J. J. Hren, J. I. Goldstein and D. C. Joy (eds.), Plenum press, New York, 387-422 (1979).

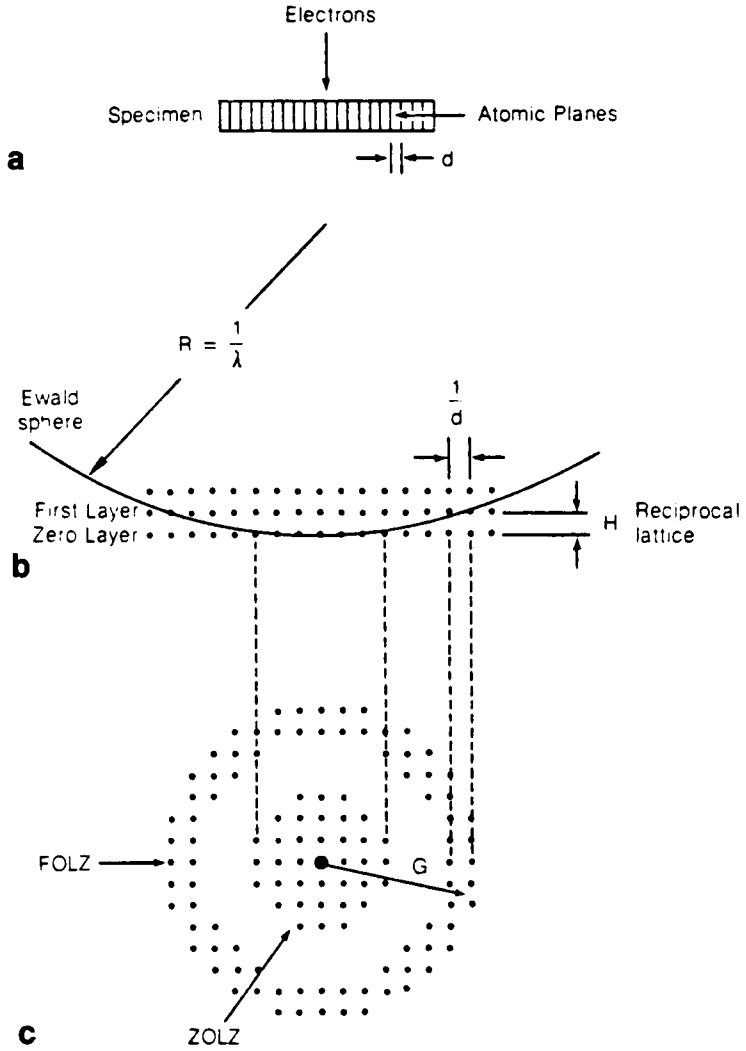


Figure III-2. Schematic illustration of the basic principles of conventional and convergent beam electron diffraction. a) Electrons incident on crystalline sample; b) Section of reciprocal lattice and Ewald sphere showing condition for diffraction; c) Electron diffraction pattern from zero layer (ZOLZ) and first layer (FOLZ).

Source: M. Raghavan, J. Y. Koo and R. Petkovic-Luton, "Some Applications of Convergent Beam Electron Diffraction in Metallurgical Research," Norelco Reporter, 31, No. 1EM, 32-38 (1984).

is directed along a zone axis, the associated family of reciprocal lattice points lie on a reciprocal lattice plane (zero layer plane) normal to the axis which, in turn, is tangential to the nearly planar Ewald sphere. At small distances from the origin (point of contact), spots lying on the zero layer, called the Zero Order Laue Zone or ZOLZ, will intersect the Ewald's sphere and provide diffraction. With increasing distance from the origin, the separation distance between the Ewald's sphere and the spots in the ZOLZ will increase until these spots will no longer intersect the Ewald's sphere and therefore will not be diffracted. Eventually, at sufficiently large distances from the origin, points lying on the first layer above, the First Order Laue Zone or FOLZ, will intersect the Ewald's sphere and provide diffraction. Successive intersections with other layers of the reciprocal lattice will produce High Order Laue Zones or HOLZ's (85).

When parallel illumination is used, as in conventional electron diffraction, only spots from the ZOLZ are produced. However, in CBED, the relatively broad angular range of the incident electrons provides the large scattering angles required to excite reflections from the HOLZ's. This effect can be alternately visualized as a toggling of the Ewald's sphere in relation to sets of electrons incident at particular angles. The visibility of the HOLZ's depends primarily on the lattice spacing in the beam direction, which, in turn, is governed by the crystal orientation, structure and dimensions. A second factor is temperature. Cooling the specimen to subzero temperatures reduces thermal vibrations and disorder and the accompanying dramatic increase in the large angle scattering can permit viewing of HOLZ's even in

cases where such scattering is not otherwise strong. Third, the microscope lens design must allow a low enough camera length to project the entire pattern within the dimensions of the viewing screen (85).

The spacing of the layer planes along the beam direction is given by:

$$H = G^2 \lambda / 2 \qquad \text{(III-1)}$$

where, G is the radius of the FOLZ and λ is the wavelength of the electrons. It should be noted that the correct magnitude of G is obtained only by dividing it by the camera constant, λL. For the <uvw> zone axis of a fcc crystal, the H_{uvw} of reciprocal lattice planes along the axis is given by:

$$H_{uvw} = p/a_o(u^2 + v^2 + w^2)^{1/2} \qquad \text{(III-2)}$$

where, a_o is the lattice parameter and p takes a value of 1 or 2 depending on whether (u + v + w) is odd or even. For a bcc crystal, the same relationship holds but p = 2 if u,v and w are all odd, otherwise p = 1. The beam direction <uvw> can be determined by indexing the spots in the ZOLZ as in conventional selected area diffraction patterns (SADP's). Thus, by measuring G on the CBED pattern, H can be calculated from equation III-1, which on substitution in equation III-2 yields the lattice parameter in the third dimension (85). Herein lies the power of the technique, since from a two-dimensional pattern, three-dimensional crystal structure data can be obtained with facility.

As pointed out earlier, Kossel patterns obtained with large size condenser apertures are generally used for obtaining information on

the overall crystal symmetry. Another advantage of working in this mode is that the lattice spacing in the beam direction can be determined more accurately. This is because the HOLZ's get compressed into nearly perfect rings and therefore their radii can be measured accurately. In general, Kossel-Mollenstedt patterns obtained with smaller apertures are used more widely. Determination of the beam direction is most easily achieved in this mode since the discs are smaller and hence can be easily resolved. Since the intensity variation within the discs carries important dynamical information, this configuration is also used to extract information on the specimen orientation, thickness and other important properties. In particular, by magnifying the individual 000 and hkl discs using large camera lengths and analyzing the HOLZ lines within the discs, the point group, and ultimately the space group of the crystal can be established unambiguously (85-87).

Thin film x-ray microanalysis. Composition analysis of phases by energy dispersive analysis of x-rays (EDAX) can be routinely performed in many modern microscopes. For instance, the Philips EM400 microscope is equipped with a software-driven EDAX attachment with which such analyses are easily accomplished. Data acquisition and analyses are performed by a PDP-11/23 computer (RT-11 operating system). To acquire data, the specimen holder is first appropriately positioned so that the EDAX detector can receive the incoming x-ray signals. The software requires two parameters to be set by the operator prior to the measurement. These are the counting rate in

cycles per second (cps) and the counting time in seconds. In the present research, the rate was set at a threshold value of about 3000 cps and the counting time at 100 seconds. Longer counting times do not improve the accuracy of the analysis by more than 0.1 pct. The objective aperture is withdrawn from the beam and the software is instructed to start the analysis. The x-ray spectrum is continuously displayed on a color graphics terminal and data acquisition is terminated upon reaching the set counting time. The x-ray spectrum from a region far away from the edges of the specimen (hole count) should also be recorded. This procedure is necessary to account for spurious contributions to the actual analysis from different parts of the microscope. The spectrums can be either stored in a file on a floppy diskette or analysed right away.

To analyse the data, the first step requires simple manipulation of a set of software instructions to identify the peaks corresponding to various elements (example NiK_{α}, MoK_{α} etc). The data are then normalized relative to the hole count, following which, an appropriate background is fit to the spectrum either automatically by the software or manually with instructions to the software from the operator. This final operation provides the desired intensity data (in cps) of the various peaks in the spectrum. The intensity data can now be analyzed to determine the composition of the structural feature being examined.

The most commonly employed method for obtaining the composition from the intensity data is the Cliff-Lorimer ratio method (209). In this method, the x-ray intensity ratio I_A/I_B of two elements A and B in the specimen, measured simultaneously, is directly related to the

mass concentration ratio C_A/C_B by the expression:

$$C_A/C_B = k_{AB}\ I_A/I_B \qquad \text{(III-3)}$$

where, the term k_{AB}, henceforth referred to as the k-factor, varies with operating voltage but is independent of sample thickness and composition provided the two intensities are measured simultaneously and the "thin film criterion" is satisfied (88). Thus, by knowing the k-factor and measuring the intensity ratio, the concentration ratio can be calculated. Determination of the composition is then a simple task involving trivial algebra.

Several methods are available to determine the k-factor: 1) theoretically by standardless analysis from the expression

$$k_{AB} = (EQwa)_B/(EQwa)_B\ A_A/A_B \qquad \text{(III-4)}$$

where, E, the detector efficiency is dependent on the mass absorption coefficient of the two atomic species relative to the beryllium window in the detector, Q is the ionization cross-section (that is, the probability per unit path length of an electron of a given energy causing ionization of a particular shell, K, L or M), w is the fluorescence yield for each element, a is the fraction of the total K or L line intensity that is measured K_α or L_α radiation and A_A, A_B are the respective atomic weights; 2) using bulk standard analysis; 3) using thin film standards and 4) from known composition of the thin film (88). The last technique is the easiest and the most accurate and was the one employed in this research on Ni-Mo-Cr alloys.

Basically, this last technique involves simultaneous acquisition of the intensity ratios of the various peaks in the spectrum from a thin region in the foil, in the manner described previously, and

substitution of the concentration ratios for the various atomic species, determined from the known composition analysis, into equation III-3 to calculate the corresponding k-factors. For the specific case of Ni-Mo-Cr alloys, the following equations can be developed by appropriate representations for the elements A and B in equation III-3:

$$C_{Ni}/C_{Mo} = k_{NiMo}\, I_{Ni}/I_{Mo} \qquad \text{(III-5)}$$

$$C_{Ni}/C_{Cr} = k_{NiCr}\, I_{Ni}/I_{Cr} \qquad \text{(III-6)}$$

$$C_{Mo}/C_{Cr} = k_{MoCr}\, I_{Mo}/I_{Cr} \qquad \text{(III-7)}$$

The 2.08 (NMCR2) and 2.97 (NMCR4) wt pct Cr alloys were selected for the analysis. Thin foils were prepared from discs in the short-range ordered fcc condition obtained by solution treatment and water-quenching from 1250^{o}C. The concentration ratios required in equations III-5, -6 and -7 were computed from the pre-determined composition analysis in Table III-1 and the corresponding intensity ratios were calculated by recording the intensity spectrum from a thin region in the foil. Substitution of these parameters in the above three equations yield the k-factors for the corresponding elements. The analysis was repeated for a number of regions in both types of foils and average k-factors were obtained as $k_{NiMo} = 0.516$, $k_{NiCr} = 0.973$ and $k_{MoCr} = 1.89$. Future analysis of various second phases of variable composition is then performed by multiplying the appropriate k-factors by acquired intensity ratios and calculating the concentration ratios according to the above three equations. The individual concentrations C_{Ni}, C_{Mo}, C_{Cr} (in at pct) are eventually obtained by the simultaneous solution of equations III-5, -6 and -7

and the mass balance

$$C_{Ni} + C_{Mo} + C_{Cr} = 1 \qquad \text{(III-8)}$$

The concentrations of the elements other than Ni, Mo and Cr are negligibly small (Table III-1) and the corresponding peaks in the intensity spectrum were below the detectible limit of the system. Hence, these elements were ignored in the analyses. To improve the analyses of second phases, the contribution to the spectrum from the underlying matrix was minimized by selecting, as far as feasible, particles located at the edges of the hole in the foil.

This type of analyses, discussed above, holds good as long as the "thin film criterion," henceforth referred to as TFC, is obeyed, that is, the spectrum is acquired from a region thin enough that absorption corrections are not necessitated. This criterion is generally interpreted to mean that if the foil is transparent to electrons, then it satisfies the thin film criterion. Tixier and Philibert (210) pointed out, however, that the TFC is violated by absorption even in cases where the film is thin enough, and that it is combination of the mass absorption coefficient and the foil thickness that is of importance. According to them (210), an absorption correction for each element measured is not needed if:

$$X_A \rho t < 0.1 \qquad \text{(III-9)}$$

The term X_A is equal to the product of the mass absorption coefficient for the characteristic x-ray of element A in the specimen composed of elements A, B, C... and $\mathrm{Cosec}\alpha$ where α is the angle between the x-ray detector and the specimen (take-off angle); ρ is the specimen density, and t is the foil thickness. According to Goldstein et al. (211), the

difference in absorption coefficients is the more important parameter, since two elements having similar mass absorption coefficients will be absorbed equally and the intensity ratio will be unaffected. Their less conservative TFC (211) is expressed as:

$$(X_A - X_B)\,\rho\, t/2 < 0.1 \qquad \text{(III-10)}$$

Typically, materials having densities less than 5 gm/cc are transparent to 100 KV electrons up to 500 nm, those in range 6 to 8 gms/cc and above 12 gms/cc are transparent up to 300 and 100 nm respectively (88).

The composition analyses obtained from the experimentally determined k-factors (method described earlier) were compared to those obtained using a standardless analysis (through software developed at ORNL). The results from both methods were closely comparable. It was observed that changing the values of the foil thickness (one input to the software) from 100 to 500 nm changed the composition of a particular element (Ni, Mo or Cr) by less than 0.5 to 1 at pct. Morever, the Tixier and Philibert TFC (210) was violated for chromium only for foil thicknesses exceeding 300 nm; for nickel and molybdenum, the TFC was not violated even for thicknesses over 500 nm. Also, the thickness of regions analyzed were generally much below 300 nm. In view of the relative insensitivity of the acquired intensity spectrum to variations in the foil thickness, within reasonable limits, and the observation that the experimentally determined k-factors inherently contain absorption effects, the more accurate method of calculating compositions from experimentally determined k-factors was used instead of the standardless analysis.

In cases where one element is excited by continuum x-ray radiation or by characteristic fluorescence due to some lines emitted in the other, an additional fluorescence correction will have to be incorporated. These are discussed in detail by Goldstein (86).

Finally, from the above discussions, the power of CBED and thin film EDAX are apparent, for verily, analytical information required for providing insight into various materials science phenomena can be obtained with facility in modern microscopes, and that too from regions at nanometer levels (<50 nm).

CHAPTER IV

RESULTS AND DISCUSSIONS

The results of this research are presented in the form of tables, figures and photomicrographs. The first major section covers the results for the binary Ni_4Mo alloy. Included are observations of changes in 1) electrical resistivity and electron microstructure on continuous heating and cooling, and in 2) microstructure following long time isothermal annealing. In the second major section, the electron microscopy of ternary Ni_4Mo alloys containing chromium are presented. In closing, a summarizing section on the effect of chromium on phase relationships in Ni-Mo-Cr alloys is presented. The individual sections are further subdivided as appropriate. Discussions on individual sections immediately follow the results. Comparisons between the binary and ternary alloys are made whenever and wherever necessary. In the author's view, this arrangement lends more coherency to the manuscript.

Ordering in Ni_4Mo During Continuous Heating and Cooling

Electrical Resistivity Behavior

The changes in resistivity associated with short range and long range order in Ni_4Mo on continuous heating and cooling in the temperature range -269 to 1300^{o}C are illustrated in Figure IV-1. In this figure, the symbols H, C and I represent heating, cooling and isothermal measurements; the numbers 1, 2 ..., denote the sequence of runs.

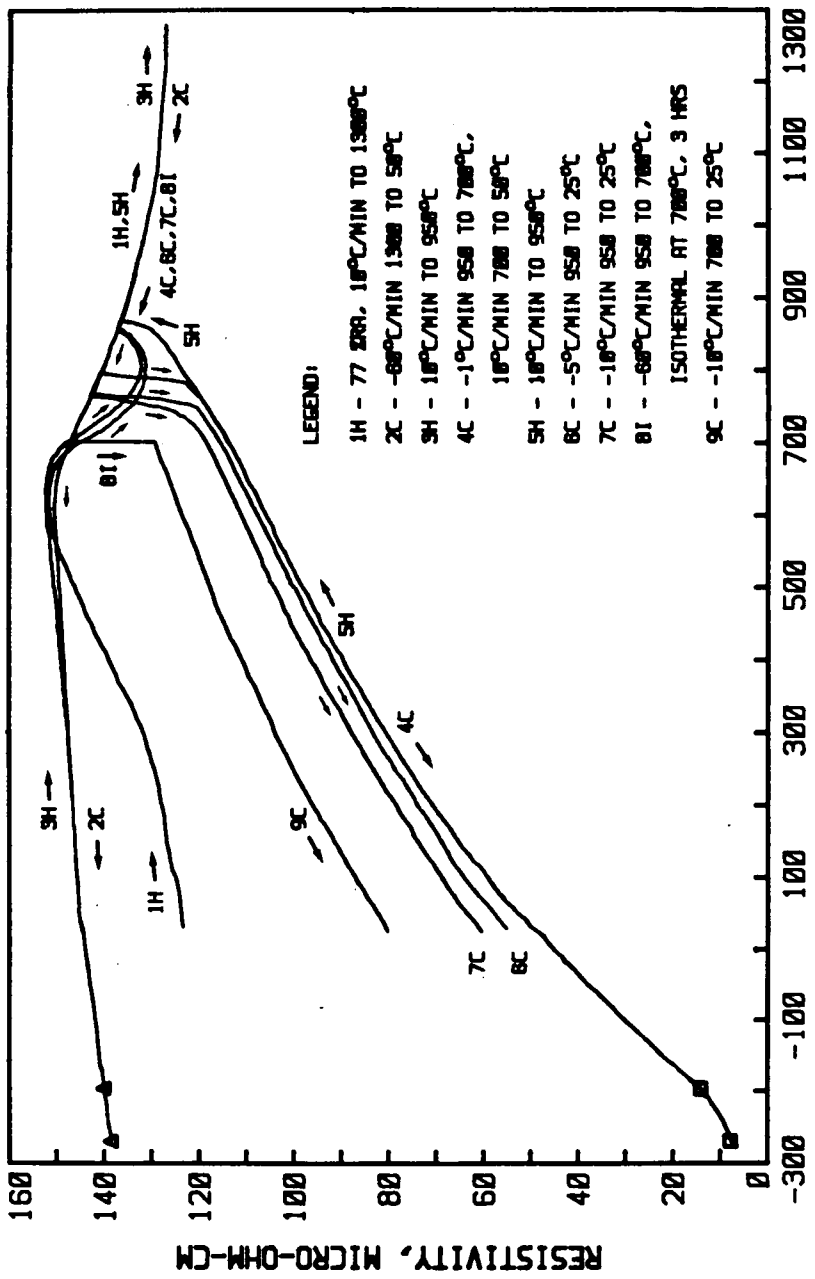


Figure IV-1. Variation of resistivity with temperature in Ni_4Mo under different indicated conditions.

In Figure IV-1, curve 1H shows that heating the initially 77% RA cold swaged alloy, increases the resistivity linearly to about 300°C due to increasing thermal scattering of electrons, followed by a non-linear rapid increase to about 650°C due to progressive return of the SRO destroyed by plastic deformation. The resistivity rapidly decreases between 650 and 800°C due to the onset of LRO, and then increases near the LRO-SRO critical temperature of 868°C due to a decrease in the degree of LRO. Above 868°C, LRO to SRO transformation occurs and the resistivity then decreases with increasing temperature with the slope of the resistivity-temperature curve becoming zero near 1300°C, indicating that the SRO is dispersed on approaching the melting temperature. This decrease in resistivity with increasing temperature results in a negative temperature coefficient of resistivity.

On cooling at 60°C/min from 1300°C (curve 2C), the resistivity initially increases to about 151 micro-ohm-cm at 650°C due to increase in the degree of SRO. Below 650°C, the SRO is effectively "frozen-in" due to inadequate atom mobility and the resistivity decreases to 144 and 139 micro-ohm-cm at 25 and -269°C respectively. In the following heating curve, 3H, the resistivity coincides with the previous curve 2C to 300°C; on heating to 650°C, increased atom mobility allows additional SRO over that frozen-in on initial cooling. Above 650°C, the behavior is similar to that of curve 1H.

Curve 4C results from slow cooling at rates of 1°C/min from 950 to 700°C and 10°C/min from 700 to 50°C respectively. The resistivity increases initially on cooling to about 800°C and then rapidly drops

in the temperature range 800 to 775°C with the onset of LRO. This cooling rate is sufficiently slow to allow complete transformation to the LRO state. The resistivity values at 25 and -269°C are 48 and 8 micro-ohm-cm respectively which contrasts markedly with the corresponding SRO resistivity values of 144 and 139 micro-ohm-cm and the cold worked state value of 124 micro-ohm-cm at 25°C.

The resistivity values on reheating the fully long range ordered Ni_4Mo alloy, curve 5H, are essentially similar to those in curve 4C to 775°C. Beyond 775°C, the slope increases gradually to 850°C, and then rapidly to the critical temperature of 868°C. The value of this temperature is in exact agreement with the results of Guthrie and Stansbury (7). Above 868°C, the behavior is similar to curves 1H and 3H. However, notably, the experimental transformation temperature itself is dependent on the initial state of order; a mixture of SRO and LRO transforms to SRO at a lower temperature (curves 1H and 3H) when compared to an initially complete LRO state (curve 5H). This result agrees with the recent radiation experiments of Banerjee et al. (160), who observed that a mixture of SRO and LRO transforms to SRO more easily than when initially in the fully LRO state. This behavior is a manifestation of the cooperational tendency of order-disorder transformations, discussed earlier in Chapter II (page 14). Another characteristic of the LRO state, shown in curve 5H, is the decrease in slope in the temperature range -150 to 600°C.

An increase in cooling rate from 1°C/min results in an increase in the LRO resistivity at 25°C to 54.5 and 60.5 micro-ohm-cm for cooling rates of 5 (curve 6C) and 10°C/min (curve 7C) respectively.

Microhardness measurements showed a corresponding decrease with values of 494, 464 and 434 DPN for cooling rates of 1, 5 and 10^{o}C/min respectively.

Curve 8I results for a sample held for 5 minutes at 950^{o}C, rapidly cooled to 700^{o}C and held for 3 hours. The change from 149 to 129 micro- ohm-cm is due to LRO. The sample was then cooled to 25^{o}C (curve 9C) which resulted in a value of 80 micro-ohm-cm, indicating a partially ordered state. The decrease in resistivity on annealing at 700^{o}C is actually preceded by a small increase as shown in Figure IV-2, which represents the change in resistivity with time.

Effect of reheating and rapid quenching on resistivity. To examine the changes in structure and resistivity near the ordering temperature, fully ordered samples (cooled at 1^{o}C/min) were reheated to 800, 825, 850, and 860^{o}C for 1/2 hour and quenched in iced brine. With an increase in reheat temperature, the resistivity increases relative to that of the fully ordered value of 48 micro-ohm-cm, being 51.9, 57.3, 58.6, and 62.54 micro-ohm-cm respectively for the aforementioned reheat temperatures.

Electron Microscopy

Representative electron micrographs are presented in Figures IV-3 to -5. All dark field (DF) micrographs were obtained using 1/5{420} superlattice spots. A DF micrograph of Ni_4Mo cooled at a rate of 1^{o}C/min from 950^{o}C is shown in Figure IV-3a. The corresponding [122] diffraction pattern (Figure IV-3b) shows superlattice spots from two variants of twin-related domains. No {1 1/2 0} SRO spots are

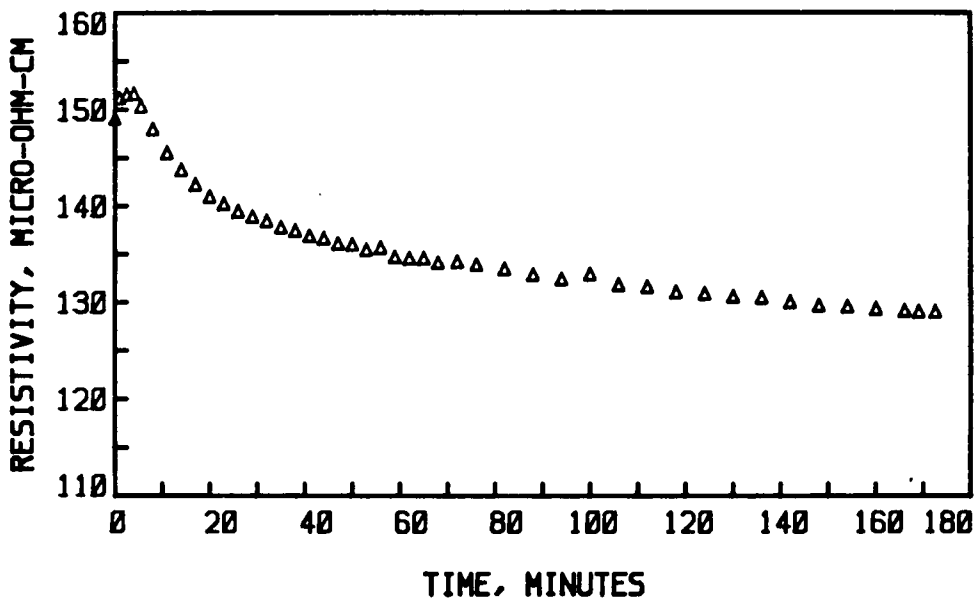


Figure IV-2. Variation of resistivity with time at 700°C in Ni_4Mo.

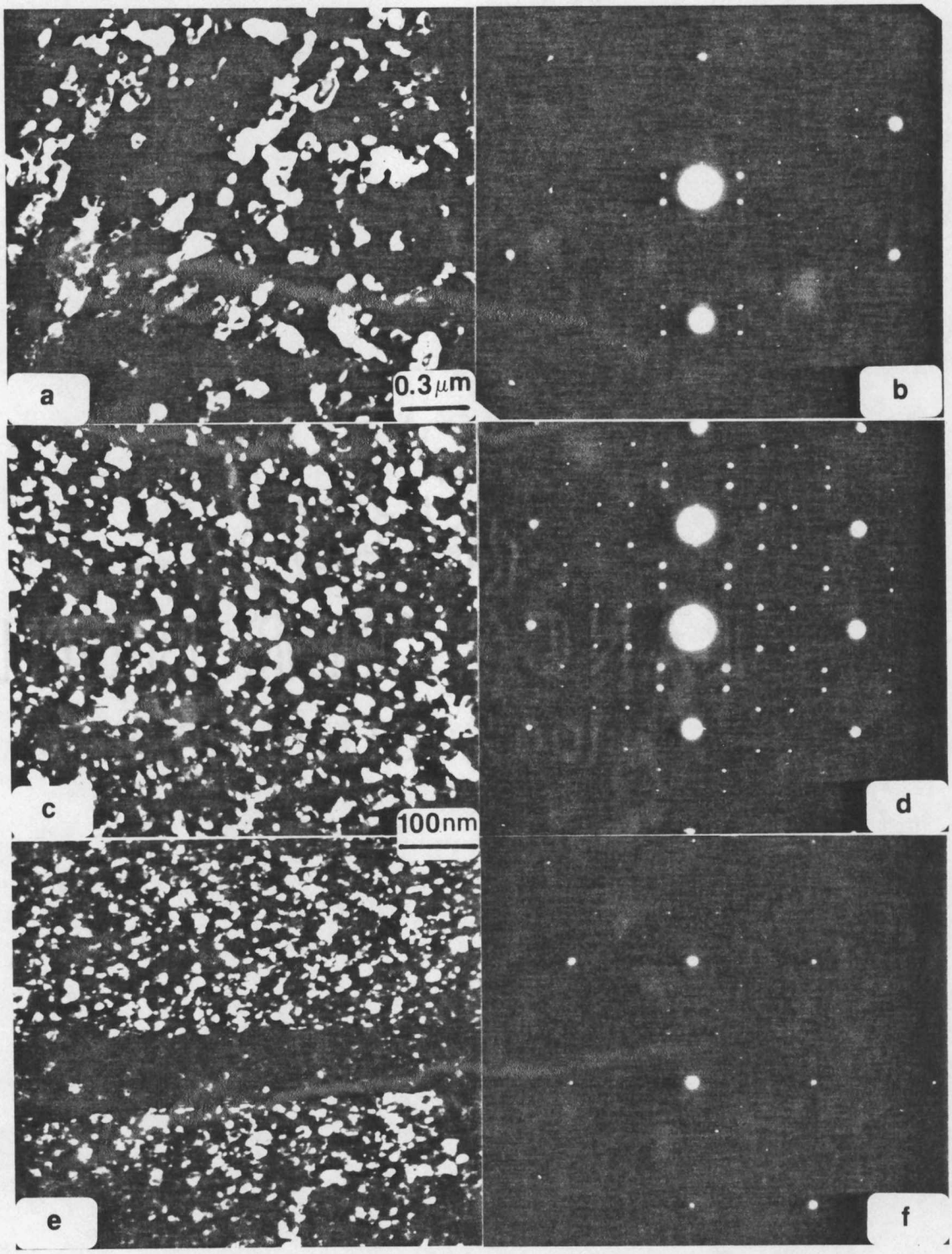


Figure IV-3. Effect of cooling rate from 950°C on the microstructure of ordered Ni_4Mo. a), c), and e) are DF micrographs from a Ni_4Mo spot in the corresponding SADP's in b) [122], d) [112] and f) [001] for samples cooled at 1, 5 and 10°C/min, respectively.

observed, thus indicating a fully ordered structure. At this cooling rate, the resulting domain size is 187 nm. With an increase in cooling rate, the domain size decreases to 80 and 36 nm for cooling rates of 5 (Figure IV-3c) and 10^{o}C/min (Figure IV-3e) respectively. Again only superlattice spots are observed; {1 1/2 0} SRO spots are absent in the [112] (Figure IV-3d) and [001] (Figure IV-3f) diffraction patterns of these samples.

The bright field (BF) structure of the fully ordered sample reheated to 800^{o}C for 1/2 hour and quenched in iced brine is shown in Figure IV-4a. One striking feature is the presence of rather large plates of Ni_3Mo at the grain boundaries. A BF micrograph and the associated [001] diffraction pattern of the same sample from another area are shown in Figures IV-4b and -4c. A DF image from a superlattice spot, Figure IV-4d, reveals both domain coarsening from the initial size of 187 nm (Figure IV-3a) to 245 nm and domain alignment along certain crystallographic directions. Increase in the reheat temperature results in further domain coarsening to 261 and 365 nm at 850 and 860^{o}C (Figures IV-5a and -5b) respectively. The DF micrograph in Figure IV-5b, obtained with the objective aperture positioned around two neighboring superlattice spots associated with two variants of the ordered phase (beam direction [112]), illustrates good contrast between perpendicular twin-related domains as well as the boundaries themselves. These boundaries are highly crystallographically controlled, developing parallel to {110} fcc planes (8-10,118,185).

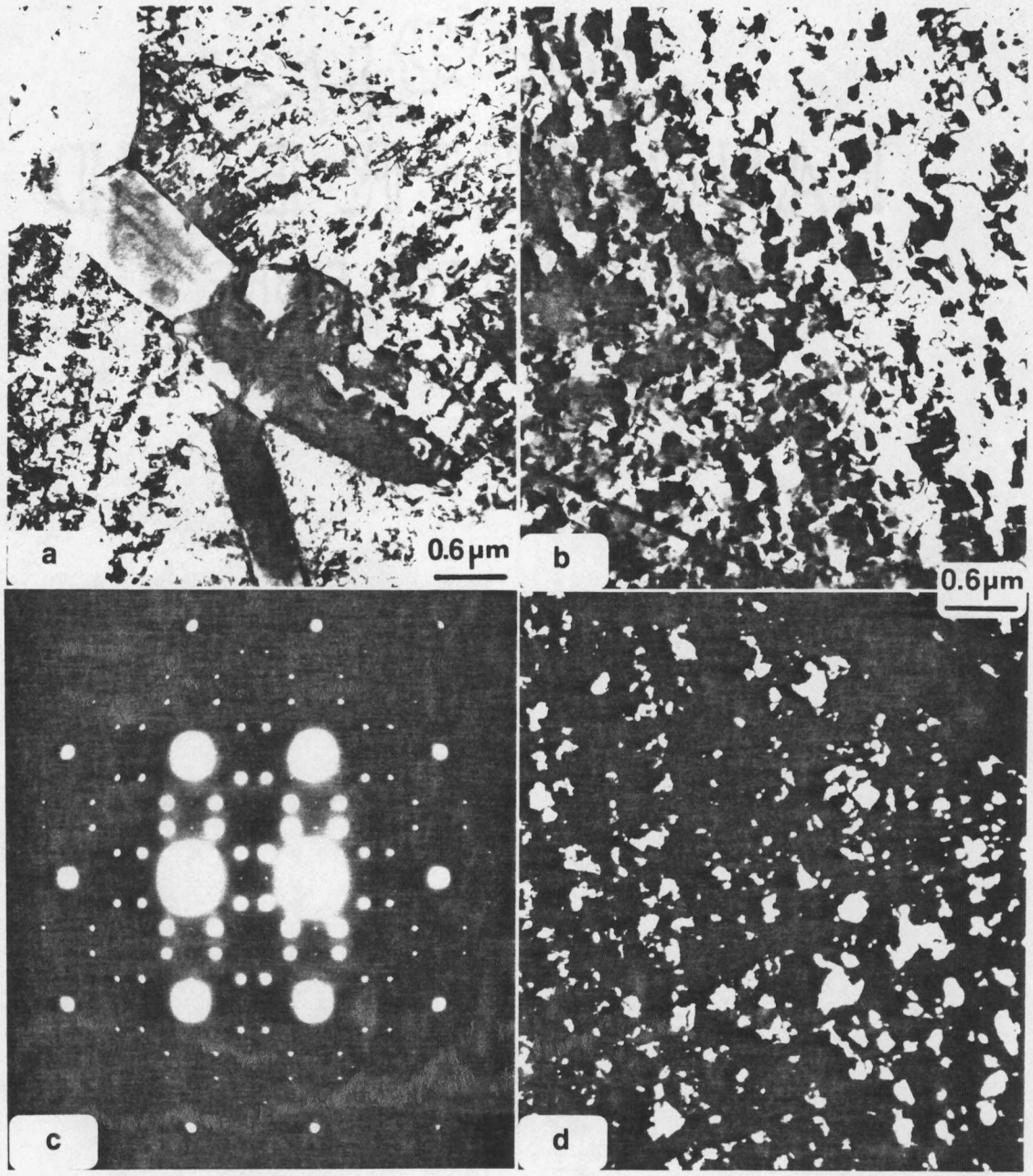


Figure IV-4. Effect of reheating on the microstructure of fully ordered Ni_4Mo. 800°C, 1/2 hr, quenched in iced brine. a) BF micrograph of large Ni_3Mo plates at grain boundaries; b) BF micrograph of Ni_4Mo domains; c) [001] SADP of b); d) DF micrograph from Ni_4Mo spot in c).

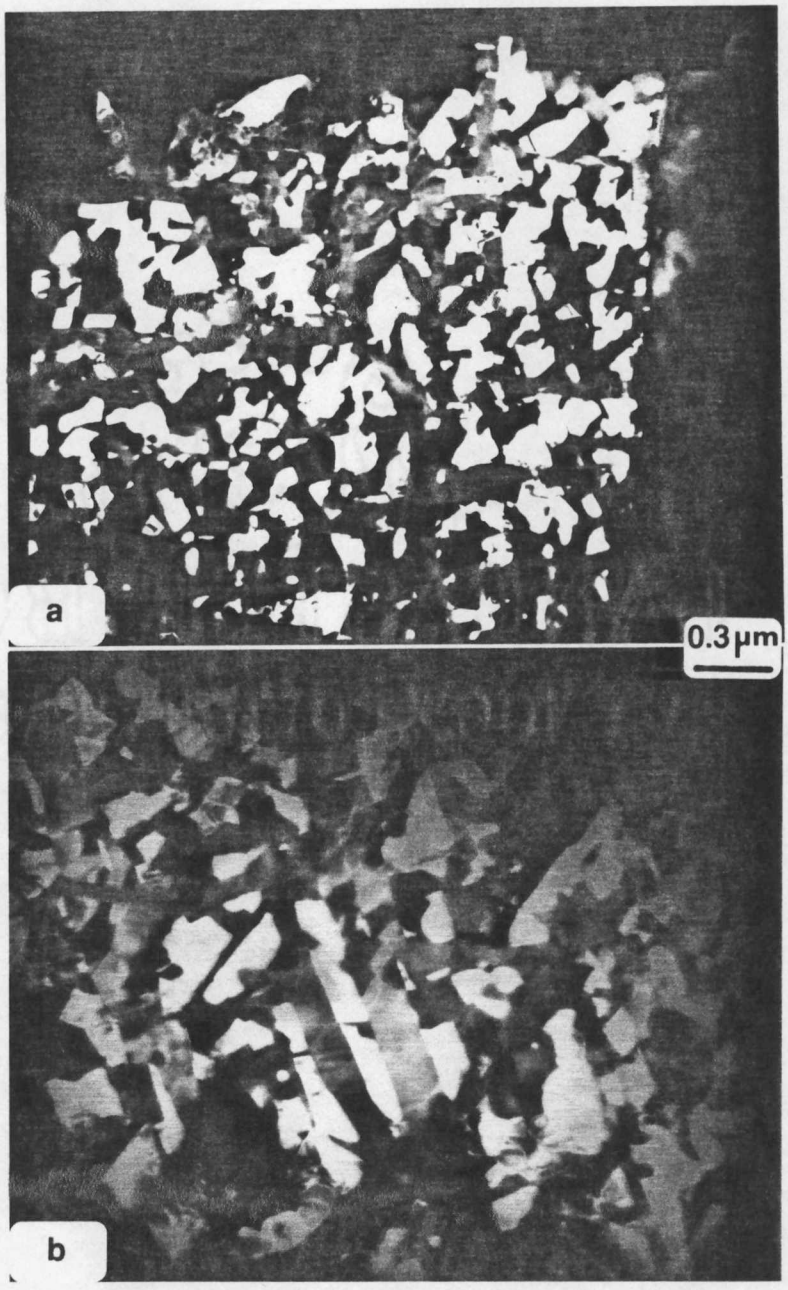


Figure IV-5. Effect of reheating on the microstructure of fully ordered Ni_4Mo. DF micrographs from Ni_4Mo spot for samples reheated to a) 850°C, and b) 860°C for 1/2 hr and quenched in iced brine.

Discussions on Resistivity and Structure

SRO resistivity. The decrease in resistivity with cold work and subsequent increase on reheating observed in this work, and previously by others (109,140,142), was first reported in several Ni-base alloys by Thomas (135) and called the "K-State" effect. Many other systems behave similarly (137,140,147,212-219). It is generally agreed that in Ni_4Mo (8,9,11,142), the decrease in resistivity with cold work (Figure II-17, page 64) is due to a decrease in the degree of SRO. The slight increase in resistivity for deformation in excess of 68% reduction is attributed to an increase in defect concentration overcompensating for the decrease in resistivity due to decrease in the degree of SRO (9,11).

The explanations of the resistivity anomalies vary and depend on the particular alloy. Several theories have been advanced to explain this behavior on the basis of changes in the electronic configuration as a result of lattice distortions (143,144). Since most alloys evincing this behavior contain at least one transition element, significance has been frequently attached to both the presence of an unfilled d-shell (135,137,145), and the degree of occupation and density of d-bands (220,221). Others have explained the increase in resistivity by proposing SRO microdomains (146), or at least nonrandom atom configurations providing more effective electron scattering than for the random solid solution. In the case of Ni_4Mo, the microdomain description of SRO (92,152,153) may not be valid and the static concentration wave model of DeFontaine (174) is most likely to be

applicable (156,157,160); the small increase in resistivity that is observed initially on isothermal annealing at 700°C (Figure IV-2) suggests amplification of the <1 1/2 0> SRO waves before LRO nucleats, confirming the wave model. If indeed the SRO state bore a structural similarity to the LRO structure, the increase would not be expected. These explanations of the resistivity anomalies are complicated by the fact that similar to Ni_4Mo, SRO increases resistivity in many systems (137,140,147,212-219), but decreases it in others (148,222,223).

Many theories relating SRO and resistivity exist (224-226). Gibson (224) has pointed out that SRO is expected to decrease the resistivity in solid solutions where component atoms differ in valence when the Fermi surface passes close to a Brillouin zone boundary for the random lattice, but increase resistivity when the Fermi surface is close to a Brillouin zone boundary for the superlattice. However, recent calculations using the coherent potential approximation (CPA) by Nicholson (227) indicate that in Ni_4Mo and perhaps in many systems evincing a high resistivity, the Fermi surface is virtually nonexistent. Although this would explain the high resistivity, the reason for the negative temperature coefficient of resistivity is unclear.

Rossiter and Wells (225) building on the framework of Gibson's theory (224) and incorporating a more reasonable scattering potential, calculated the residual resistivity for a binary alloy in terms of the degree of short range order, alloy composition and number of conduction electrons per atom. By considering only s-s electron scattering, in which, the s electrons are described by free electron

wave functions, they obtained the following expression for the resistivity:

$$\rho \propto \Sigma C_i \alpha_i Y_i \qquad \text{(IV-1)}$$

where, α_i is the Cowley short range order parameter, C_i is the concentration of atoms in the i^{th} shell at distance R_i, Y_i is an integral which may be positive or negative depending on R_i and the number of conduction electrons per atom, n. They showed that the sign of $d\rho/dT$ depended on the sign of α_i, the sign and magnitude of Y_i, and n.

For n = 1, $\alpha_1 < 0$ (for SRO), and $Y_1 < 0$, the theory of Rossiter and Wells (225) predicts a negative $d\rho/dT$. For transition metals, it is difficult to state the exact number of conduction electrons, since the number of valence electrons is variable. Nevertheless, since n = 1 is a possible value for nickel-molybdenum alloys, it is evident that the experimental results on Ni_4Mo qualitatively agree with this theory as can be seen from Figure IV-6, where $d\rho/dT$ (obtained graphically from curve 2C in Figure IV-1) is plotted against temperature. In Figure IV-6, $d\rho/dT$ is zero near 1300°C and becomes progressively more negative with a maximum at about 750°C. Following this, the slope becomes rapidly less negative in a narrow temperature range, and then changes sign near 600°C, whereupon the amount of SRO is "frozen-in" due to insufficient atom mobility.

The occurrence of the negative temperature coefficient of resistivity has received some attention (221,228,229) with formulation of the well known "Mooji Rule" (228), that is, independent of structure or electronic configuration, $d\rho/dT$ decreases with an

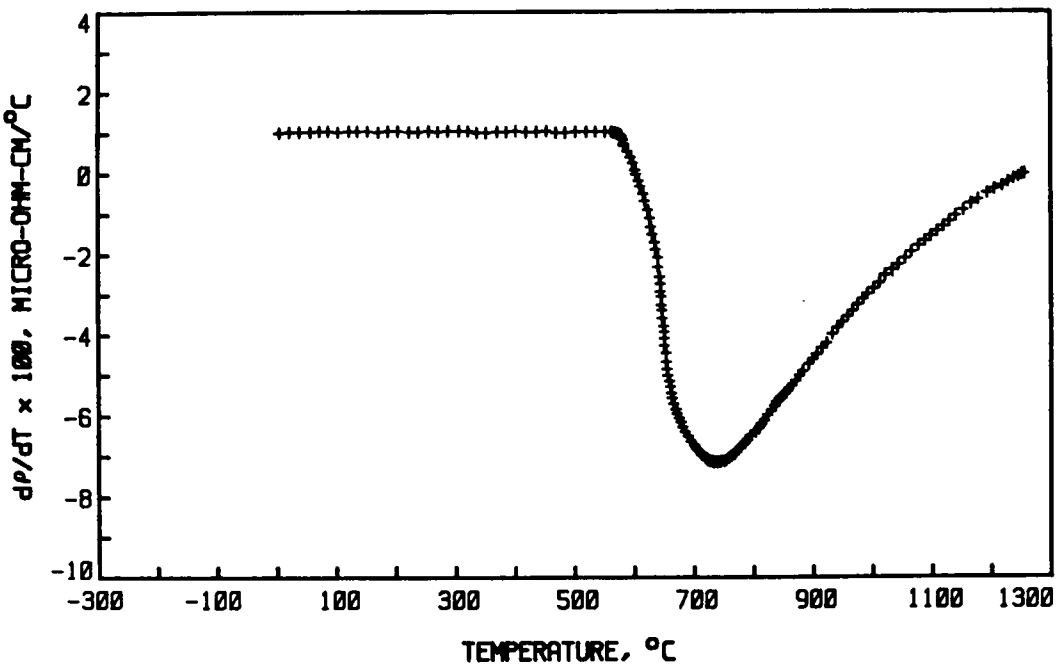


Figure IV-6. SRO dρ/dT versus temperature.

increase in resistivity in several disordered, as well as short-range ordered transition metal alloys. Mooji (228) has attributed this to the very small electron mean free path existing in these alloys. Though this may be true in Ni_4Mo, it appears that the explanation for the negative temperature coefficient of resistivity more probably relates to the nature of interactions between the degree of SRO and the density of d-states and how these change with temperature. Thus, if the SRO results in an increase in the number of unfilled d-shells, then a decrease in the degree of SRO (increase in temperature) can be visualized as decreasing the density of unfilled d-shells and therefore decreasing the s-d electron scattering and the resistivity.

LRO resistivity and structure. Although there are few systems in which LRO leads to an increase in resistivity (230,231), similar to Ni_4Mo, most systems (140,215,217,232) show a decrease. Several theories have been formulated relating LRO and resistivity (233-237). Rossiter (236,237) derived a simple expression combining the effects of LRO on the relaxation time to give an overall dependence of the resistivity on LRO as follows:

$$\rho(S,T) = \rho_0(0) \frac{(1 - S^2)}{(1 - A S^2)} + \frac{BT}{n_{eff}} \qquad \text{(IV-2)}$$

where, S is the Bragg-Williams LRO parameter, B is a constant, A is a parameter whose sign and magnitude depends on the relative positions of the Fermi surface and the superlattice Brillouin zone boundary, n_{eff} is the effective number of conduction electrons, and $\rho_0(0)$ is the residual resistivity for S = 0. The first term in the expression represents the contribution to the resistivity from S and the second

term represents the phononic contribution which varies with temperature as follows:

$$\rho_p(T) = T\frac{d\rho}{dT} = \frac{BT}{n_{eff}} \qquad \text{(IV-3)}$$

Thus, $d\rho/dT$ varies inversely with n_{eff}, which can increase or decrease with temperature depending on the alloy. In his analysis on quenched results of resistivity of FeCo (237), $d\rho/dT$ increased with increase in temperature due to a decrease in n_{eff}. An at-temperature analysis on Ni_4Mo using graphically determined values of $d\rho/dT$ obtained from curve 5H in Figure IV-1 is shown plotted versus temperature in Figure IV-7. In the temperature range -150 to 600°C, $d\rho/dT$ decreases which is opposite to his results. In fact, Rossiter (236) has pointed out that the linear relationship in equation IV-3 may not be valid for transition metal alloys owing to the dependence of s-d electron scattering on temperature. Therefore, it appears that in long range ordered Ni_4Mo, s-d scattering (density of d-states) decreases with temperature, leading to an increase in n_{eff}. As a result, $d\rho/dT$ will decrease, resulting in a relative decrease in resistivity as deduced from equation 1. Hence, the LRO resistivity behavior qualitatively agrees with the theory of Rossiter (236,237). Above 600°C, the $d\rho/dT$ increases (Figure IV-7) due to the greater influence of a decreasing degree of LRO as the order-disorder temperature of 868°C is approached.

The increase in room temperature resistivity with an increase in cooling rate from 1 to 10°C/min cannot be entirely accounted for by scattering due to smaller-sized domains observed in Figures IV-3a,

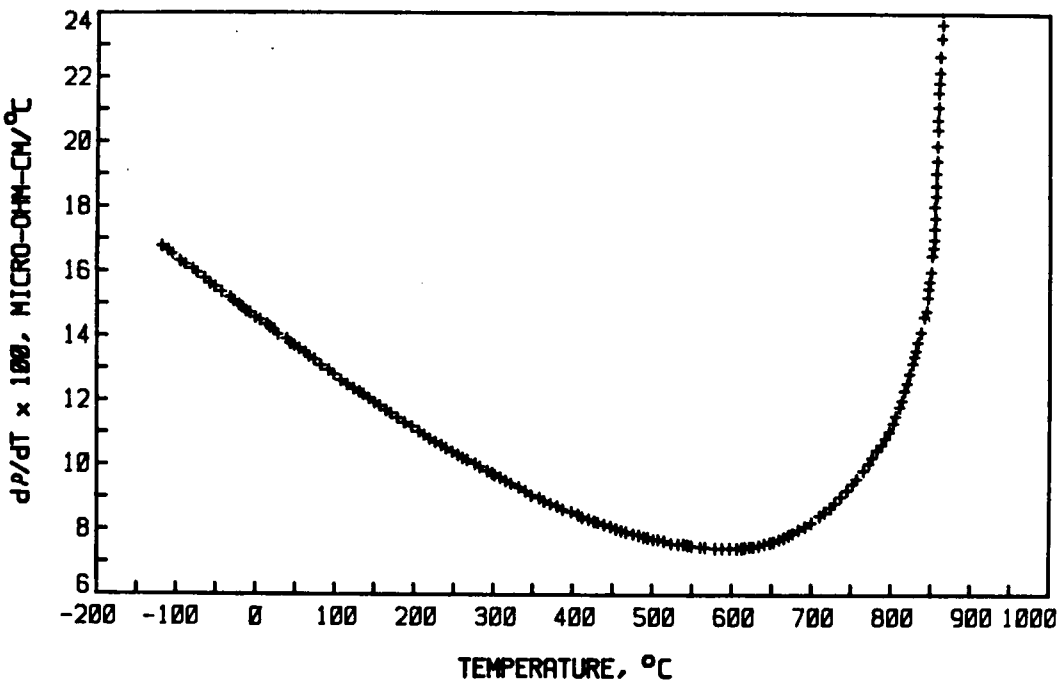


Figure IV-7. LRO dρ/dT versus temperature.

-3c, and -3e. This is because the domain sizes are large compared to typical values of the electron mean free path, and also it has been observed (8-10) that samples with very large domain sizes had resistivity values at 25°C identical to that of the sample cooled at 1°C/min. Thus, the major factor increasing the resistivity appears to be the decreasing degree of LRO with increasing cooling rate.

The interfaces between aligned domains in reheated samples develop parallel to {110} fcc planes and are perpendicular twin boundaries. These are similar to the {110} fcc striations occurring in the optical microstructure of isothermally ordered Ni_4Mo (8-10,185). Finally, the first order phase change in Ni_4Mo, indicated by the discontinuous change in resistivity on continuous heating and cooling (curves 5H and 4C in Figure IV-1), permits quenching-in from near the ordering temperature finite degrees of LRO as is evident from quenched-in increases in resistivity values.

Ordering in Ni_4Mo During Isothermal Annealing

The changes in the optical microstructure of ordered Ni_4Mo as a function of temperature and time were presented in detail in Chapter II. In particular, four different features were addressed, namely:

1. The nature of the {111} fcc striations.
2. The nature of the {110} fcc striations.
3. Domain structure and growth.
4. Grain boundary and annealing twin boundary instabilities.

In the following, the results of electron microscopy are presented to provide better understanding of these features.

The Nature of the {111} Fcc Striations

The {111} fcc striations develop as thin bands parallel to annealing twin boundaries, which are traces of {111} fcc planes, and span across distances orders of magnitude larger than the domain size (8-10). The evolution of these striations as a function of cooling rate and grain size are depicted in the optical micrographs in Figures IV-8a-d. To study the effect of cooling rate from the annealing temperature, large grain size (1 mm) samples were annealed at 800^{o}C for 16 hours and quenched in three different cooling mediums, namely: ice water at 0^{o}C, water at 25^{o}C and air. In general, fewer striations are observed at lower cooling rates (compare Figure IV-8c to -8a and -8b), thus indicating that quenching stresses contribute to the formation of the striations. Prior grain size, on the other hand, does not appear to have much influence on the formation of the striations. Careful examination of the microstructure of the small grain size sample, Figure IV-8d, reveals that the striations although fainter, are still present.

Thin foils prepared from the heat treated samples were studied in the TEM using bright field (BF), centered dark field (DF) and electron diffraction (SAD) modes. Throughout this research, the subscripts "c" and "t" are used to denote fcc and tetragonal indices respectively. Where no subscripts are present, the indices refer to fcc. The results for the large grain size specimen quenched in water are illustrated in Figures IV-9 and -10. In the BF image in Figure IV-9a, the striations occur as thin bands in two different orientations. The corresponding [011] SAD in Figure IV-9b (indexed in

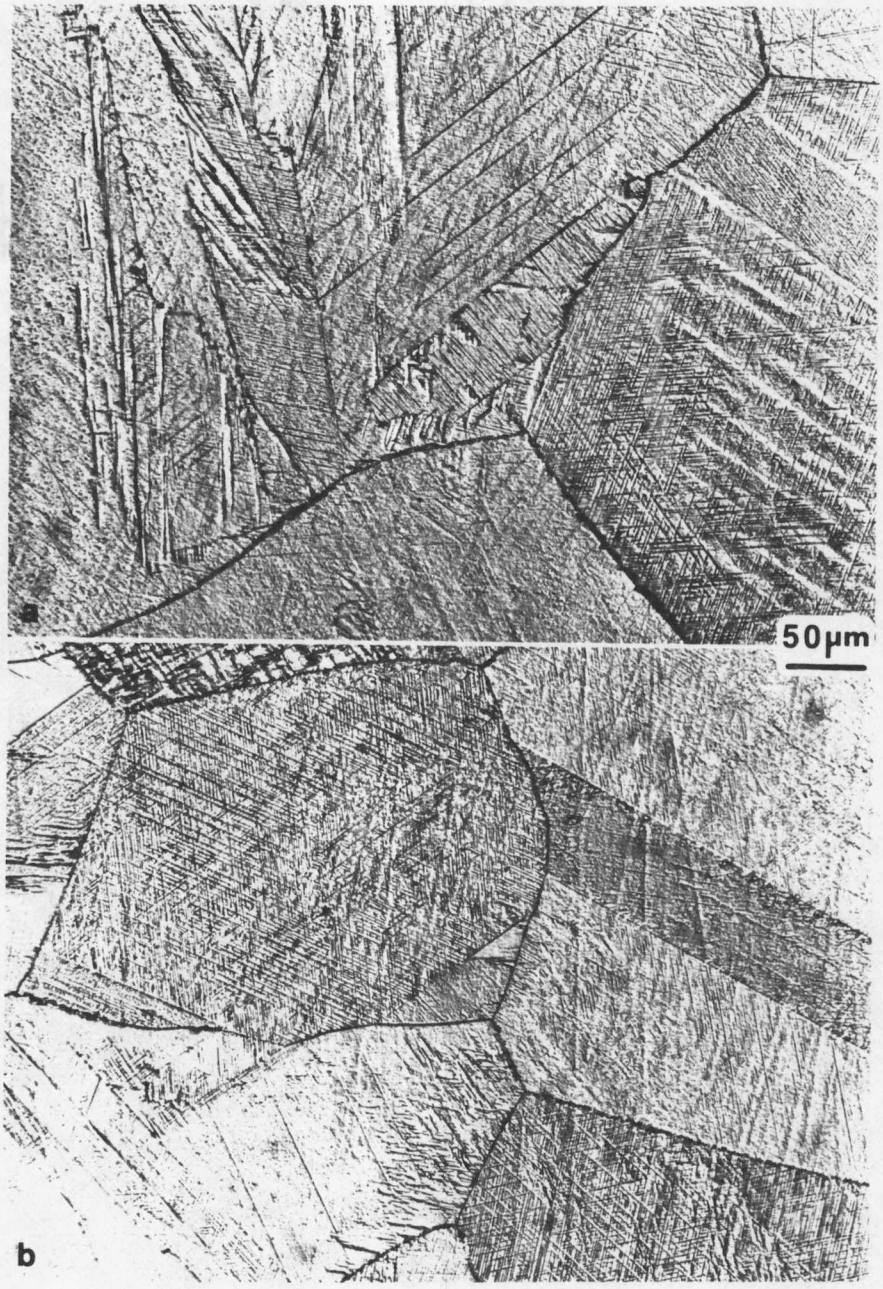


Figure IV-8. Optical micrographs showing the effect of cooling rate and grain size on the formation of the {111} fcc striations in ordered Ni_4Mo. Aged 16 hrs at 800°C and cooled in a) ice-water, b) water, c) air, and d) water (fine grain size sample).

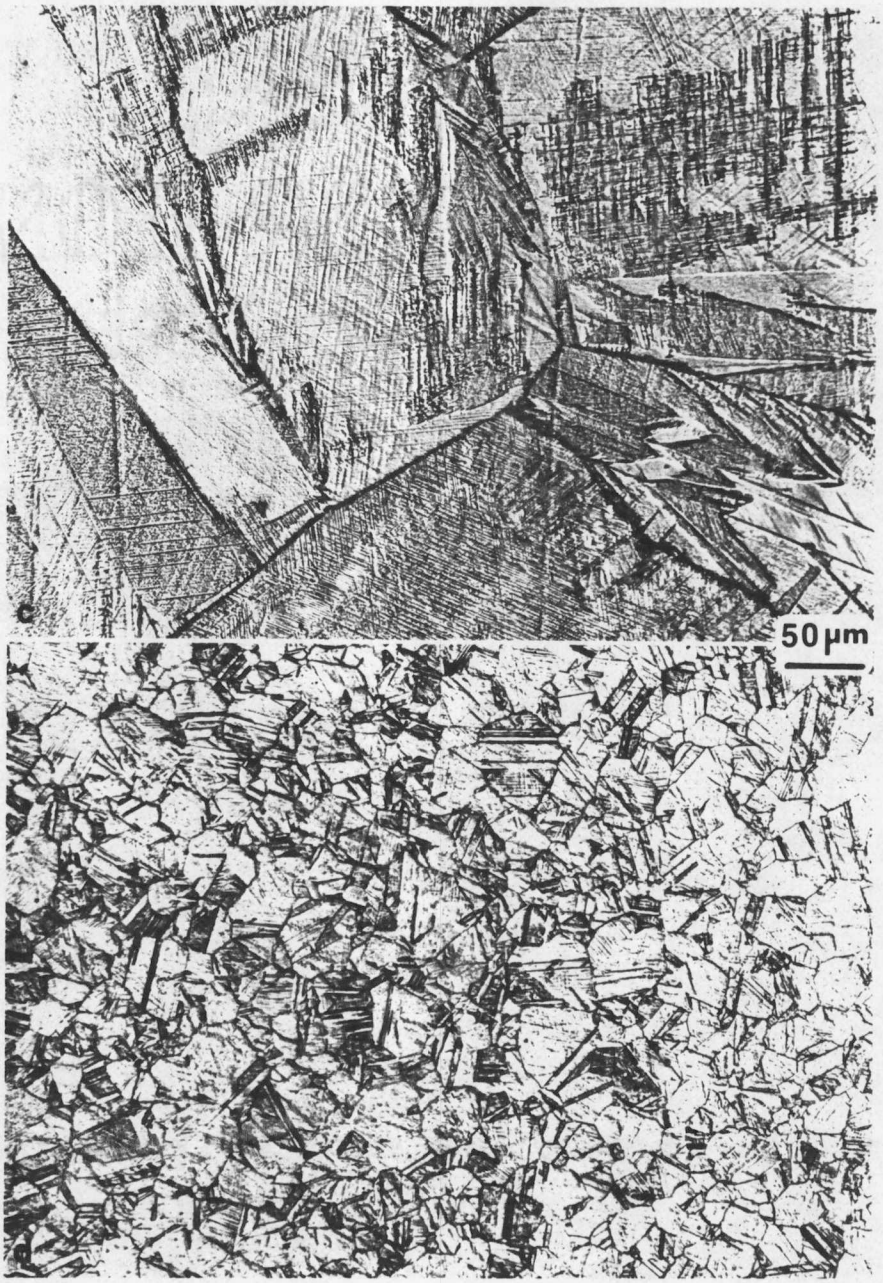


Figure IV-8. (Continued).

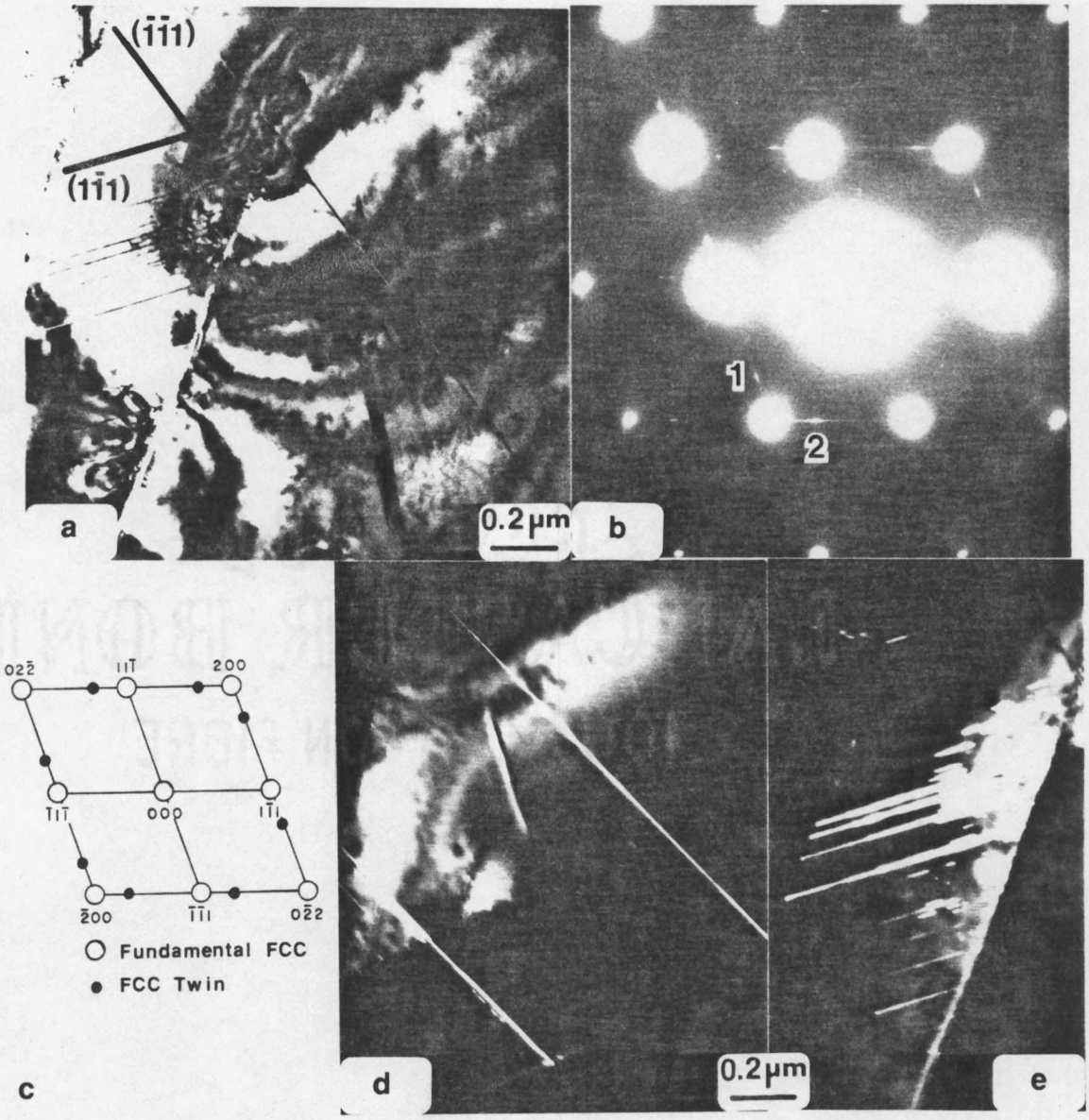


Figure IV-9. TEM micrographs of the {111} fcc striations imaging as twins. Aged 16 hrs at 800°C, water-quenched. a) BF; b) [011] SADP of a); c) indexing of b); d), e) DF images from twin spots labelled 1 and 2 in b).

IV-9c) shows besides the fundamental fcc spots, additional spots positioned along one third $[\bar{1}\bar{1}1]$ and $[1\bar{1}1]$ directions. These spots appear due to twinning (15,186,207 page 97). Additional confirmation for the twins is obtained by imaging them in DF with a twin spot. Figures IV-9d and -9e represent the DF images taken from the twin spots 1 and 2 in Figure IV-9b. The SAD in Figure IV-9b also shows elongation of the twin spots and streaks along the <111> directions. This streaking is associated with the thinness of the twinned regions and is normal to the thin dimension of the twin. Correlation between the SAD and the BF and DF images establishes the twin planes corresponding to twins 1 and 2 as the $(\bar{1}\bar{1}1)$ and $(1\bar{1}1)$ fcc planes respectively.

In another region in the same grain, the striations on the two other {111} fcc planes when imaged under two-beam conditions in BF (Figure IV-10a) and DF (Figure IV-10b) appear as alternate dark (D) and bright (B) fringes characteristic of stacking faults. The beam direction, $\underline{n}$ is [011] and the operating reflection (g) is $[\bar{1}\bar{1}1]$. That the striations are stacking faults is established by examination of the nature of the outermost fringes in BF and DF; these fringes are symmetrical in the former (both dark in Figure IV-10a) and asymmetrical in the latter image (one dark and one bright in Figure IV-10b).

The image of the stacking fault is characterized by the "phase angle," $\alpha = 2\pi \mathbf{g}.\mathbf{R}$, where g is the operating reflection (diffracting vector) and R is the displacement vector associated with the fault (207 page 161, 238). This parameter enters into the expressions for

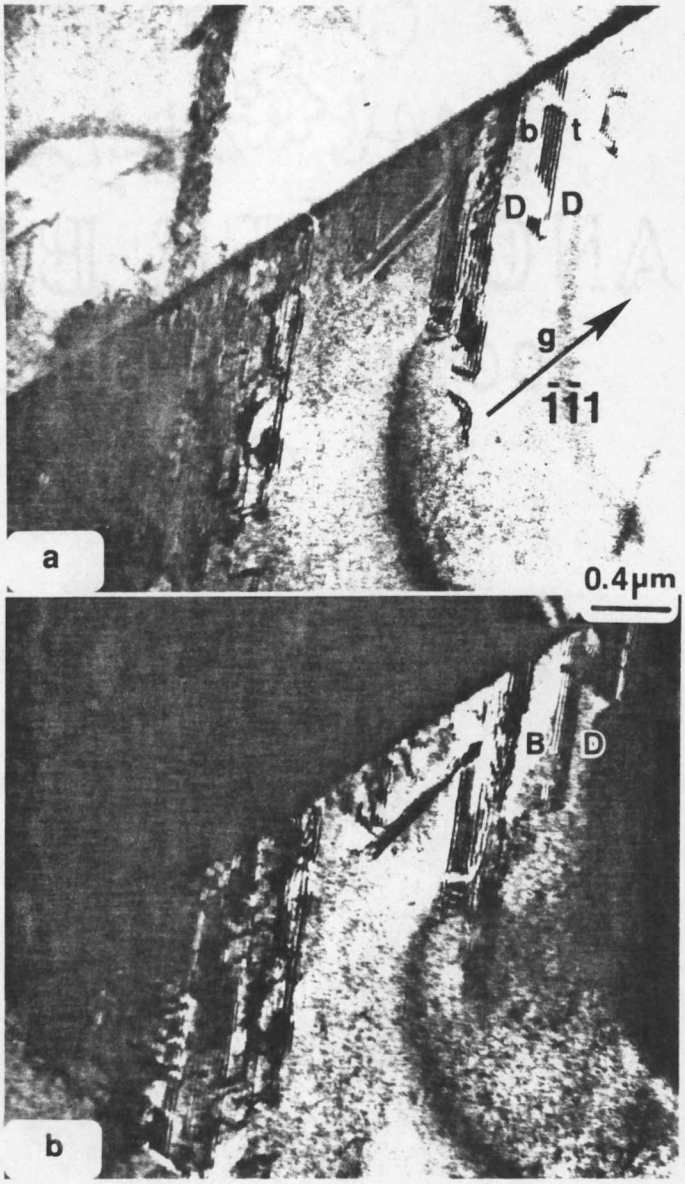


Figure IV-10. TEM micrographs of the {111} fcc striations imaging as stacking faults. Aged 16 hrs at 800°C, water-quenched. n=[011], g=[$\bar{1}\bar{1}1$]. a) BF; b) DF. B denotes a bright fringe, D a dark fringe; t and b denote the top and bottom surfaces.

the intensity variation of the electron beam as it traverses through the thin foil and is responsible for the contrast features associated with various defects (207 page 145, 238). In fcc metals, stacking faults may be produced on {111} planes by a shear of type <112>/6, or by the removal or insertion of a plane of atoms. For a fault on the (111) plane with shear vector $[\bar{1}2\bar{1}]/6$ and g = (hkl), α is given by

$$\alpha = \pi(h-2k+l)/3 \qquad \text{(IV-4)}$$

Since in the fcc lattice, h, k, l are either all odd or all even, α becomes $2n\pi/3$, where n can take positive or negative values of 0,1,2 etc., depending on the indices of (hkl). It is customary to refer to α modulo 2π ($-\pi<\alpha<\pi$). The possible values of α are 0, $\pm 2\pi/3$ modulo 2π. For $\alpha = 0$, the fault will be invisible. This vanishing criterion can be used to determine the direction of R (that is, the fault plane) by examining the visibility of the fault in a number of reflections. If α is negative, then the outermost fringes in BF are dark, if positive, the fringes are bright (238). For the particular case in Figure IV-10a, the outermost fringes are dark and therefore α is negative.

The geometry, that is, inclination of the faults (Figure IV-11) and the sense of R can also be deduced from the nature of the edge fringes in the BF and DF images. The BF and DF images remain unchanged at the top (t) surface and are complementary at the bottom (b) surface (238). The geometry of the fault in Figure IV-10a is indicated by the letters t and b. The sense of R enables determination of whether the fault is intrinsic or extrinsic. One method for determining the sense of R involves knowledge of the sign of α from the edge fringe of the BF image and the fault plane (238). This method is well illustrated by

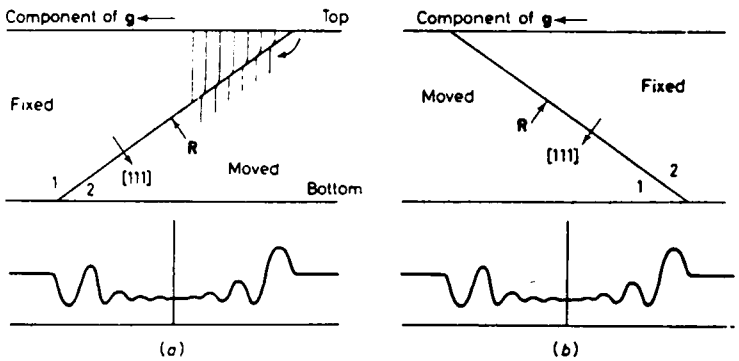


Figure IV-11. Illustration of the two possible senses of inclination of a stacking fault. The BF images would differ. In a) $\alpha = 2\pi/3$ and the edge fringes would be bright; In b) $\alpha = -2\pi/3$ and the edge fringes would be dark. The dark field image of both cases is the same as indicated by the intensity variation shown in the lower part of the figure.

Source: M. J. Whelan, "Dynamical Theory of Electron Diffraction," in Diffraction and Imaging Techniques in Materials Science, S. Amelinckx, R. Gevers and J. Van Landuyt (eds.), North-Holland, New York, Volume I: Electron Microscopy, 43-106 (1978).

an example. If R (in Figure IV-11) is defined as the sense of movement of the bottom of the crystal, then an intrinsic fault has R in the same sense as the upward drawn normal to the fault plane and an extrinsic fault in the opposite sense (239 page 68). Suppose the fault plane is (111) and g = $[\bar{1}\bar{1}1]$. Then $\alpha = 2\pi g.R = -2\pi/3$, that is negative. If the fault is intrinsic, then the edge fringes will be dark ($\alpha<0$), if extrinsic, the edge fringes will be bright ($\alpha>0$).

A simpler method which requires neither the knowledge of the fault plane nor the sense of inclination has been elaborated by Gevers et al. (240), who pointed out that the type of the fault can be determined from the DF image alone. This is understandable in terms of Figure IV-11, where it can be noted that although for the same type of fault the sign of α will be different in the two situations illustrated, the DF image will be unchanged. Gevers et al. (240) have given a rule, illustrated in Figure IV-12, which facilitates easy determination of the fault type. On the DF image, the diffraction vector g is drawn as an arrow with its origin at the center of the fault and pointing to the right as in Figure IV-12. Figure IV-12 then lists the sense of the edge fringes bordering the fault for two possible inclinations of the fault and the two possible types of faults. B and D denote a bright and dark fringe respectively. Full lines denote the top surface fringe, broken lines, the bottom surface fringe. A and B represent two classes of operating (Bragg) reflections. A includes {200}, {222}, {440}; B includes {111}, {220}, {400}. For a given class (A or B), the DF image (with g inscribed as above) permits the fault type to be determined by inspection of Figure

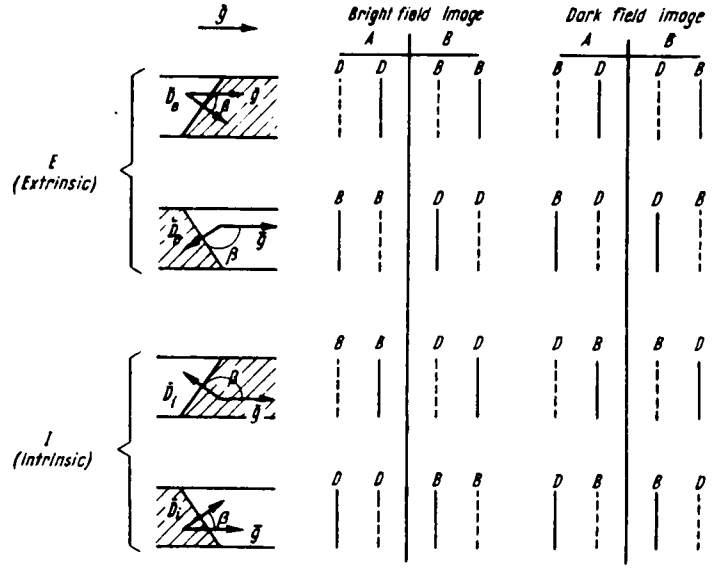


Figure IV-12. Schematic diagram to enable determination of whether a stacking fault is intrinsic or extrinsic. The nature of edge fringes at $\pm 2\pi/3$-faults for various cases is indicated.

Source: After ref. 26 in M. J. Whelan, "Dynamical Theory of Electron Diffraction," in Diffraction and Imaging Techniques in Materials Science, S. Amelinckx, R. Gevers and J. Van Landuyt (eds.), North-Holland, New York, Volume I: Electron Microscopy, 43-106 (1978).

IV-12. For the faults in Figure IV-10b, g points towards the dark fringe. The reflection is of class B (111), and therefore the fault is intrinsic by comparison with column B for intrinsic faults. Knowledge of the geometry of the fault from the BF and DF images and utilization of an alternate method of Art et al. (241) permits even easier establishment of the fault type.

The results for the large grain size specimen quenched in ice water are presented in Figures IV-13 and -14. Figures IV-13a-f represent pairs of two-beam BF and DF images of the striations using different indicated reflections. The beam direction is [011]. The nature of the edge fringes is indicated in the micrographs. The geometry of the fault is once again established by comparison of the BF and DF images and is also indicated in Figure IV-13a. The fault in this case shows several discontinuities as well as a change in contrast at each discontinuity. Typically, the contrast appears as a repeating sequence of grey-dark-white fringes. This type of contrast is associated with overlapping stacking faults, that is stacking faults on closely spaced {111} fcc planes (207 page 166, 238). When the fault is imaged with $g = [0\bar{2}2]$, dislocations at the locations of the discontinuities can be clearly seen (Figures IV-13c and -13d). These dislocations are of either the $1/6[11\bar{2}]$ or the $1/6[1\bar{2}1]$ type (186,242). Examination of the nature of the edge fringes in BF and DF and application of either the method of Gevers et al. (240) (Figure IV-12) or Art et al. (241) once again establishes the fault type as intrinsic. When the fault is examined with $g = [\bar{2}00]$ ($\underline{n}$ =[001]), additional dark patches appear within segments of the fault of constant contrast, such as at locations P in Figures IV-13e-f.

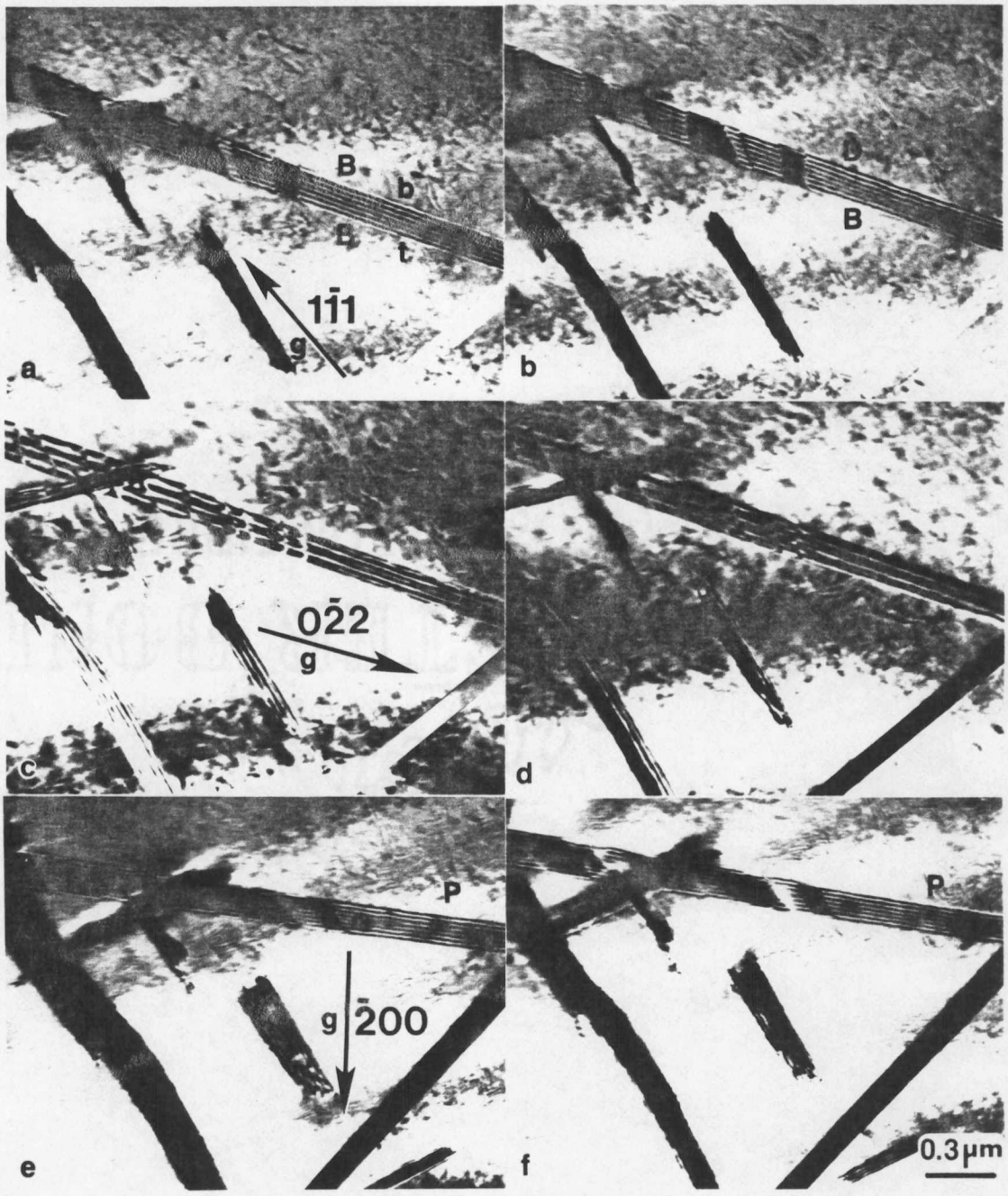


Figure IV-13. TEM micrographs of the {111} fcc striations imaging as overlapping stacking faults. Aged 16 hrs at 800°C, ice-water quenched. a) through f) are BF (left) and DF (right) pairs under different indicated two-beam conditions; n is [011] for a) to d) and [001] for e) and f); B, D, $\bar{t}$ and b have same meaning as in Figure IV-10; g) BF of underlying domain structure; h) [001] SADP of g; i) DF from Ni_4Mo spot in h).

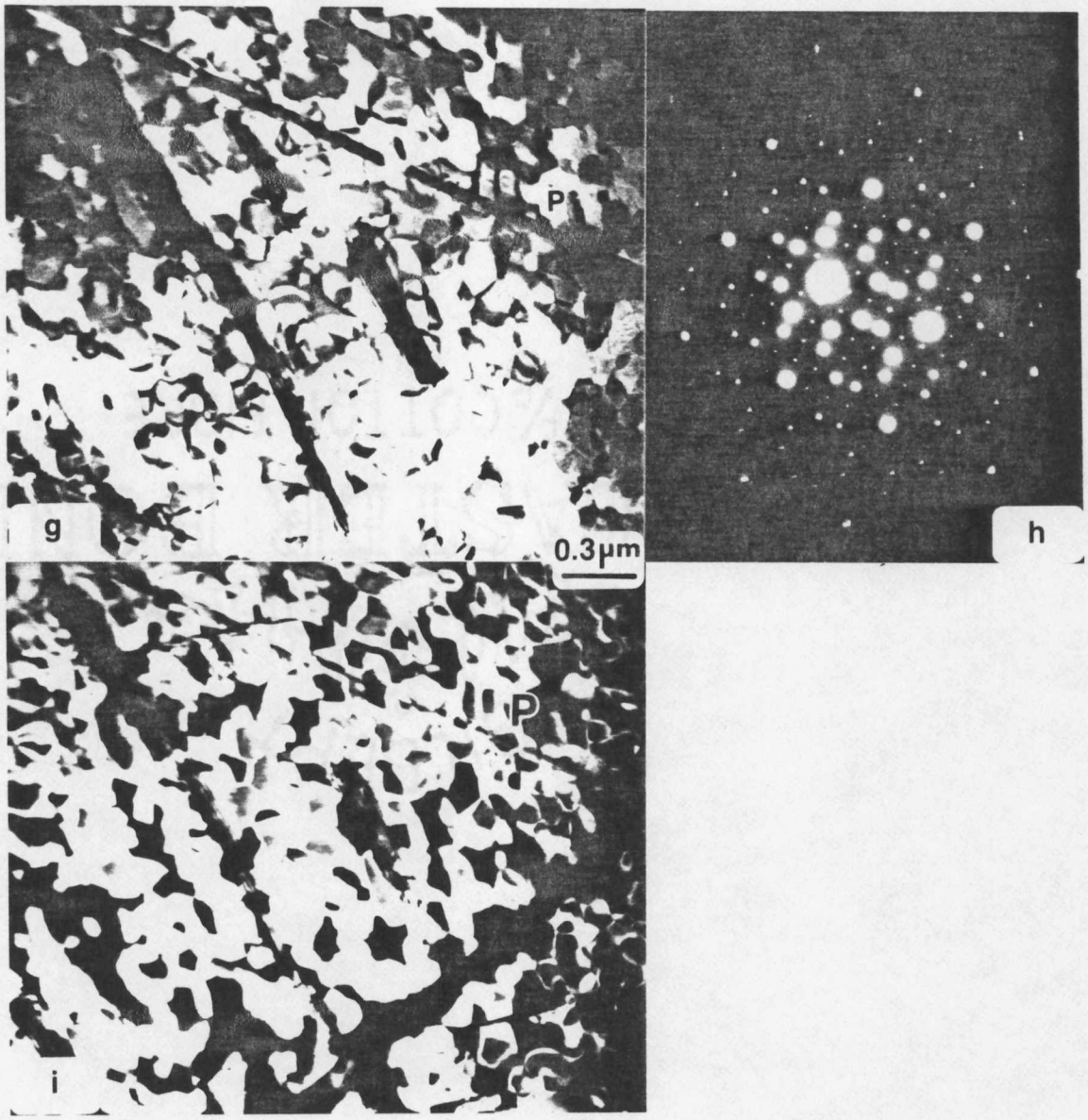


Figure IV-13. (Continued).

Tilting the sample to the [001] orientation reveals the underlying domain structure. The BF image in Figure IV-13g reveals APT-related Ni_4Mo domains corresponding to the set of superlattice spots in the [001] SAD in Figure IV-13h. A DF image obtained from a single Ni_4Mo spot (Figure IV-13i) reveals that the fault, for the most part, progresses through regions of antiphase domains. At locations such as P in Figure IV-13g and -13i, where the fault crosses an APT boundary, the contrast changes. Thus, it appears that the dark patches observed in Figures IV-13e and -13f correspond to these regions.

Figure IV-14a illustrates a BF image of overlapping stacking faults from another region of the same sample observed with $\underline{n}$ = [001] and g = [200]. When the sample is tilted to the [011] orientation, the faults give rise to extra twin spots along the $[\bar{1}\bar{1}1]$ direction in the SAD pattern (Figure IV-14b). A DF image from the twin spot encircled in Figure IV-14b is shown in Figure IV-14c. Thus, there is a one-to-one correspondence between the overlapping stacking faults and the twins.

The nature of the faults in specimens of large domain size, produced by aging at 800°C for 840 hours, were also examined. The results are depicted in Figures IV-15a-f. The BF and DF images in Figures IV-15a and -15b obtained under the diffraction conditions n = [011] and g = $[\bar{1}1\bar{1}]$ clearly image the grey-dark-white fringe contrast associated with overlapping stacking faults. The contrast features associated with overlapping stacking faults can be understood by analysis of the change of sign of the phase angle α (Figure IV-16). If α is $2\pi/3$ for a single fault, the net phase angle for n overlapping

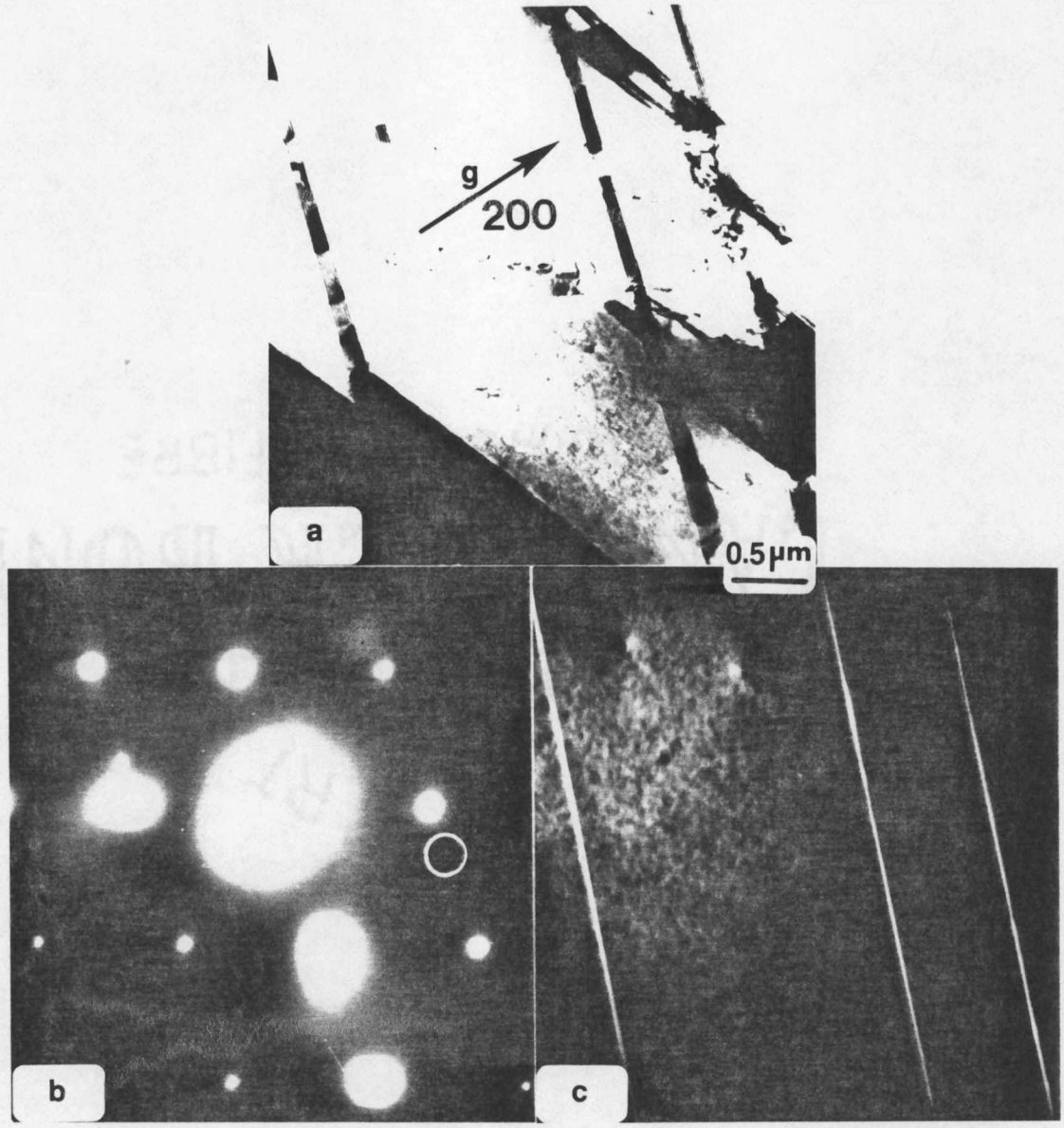


Figure IV-14. TEM micrographs of the {111} fcc striations showing one-to-one correspondence between overlapping stacking faults and twins. Aged 16 hrs at 800°C, ice-water quenched. a) BF showing stacking faults (n=[001], g=[200]; b) [011] SADP of a); c) DF from twin spot $\bar{t}$ encircled in b).

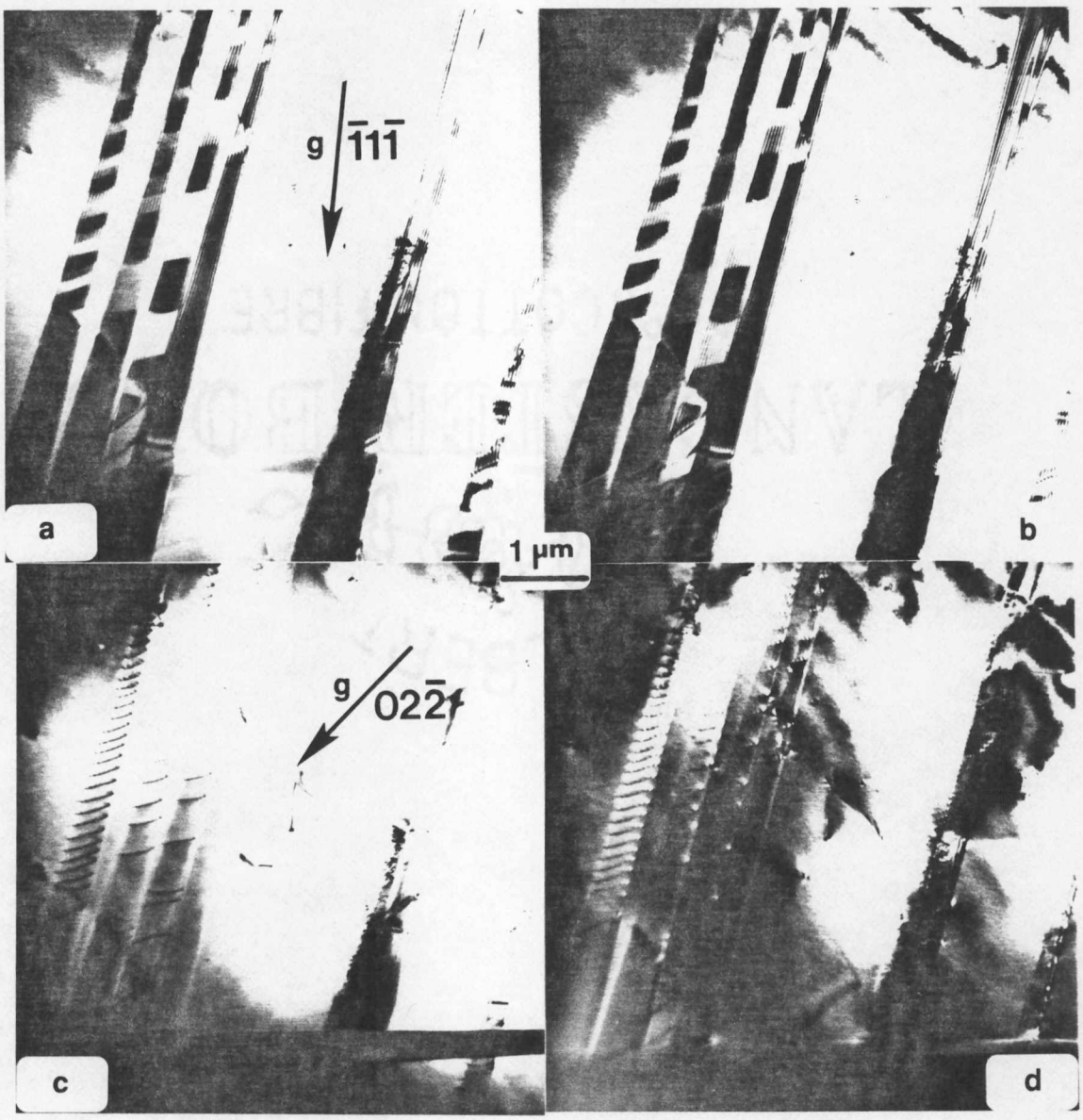


Figure IV-15. TEM micrographs of the {111} fcc striations in large domain size Ni_4Mo. Aged 840 hrs at 800°C, water-quenched. a), b) BF-DF pair showing overlapping stacking (n=[011], g=[$\bar{1}1\bar{1}$]); c), d) BF-DF pair showing partial dislocations in a) (n=[011], g=[$02\bar{2}$]); e) BF and f) DF showing Ni_4Mo domains (n=[112]).

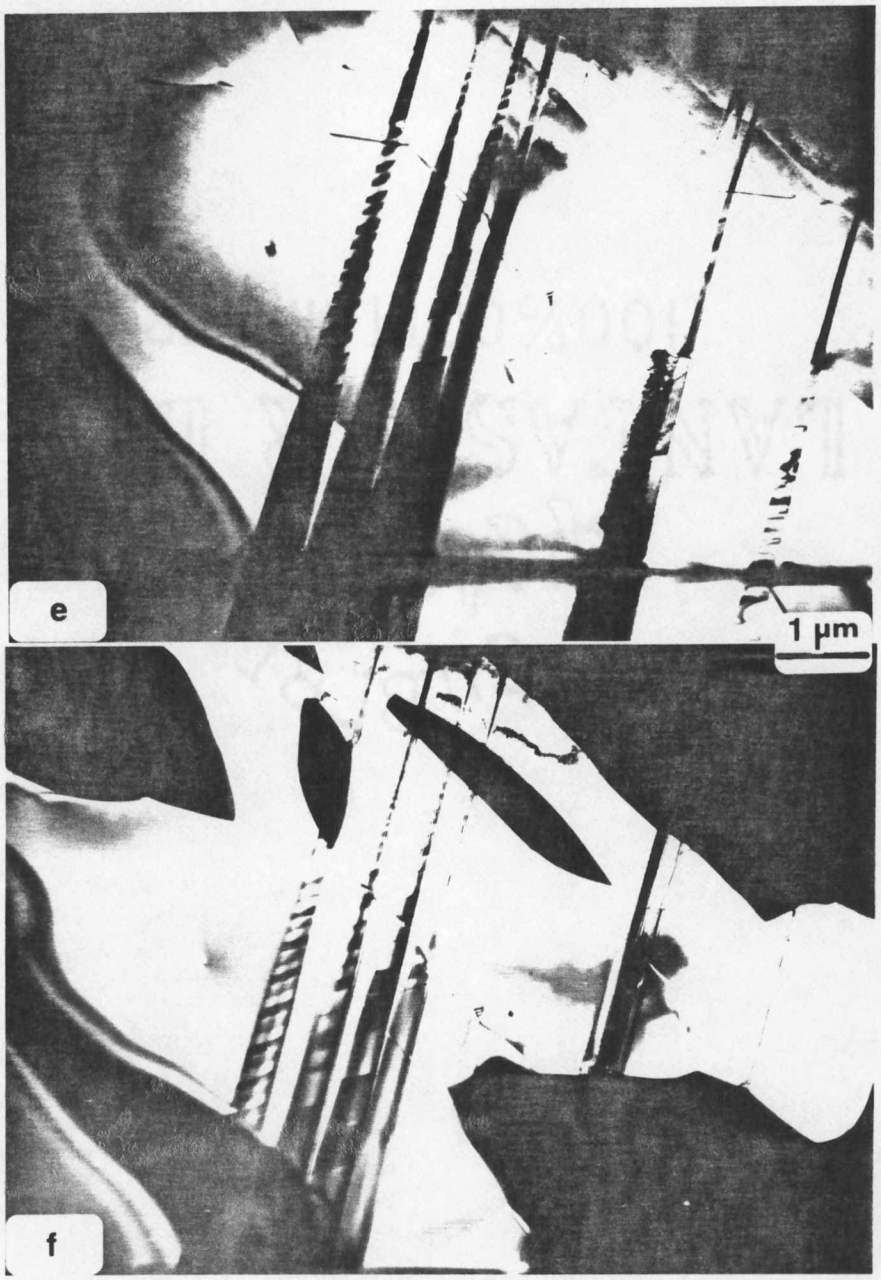


Figure IV-15. (Continued).

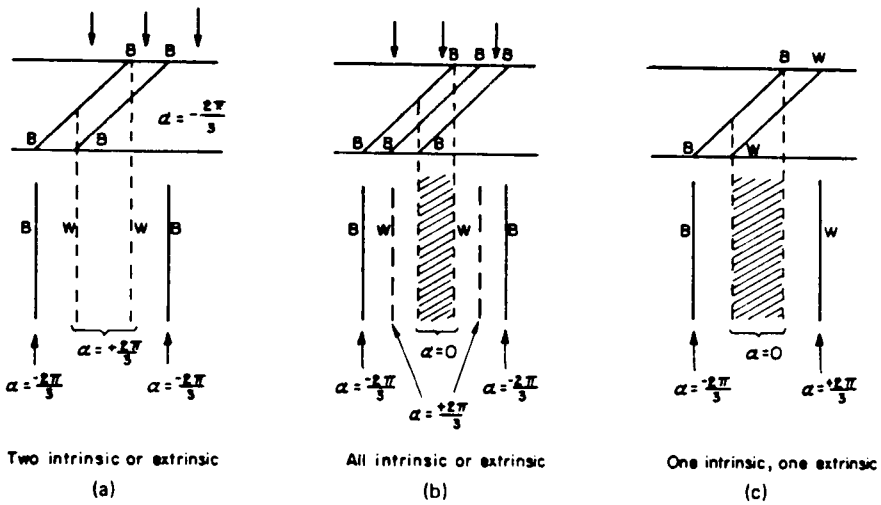


Figure IV-16. Schematic drawing showing contrast expected from overlapping stacking faults in fcc crystals with $\alpha=2\pi/3$. B and W are dark and white fringes, respectively.

Source: G. Thomas and M. J. Goringe, "Introduction to Contrast Analysis and its Applications," in Transmission Electron Microscopy of Materials, Wiley, New York, 139-222 (1979).

faults will be $2n\pi/3$. Thus, for two intrinsic faults (Figure IV-16a) α is $4\pi/3$ or $-2\pi/3$ (modulo 2π). The sign of α changes and as a result a reversal in fringe contrast occurs at the point of overlap. For three overlapping faults α is 0 (Figure IV-16b). Therefore, a characteristic set of fringes corresponding to every third set of faults will show no contrast (207 page 166, 238). Such a sequence of fringes is visible in Figures IV-15a and -15b.

Individual sets of fault ribbons in Figure IV-15a are themselves separated by closely spaced as well as widely spaced partial dislocations. When the faults are imaged with $g = [02\bar{2}]$, these dislocations are clearly visible at the point of overlap of the faults (Figures IV-15c-d). The burgers vector for these dislocations has been established using the $g.b = 0$ invisibility criterion as $1/6[11\bar{2}]$ or $1/6[1\bar{2}1]$ (186,242). In Figures IV-15c-d, the faults themselves are invisible under these diffraction conditions. Based on the $g.R = 0$ invisibility criterion, the fault plane can be either (111) or $(\bar{1}11)$. On tilting the specimen to the $[\bar{1}01]$ orientation, the faults appeared as thin bands and produced extra twin spots along the [111] direction. Thus, the fault plane is established as (111). Similar to earlier observations there exists a one-to-one correspondence between the overlapping stacking faults and the twins.

On tilting the specimen to the [112] orientation, the underlying domain structure is revealed. The BF image (Figure IV-15e) and the DF image (Figure IV-15f) obtained from a Ni_4Mo superlattice spot show that the overlapping stacking faults and the partial dislocations at the points of overlap occur within single Ni_4Mo domains.

Another feature frequently observed is the creation of perpendicular twins when a twin passes through a set of domains. An example is shown in Figures IV-17a and -17b. In the BF image in Figure IV-17a, a set of APB-related Ni_4Mo domains are identified by the letter A and a twin is denoted by the letter B. The corresponding [112] SAD in Figure IV-17b shows Ni_4Mo spots from two perpendicular twin-related variants. It was established by DF imaging that the brighter spots (A) were caused by the domains A in Figure IV-17a and the weaker spots (B) by domains within the twin B. The weaker spots are also elongated and streaked in the $[\bar{1}\bar{1}1]$ direction, which is normal to the thin dimension of the twin. It is clear therefore that the twins as referred to the fcc lattice are simultaneously true twins in relation to the ordered Ni_4Mo lattice. This feature has also been reported by Nesbit and Laughlin (186).

Rationalization for the existence of the faults/twins based on structural considerations. The results presented above have shown that the {111} fcc striations are intrinsic stacking faults/mechanical twins. A major factor responsible for the formation of the striations in ordered Ni_4Mo are stresses generated by quenching from the annealing temperature. The stresses caused by the change in crystal structure due to ordering play a small role. The faults/twins produced by quenching stresses are identical to those produced by deformation of the ordered Ni_4Mo alloy (15,186,242). The deformation microstructure of the disordered alloy is characterized by an absence of either stacking faults or twins (12,13,15-18,186,242). The presence of

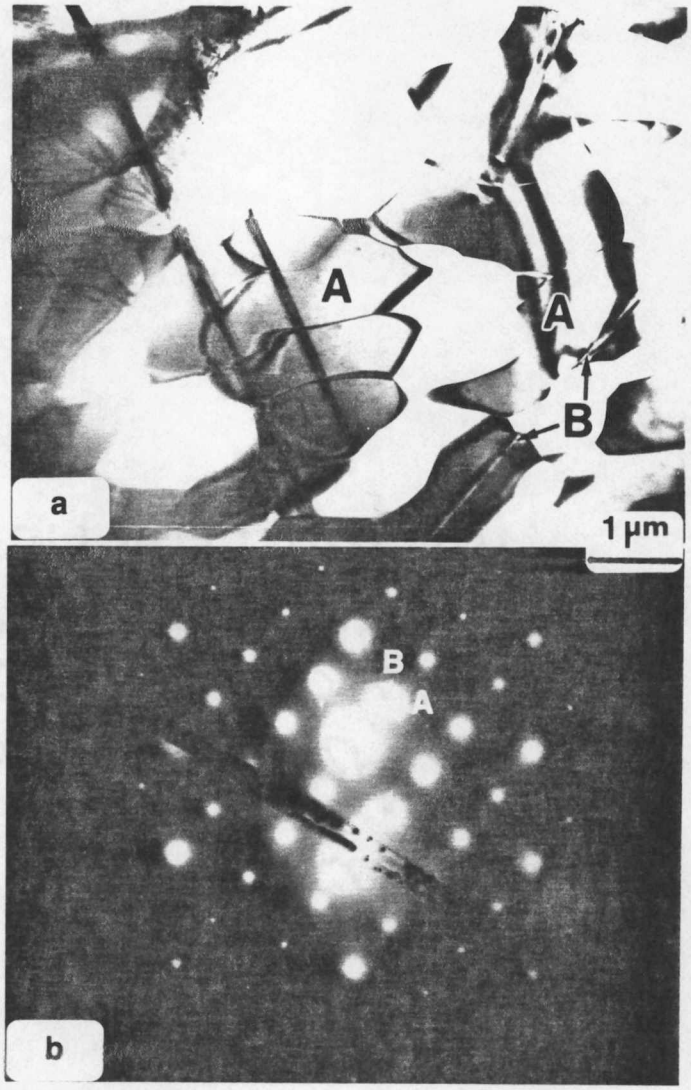


Figure IV-17. TEM micrographs showing the creation of perpendicular twins when a twin passes through antiphase domains. Aged 384 hrs at 800°C. a) BF; a group of antiphase domains and a twin are identified by the letters A and B, respectively; b) [112] SADP of a) showing PT-related spots.

the stacking faults and twins in the ordered alloy implies that ordering in Ni_4Mo lowers the stacking fault energy. The initiation and propagation of the faults and the associated partial dislocations can occur only if the passage of these faults does not disrupt the prevailing order. This can be understood by considerations of the relation between the faults/twins and the atomic arrangement on the slip plane. Since the c/a ratio of ordered Ni_4Mo is near unity, the slip planes are expected to be the $\{111\}_c$ planes or equivalently the $\{121\}_t$ planes and the slip directions to be the $\langle 110\rangle_c$ or $\langle 120\rangle_t$ directions (15,186).

The atomic arrangement on the $(111)_c$ plane of ordered Ni_4Mo is depicted in Figure IV-18. The <110> and <112> directions on this plane are as shown. To explain the prevalence of stacking faults in ordered Ni_4Mo, the effect of the passage of a partial dislocation with burgers vector 1/6<112> must be considered. The results of Nesbit and Laughlin (186) and Kao (242) have established that the partial dislocations separating the fault are of one type either the $1/6[11\bar{2}]$ or the $1/6[1\bar{2}1]$, that is, of the three possible burgers vectors only two are observed. Depending on the particular geometry of the stress axis in relation to the fault, only one of the two possible burgers vector occurs (242), as verified for example in Figures IV-15c-d. In other words, the stacking faults are produced by partial dislocations of the same burgers vector. The atomic arrangement on the $(111)_c$ plane (Figure IV-18) shows that in the stable condition a molybdenum atom has 12 nearest neighbor (NN) nickel atoms and 0 NN molybdenum atoms; a nickel atom has 9 NN nickel atoms and 3 NN molybdenum atoms. Detailed

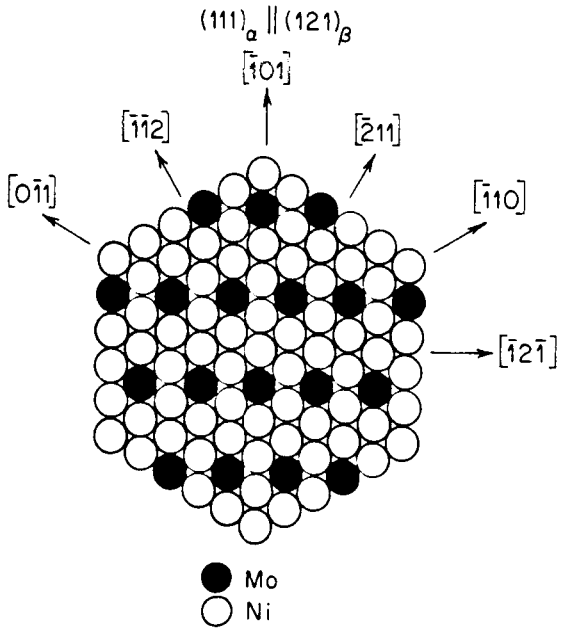


Figure IV-18. The close-packed plane of ordered Ni_4Mo. Filled circles indicate Mo atoms, open circles Ni atoms.

Source: L. A. Nesbit and D. E. Laughlin, "The Deformation Microstructure of the Ni-Ni_4Mo System," Acta Met., 28, 989-998 (1980).

analysis shows that the passage of either the $1/6[11\bar{2}]$ or $1/6[1\bar{2}1]$ dislocations does not change the number of each kind of NN nickel-molybdenum bonds, whereas the $1/6[\bar{2}11]$ type changes the number of NN's (186,242). This crystallographic characteristic of the ordered Ni_4Mo structure accounts for the presence of the stacking faults.

A second feature of the striations is that they occur simultaneously as intrinsic overlapping stacking faults or twins. The mechanism for such an occurrence is complex. Venables (243) and recently Paidar (244) have demonstrated that a twinned crystal in a fcc lattice can be built by a series of overlapping intrinsic stacking faults on successive {111} planes. The model of Paidar (244) proposes that the atomic configuration of a twin can be described as a three-layer overlapping fault composed of three partial dislocations $1/6[11\bar{2}]$, $1/6[\bar{2}11]$, $1/6[1\bar{2}1]$ with the net sum of the displacement vectors adding to zero. That of Venables (243) essentially requires that the stacking faults be produced by partial dislocations of the same Burgers vector on each parallel plane. Since the overlapping stacking faults in Ni_4Mo are composed of the same Burgers vector (186,242), the model of Venables (243) provides the better explanation for the twin formation by this mechanism.

A related characteristic of such mechanical twins in Ni_4Mo is that they are not only twins of the fcc lattice but true twins relative to the ordered lattice (Figures IV-17a-b). Nesbit and Laughlin (186) have forwarded a mechanism for this phenomenon, which is elucidated in Figures IV-19a-b. In Figure IV-19a, the positions of molybdenum atoms on three successive $(111)_c$ (bottom, middle, top)

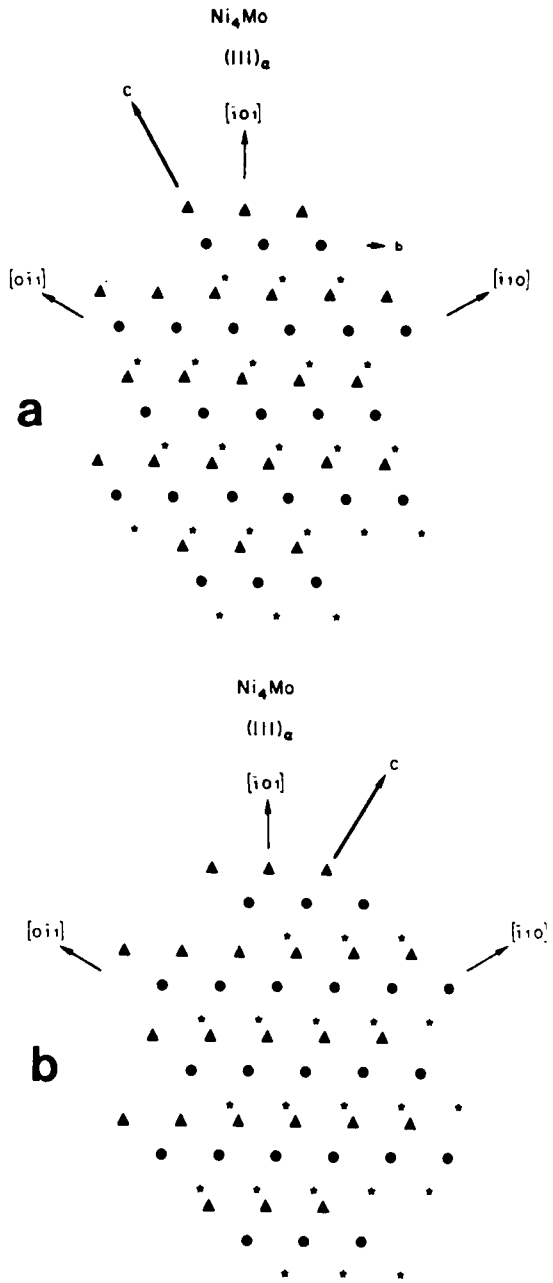


Figure IV-19. The positions of Mo atoms on three successive (111) planes in fully ordered Ni_4Mo. The positions on the bottom, middle and top planes are designated by the triangles, circles and the stars, respectively. a) The positions of the Mo atoms before twinning; the arrow by the letter b indicates the magnitude and direction of $1/6[\bar{1}2\bar{1}]_\alpha$ partial dislocation which moves on successive $(111)_\alpha$ planes to produce the twinned structure in b).

Source: L. A. Nesbit and D. E. Laughlin, "The Deformation Microstructure of the Ni-Ni_4Mo System," Acta Met., 28, 989-998 (1980).

planes are indicated by triangles, stars and circles respectively. The projection of the Ni_4Mo c-axis is delineated by a triangle, a star, and a circle in succession and is indicated in Figure IV-19a; the c-axis is in the $[001]_c$ direction and its projection is along the $[\bar{1}\bar{1}2]_c$ direction. Using the bottom plane as a reference plane, the passage of a partial dislocation of $b = 1/6[\bar{1}2\bar{1}]$ between the bottom and top planes will shift the molybdenum atoms in the middle and top planes (the circles and stars, respectively) in the $[\bar{1}2\bar{1}]$ direction by $a/\sqrt{6}$). A similar succeeding shift of the molybdenum atoms by the passage of a second dislocation between the middle and top planes will lead to configuration represented in Figure IV-19b. Once again the Ni_4Mo c-axis projects along the direction delineated by a triangle, a circle and a star in succession; however, its sense is changed, since it now projects along the $[\bar{2}11]_c$ direction, which corresponds to the $[100]_c$ direction. Thus, the twinned region retains the ordered structure but the domains within the twins are in a perpendicular twin relation to the neighboring domains.

The Nature of the {110} Fcc Striations

The {110} fcc striations appear in the optical microstructure as tapered bands parallel to {110} fcc planes (8-10,185). The boundaries of the striations are PT boundaries and are observable due to preferential etching (185). Regions on either side of the striations contain APT-related Ni_4Mo domains (185). TEM studies of these striations were undertaken to confirm these results and to gain some ideas on the mechanism by which these striations become straight at long annealing times.

A BF micrograph of the Ni_4Mo alloy aged at 800°C for 16 hours is shown in Figure IV-20a. Two sets of tapered striations in two different orientations can be seen. One set is identified by the letters P, R, T, the second set by the letters A, C, E. The intervening spaces between each set are identified by the letters Q, S and B, D respectively. It was established by electron diffraction that the set P, R, T were parallel to the (110) fcc plane trace, the set A, C, E to the $(\bar{1}10)$ fcc plane trace. The traces of these planes are also shown in Figure IV-20a. The SAD pattern corresponding to Figure IV-20a, depicted in Figure IV-20b, shows two sets (1 and 2) of PT-related superlattice spots. The beam direction is near [116] and [129]. A DF image from spot 1 images domains in plates P, R, T and A, C, E (Figure IV-20c), whereas that from spot 2 images domains in the intervening spaces Q, S and B, D (Figure IV-20d). When the same area is viewed under two-beam conditions in BF (Figure IV-20e) and DF (Figure IV-20f) under the diffraction conditions $\underline{n}$ = [011], g = $[02\bar{2}]$, the striations appear as alternate bright and dark fringes. The edge fringes in BF are asymmetrical (one dark and one bright) and symmetrical (both dark or both bright) in DF; the background intensity differs from that within the striations. These image characteristics correspond to the δ-fringes reported for PT boundaries by Ruedl et al. (118). Thus, it is unambiguously established that domains within the plates P, R, T and A, C, E are in PT-relation to the domains in the intervening regions Q, S and B, D.

Figure IV-21a is a lower magnification BF image of the same area as Figure IV-20a. The sample has been tilted to reveal the domains

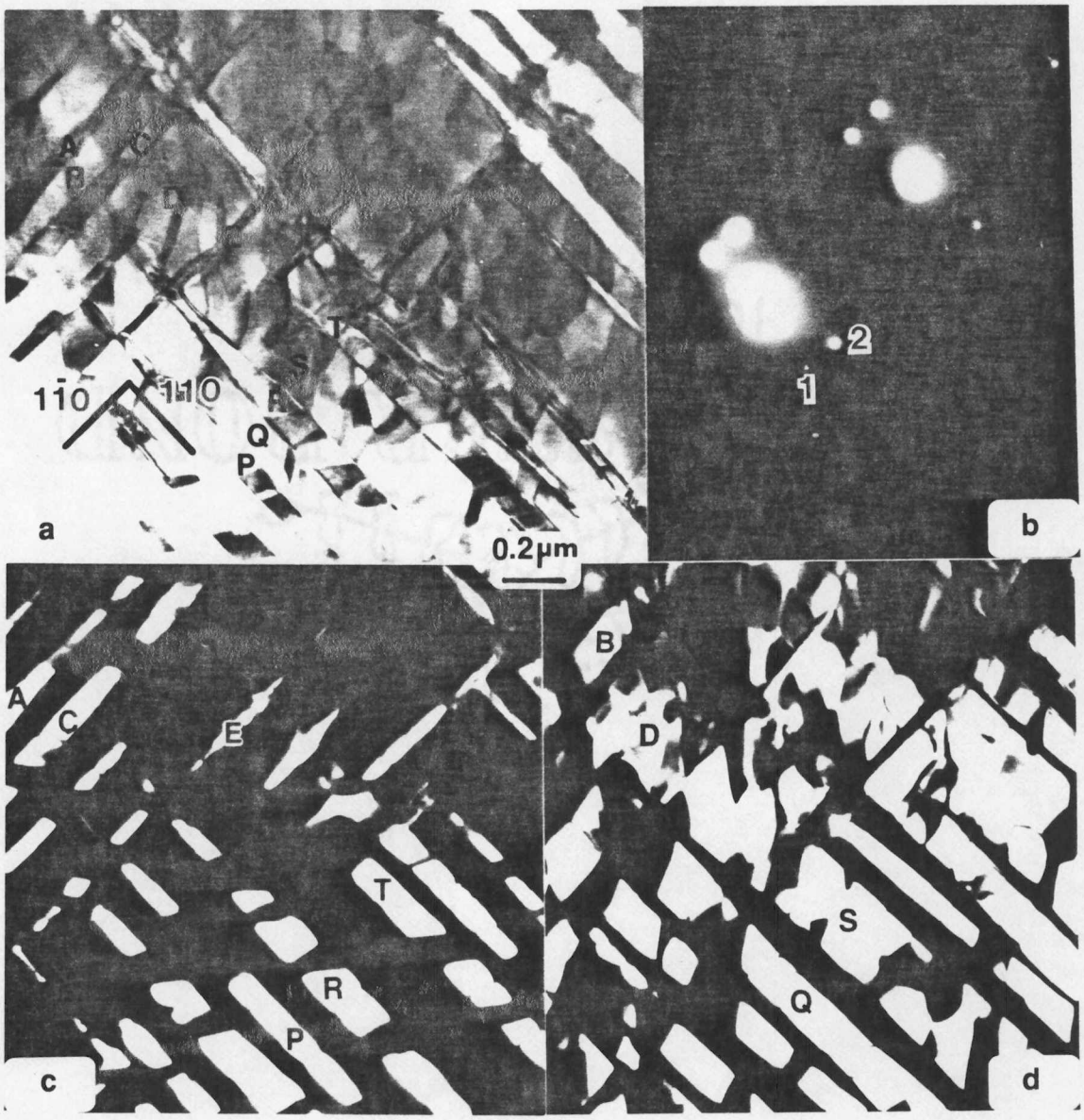


Figure IV-20. TEM micrographs of the {110} fcc striations in ordered Ni_4Mo. Aged 16 hrs at 800°C, air-cooled. a) BF image of two sets of striations P, R, T and A, B, C; spaces between striations are identified by the letters Q, S and B, D; b) SADP of a) (n near [116] and [129]); c), d) DF images from spots labelled 1 and 2 in b); e), f) Two-beam BF-DF pair taken with $\underline{n}$=[011] and g=[02$\bar{2}$].

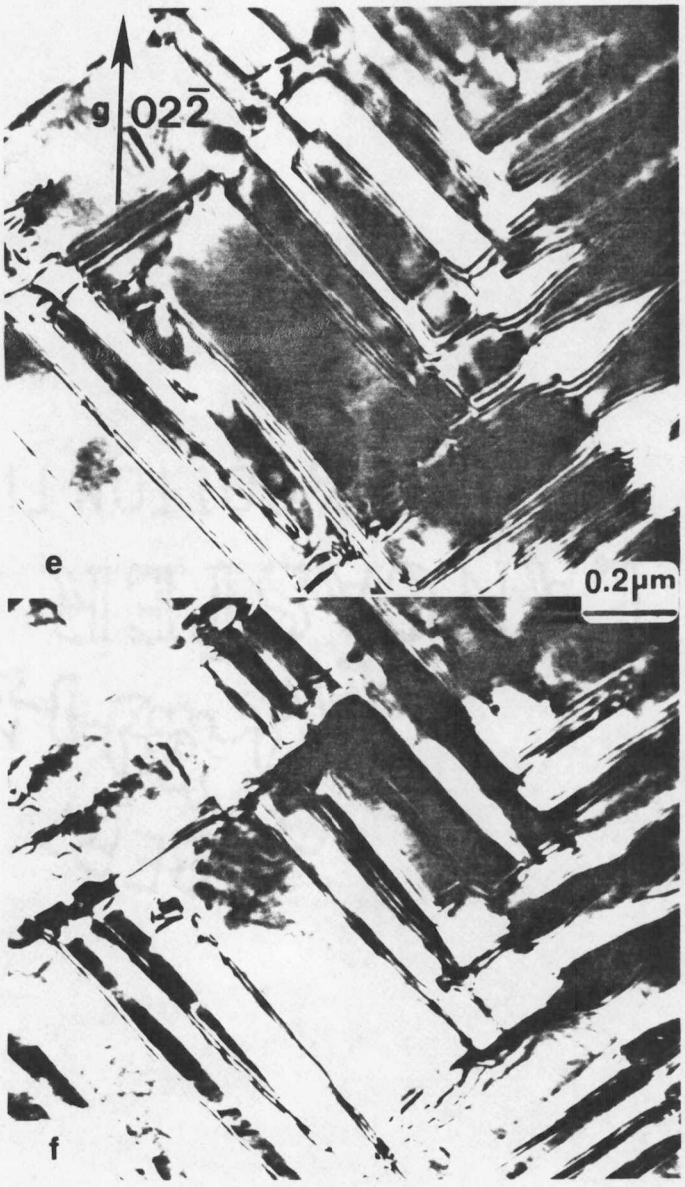


Figure IV-20. (Continued).

within regions Q, S and B, D in Figure IV-20a. The identifiers P, Q... and A, B... are all imprinted in Figure IV-21a. The SAD pattern of Figure IV-21a, depicted in Figure IV-21b (n near [012]), shows two sets (1 and 2) of APT-related superlattice spots. DF images from these spots 1 and 2 are shown in Figures IV-21c and -21d, which establish that the regions Q, S and B, D consist of groups of domains in APT relation. It was confirmed that domains within the plates P, R, T and A, C also bear the same relationship. All of the above results establish, in good agreement with the reports of Saburi et al. (185), that the {110} fcc striations appearing in the optical microstructure (8-10) are perpendicular twins, each such twin being composed of domains in antiparallel twin relation.

Examples of the {110} striations at 850°C are presented in the BF micrographs in Figures IV-22 and -23 for samples aged for 16 and 96 hours respectively. In Figure IV-22a and -22b, two sets of domains A, B and a striation C are identified. It was established by electron diffraction and DF imaging that domains in sets A and B are in APT relation to each other and both are in PT relation to domains in the band C. The domains composing the individual sets A and B are separated by APB's, those within striation C are in APT relation. Similar sets of domains bearing the same relationships are indicated in Figures IV-23a and -23b for the 96 hour aging treatment. In Figures IV-22a and -22b, it can be noticed that the striations are tapered, whereas those after longer aging times in Figures IV-23a and -23b are narrower and very straight. There is some indication in Figures IV-22a and -22b of small steps at points where the domains in sets A and B

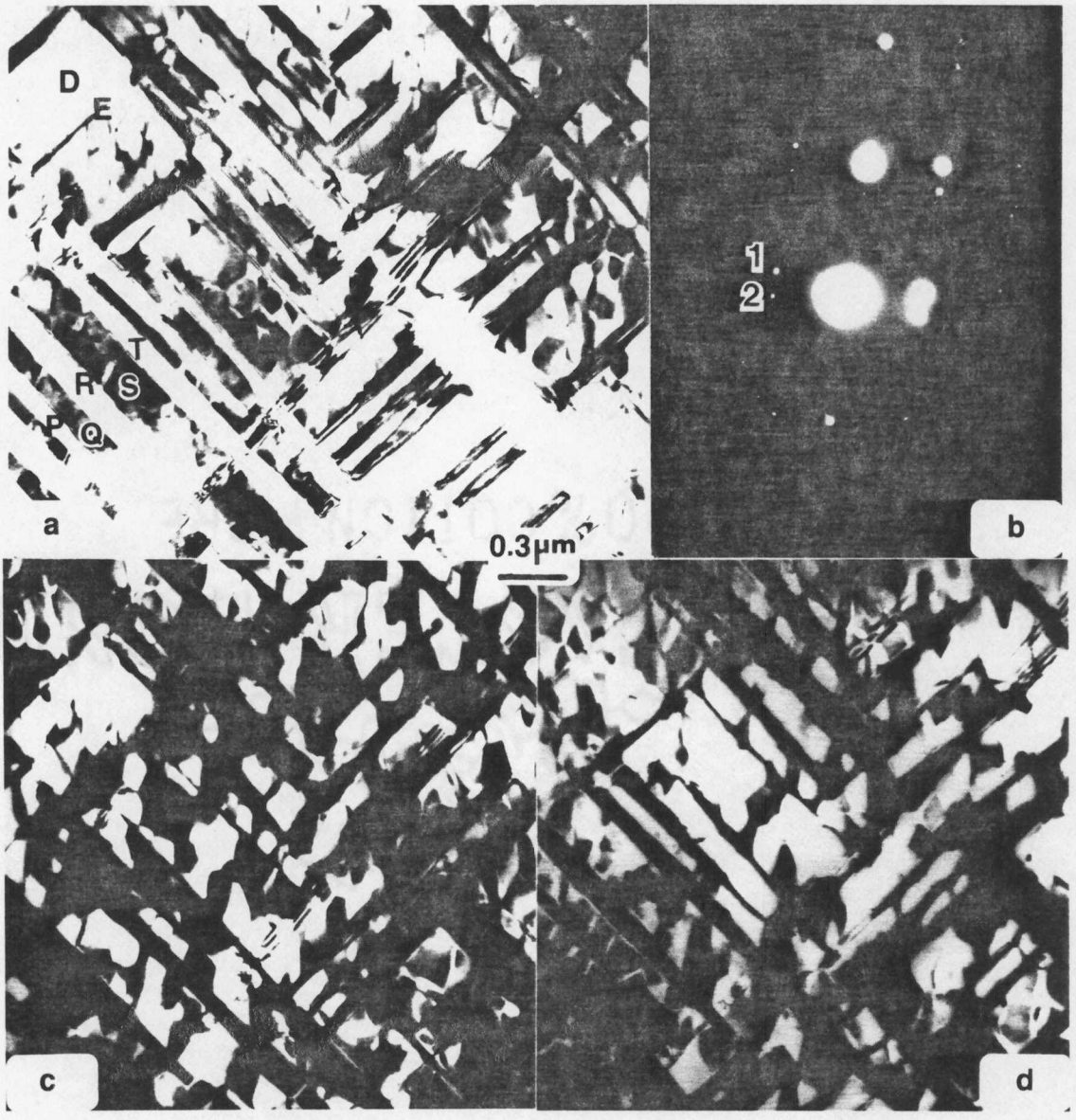


Figure IV-21. TEM micrographs of the domain structure between the {110} fcc striations in Figure IV-20. a) BF; b) SADP of a) (n near [012]); c), d) DF from spots labelled 1 and 2 in $\bar{b}$).

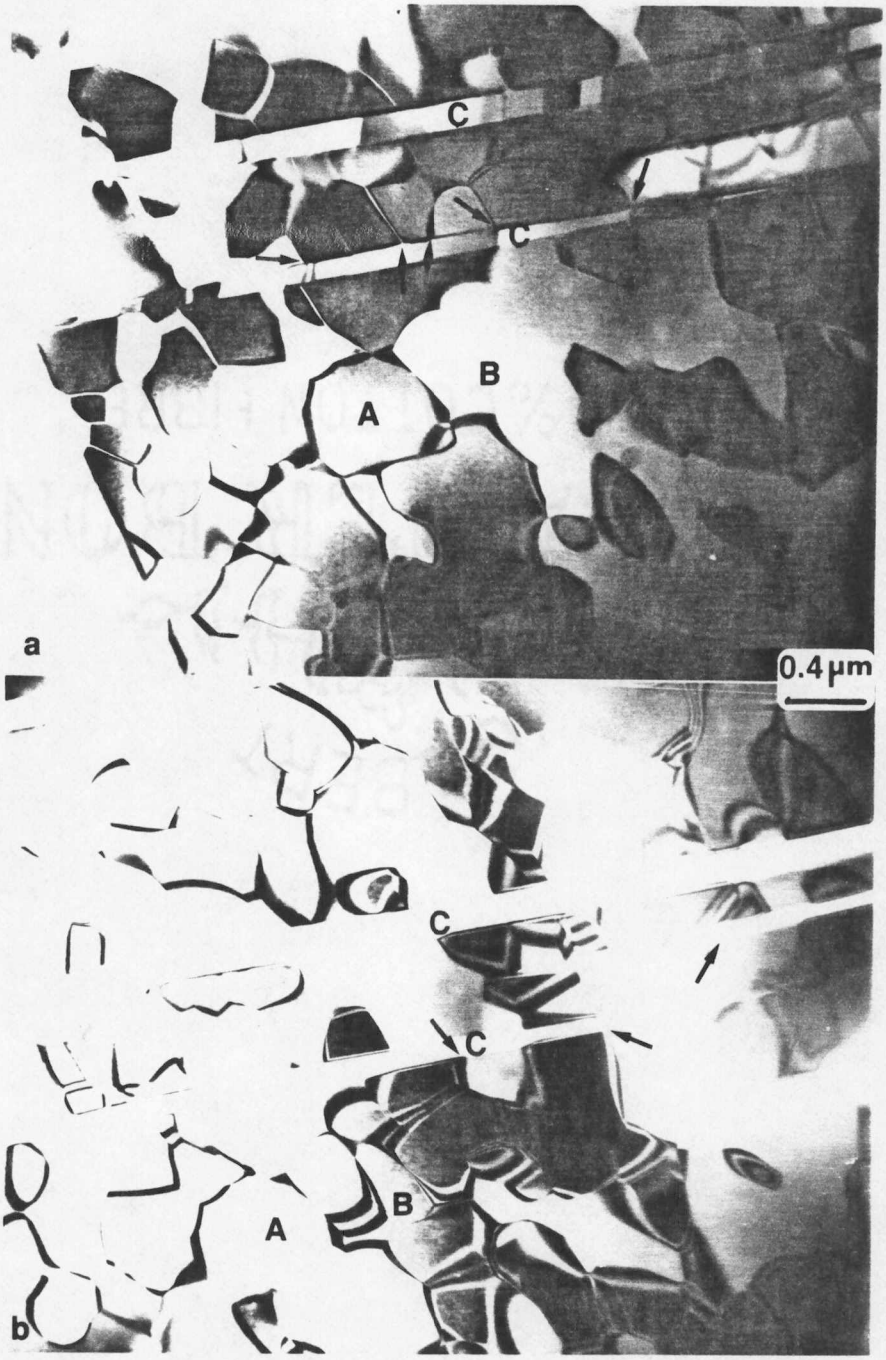


Figure IV-22. TEM micrographs showing the tapered nature of the {110} fcc striations at short times. Aged 16 hrs at 850°C. a), b) BF micrographs; domains in groups A and B are APT-related and both are PT-related to domains in striation C.

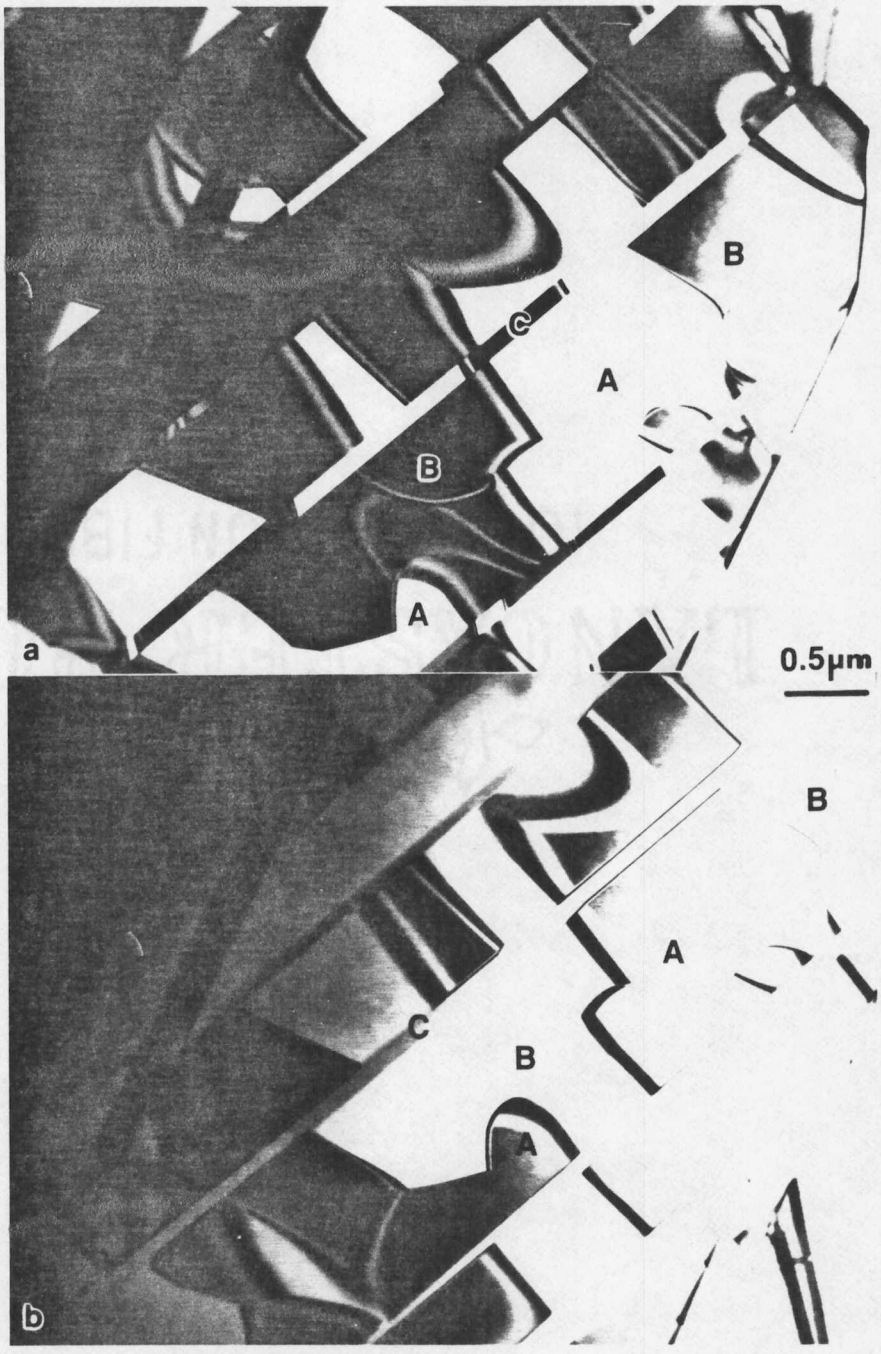


Figure IV-23. TEM micrographs showing straightening of the {110} fcc striations at longer times. Aged 96 hrs at 850°C. a), b) BF micrographs; domains in groups A and B are APT-related and both are PT-related to domains in striation C.

meet those in striation C. The locations of these apparent steps are indicated by arrows in Figures IV-22a-b.

Mechanisms involved in the straightening of the striations. The tapered nature of the striations at short aging times and subsequent straightening at longer times can be understood by considering the process by which individual domains nucleated in different parts of the crystal impinge during domain growth. At 850 and 800°C, the ordering process involves nucleation of individual domains in a SRO matrix (8,157,171). The reported shape of the domains is that of a tetragonal prism (8,157,171), being square when the c-axis is normal to the plane of the domain and rectangular with narrower ends when the c-axis lies in the plane of observation. Since the c/a ratio for Ni_4Mo is less than unity, accumulated misfit strains restrict growth at the ends in a manner similar to that proposed by Tanner (133) for Ni_2V. When growing domains with c-axis normal to each other come into contact, the PT interfaces are created; groups of these constitute the {110} striation. An idealized representation of such a striation is shown in the schematic in Figure IV-24. The locations of steps (ends of ledges) are also indicated.

Of the three possible domain interfaces in Ni_4Mo, the PT interface possesses the highest surface and elastic energy (118). A curved interface would have a higher interfacial area and therefore a higher associated interfacial energy than a straight one. Since the system would tend to progress towards a lower energy configuration, the extra energy associated with the PT interface can be reduced by



Figure IV-24. Schematic idealization of the tapered morphology of the {110} fcc striation. Dotted lines delimit individual domains.

elimination of the apparent steps giving rise to the curvature of the striation. This can be accomplished by preferential lateral growth of either the domains at the tapered parts of the striation or by growth of domains from outside into the thicker parts of the striation. The former would thicken the striation, whereas the latter would make it narrower, which is the situation observed at longer annealing times (Figures IV-23a and -23b).

The diffusion processes required to accomplish this can be understood by considering the atomic arrangement within domains across the PT interface. The atomic arrangement on the (100) plane of two domains (A and B) with c-axis in head-to-head coupling, reproduced from the work of Ruedl et al. (118), is depicted in Figure IV-25a. The large circles represent molybdenum atoms, the small ones nickel; open circles denote atoms in the top plane and the cross-hatched circles refer to the plane a/2 below the top plane. The plane along which two domains meet is the PT interface and is the $(011)_c$ plane. If the molybdenum and nickel atoms on two succesive (011) planes were to exchange positions along the [110] direction shown by the arrows in Figure IV-25a, then the PT interface would advance to the new position shown in Figure IV-25b. Repetitions of this process can eventually lead to narrowing and straightening of the striations. Although the mechanism proposed may be an oversimplification, it can account for the observed change in morphology of the {110} fcc striations.

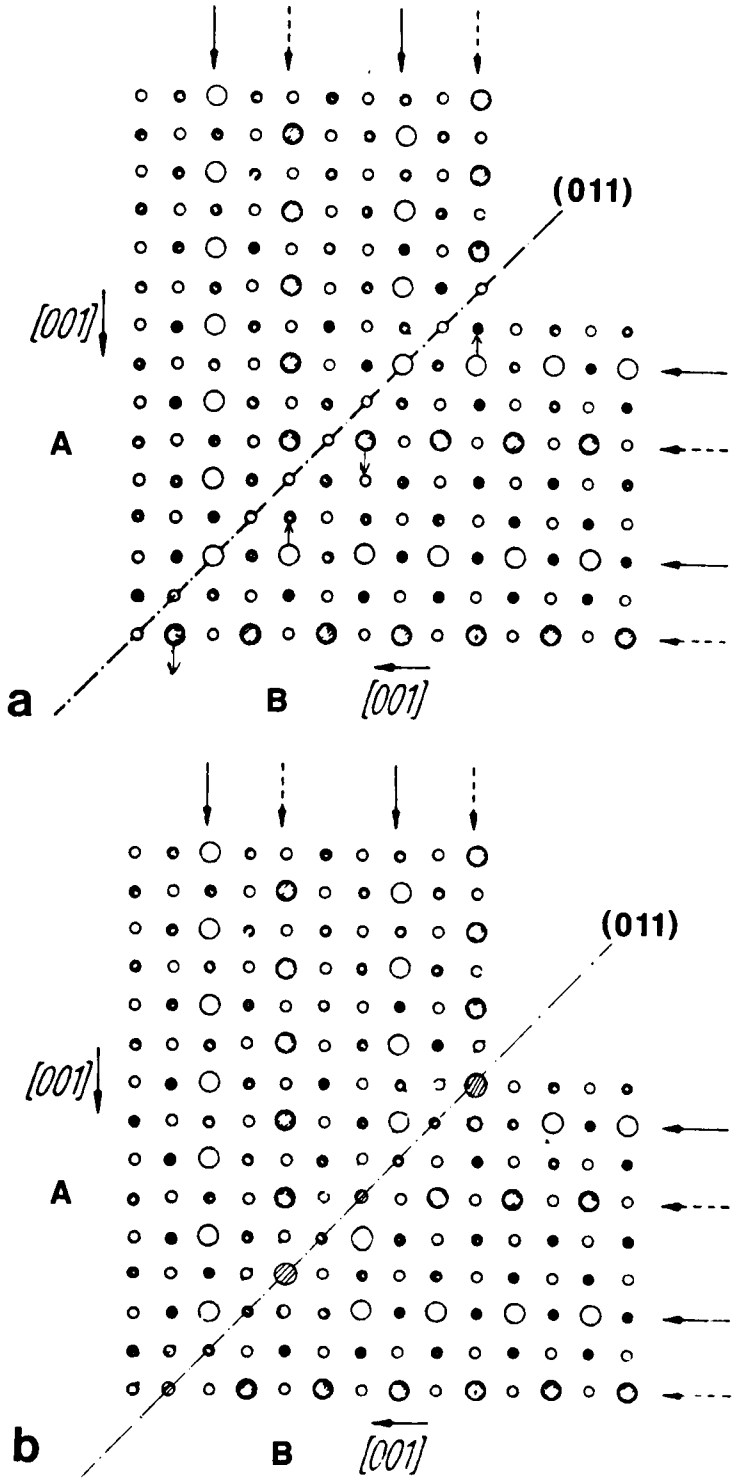


Figure IV-25. Mechanism for the narrowing and straightening of the {110} fcc striation. Atomic arrangement in the (100) plane of two PT-related domains A and B is shown. The PT interface can advance from the position in a) to that in b) by exchange of Ni and Mo atoms on two successive (011) planes in the [110] direction shown by arrow in a).

Domain Growth in Ni_4Mo

Other than the report of Ling and Starke (178), who used x-ray diffraction to determine the change in domain size as a function of time at 700°C, there have been limited systematic studies of domain growth in Ni_4Mo over a wide range of temperatures and times. In the following, the results of TEM studies on domain growth at 850, 800, 700 and 600°C for times to 4500 hours are presented. The domain size was measured in BF and DF images taken from a single Ni_4Mo spot, that is, for antiphase domains belonging to a single variant. For very fine domains, the sizes of a number of domains were measured on enlargements made from the negatives and the average calculated. Two methods were used for coarser domains. In the first, the longest and shortest dimensions of a number of domains were measured directly on the negative and the average computed. In the second, intercepts of specific length at a number of inclinations were drawn through antiphase domains and the size determined by the ratio of the line length and the number of domains intercepted. Both methods gave comparable results. It is estimated that the error in the measured domain size is about ±10%.

Aging at 850°C. Within 10 minutes, single domains of average size 37 nm form in a SRO matrix as shown in the DF image in Figure IV-26a. This size is comparable to Lei's reported value of 100 nm at 1 hour (8). The reaction is confirmed as first order (8,157,171) from the distinct set of Ni_4Mo and SRO spots in the [001] SAD in Figure IV-26b. Frequently, single domains were found to nucleate at

dislocations. Observations of the domains in several orientations confirmed the three-dimensional model proposed for single Ni_4Mo domains (8,171). Nucleation is followed by rapid growth and within 16 hours the domains are large and in contact (Figure IV-26c). With further aging, the domains enlarge progressively (Figures IV-26d-f), becoming about 4200 nm at 2000 hours (Figure IV-26g). The growth process also frequently results in isolated APB's attached to dislocations or other debris.

It can be noted in Figures IV-26c-e that frequently isolated domains in one orientation are imbedded among a group of domains in another orientation (see arrows). In fact, these domains are in APT relation to the neighboring ones, as judged from the difference in contrast and by SAD patterns. It can also be seen that these isolated domains are much smaller than others belonging to the same group. Thus, it is apparent that small APT domains present within a group of antiphase domains will be consumed. In other words, the APTB is removed in preference.

Aging at 800°C. The transformation progresses faster at 800°C than that at 850°C. Within 10 minutes, distinct, spherical Ni_4Mo spots are present in the [112] SAD in Figure IV-27a; no SRO is present, indicating that the disordered phase has completely transformed to LRO, and moreover, the transformation is first order. Sharp double diffraction spots are also seen, which indicates the presence of numerous interfaces. The average domain size is 20 nm at this time which compares to 15 nm at 5 minutes reported by Saburi et al. (150)

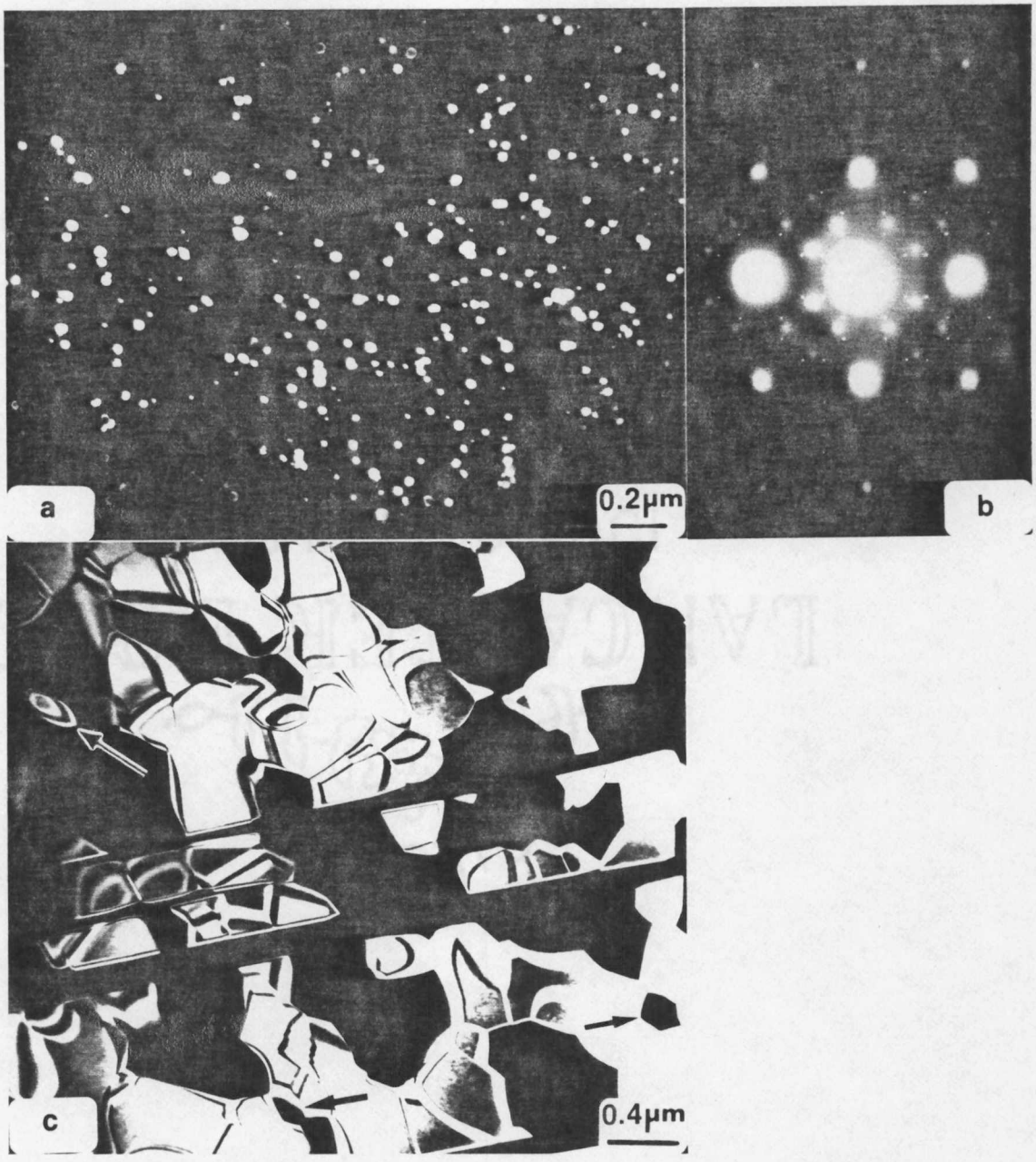


Figure IV-26. Domain growth in Ni_4Mo aged at 850°C. a) 0.16 hrs--DF micrograph from Ni_4Mo spot in [001] SADP in b); c) 16 hrs--DF micrograph; BF micrographs--d) 96 hrs; e) 384 hrs; f) 840 hrs and g) 2000 hrs.

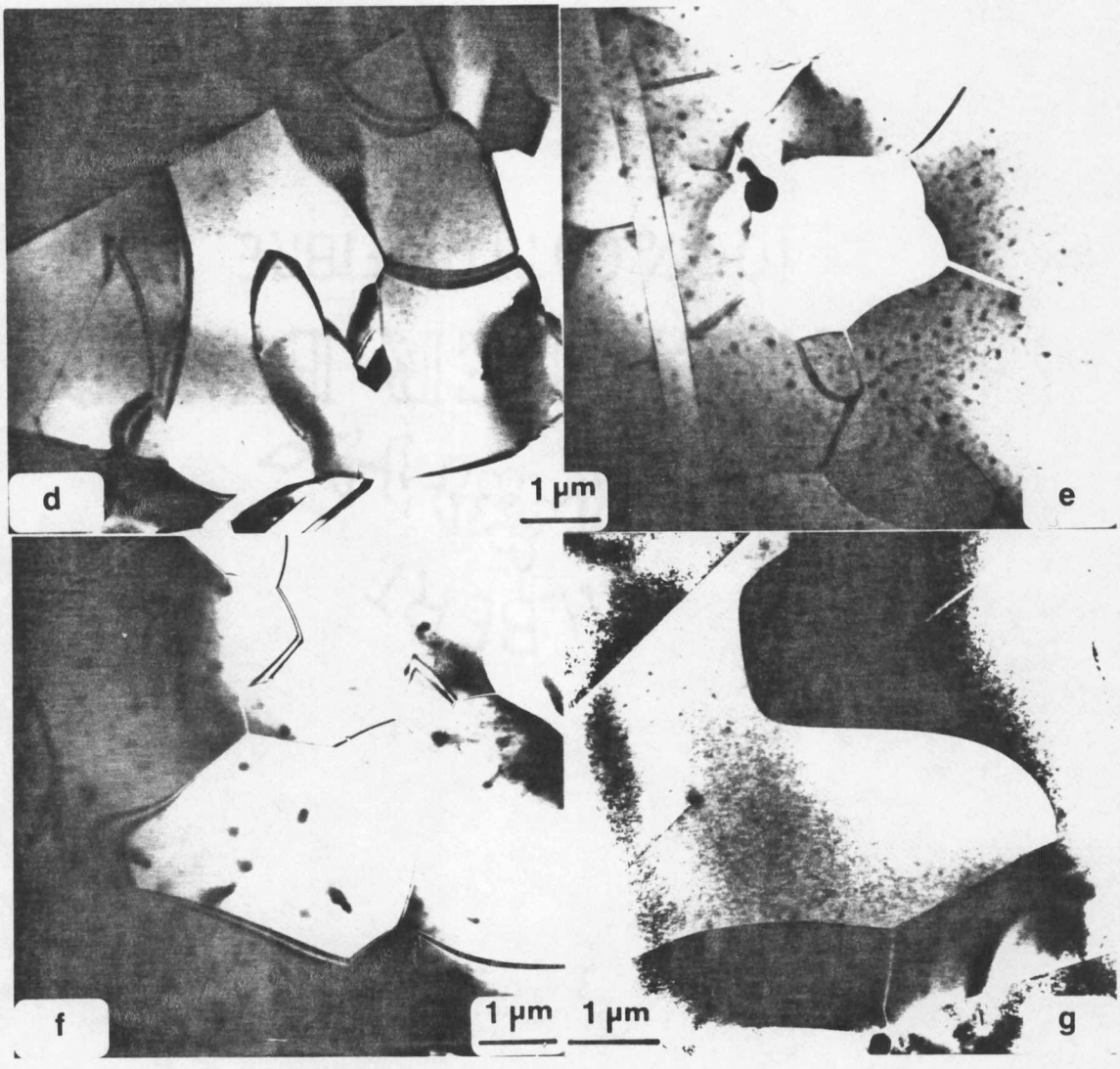


Figure IV-26. (Continued).

at the same temperature. The domain size is much smaller than that at 850°C (37 nm) and this is true throughout the annealing period of 4500 hours. With further aging in the time range 1 (Figure IV-27c) to 10 hours (Figure IV-27d) domains grow further and the microstructure at this time resembles the soap froth or foam structure (Figure IV-27d) reported by Ruedl et al. (118). DF micrographs representing the growth of domains during the remainder of the time period of 96 to 4500 hours are shown in Figures IV-27e-h. Observations similar to those at 850°C can be made. The domain size at 4500 hours is about 3100 nm.

Aging at 700°C. The transformation is slower at this temperature in comparison to that at the higher temperatures. At 1 hour, the [001] SAD in Figure IV-28a shows superlattice Ni_4Mo spots together with bridges of weak diffuse intensity connecting these spots to weak intensity at the {1 1/2 0} SRO positions. This is taken as evidence for a continuous ordering mechanism (155-160,174) in difference to the nucleation and growth process at the higher temperatures. The domain size is 3.8 nm (Figure IV-28b), which is much smaller than that at 800 and 850°. At 10 hours, as shown in Figure IV-28c, the remaining SRO has completely transformed to LRO; the superlattice spots are sharp and well rounded and there appears to be weak lines of intensity along <100> directions connecting the two variants of superlattice spots. In the [112] section, similar lines of intensity were observed, but along the <111> direction. The domain size continues to increase in the time range 10 to 96 hours (Figures IV-28d-f), albeit at a much slower rate relative to that at the higher

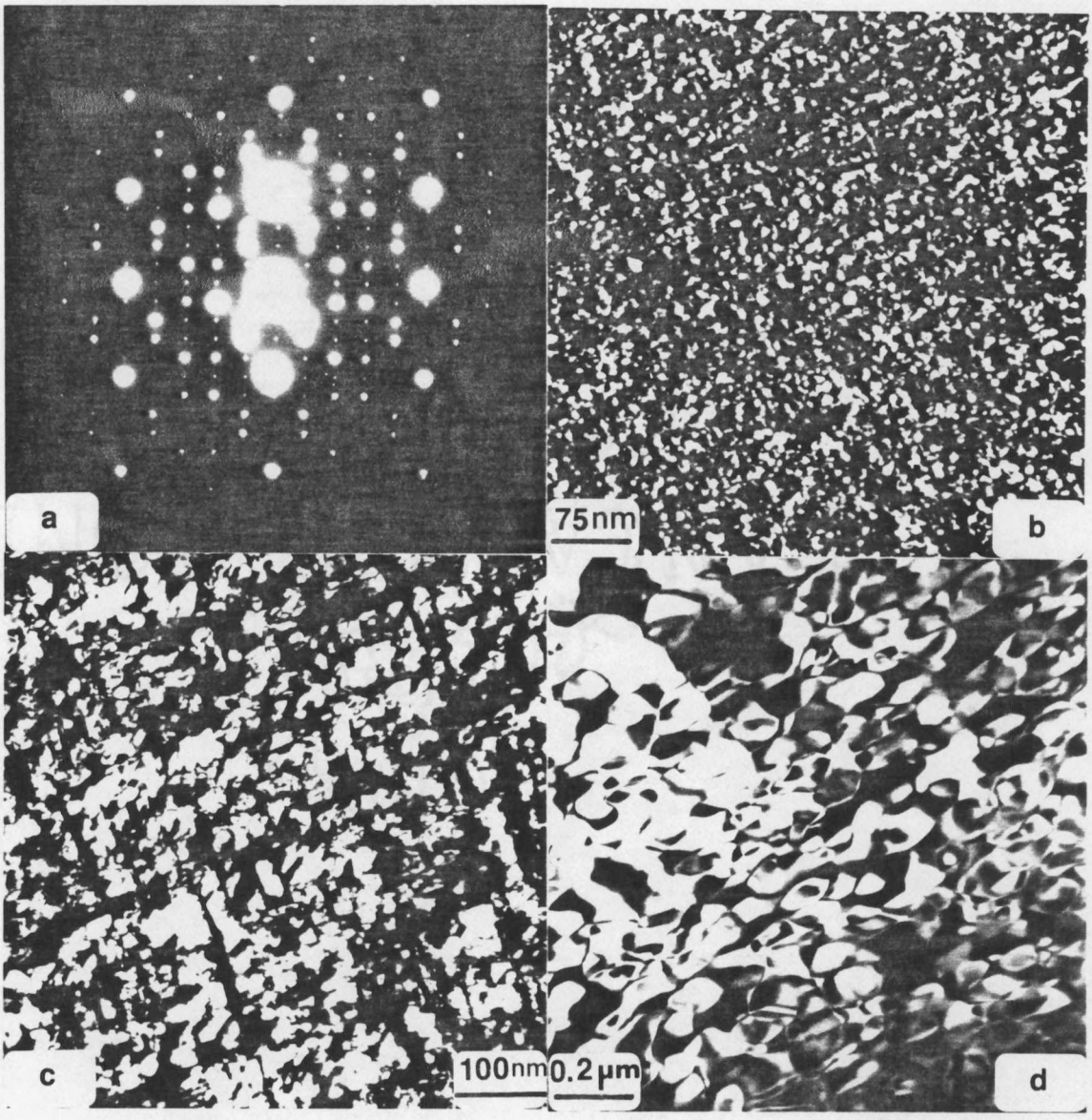


Figure IV-27. Domain growth in Ni_4Mo aged at 800°C. a) 0.16 hrs--[112] SADP; b) DF micrograph from Ni_4Mo spot in a); DF micrographs--c) 1 hr; d) 10 hrs; e) 96 hrs; f) 384 hrs; g) 2000 hrs and h) 4500 hrs.

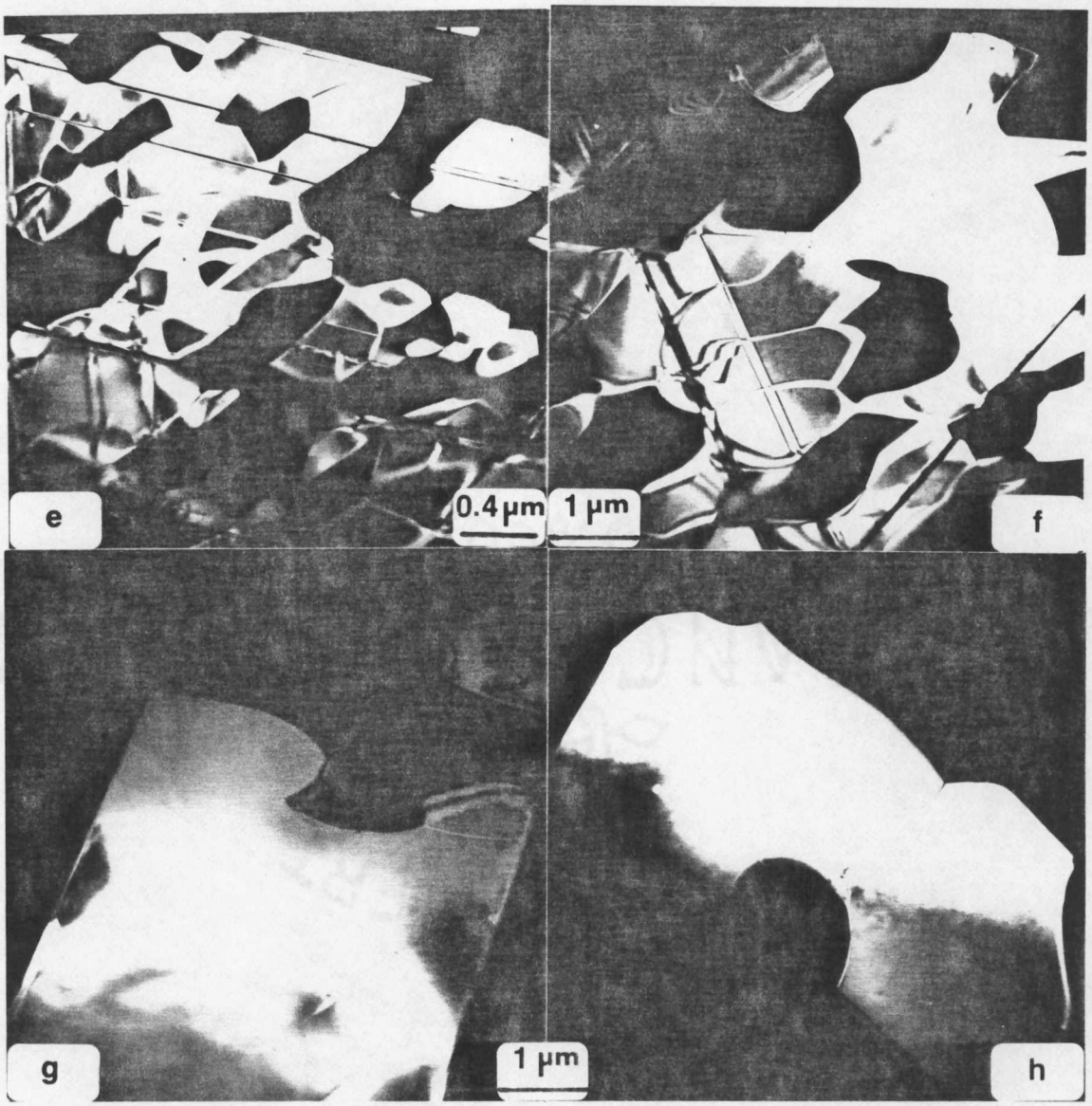


Figure IV-27. (Continued).

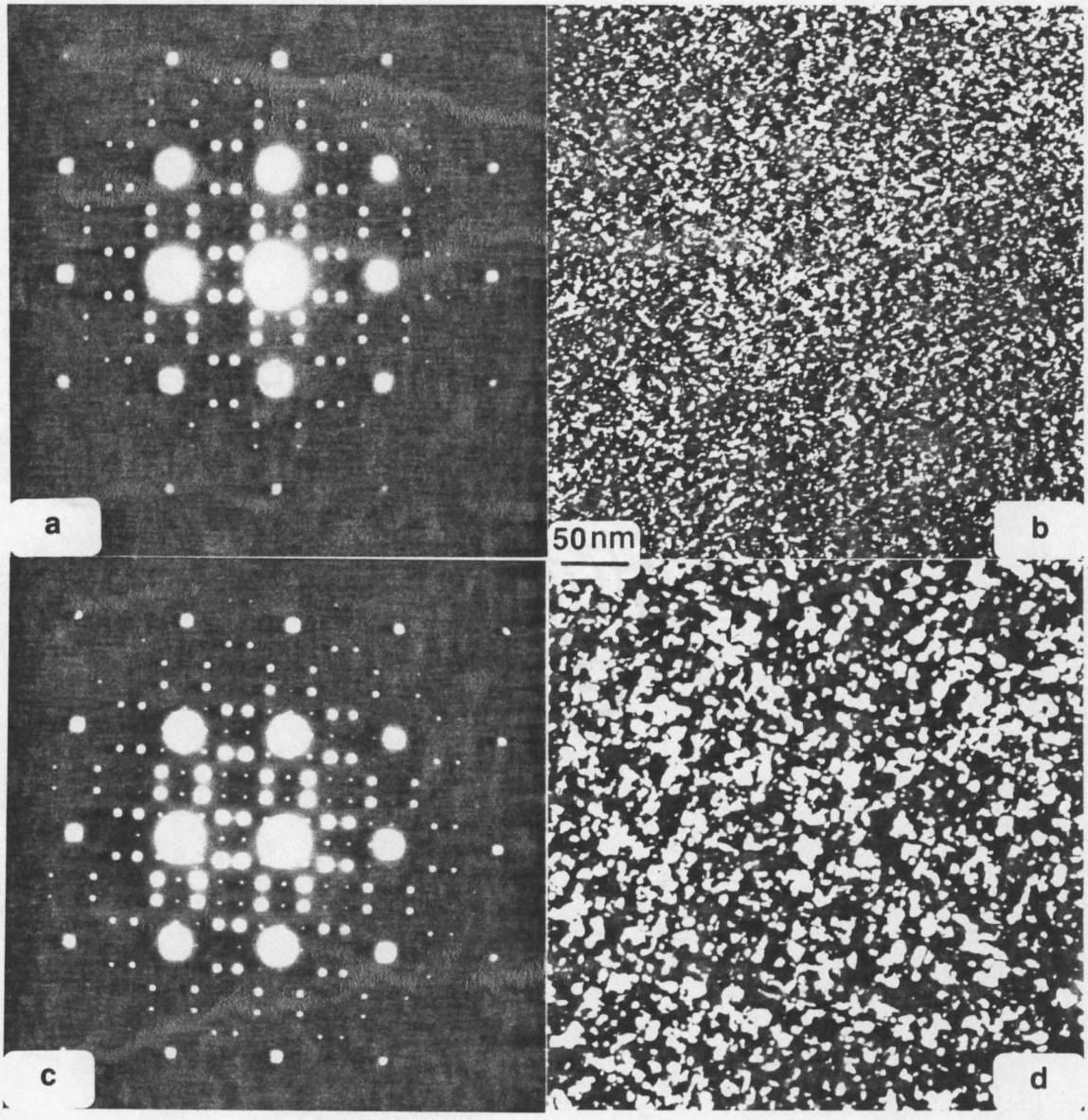


Figure IV-28. Domain growth in Ni_4Mo aged at 700°C. a) 1 hr--[001] SADP; b) DF micrograph from Ni_4Mo spot in a); c) 10 hrs--[001] SADP; d) DF image from Ni_4Mo spot in c); DF micrographs--e) 16 hrs and f) 96 hrs--DF.

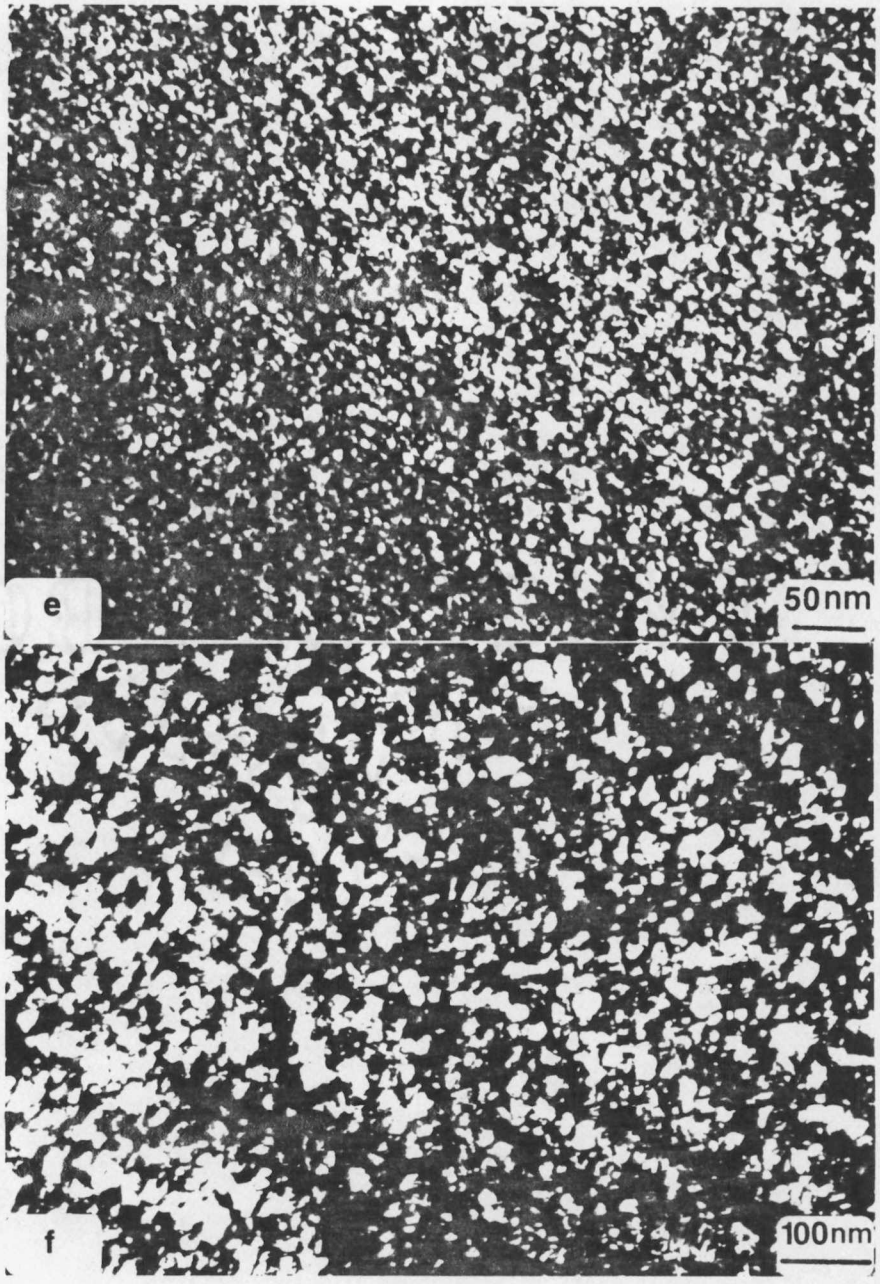


Figure IV-28. (Continued).

temperatures. Concurrently, a domain coarsening reaction initiated at the grain boundaries and progressed rapidly and virtually consumed large portions of the microstructure. As a result, for times beyond 96 hours it became difficult to distinguish between the domains growing within grains and those formed by the coarsening reaction. This feature has also been reported by Chakravarti et al. (13) at 700°C. The evolution of this grain boundary reaction is presented later. Domain size measurements for the longer times are therefore not reported.

Aging at 600°C. The transformation proceeds exceedingly slowly at this temperature. At 16 hours, the [112] SAD in Figure IV-29a shows superlattice spots broadened in the <420> directions along with bridges of diffuse intensity connecting these spots to weak SRO spots. Note the absence of double diffraction spots. These features are in general agreement with other reports (92,126). Like the behavior at 700°C, the reaction occurs by the continuous ordering mechanism (155-160,174). At 96 hours, no SRO is present (Figure IV-29b). Figures IV-29c-g are DF images illustrating the growth of domains in the time period 96 to 2000 hours. The domains grow very slowly in this time range from 2.5 nm to 8 nm. Also, it can be seen in the [112] SAD in Figure IV-29f corresponding to the 840 hour aging (Figure IV-29e) that the superlattice spots are still slightly broadened in the <420> directions. This cannot be a shape effect and implies that the LRO is not yet perfect, that is, S<1 (92). Also, weak lines similar to those at 700°C can be seen between the LRO spots along the <111> direction.

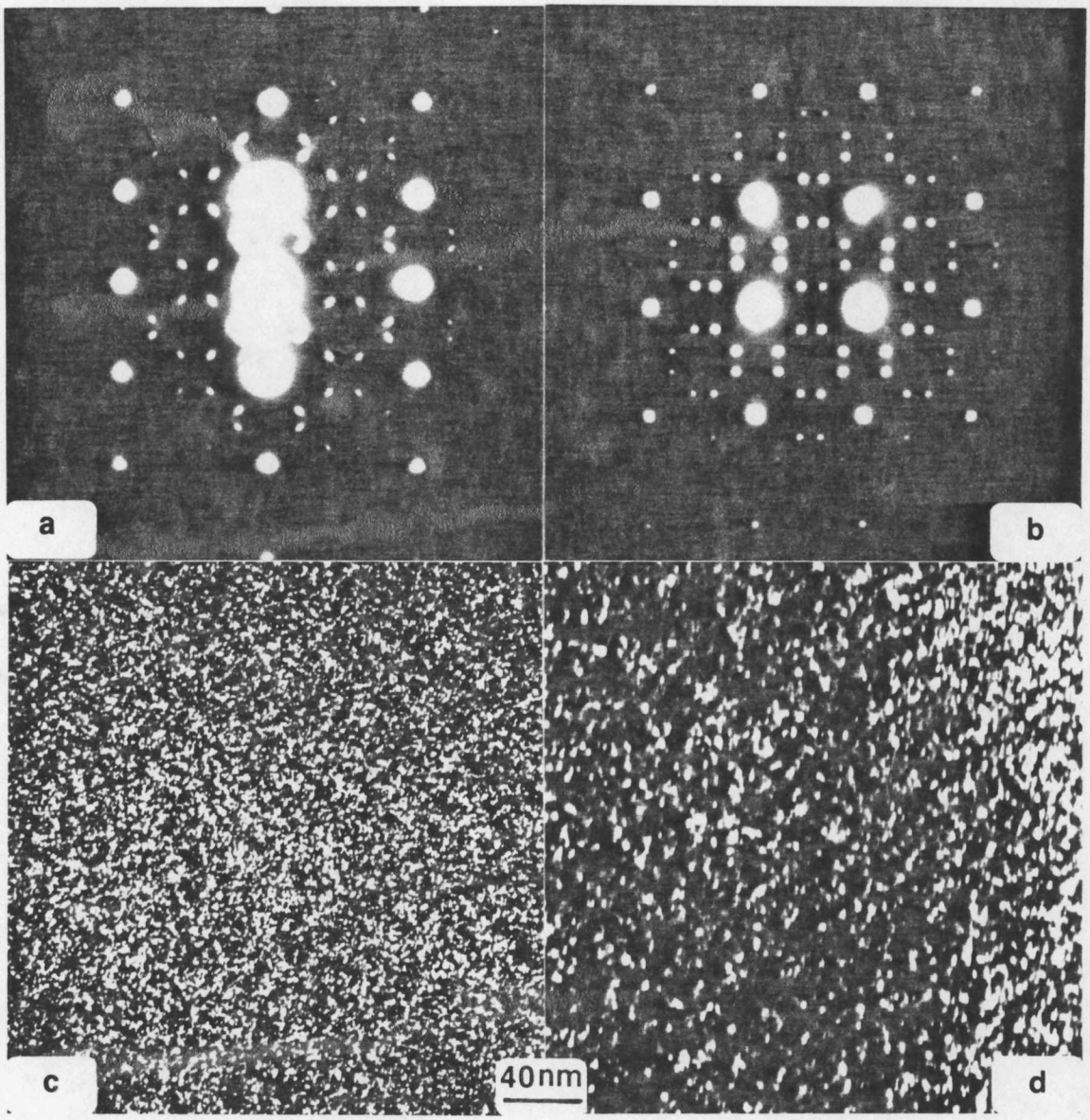


Figure IV-29. Domain growth in Ni_4Mo aged at 600°C. a) 16 hrs--[112] SADP; b) 96 hrs--[001] SADP; c) DF micrograph from Ni_4Mo spot in b); d) 384 hrs--DF micrograph; e) 840 hrs--DF micrograph; f) [112] SADP of e); g) 2000 hrs--DF micrograph.

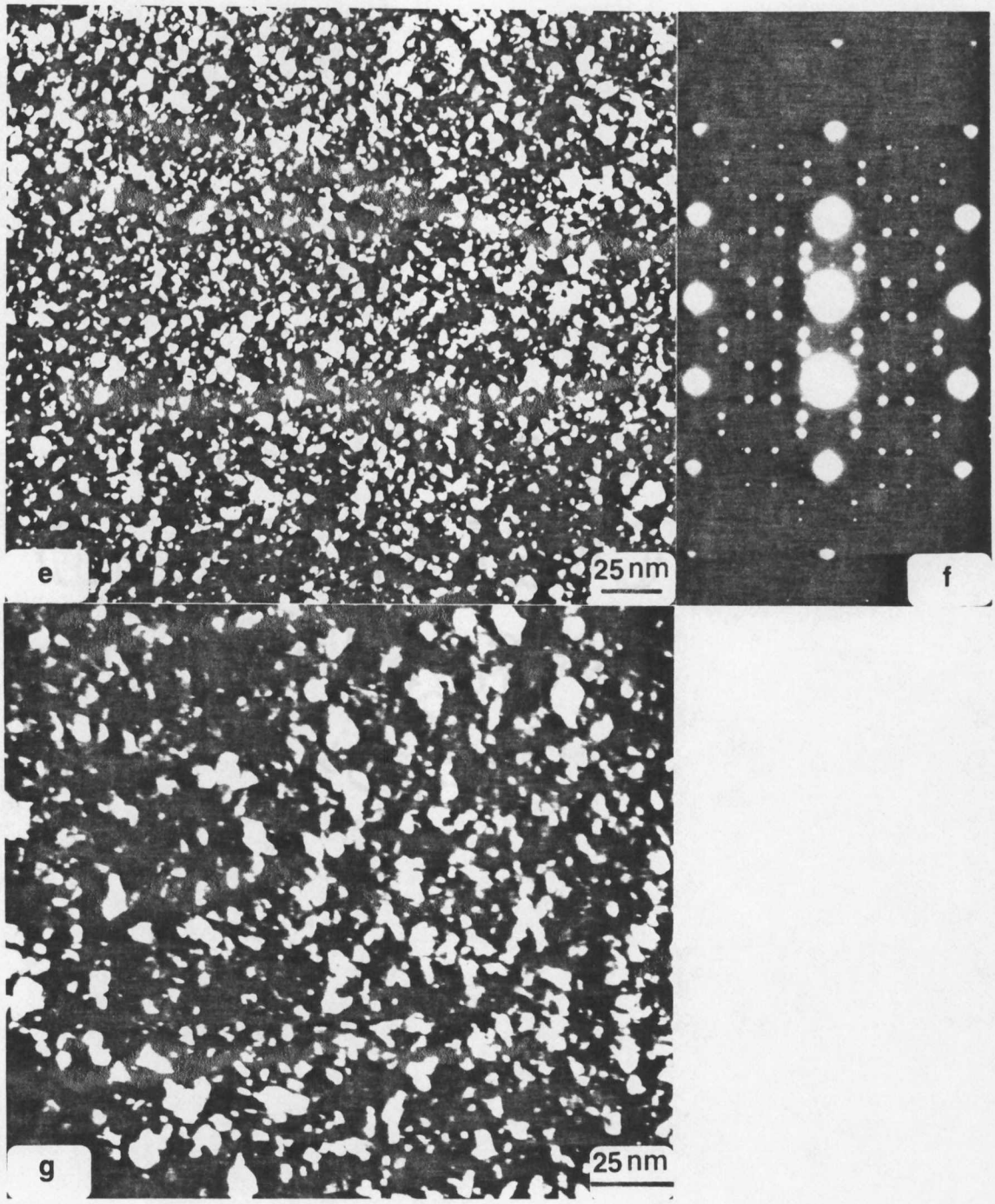


Figure IV-29. (Continued).

Domain coarsening at grain boundaries also occurred, but at a slower rate than that at 700°C and consumed vast portions of the microstructure. At 4500 hours, it appeared to have progressed throughout the microstructure. The development of this reaction is presented later.

Summary of domain size measurements. The results of domain size measurements as a function of temperature and time are summarized in Table IV-1 and plotted in Figure IV-30. The data of Ling and Starke (178) at 700°C and that of Kao (242) at 775 and 725°C are also included. A log-log plot of the temperature dependence of the domain size (nm) against aging time (hours) is shown in Figure IV-30. The straight lines drawn through the data points at different temperatures were obtained by a least squares fit to the data. It is clear that domain growth in Ni_4Mo is analogous to conventional grain growth and follows the relationship $D^n = kt$, where k is a constant related to the activation energy for the growth process. The value of the exponent n (1/slope) varies with temperature and is 2 at 850 and 800°C, 2.3 at 775, 2.4 at 725°C, 2.9 at 700°C and 3.0 at 600°C. It is encouraging to note that the results at 700°C are in excellent agreement with those of Ling and Starke (178), who also reported a value of 2.9 for n.

Conventional grain growth can be expressed as:

$$D^n = k_o \exp(-Q/RT)\, t \qquad \text{(IV-5)}$$

where, D is the average grain diameter, k_o is a constant, Q is the activation energy, R is the gas constant, T is the temperature (°K) and t is the annealing time (245). Rearranging terms in the equation

TABLE IV-1

Domain size as a Function of Aging Temperature and Time in Ni_4Mo

Aging Time (hours)	Domain Size (nm)						
	850°C	800°C	775°C[a]	725°C[a]	700°C[b]	700°C	600°C
0.05	---	---	---	3	---	---	---
0.167	37	20	15	---	---	---	---
0.5	---	---	---	6.2	---	---	---
1	100	45	---	---	4.5	3.8	---
1.67	---	---	37.4	9.7	---	---	---
10	---	157	---	---	10	8.9	---
16	470	160	---	---	12	9.2	---
16.67	---	---	---	24.3	---	---	---
96	960	470	---	---	22	17.1	2.54
167	---	---	264	74.7	---	---	---
384	1819	1072	---	---	---	---	4.5
600	---	---	---	125	---	---	---
840	2325	1600	531	---	---	---	6
1667	---	---	700	208	---	---	---
2000	4164	2350	---	---	---	---	8
4500	---	3075	---	---	---	---	---

[a]After H. P. Kao, ref. 242.
[b]After F. W. Ling and E. A. Starke, ref. 178.

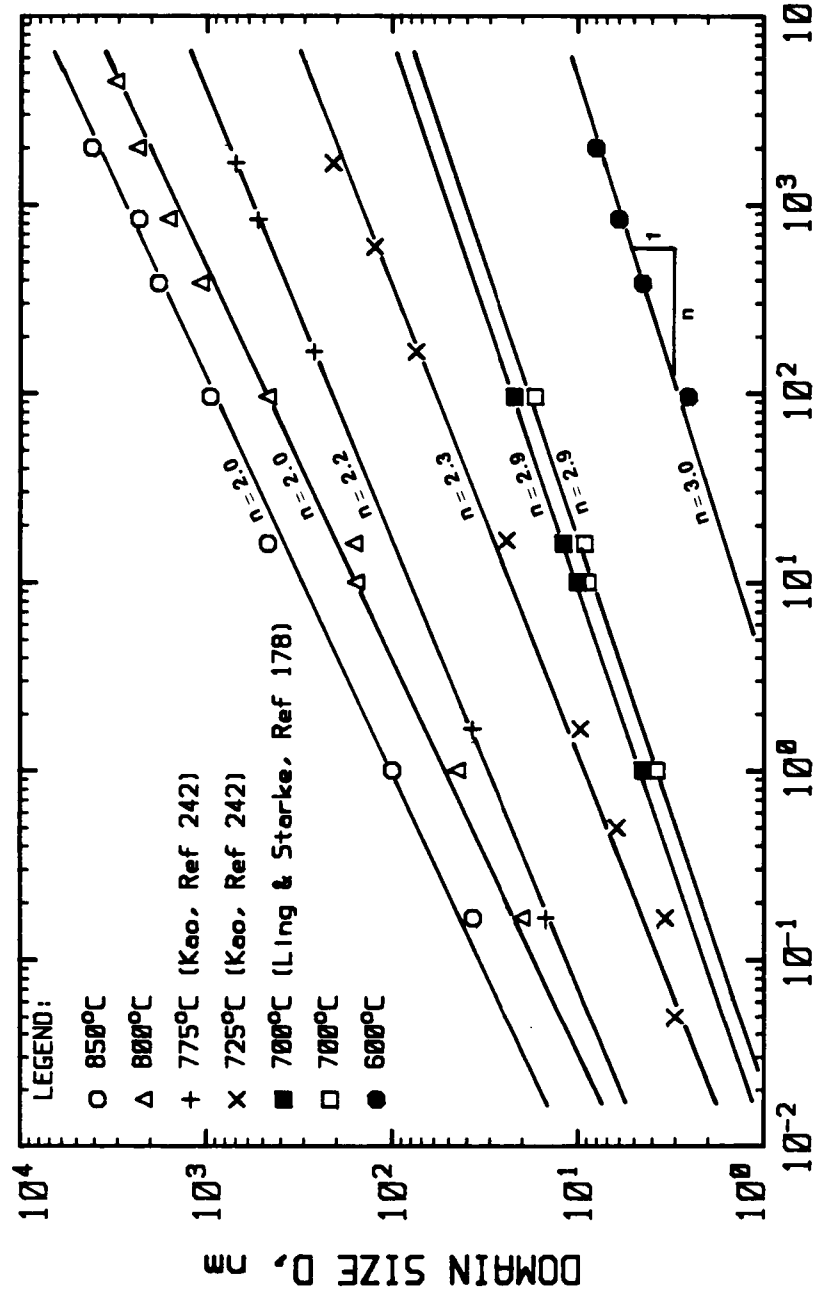


Figure IV-30. Log-log plot of domain size, D, against aging time, t, for Ni_4Mo aged at the indicated temperatures.

and taking logs we obtain

$$\log(D^n/t) = \log k_o - Q/2.3RT \qquad \text{(IV-6)}$$

A plot of $\log(D^n/t)$ against 1/T should yield a straight line of slope -Q/2.3R. Such a plot based on data (Table IV-2) derived from Figure IV-30 is shown in Figure IV-31. The value of n chosen for the different temperatures is as quoted above. D^n/t is based on the time required to attain a particular domain size. The straight line drawn through the data points was obtained by a least squares fit. The activation energy Q for domain growth was determined from the slope as 80 kcal/mole.

Mechanism of domain growth. In most studies of metallurgical grain growth, 1/n is less than 1/2, usually 1/5 to 1/3, and approaches 1/2 only at higher temperatures. This has been explained in terms of several factors which can affect grain growth, such as the presence of impurities, free surface effects and the relative orientation of grains (245). At 800 and 850°C, antiphase domain growth in Ni_4Mo follows classical grain growth behavior as evidenced by the value of 1/n = 1/2. This behavior has also been reported in Cu_3Au by Poquette and Mikkola (246). As the temperature is lowered, the value of 1/n appears to change gradually to 1/3 at 600°C. This implies that the activation energy for domain growth should also correspondingly change to higher values. However, the data plotted in the manner shown in Figure IV-31 yields a single value for Q over the temperature range considered. A rational justification for this is provided in the following.

TABLE IV-2

Time* Required to Attain a Certain Domain Size as a Function of Temperature

	$1/T \times 10^4$ ($^oK^{-1}$)					
Domain Size (nm)	8.9 (850°C)	9.32 (800°C)	9.54 (775°C)	10.02 (725°C)	10.28 (700°C)	11.45 (600°C)
5	3.98	3.40	3.41	2.11	1.68	-0.68
10	4.00	3.40	3.35	2.10	1.70	-0.57
50	3.95	3.40	3.24	2.06	1.73	-0.40
100	3.92	3.40	3.18	2.05	1.70	-0.35
300	3.93	3.43	3.10	2.02	1.71	-0.24
500	3.90	3.42	3.06	2.00	1.70	-0.20
1000	3.90	3.40	3.00	1.95	1.70	-0.13

*Quantity tabulated is $\log(D^n/t)$

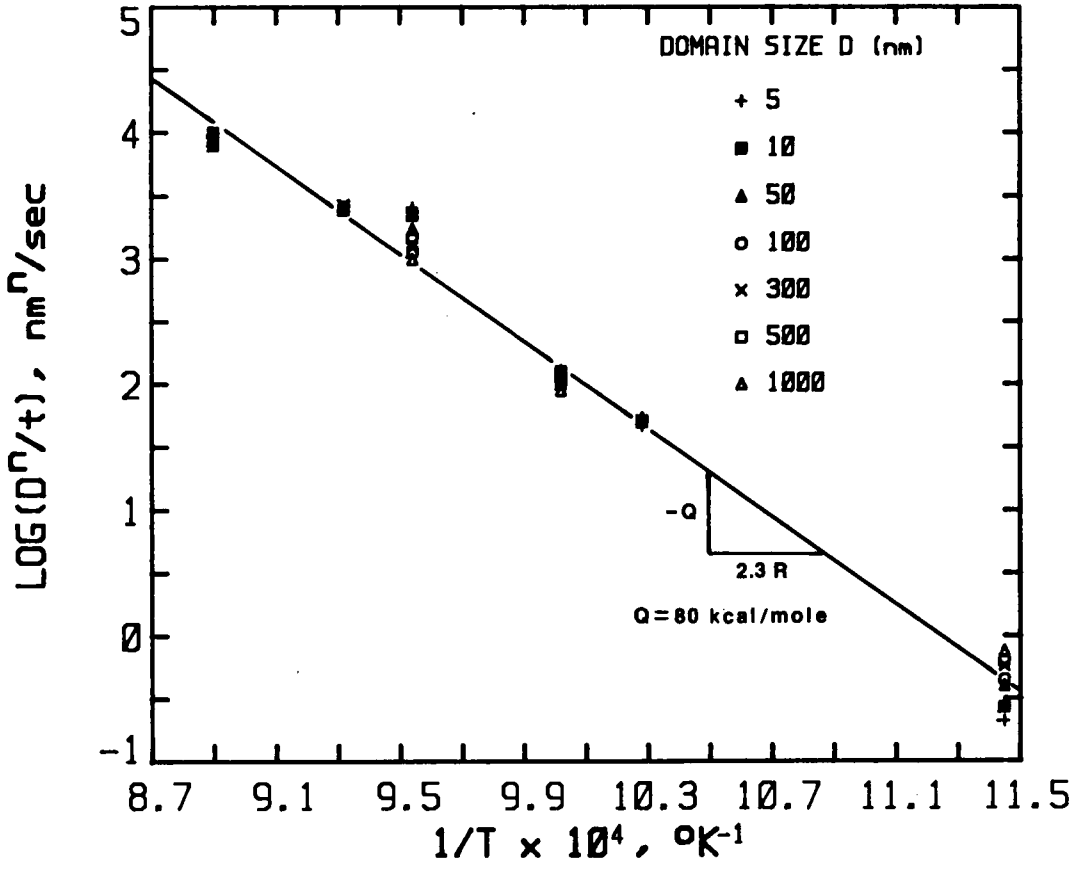


Figure IV-31. Plot of $\log(D^n/t)$ against 1/T. The plot shows the the relationship between time required to attain a particular domain size and aging temperature. The slope of the plot gives the activation energy for domain growth as 80 kcal/mole.

The change in the value of n cannot obviously arise due to impurity drag effects. This is because the domains are distributed on a fine scale and the thickness of the domain boundaries (at most few atomic layers) is such that impurities are not expected to segregate to them preferentially. Free surface effects can also be overruled, since we are dealing with domain growth far beneath the surface. The third factor, namely, the relative orientation of domains appears to be mainly responsible for the change in n and therefore the change in domain growth behavior. In Ni_4Mo, there are six possible orientations for the domains (6,7). This gives rise to a variety of domain interfaces: APB's, APTB's and PTB's in increasing order of surface energy (118). The mechanism of ordering changes with temperature from a nucleation and growth process above about 735^{o}C to continuous ordering below this temperature (8,157,171,174). In the nucleation and growth regime (close to T_c), single but fewer domains of Ni_4Mo nucleate initially in the SRO matrix and then rapidly grow. In the continuous ordering regime (far below T_c), many more domains are nucleated by continuous transfer of diffracted intensity from SRO to LRO, that is, by increasing accumulation of molybdenum atoms on {420} fcc planes. Thus, a single domain would be surrounded by many more domains in the other possible 5 orientations. This would, in turn, hinder the coordinated atom jump processes required to enable domains belonging to the same variant to grow.

The driving force for antiphase domain growth is the reduction in surface energy by reduction in total surface area of the boundaries. It occurs when atoms in antiphase domains jump the

required distance (the displacement vector of the APB's) and so become in phase with other atoms in the growing domain. Explanations for change in n with temperature in terms of changes in Q would require the mechanism of domain growth to change with temperature. This is clearly unrealistic, since the displacement vectors of the APB's, that is, the types of APB's are not expected to change with temperature. Hence, the activation energy for the jump processes required for antiphase domain growth should remain the same, whereas the growth rate (reflected by change in n) decreases at the lower temperatures due to constraints imposed on growing domains by neighboring domains in other orientations.

The activation energy for antiphase domain growth found in the present study is 80 kcal/mole. That for self diffusion of nickel has been reported as 67 kcal/mole (247), self diffusion of molybdenum as 96-100 kcal/mole (248) and for diffusion of molybdenum in nickel as 69 kcal/mole (249). The last data applies to disordered alloys; there is no available data for diffusion in the ordered alloy, but Q is expected to be higher (82). Truly speaking, it is the activation energy for interdiffusion that is of importance in ordered alloys (250). Despite the experimental errors involved in the measurement, it is evident that the present results are in good agreement with available data and follow the expected trend. It can be concluded that antiphase domain growth in Ni_4Mo is a diffusion-controlled process.

The results have also shown that APT's when present among a group of APB's are preferentially eliminated. The driving force for this process is associated with the reduction in the higher surface

energy of APTB's relative to the APB's. The physical processes involved can be understood on the basis of the atomic arrangement in two APT-related domains (A and B) portrayed in Figure IV-32. It is clear that a displacement of one domain relative to the other can give rise to a combination of a APTB and an APB (118). If the molybdenum atoms were to contrive to exchange positions with the nickel atoms along the $\langle 110 \rangle_c$ directions indicated by arrows in Figure IV-32, then the new positions of the atoms in domain B would be in phase with those in domain A and a portion of the APTB would have been removed. Repetitions of this process could eventually lead to elimination of the APTB's.

Domain Coarsening at Grain Boundaries in Ni_4Mo

As pointed out earlier, a domain coarsening reaction accompanied by extensive grain boundary migration occurs at the grain boundaries on annealing at 700 and 600°C. This reaction occurs to a very limited extent at 800°C and is absent at 850°C. The development of this structure has received little attention. It was therefore deemed worthwhile to study the continuous evolution of the reaction with time at 700 and 600°C. The results are presented in the series of micrographs in Figures IV-33 to -36.

The reaction develops initially at the original α grain boundaries in 1 hour at 700°C (Figures IV-33a-b), a stage at which ordering within the grains has not yet attained perfection (Figure IV-28a). In the BF micrographs in Figures IV-33a and -34a, in some regions the boundaries advance in opposite directions. The advancing

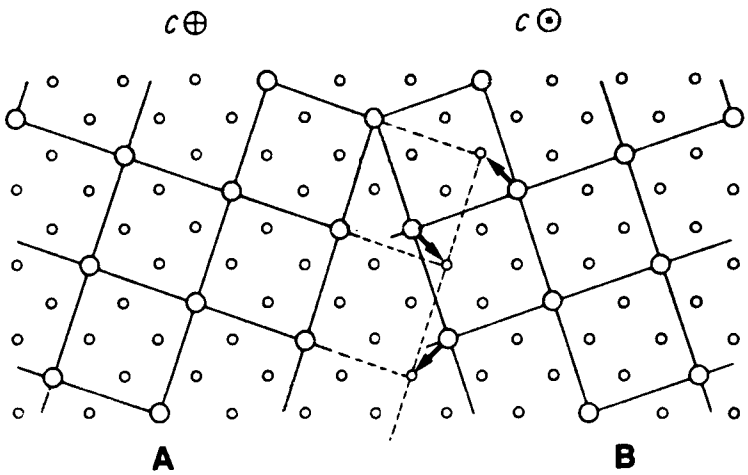


Figure IV-32. Mechanism for the preferential elimination of APTB's. Atomic arrangement in the (001) plane in APT-related domains A and B is shown; large circles denote Mo atoms, small ones Ni. If the Ni and Mo atoms exchange positions along the <110> direction shown by the arrow, then the new positions of atoms in domain B would become in-phase with those in domain A and a portion of the APT interface would be removed.

interface is either straight or undulated. A DF image obtained from a Ni_4Mo spot (Figure IV-33b) reveals fine domains within the grain and larger, columnar domains in the migrated regions behind the moving boundary. Groups of grain boundary domains are primarily in antiphase relationship. It was also established by electron diffraction that the moving boundaries, although occasionally straight, are high-angle incoherent boundaries. The domains nucleate in one grain and then proceed to advance into the opposite grain.

With continued aging at 700°C, the volume fraction of the grain boundary product increases. The microstructure at 10 hours (Figures IV-33c-d) shows a well-defined mosaic assembly of APB's. The fine domains ahead of the migrated boundaries are also visible. At 96 hours, the coarsening reaction has progressed rapidly, virtually consuming over a third of the microstructure (Figures IV-33e-f). SAD patterns from the grain boundary domains showed sharp and spherical superlattice spots, which indicates that these domains possess a high degree of order (S near 1) (92). The APB's in Figures IV-33e-f appear anisotropic and have enlarged relative to those at 10 hours. Also, notice in Figures IV-33c-f that the interface separating the migrated region from the fine domains is very straight and there is no change in the size or morphology of the fine domains at the interface. It appears from the configuration of the large domains that spontaneous "recrystallization" of the fine domains and rapid diffusion across the incoherent interface leads to epitaxial attachment. This causes the boundary to advance. With further aging to about 400 hours, it appeared that the grain boundary product had virtually occupied the

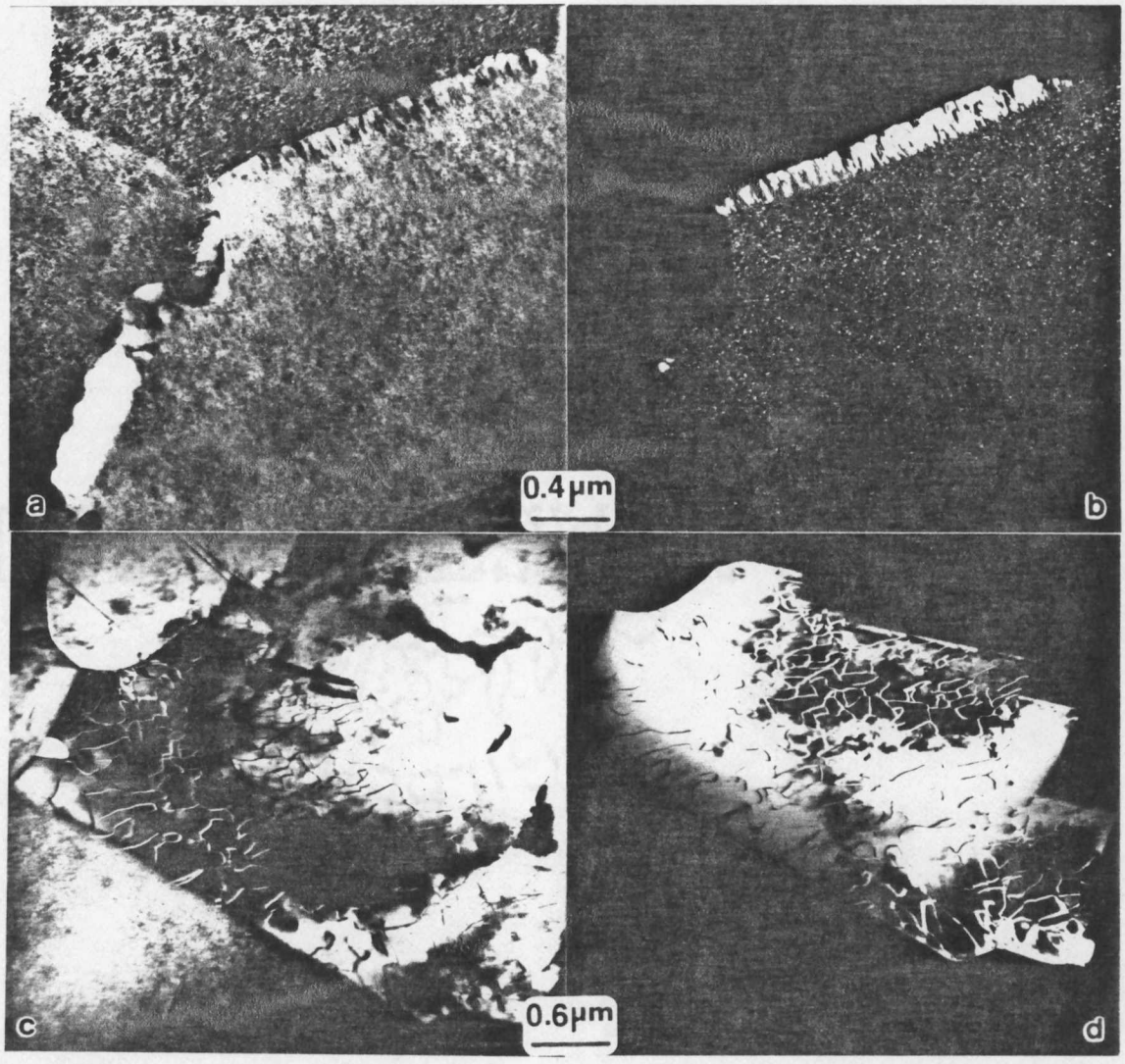


Figure IV-33. Domain coarsening reaction at grain boundaries in Ni_4Mo aged at 700°C. a) through f) are BF (left) and DF (right) (from Ni_4Mo spot) pairs of micrographs on aging for 1, 10 and 96 hrs, respectively; g) 840 hrs--BF micrograph.

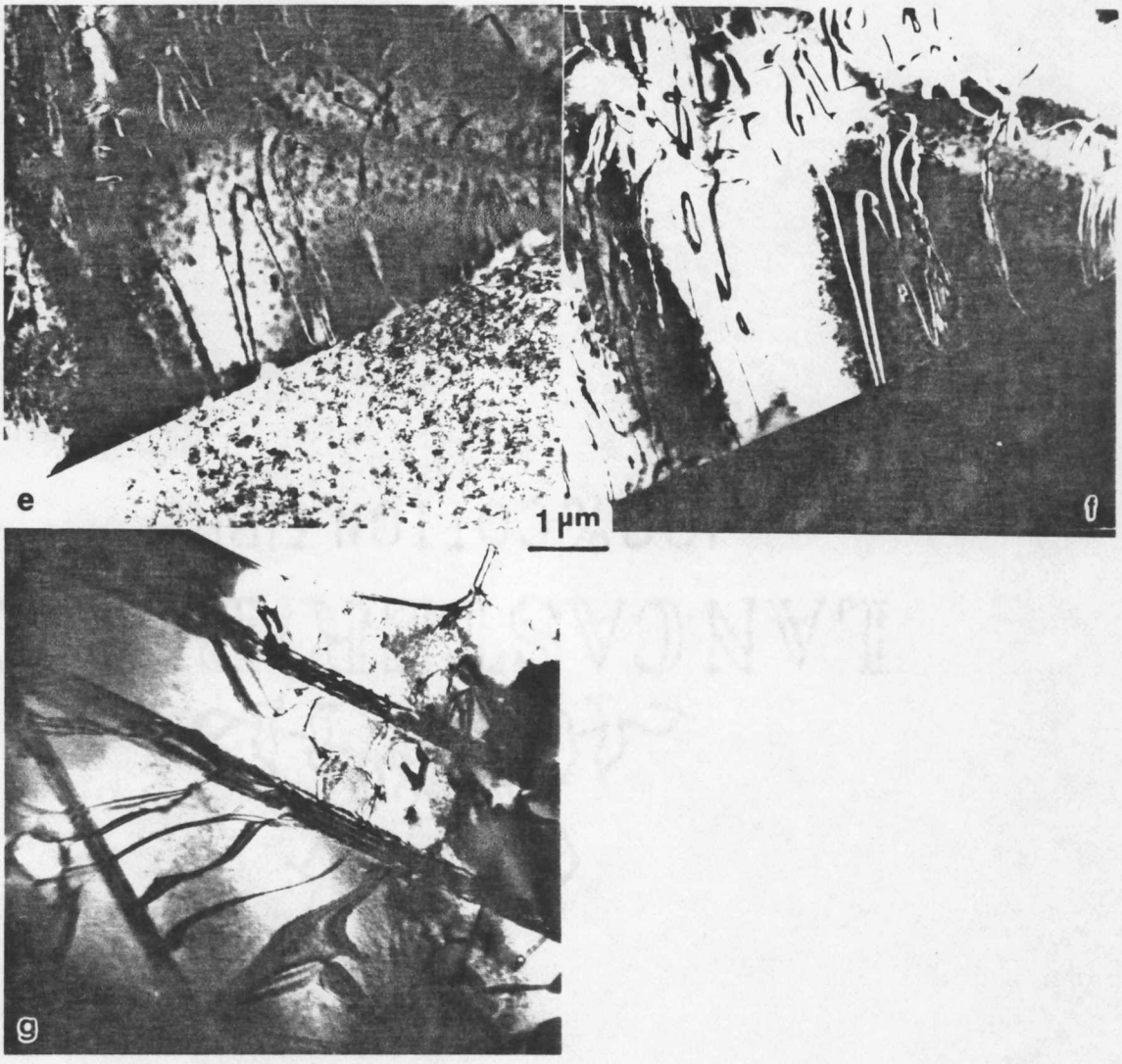


Figure IV-33. (Continued).

entire microstructure. The grain boundary domains continue to grow with time (Figure IV-33g) and frequently overlapping stacking faults and twins are observed in these regions.

At 600°C, the grain boundary reaction is initially observed at 16 hours (Figure IV-34a) and like at 700°C the intragrain ordering is not yet complete (Figure IV-29a). The reaction develops somewhat slower than that at 700°C. An example is shown in the DF micrograph obtained from a Ni_4Mo spot in Figure IV-34b for a sample aged for 96 hours. General characteristics of the reaction and the morphology of the coarsened domains are the same as at 700°C. With time, the grain boundary product proceeds to occupy larger and larger portions of the microstructure. At 840 hours, very small regions of fine intragrain domains exist. The shape of the superlattice spots in SAD's obtained from these regions indicated that S was still less than 1 (Figure IV-29f). Examples of the grain boundary coarsened domains at this time are shown in Figures IV-34c-e. In the BF micrograph in Figure IV-34c, a set of elongated and anisotropic domains appears vertically and a second set horizontally. Domains may form in a dense and very thin morphology and as complex, helix-like shapes (left center of micrograph). Few APB's show α-fringe contrast; rather a majority of these (top left) appear as thin dark lines. It is also observed that the growth front (at the bottom of the micrograph) may be wavy; a facetted morphology is also observed.

A [001] SAD pattern obtained from the area encircled in Figure IV-34c, shown in Figure IV-34d, reveals that domain groups A and B are in APT relation. In fact, an angular interface separating the two

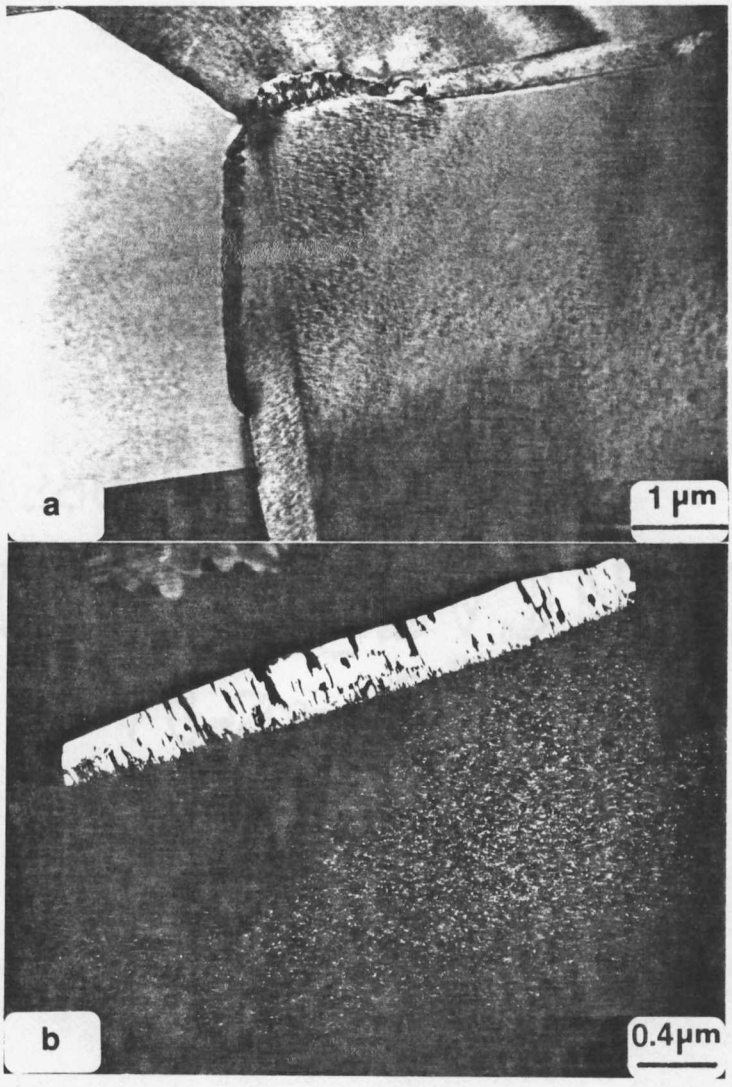


Figure IV-34. Domain coarsening reaction at grain boundaries in Ni_4Mo aged at 600°C. a) 16 hrs--BF micrograph; b) 96 hrs--DF micrograph from Ni_4Mo spot; 840 hrs--c) BF micrograph showing two domain groups (A and B) separated by anisotropic APB's; d) [001] SADP of region encircled in c); e) DF micrograph from Ni_4Mo spot labelled A in d); f) DF micrograph showing stacking faults in the coarsened product ($\underline{n}$=[112], g=[11$\bar{1}$]).

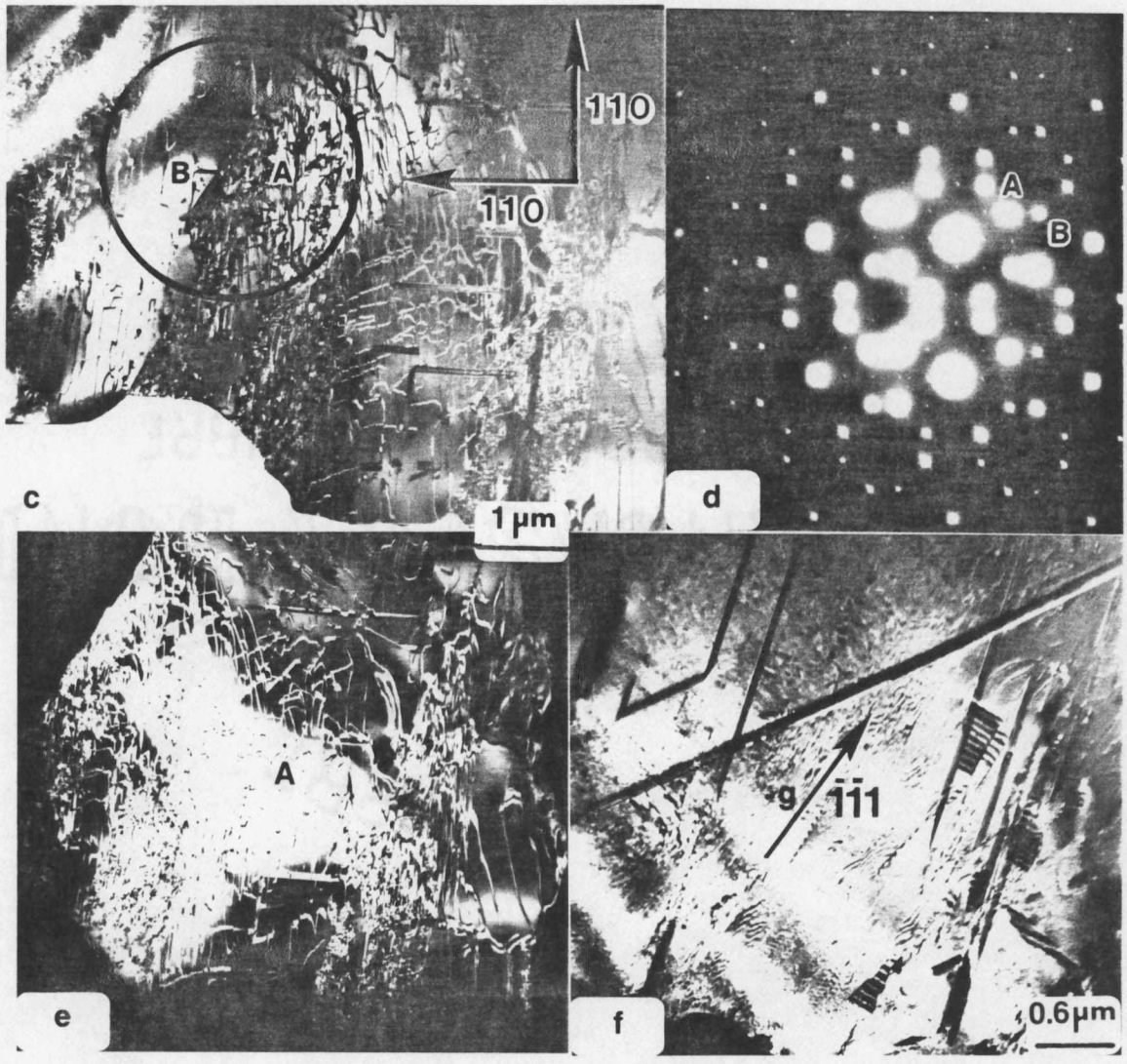


Figure IV-34. (Continued).

groups can also be seen in Figure IV-34c. Individual groups A and B are composed of APB's, as evident, for example, in the DF image in Figure IV-34e obtained from the superlattice spot encircled in Figure IV-34d. The degree of order within the domains is high, as deduced by the well-rounded shape of the superlattice spots in the SAD. Another prominent feature is that both superlattice and fundamental spots show small streaks passing through individual spots. The streaks appear in two orientations normal to each other, one set sharp, the other weaker. The direction of the streaks deviates by about 3^{o} from the <110> directions. Careful inspection evinces that there is a small latitude in the direction of the streaks associated with different spots. Moreover, in some distant spots, the streaks appear as satellites. For all practical purposes, it is concluded that the streaks are parallel to the $\langle 110 \rangle_c$ or equivalently $\langle 210 \rangle_t$ directions. This fine structure of the spots is associated with the APB's (118).

Gevers and co-workers (251,252) carried out detailed theoretical and experimental studies on the origin of the fine structure of diffraction spots associated with planar defects such as stacking faults and APB's. As the electron beam traverses through an area containing planar defects (APB's in the present case) interference between waves of slightly differing wave vectors produces this fine structure (251). The direction of the streak or that of the line joining the satellite spot to the associated fundamental spot will be normal to the intersection of the fault and the foil surface (251,252). The two $\langle 110 \rangle_c$ directions of the streaks in Figure IV-34d are drawn in Figure IV-34c after due rotation corrections. It is

evident that the $[\bar{1}10]$ streak is nearly normal to the vertical APB's and the [110] streak to the horizontal APB's. Moreover, from the geometry of the APB's it is deduced that the electron beam is incident at a sharp angle, that is, the APB's are almost parallel to the incident beam. Based on this, it is concluded that the defect planes of the vertical and horizontal APB's are the $(\bar{1}10)_c$ and the $(110)_c$ planes respectively.

Another feature that is commonly observed at 600°C, similar to that at 700°C, is the presence of overlapping intrinsic stacking faults and twins within the coarsened regions, as shown in Figures IV-34f. At the longer aging times, the coarsening reaction also affects annealing twins. BF micrographs illustrating this feature are shown in Figures IV-35a-b. In Figure IV-35a, the growth front of a coarsened region impinges on an annealing twin. The end of the twin in contact with the growth front is deeply penetrated as rectangular troughs and it appears from the presence of bend contours in these troughs that they are also composed of coarsened domains. This is based on the observation that the coarsened domains exhibit a lower hardness than the fine domains within the grain interiors (242) and therefore bend more easily during specimen handling. It is significant that in Figure IV-35a the domains within the unpenetrated twin and on either side are very small. Thus, the stepped appearance of annealing twin boundaries frequently observed in the optical microstructure is indeed associated with the domain coarsening reaction, as concluded previously (10). At a more advanced stage in the process, domains within the twin also coarsen as shown in the BF micrograph in Figure

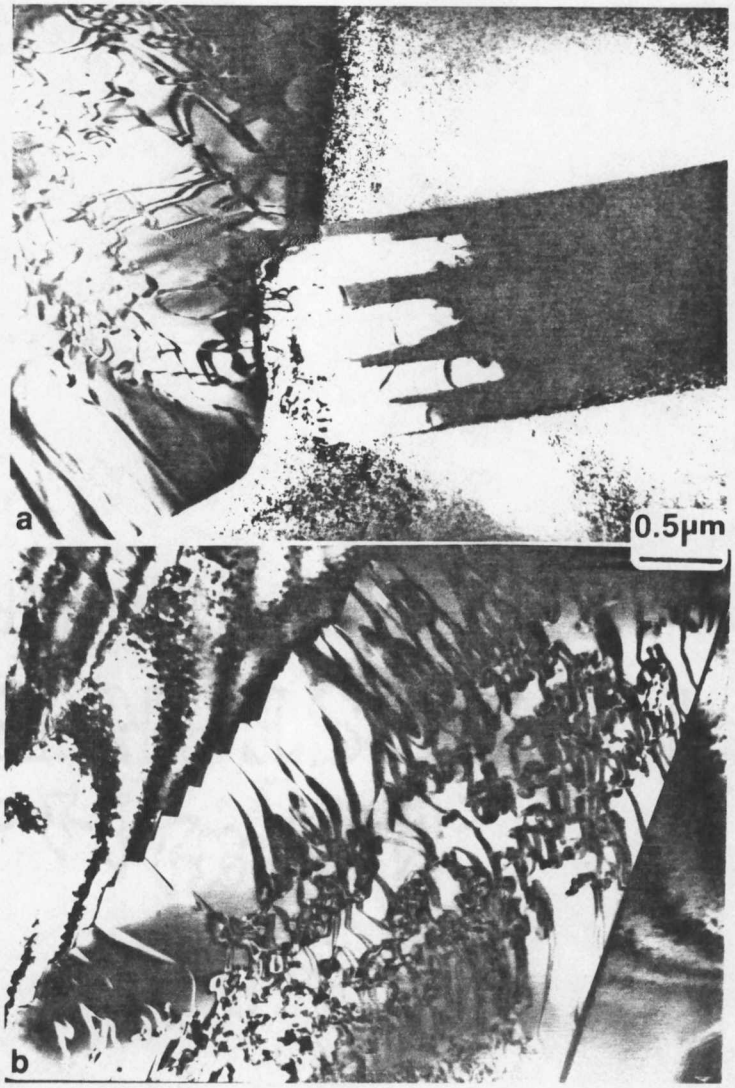


Figure IV-35. TEM micrographs showing the interaction between the coarsening reaction and annealing twins. Aged 840 hrs at 600oC.

IV-35b. The figure also shows one side of the twin as straight and coherent, the other side (presumably incoherent) as stepped. Large domains appear to commence on both sides of the twin and grow towards the center, where the domains are finer. There does not appear to be any consistent correspondence between the starting points of the domain boundaries on the stepped side and the corners of the steps. It should be noted that regions outside the twin also contain large domains which are out of contrast in this particular orientation. It appears that the incoherent side of the twin boundary is being progressively eroded by growth of domains from outside the twin.

At 4500 hours, the entire microstructure consists of the coarsened domains. A region of coarsened domains is shown in the BF and DF images in Figures IV-36a and -36b. The associated [112] SAD pattern (Figure IV-36c) reveals strong superlattice spots from one variant and weaker spots from a second variant which are streaked in the $[\bar{1}\bar{1}1]_c$ direction. These spots arise from perpendicular twins produced by the passage of the {111} fcc striations through the antiphase domains. The striations are very thin (indicated by circles in Figures IV-36a-b) and produce streaks in the ($[\bar{1}\bar{1}1]$) direction normal to the thin dimension. In the SAD pattern in Figure IV-36c, weak satellite spots appear in two locations near both superlattice and fundamental spots. Although it was difficult to establish the exact direction of the satellites, they appear to deviate slightly from <402> directions. The two <402> directions appearing in this SAD pattern are inscribed in Figure IV-36a. One of these, the $[\bar{4}02]$ is closely normal to the width of one set of APB's. Other relevant

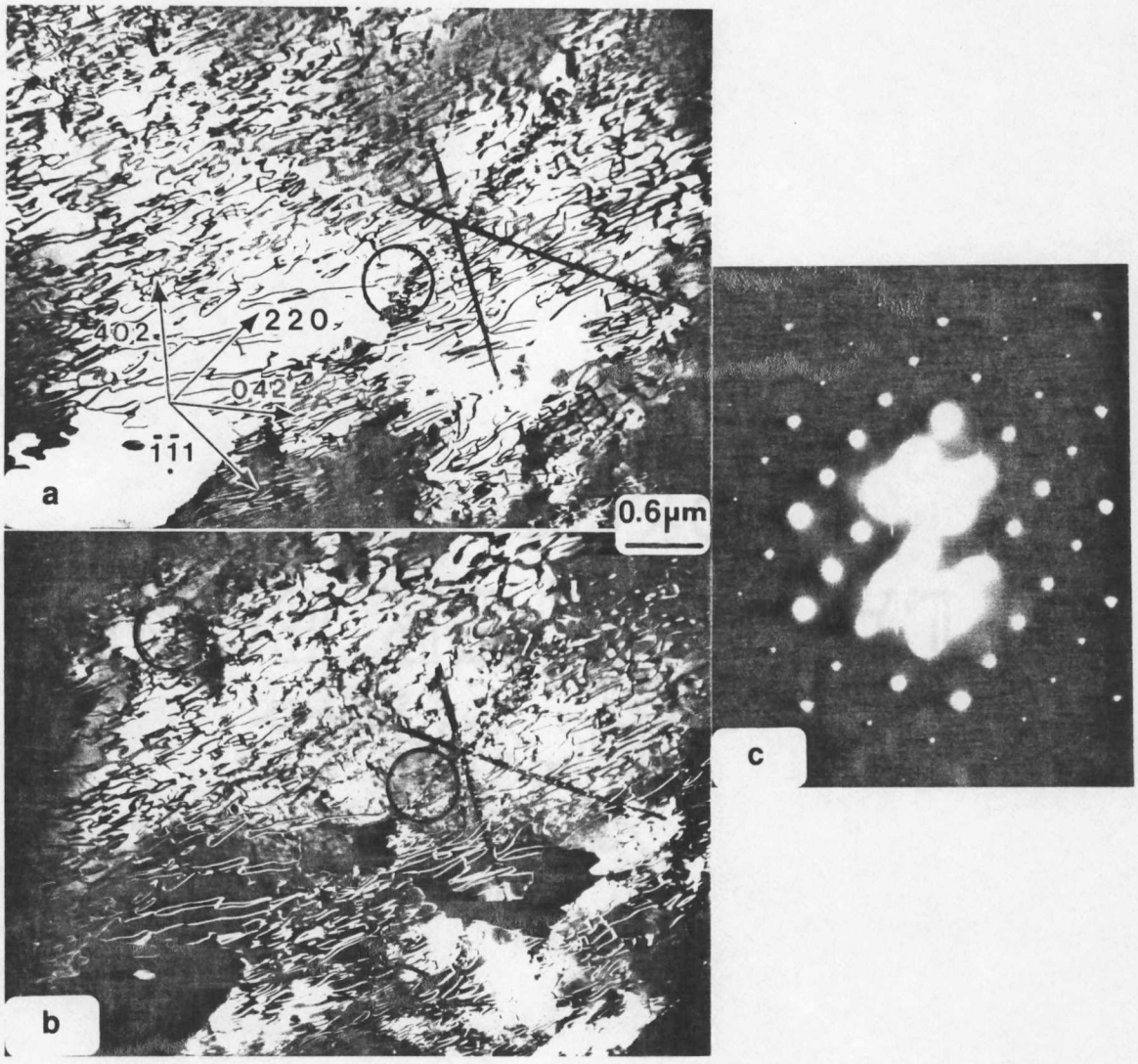


Figure IV-36. Another example of the domain coarsening reaction at grain boundaries in Ni_4Mo aged at 600°C. Aged 4500 hrs. a) BF micrograph; b) DF micrograph from Ni_4Mo spot in the [112] SADP in c). The location of a thin twin is shown by the circles in a) and b).

directions are also inscribed in Figure IV-36a. The geometry of the APB's indicates that they lie nearly parallel to the incident electron beam. Based on this, it appears reasonable to conclude that in this case the APB's form parallel to $\{402\}_c$ planes.

Mechanism and driving force for the domain coarsening reaction. The grain boundary reaction described in the preceding has been reported previously in Ni_4Mo (12,13,126,190) and in other ordering alloys undergoing a cubic to non-cubic structure change, such as CuAu (180), CuPt (181), Ni_2V (106,133) and Ni_3V (191). This type of behavior has been described as recrystallization by stress-induced boundary migration in CuAu, CuPt and Ni_4Mo by Arunachalam and Cahn (180), Irani and Cahn (181) and Snyder and Brooks (12), respectively. Tanner (133) refers to the initial nucleii as coherent (or single-sided) allotriomorphs and the subsequent growth process in which the fine intragrain domains are consumed as recrystallization. All of these investigators emphasize that the driving force for the coarsening process is the difference in strain energy across the migrating interface. Chakravarti et al. (13), in contrast, argued that the reduction in energy of the system obtained by eliminating the APB's between the small domains is the primary driving force.

From the results of the present investigation, a somewhat better picture of the heteregeneous domain coarsening reaction has emerged. There are three main factors to be considered for explaining the origin and the growth of this reaction. These are: ordering strains, degree of order and interfacial energy associated with APB's. In the

case of Ni_4Mo, the last factor provides the major contribution; the difference in the degree of LRO between the grain boundary domains and the fine intragrain domains is also influential, albeit to a lesser extent, whereas the strains associated with the change in crystal symmetry (that is, reduction in the c/a ratio) during ordering play a relatively insignificant role. A rational justification for this conclusion is elaborated in the following.

In agreement with other reports (12,13,126,190), the domains formed along the grain boundaries initially nucleate in one grain and then proceed to grow into the neighboring grain. In this sense, the initial nucleii are appropriately referred to as coherent allotriomorphs (133). The nucleation of the domains at the grain boundaries is somewhat random, profuse at some and completely absent at others. This is related to the fact that non-coincidence high-angle boundaries are more potent nucleation sites than high-coincidence low-angle boundaries (133). Moreover, frequently, different variants of domains are nucleated at different parts of the grain boundary. Within one set, all domains are separated by APB's. As the domains grow towards the grain interiors the original incoherent boundary is carried ahead of them.

APB's are generally specified in the form (hkl)[R], where (hkl) refers to the indices of the plane of the APB and R is the associated displacement vector. In Ni_4Mo, the plane of the APB's is generally the $(110)_c$ or $(420)_c$, or equivalently the $(420)_t$ or $(110)_c$ (92,118). There are other possibilities for the APB plane, but are ignored in the present discussion, since the associated interfacial energies are

higher (13). The displacement vector of the APB's can be of four types: R_1 = [110]/2, R_2 = [010]/2, R_3 = [01±1]/2 and R_4 = [10±1]/2 referred to the fcc cell or equivalently [210]/5, [310]/5, [13±1]/10 and [3$\bar{1}$±1]/10, respectively, in terms of the tetragonal superlattice cell; however, these APB's cannot be distinguished by the extinction criterion (118,128). Generally, two types of APB's, referred to as conservative or non-conservative, can be distinguished depending on the relative orientation of the displacement vector R and the unit normal on the boundary plane $\underline{n}$. If $\underline{n}$.R = 0 (that is, R lies in plane of APB), then the boundary is called conservative; if $\underline{n}$.R = t with t≠ 0, a slice of material of thickness, t, is either removed or inserted and the boundary is called non-conservative (92,253,254). Non-conservative APB's are also associated with a local composition change across the boundary and as a result they have a higher energy relative to conservative APB's (255,256). Moreover, they can change their orientation and become conservative as the degree of order increases, that is, at equilibrium the APB's will tend to adopt a low energy configuration (92,253,254).

In the present study, the plane of the grain boundary APB's is positively established as the $\{110\}_c$ plane (Figures IV-34c-e). Another possibility is the $\{210\}_c$ plane (Figures IV-36a-c), but this was not positively ascertained. Nevertheless, based on observations made from Figures IV-36a-c it is reasonable to conclude that the APB's between coarsened domains can also form parallel to $\{201\}_c$ planes. The small deviation from these planes is not understood, but is probably related to the fact that the APB's possess a certain amount of curvature. For

the (110) plane, the APB's can be either conservative or non-conservative depending on R. For example, the combination $(110)_c 1/2[\bar{1}10]_c$ is conservative, all others are non-conservative. For the $(210)_c$ plane, all APB's are non-conservative. Thus, establishing the conservative/non-conservative property requires determination of the specific R, but this was not attempted because of the attendant difficulties (128). A rational basis for the observed preferential adoption of the $\{110\}_c$ plane as the plane of the APB lies in the calculations of Chakravarti et al. (13), who found that the APB energy is least for the $\{110\}_c$ planes. These arguments lead to the conclusion that the grain boundary domains form on planes for which the APB energy is lowest. The APB's may be initially non-conservative, but become conservative as these domains quickly increase in size and degree of order during the growth process.

The present results have also shown that the coarsening process commences before the intragrain structure has attained perfection. This is supported by the diffraction evidence (Figures IV-28a and -29a) and also by the x-ray diffraction observations of Ling and Starke (178) on single crystals of Ni_4Mo. Simultaneously, the degree of order of the coarse domains is higher. An important conclusion arising from the research of Ling and Starke (178) is that the strains due to ordering are largely dependent on the degree of long range order and <u>not</u> on the domain size. There was no detectible increase in internal strains till about 1 hour at 700°C, at which time the degree of order was about 0.7. Subsequently, the strains continue to increase as S approaches 1 at 15 hours and remain at a constant maximum for

longer times, even though the domain size continues to increase (178). These results establish that the grain boundary domains, although large, should have a higher degree of internal strain relative to the fine intragrain domains, since the former are of almost perfect order. Moreover, even after the intragrain domains have attained perfection, the grain boundary coarsening continues to progressively occupy increasing portions of the microstructure. This clearly proves that internal strains due to ordering provide a negligible driving force for the grain boundary coarsening process. Additional support for this conclusion is gathered from the observation that the coarsening reaction is virtually absent at higher temperatures (8-10), where the internal strains are expected to be higher (13), and moreover, the faster ordering rate (8-10 and this research) would lead to rapid increase in the strain level in short times. The mechanism of recrystallization by strain-induced boundary migration requires that varying levels of strain exist in different grains, so that preferential migration of boundaries occurs into grains of lower strain energy (180,181). This mechanism presupposses that ordering proceeds to different extents in different grains, for which there is no rational justification.

The picture that emerges now, in view of the preceding discussion, is that the primary driving force for the coarsening reaction in ordered Ni_4Mo is the reduction in interfacial energy of the system obtained by elimination of the APB's between the small domains, in support of the earlier observations of Chakravarti et al. (13). The heteregeneous grain boundary product consists of groups of

large domains separated by APB's on planes of lowest interfacial energy (the $\{110\}_c$ planes). The APB's are probably initially non-conservative, but become conservative by diffusion as the degree of order within the domains increases (92). The difference in the degree of long range order between the coarse grain boundary domains and the fine intragrain domains also probably provides a small driving force, at least initially. Thus, the progression of the coarsening reaction has the dual advantage of lowering the energy of the system by eliminating the extra interfacial energy of the APB's, while simultaneously causing the overall degree of long range order to become perfect. Since it is essentially the difference in interfacial energy across the migrating interface that provides the driving force, it is probably more apposite to regard the coarsening process as "secondary recrystallization."

The mechanism by which the coarsening reaction grows in extent has been discussed in detail by Tanner (133) in Ni_2V, in which the reaction bears a remarkable resemblence to that in Ni_4Mo. Interestingly, Ni_2V is isotypic with Ni_2Mo (126) and is also classified as a "420" alloy (133). Basically, the growing domains carry the original incoherent α grain boundary ahead. Since the transfer of atoms requires much less energy at grain boundaries (50 pages 433-440), this interface provides a substrate for rapid diffusion, which, in turn, results in rapid growth. The intragrain domains do not have a presentiment of the dangerous fate that awaits them, that is, they show no change in morphology or shape right upto the interface (Figures IV-33a-f, -34a-b). They appear to spontaneously

recrystallize and the rapid atom transfer at the boundary permits epitaxial attachment to preexisting domains behind the interface, which, in turn, advances the migrating boundary. The frequent undulated appearance of the migrating interface implies that there is a variation in the mobility of the boundaries. Tanner (133) has provided an adequate explanation for this feature in Ni_2V on the basis of Gleiter's model for grain boundaries and the mechanism involved in their migration (257). Basically, the grain surface is considered to be composed of ledges and the migration process is related to variations in the movement of atoms on these ledges. The interested reader is referred to Tanner's exposition (133) for further details. A satisfactory explanation for the interaction between the heteregeneous reaction and annealing twins and the mechanism by which domains within twins coarsen has not been achieved. Conceivably, even coherent twin boundaries possess a higher energy relative to the APB's and therefore tend to be preferentially removed. High resolution electron microscopy is expected to provide better insight into the coarsening process and into the atomic configuration in domains on either side of the migrating interface.

Ordering in Ni_4Mo-Cr Alloys During Continuous Heating and Cooling

Electrical Resistivity

Vasudevan's (9) results on the resistivity changes associated with SRO and LRO in Ni_4Mo-based alloys containing 0 to 4 wt pct chromium were presented earlier in Chapter II (pages 131-136). His results are briefly reiterated here to provide a framework for

subsequent understanding of these changes by electron microscopy. The difference in transformation behavior between Ni_4Mo and alloys containing chromium was shown by comparing their resistivity values under the following conditions:

1. As cold reduced 68% RA.
2. As water-quenched from 950°C.
3. During rapid cooling from 950 to 25°C at 60°C/min in vacuum.
4. During slow cooling from 950 to 25°C at 1°C/min in vacuum.

In addition, the temperature dependence of structural changes was inferred by analysis of changes in slope of the resistivity-temperature curve on heating and cooling. The behavior is summmarized in Table II-1 and Figures II-36 and -37 (pages 133-135). Several consistent changes in resistivity as a function of chromium content are evident.

In the conditions 1, 2 and 3, the alloys were short-range ordered and from the results in Table II-1 (page 133) and Figure II-36 (page 134) it was concluded that chromium decreases the degree of SRO in as-quenched alloys independent of either cooling rate or cold working. In alloys cooled slowly at 1°C/min from 950°C (condition 4) the room temperature resistivity increases with an increase in chromium content (Table II-1 and Figure II-37). The increase in resistivity is small to 0.74 wt pct Cr, beyond which there is a sharper rise. The high value for the 3.84 wt pct Cr alloy indicates complete suppression of LRO for cooling rates exceeding 1°C/min from above the ordering temperature. In Ni_4Mo + Fe alloys under the same conditions, complete suppression of LRO occurs above 4.4 wt pct Fe

(8), indicating that chromium is somewhat more effective than iron in slowing the kinetics of LRO of Ni_4Mo. Other examples of third element suppression of LRO include cobalt (258) and vanadium and copper (259) on the Ni_3Fe superstructure. Factors contributing to the increase in resistivity by third elements include: 1) increase in lattice distortion, 2) decrease in the degree of long range order, 3) increased domain boundary area associated with decreased domain size, and 4) partial or complete retention of SRO. The influence of these factors will be discussed under the section on electron microscopy.

Electron Microscopy

Composite (001) and (112) reciprocal lattice sections identifying the relative locations of the SRO, Ni_4Mo, Ni_2Mo, and DO_{22} reflections are shown in Figures IV-37a and -37b respectively. Examination of electron diffraction patterns in these orientations greatly facilitates identification of one or more phases in the microstructure. Therefore, these orientations are the ones most commonly employed for observation.

The [001] and [112] diffraction patterns for the 2.08 wt pct Cr alloy following slow cooling at 1^oC/min from 950^oC (Figures IV-38a and -38b), show in addition to the Ni_4Mo superlattice spots from two variants, weak spots at the Ni_2Mo positions. The Ni_2Mo spots are streaked towards the Ni_4Mo spots in the <210> direction. No {1 1/2 0} SRO spots are observed. The network of faint spots outlining the inner square is caused by double diffraction (118). It should be noted that the Ni_2Mo phase has been observed in the binary Ni_4Mo alloy on aging

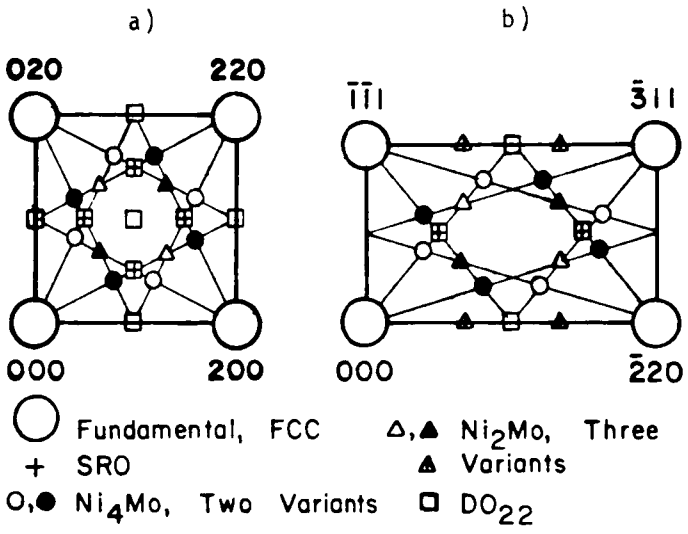


Figure IV-37. Reciprocal lattice sections identifying the relative locations of different indicated reflections. a) (001); b) (112).

at 600°C (8) and 650°C (126), in a ternary Ni_4Mo + 2.4 at pct V alloy at 700°C (28), and in the initial stages of ordering of Ni_3Mo (124-126). The streaking of the Ni_2Mo spots is associated with thin plates of Ni_2Mo in the Ni_4Mo matrix (126). The Ni_4Mo domain size as revealed by DF images (Figure IV-38c) from a 1/5{420} superlattice spot (indicated by an arrow in Figure IV-38b) was determined to be 10.7 nm, which is much smaller than the value of 187 nm for the binary alloy under the same conditions (11 and this research). In addition, a few large plates of Ni_3Mo are present at grain boundaries (Figure IV-38d); these plates contain stacking faults associated with the transformation to Ni_3Mo, similar to those reported by Van Tendeloo and co-workers (122,127,128). Since the Ni_2Mo and Ni_3Mo are ordered phases and occur in very small amounts, it is doubtful that their presence contributes to the increase in resistivity (Figure II-37, page 135). Scattering caused by increased domain boundary area cannot be overruled since the average domain size is comparable to typical values of the electron mean free path. Therefore, it appears that the primary factors contributing to the increase in resistivity of the 2.08 wt pct Cr alloy are increased electron scattering caused by chromium, a decreased degree of LRO, and scattering by increased domain boundary area.

The diffraction pattern of the 2.97 wt pct Cr alloy shows both Ni_4Mo superlattice and {1 1/2 0} SRO spots linked by diffuse intensity (Figure IV-38e). Neither Ni_2Mo nor Ni_3Mo are observed in this alloy. It is evident that the high resistivity of this alloy (Figure II-37, page 135) is caused by an increasing influence of SRO. In the 3.84 wt

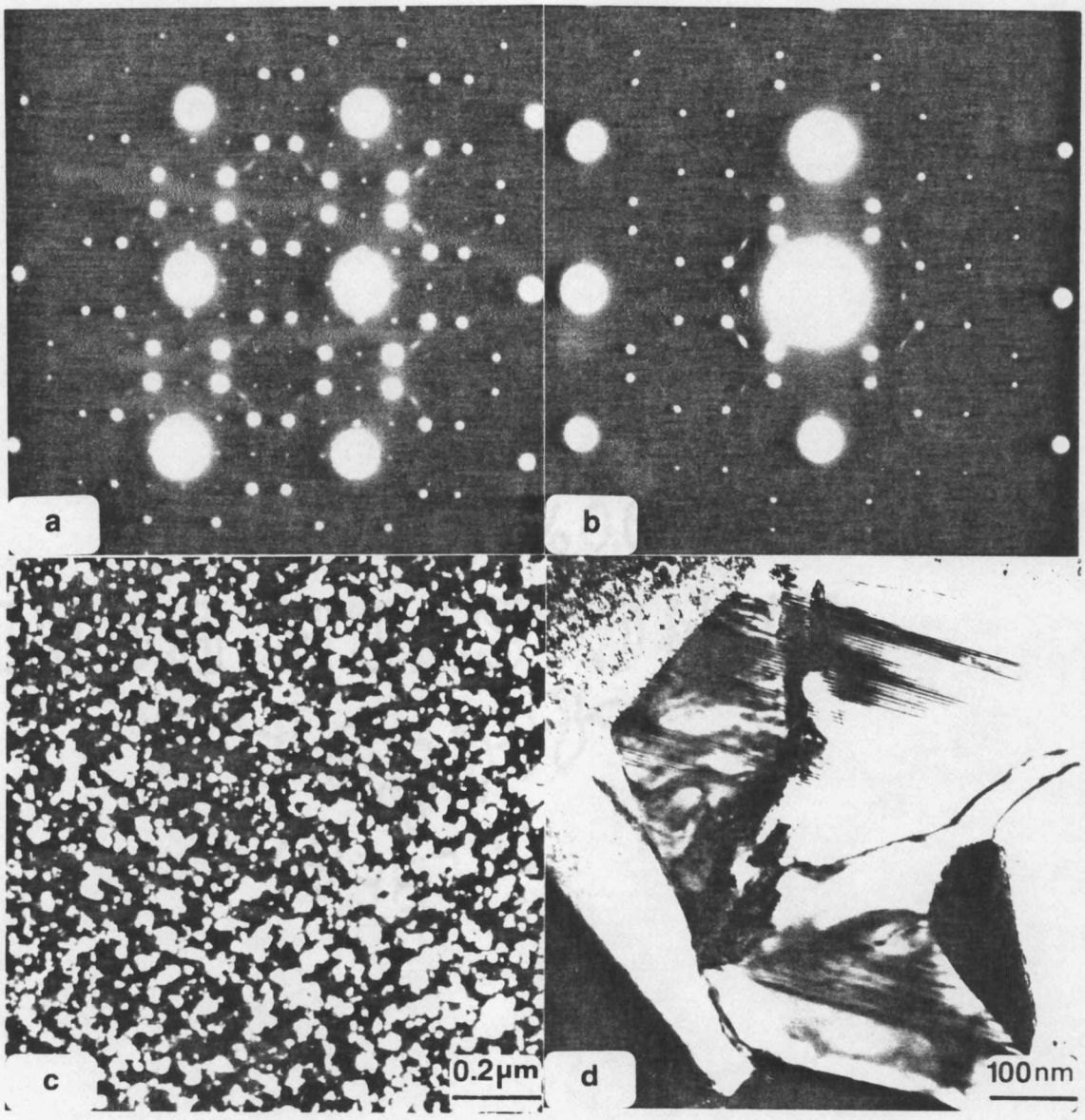


Figure IV-38. TEM micrographs of continuously cooled Ni_4Mo-Cr alloys. Cooled at $1^{o}C$/min from $950^{o}C$. 2.08 wt pct Cr--a) [001] SADP; b) [112] SADP; c) DF from Ni_4Mo spot in b); d) BF micrograph of grain boundary Ni_3Mo; e) 2.97 wt pct Cr--[001] SADP; f) 3.84 wt pct Cr--[001] SADP.

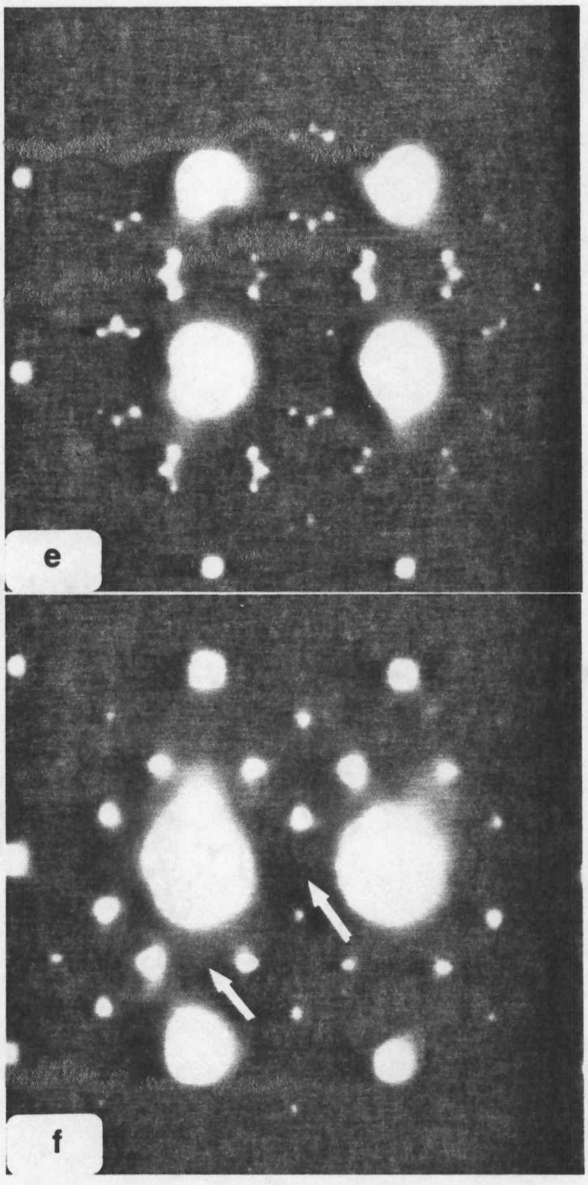


Figure IV-38. (Continued).

pct Cr alloy, LRO of Ni_4Mo is completely suppressed; the diffraction pattern shows predominantly the {1 1/2 0} SRO spots, with very weak intensity at some of the DO_{22} positions (indicated by arrows in Figure IV-38f). In addition, weak intensity in the form of pseudo-circles connecting the SRO spots, between these circles in <100> directions, and diametrically between SRO spots within the circles towards the {110} positions, are observed. The first two have been reported by De Ridder et al. (172) in the binary Ni_4Mo alloy when SRO forms at a slower cooling rate and has been attributed to clusters in the SRO state. However, the diametrical intensity is not supported by any of the models presented and needs further analysis. It should be noted that the DO_{22} phase has been observed under isothermal aging conditions in a Ni_4Mo + 2.4 at pct V alloy (24), in Hastelloy B (29), in Hastelloy B2 (31), and in the early stages of ordering of Ni_3Mo (127,128). It is clear that the rather high resistivity of this alloy (Figure II-37, page 135) is caused by a completely SRO state.

Fundamental knowledge of the effect of third elements on long-range ordering of Ni_4Mo is lacking. In the present study, the question of how chromium suppresses LRO concerns whether it replaces the nickel or the molybdenum atoms in the ordered Ni_4Mo lattice. Examination of the results of other alloy systems (258-261) and of the nickel-chromium and chromium-molybdenum constitution diagrams suggests that the bond between nickel and chromium is stronger than that with molybdenum. Chromium atoms will therefore replace the molybdenum atoms in the Ni_4Mo superstructure and thus perturb this periodicity. On the other hand, the free energy difference between the disordered and

ordered phases is small and only a small perturbation in any periodicity associated with chromium imbalances this difference such that the ordered phase is no longer thermodynamically stable. It will shown later that chromium does have a tendency to replace molybdenum in Ni_4Mo-based alloys.

Ordering in Ni_4Mo-Cr Alloys During Isothermal Annealing

The transformation behavior of Ni_4Mo alloys containing 2.08, 2.97 and 3.84 wt pct chromium following isothermal annealing at 850, 800, 700 and 600°C for times to 4500 hours was investigated using optical microscopy and transmission electron microscopy. During the course of the study, it was found that prior grain size was an important factor in governing the type, volume and distribution of second phases. Therefore, the structural changes were followed in samples having two different prior grain sizes of 0.1 mm and 0.5 mm. Details of the heat treatment procedures employed have been described in Chapter III (166).

Optical Microscopy

The effect of grain size on the optical microstructure is illustrated in Figures IV-39, -40 and -41 for samples aged for 400 hours at 850, 800 and 700°C respectively. At 600°C, the hardness and resistivity changes have indicated that structural changes are occurring (9). However, the optical microstructures generally did not show any discernible changes and are therefore not presented. The microstructural features at the higher temperatures are described based on the electron microscopy results, which follow.

Aging at 850°C. In all three alloys, the fine-grained samples show large plates of Ni_3Mo at the grain boundaries (indicated by arrows in Figures IV-39a-c), whereas the coarse-grained samples undergo a discontinuous precipitation reaction at both grain boundaries, and on occasion, at annealing twin boundaries. Generally, the discontinuous precipitation reaction increases in extent with increasing chromium. It is shown later that the precipitates along the initial fcc α phase grain boundaries, as well as a major portion of those involved in the discontinuous precipitation reaction are eta-carbides. In the fine-grained specimens aged for longer times to 4500 hours, the amount of grain boundary Ni_3Mo increased slightly with increase in chromium from 2.08 to 2.97 wt pct, followed by a decrease at 3.84 wt pct.

Aging at 800°C. In the 2.08 wt pct Cr alloy, the fine-grained and coarse-grained samples show respectively many in contrast to few Ni_3Mo plates emanating from the grain boundaries. Also, thin striations of the DO_{22} phase occur in the coarse-grained sample (indicated by arrows in Figure IV-40a). In both samples, the morphology within the grains consists of Ni_4Mo domains in a short-range ordered (SRO) matrix. The coarse-grained sample also contains eta-carbides along the grain boundaries; the fine-grained sample is devoid of these carbides.

In contrast to the 2.08 wt pct Cr alloy, neither the fine-grained nor coarse-grained samples of the 2.97 and 3.84 wt pct Cr alloys contain any Ni_4Mo. The microstructure of the fine-grained

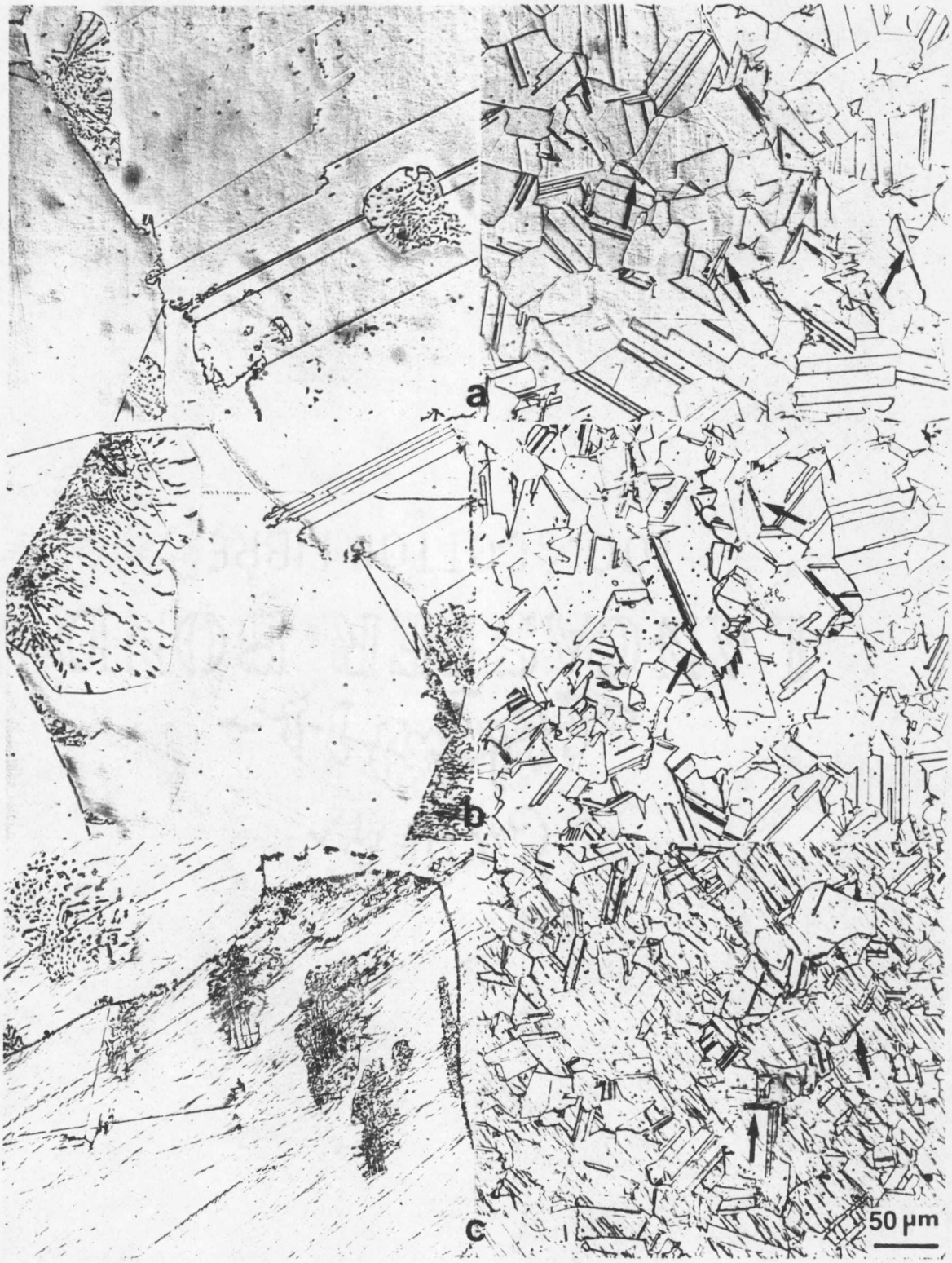


Figure IV-39. Optical micrographs showing the effect of grain size on the microstructure of Ni_4Mo-Cr alloys aged at 850°C. Aged 400 hrs. a) 2.08, b) 2.97 and c) 3.84 wt pct Cr.

samples of both alloys is composed of numerous large plates of Ni_3Mo distributed in a SRO matrix (Figures IV-40b and -40c). In the coarse-grained samples of both alloys, numerous thin striations of the DO_{22} phase are present in a SRO matrix. Frequently, these striations occur in groups originating from the grain boundaries. The discontinuous precipitation reaction is also observed at the grain boundaries. Occasionally, massive Ni_3Mo plates nucleate at the grain boundaries and pass through the discontinuous precipitation reaction regions (Figure IV-40b). Many small Widmanstatten precipitates both along annealing twin boundaries (traces of {111} fcc planes) as well as in the SRO matrix are also present. These precipitates could not be identified, but appeared to be rich in molybdenum, since the adjacent regions were preferentially attacked by the polishing solution leaving holes where the particles were located. Some of the particles which survived the polishing process were also identified as eta-carbides.

Aging at 700°C. Although the microstructures of the coarse-grained samples of all three alloys appear featureless, it was established by electron diffraction that the morphology within the grains consists of fine precipitates of Ni_2Mo and Ni_4Mo domains (Figures IV-41a, -41b and -41c). The structure within the fine grains of the 2.08 and 2.97 wt pct Cr alloys is also composed of Ni_2Mo and Ni_4Mo, whereas in the 3.84 wt pct Cr alloy neither of these phases are present. In the fine grained samples of all three alloys, large plates of Ni_3Mo form at the grain boundaries, increasing in proportion with increasing chromium, till eventually at 3.84 wt pct Cr, the entire

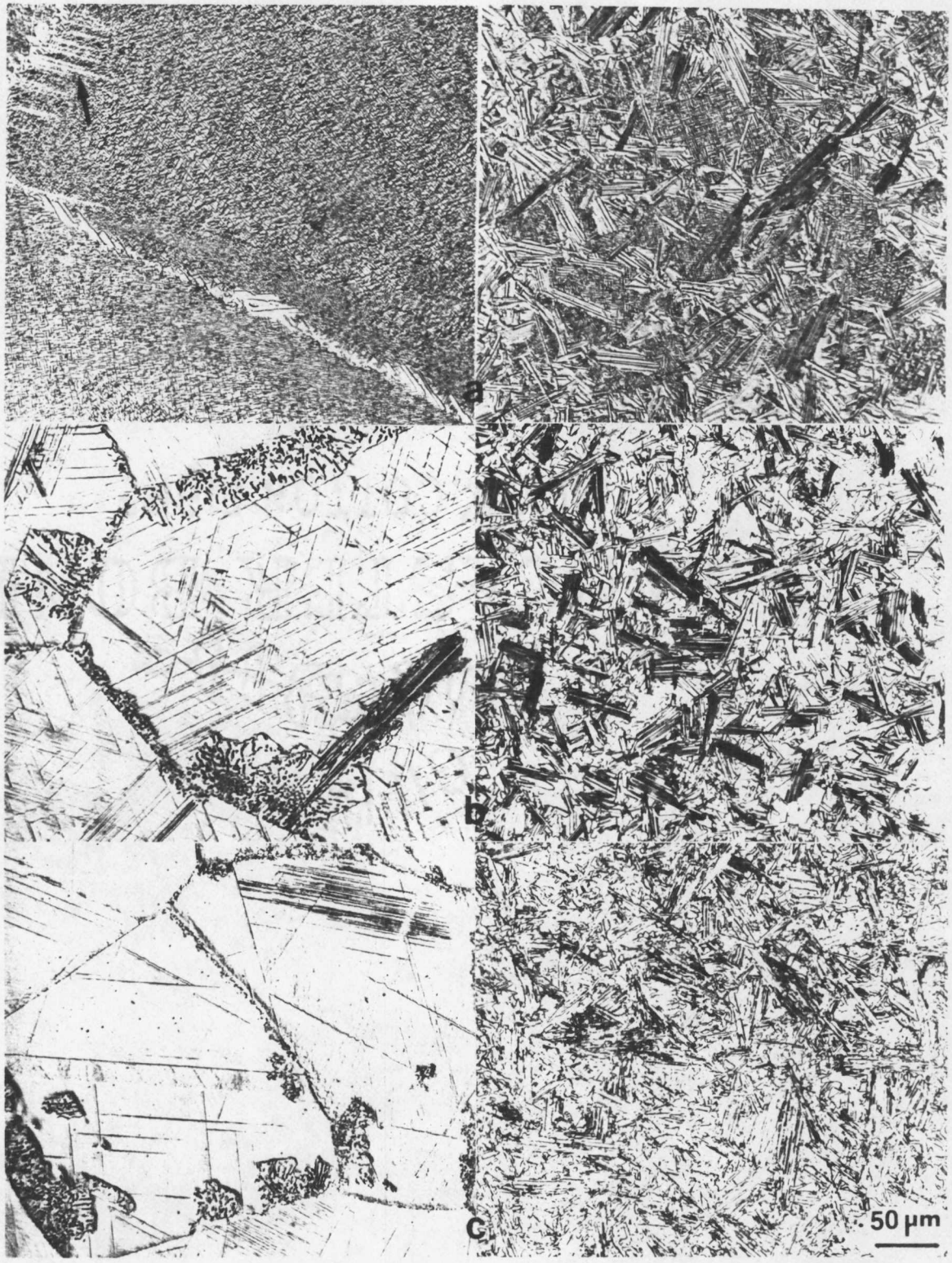


Figure IV-40. Optical micrographs showing the effect of grain size on the microstructure of Ni_4Mo-Cr alloys aged at 800°C. Aged 400 hrs. a) 2.08, b) 2.97 and c) 3.84 wt pct Cr.

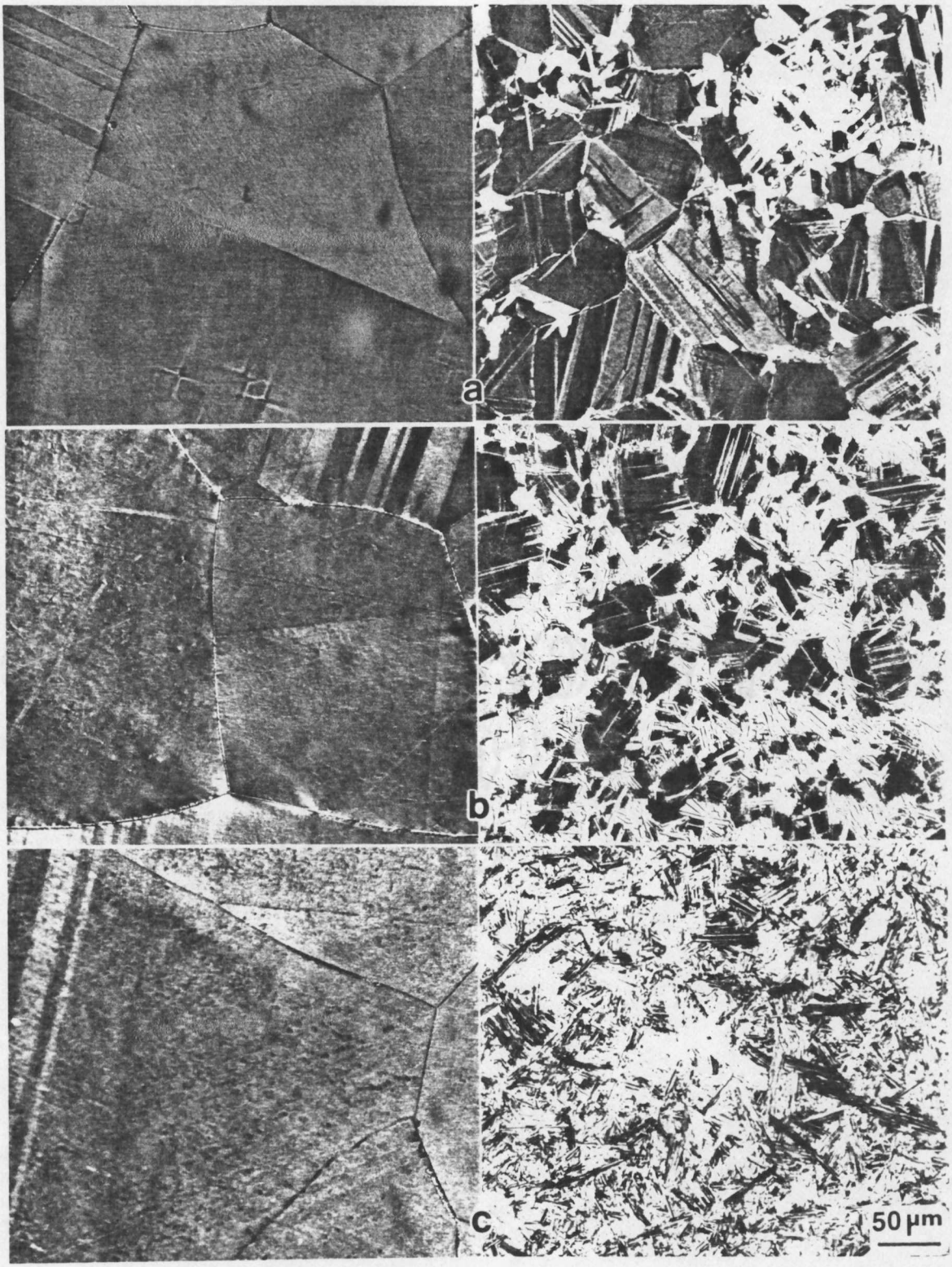


Figure IV-41. Optical micrographs showing the effect of grain size on the microstructure of Ni_4Mo-Cr alloys aged at 700°C. Aged 400 hrs. a) 2.08, b) 2.97 and c) 3.84 wt pct Cr.

microstructure is composed of Ni_3Mo plates in a SRO α matrix (Figures IV-41a, -41b, -41c).

Electron Microscopy

Identification of grain boundary precipitates in coarse-grained samples. In Chapter III (pages 172-173), the difficulties encountered in electropolishing specimens of the chromium alloys containing a high volume of grain boundary precipitates and the techniques used to produce thin foils adequate for successful identification by TEM were described. As-thinned foils were examined in a Philips EM430 at 300 KV and foils ion-milled following thinning by jet-polishing were examined in a Philips EM400 at 100 KV. One disadvantage of the ion-milling thinning operation is that it introduces bend contours in the foil, presumably due to thermal stresses. This was not a major drawback from the standpoint of particle identification. The results obtained from both methods are presented in the following.

The results of TEM observations at 300 KV for the 2.97 wt pct Cr alloy aged at 850°C for 400 hours are presented in Figures IV-42 and -43. In Figure IV-42a, a low magnification micrograph of the discontinuous precipitates sticking out at the edge of the hole in the thin foil is depicted. Figure IV-42b is a higher magnification micrograph of approximately the same region, but slightly away from the hole edge. The precipitates vary in size and are generally oval-shaped with pointed ends. The regions surrounding these particles was established by electron diffraction to be α and contained a lower molybdenum content relative to the general α matrix away from the

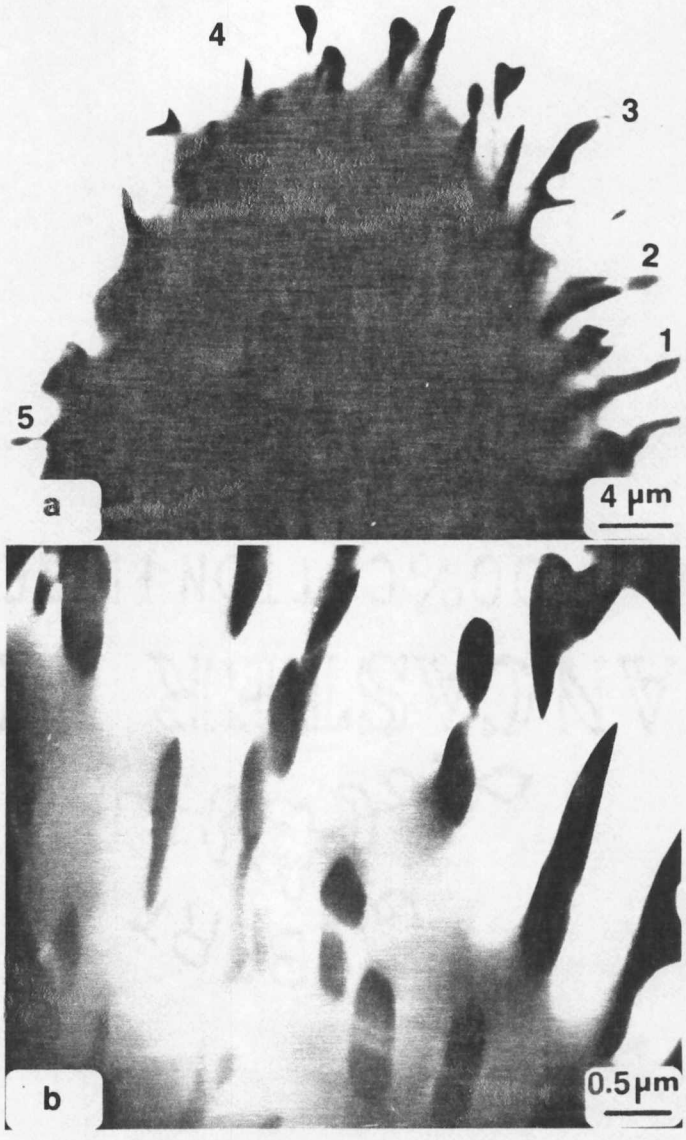
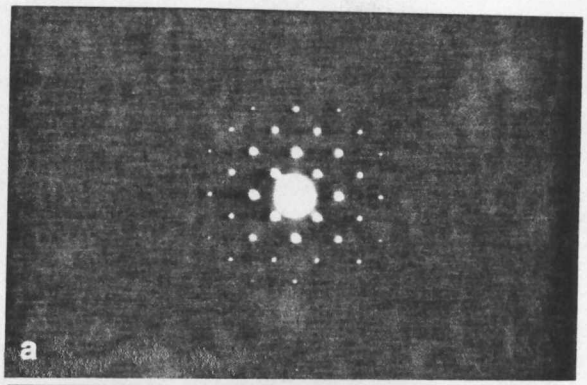
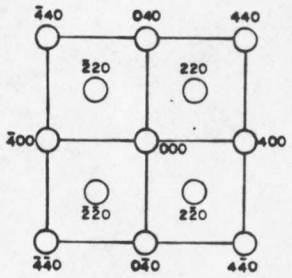


Figure IV-42. TEM micrographs of the discontinuous precipitation reaction. 2.97 wt pct Cr alloy, aged 400 hrs at 850°C. a) BF micrograph; b) BF micrograph of area near a).

grain boundaries. SAD patterns of the particles labelled 1 to 5 in Figure IV-42a are shown in Figures IV-43a-d. All the diffraction patterns could be consistently indexed in terms of a fcc lattice. The indexing of each pattern is illustrated schematically alongside; the beam directions are listed in the figure caption. To obtain accurate values for the lattice parameters (a_0) of the precipitates, the known lattice parameter of the SRO α phase (9) was used as an internal calibration standard for the camera constant (λL). The a_0 values thus calculated from each diffraction pattern and imprinted in Figure IV-43 vary slightly from 1.086 to 1.105 nm, which establishes that at least a majority of the discontinuous precipitates are eta-carbides of type M_6C or $M_{12}C$ (194,195). The absence of the {200} spots in the [001] SAD in Figure IV-43a provides positive evidence for the eta-carbides. Since there is a diamond glide d in the structure of the eta-carbide (space group Fd3m), the hk0 reflections with h + k = 4n are forbidden and they will not appear in the [001] SAD pattern (262,263). In other orientations, such as the [011] (Figure IV-43c), the {200} spots can appear due to double diffraction. An EDAX intensity spectrum obtained from particle 5 established its composition as: 51.83 at pct Ni, 46.86 at pct Mo and 1.31 at pct Cr, that is, nearly 50:50 Ni:Mo.

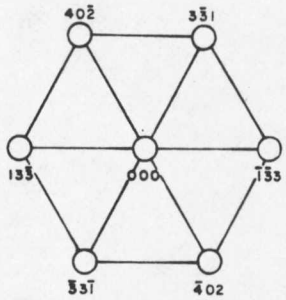
A BF micrograph of an ion-milled specimen of the 2.97 wt pct Cr alloy aged at 850^{o}C for 200 hours is shown in Figure IV-44a. Several fine precipitates can be seen parallel to annealing twin boundaries (which are traces of {111} fcc planes) as well as along the twin boundaries. A CBED pattern of the particle indicated by the arrow in Figure IV-44a is shown in Figure IV-44b. Once again, the pattern is



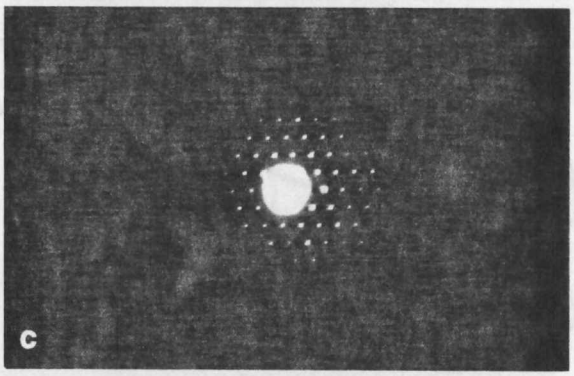


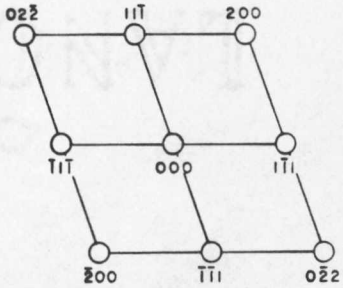
a_o= 1.103 nm



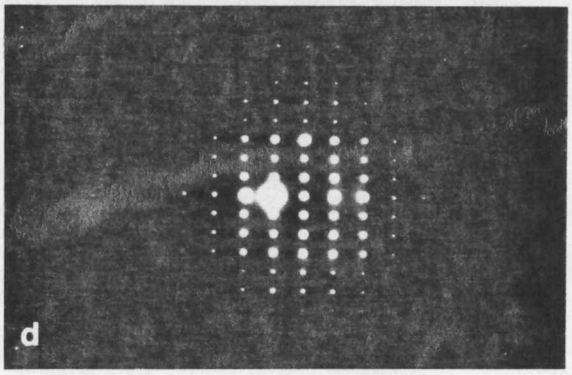


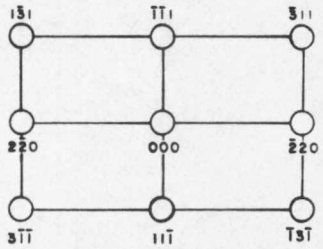
a_o= 1.086 nm





a_o= 1.1045 nm





a_o = 1.105 nm

Figure IV-43. Diffraction patterns of the precipitates labelled 1 to 5 in Figure IV-42. a) ppts. 1 and 3--[001]; b) ppt. 2--[356]; c) ppt. 4--[011]; d) ppt. 5--[112]. Lattice parameter and indexing is shown alongside each pattern.

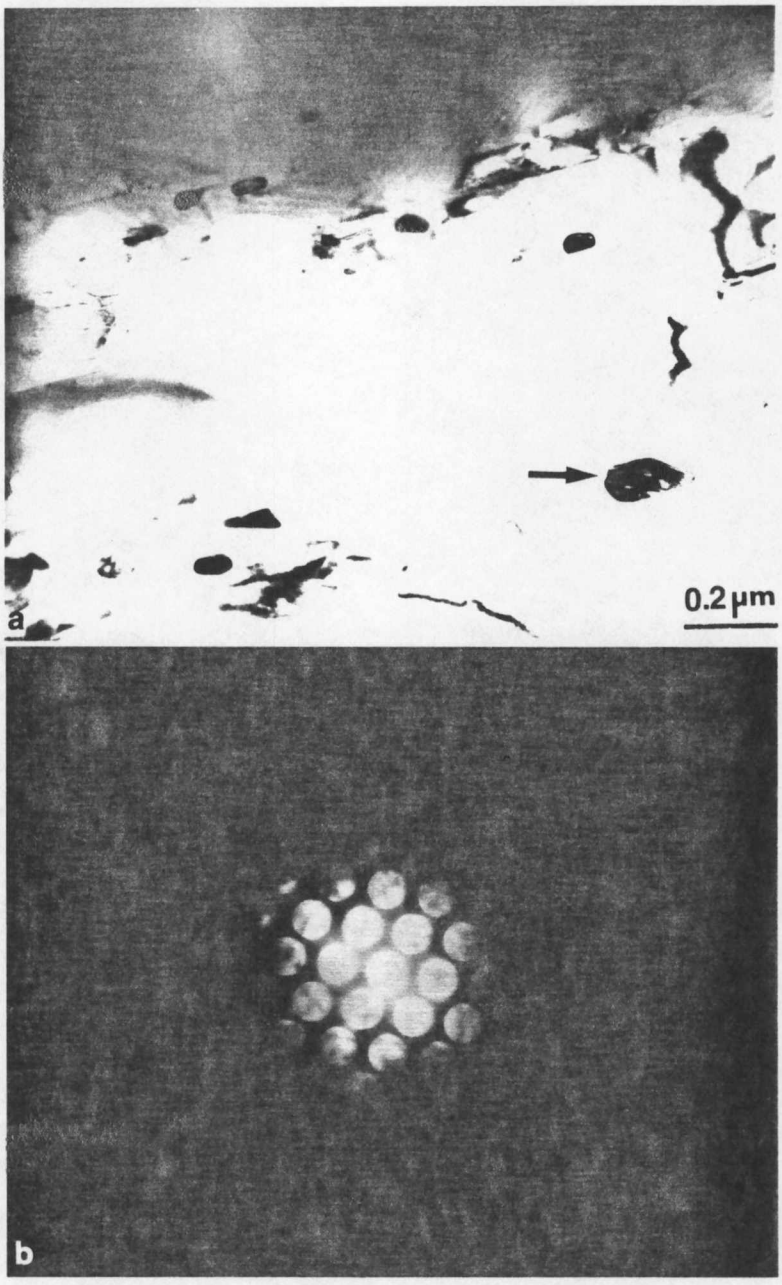


Figure IV-44. Micrographs showing precipitates on annealing twin boundaries. 2.97 wt pct Cr alloy, aged 200 hrs at 850°C. a) BF; b) [114] CBED of ppt. shown by arrow in a); a_o = 1.09 nm.

indexed easily in terms of the fcc lattice. The beam direction is [114] and a_o was calculated to be 1.09 nm, which is almost equal to the value of 1.0894 nm of the eta-carbide of type $M_{12}C$ (194). Several other particles in Figure IV-44a were similarly established from CBED patterns as eta-carbides. The composition of the precipitate in Figure IV-44a was determined as 46.98 at pct Ni, 48.01 at pct Mo and 5.01 at pct Cr, which differs appreciably in chromium levels from that of the grain boundary precipitates. This implies that the formation mechanism of the precipitates along the twin boundary may be different from that of the discontinuous precipitates.

A BF micrograph of an ion-milled specimen of the 2.08 wt pct Cr alloy aged at 800°C for 200 hours is shown in Figure IV-45. The optical microstructure revealed that the grain boundary precipitates were generally restricted to small regions around the boundaries. In Figure IV-45, several precipitates can be seen located approximately near a grain boundary, which could not be discerned due to the bending introduced by the ion-milling. A number of precipitates in Figure IV-45 were once again established by CBED analysis as eta-carbides. Representative examples for the particles labelled A and B in Figure IV-45 are shown in Figures IV-46 and -47. A [111] CBED pattern of particle A, together with its EDAX intensity spectrum are shown in Figures IV-46a and -46b. Due to the large a_o, many HOLZ's were visible, although only the FOLZ can be seen clearly in Figure IV-46a. The a_o was calculated from the pattern in Figure IV-46a and from calculations of the lattice spacing in the beam direction in CBED patterns obtained using the large condenser aperture and low camera

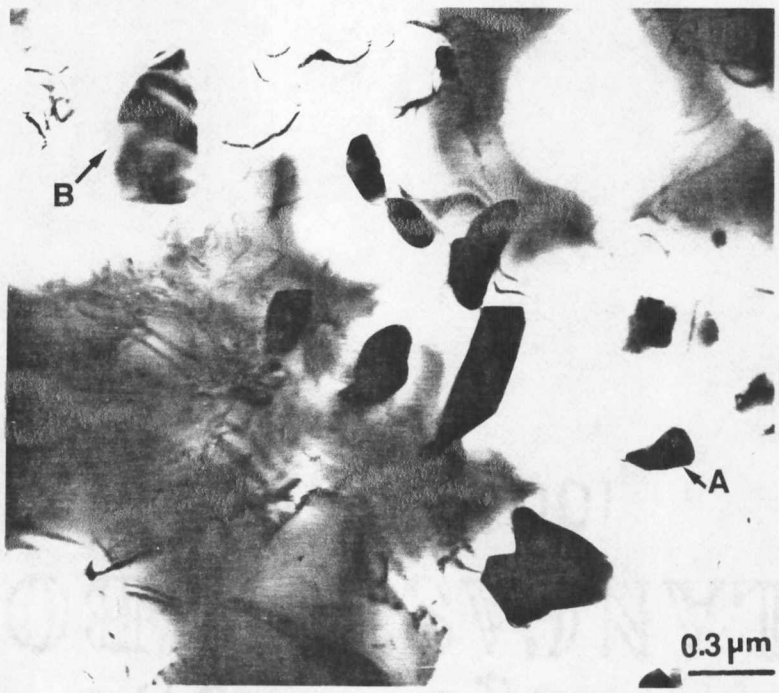
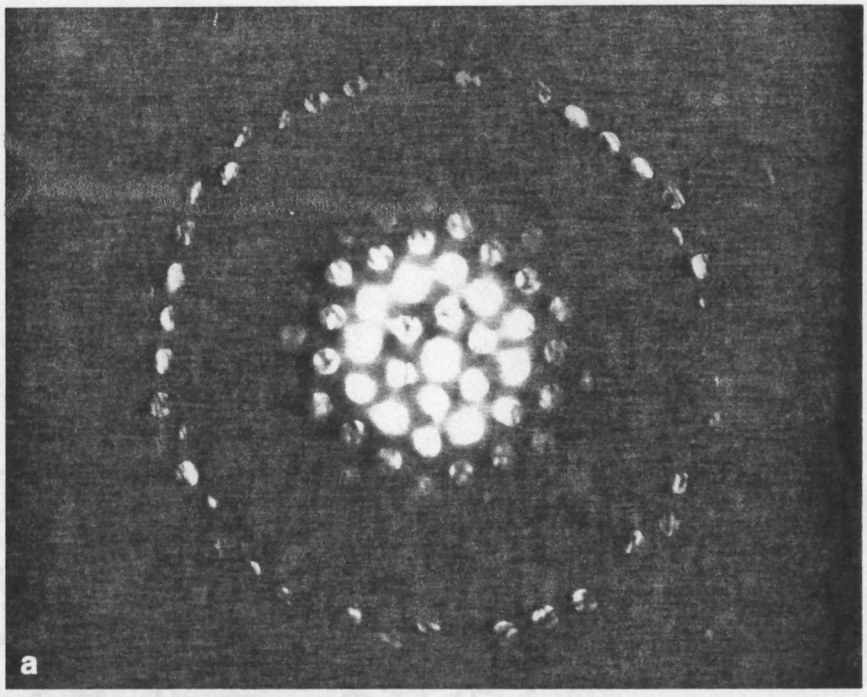
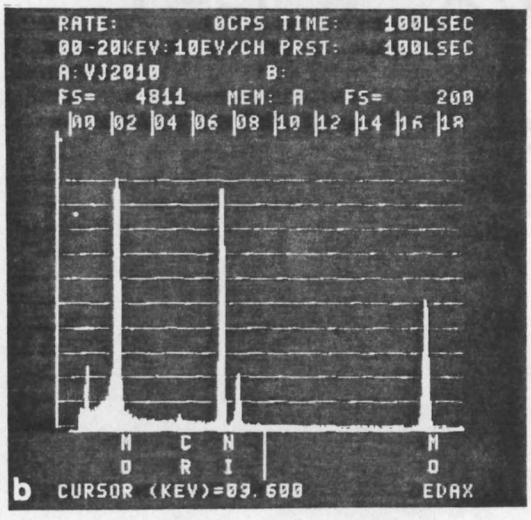


Figure IV-45. TEM micrograph of grain boundary precipitates. 2.08 wt pct Cr alloy, aged 200 hrs at 800°C, ion milled.





LATTICE PARAMETER: 1.101 NM

COMPOSITION (AT PCT): NI - 49.60

MO - 49.48

CR - 0.92

c

Figure IV-46. Diffraction and composition analyses of particle A in Figure IV-45. a) [111] CBED pattern; b) EDAX intensity spectrum; c) Lattice parameter and composition.

lengths (see Chapter III, pages 174-180 for details on the method). The a_o determined both ways were very close; the average of the two calculations (1.102 nm) together with the composition analysis are shown in Figure IV-46c.

A [011] CBED pattern of particle B in Figure IV-45 is depicted in Figure IV-47a; a SAD pattern taken by including the surrounding matrix, the corresponding EDAX intensity spectrum and calculated values of a_o and the composition are shown in Figures IV-47b, -47c and -47d respectively. These two examples once again establish that the grain boundary precipitates are eta-carbides. Indexing the spots in the SAD pattern yields the following orientation relationship between eta-carbide and the fcc phase:

$$[011]_{eta} \;//\; [111]_{fcc}$$
$$(0\bar{1}1)_{eta} \;//\; (\bar{1}10)_{fcc}$$
$$(11\bar{1})_{eta} \;//\; (\bar{1}2\bar{1})_{fcc}$$
$$(100)_{eta} \;//\; (11\bar{2})_{fcc}$$

The composition analyses (in at pct in Figures IV-46c and -47d) reveal that the precipitates are composed of nearly 50-50 Ni:Mo. In general, the particles maintain a Ni:Mo ratio of 1:1 and the chromium content in comparison is very small (<1 at pct). There is difficulty in establishing whether the precipitates observed in this study are eta-carbides of type M_6C or $M_{12}C$, since the lattice parameters of these two carbides are quite close, and moreover, are dependent on the alloy composition (194,195). Ruedl (29) has reported M_6C eta-carbides in Hastelloy B solution annealed at 1000°C, whereas Tawancy (196) has identified the $M_{12}C$ carbide in Hastelloy B-2 aged at 800°C for 100

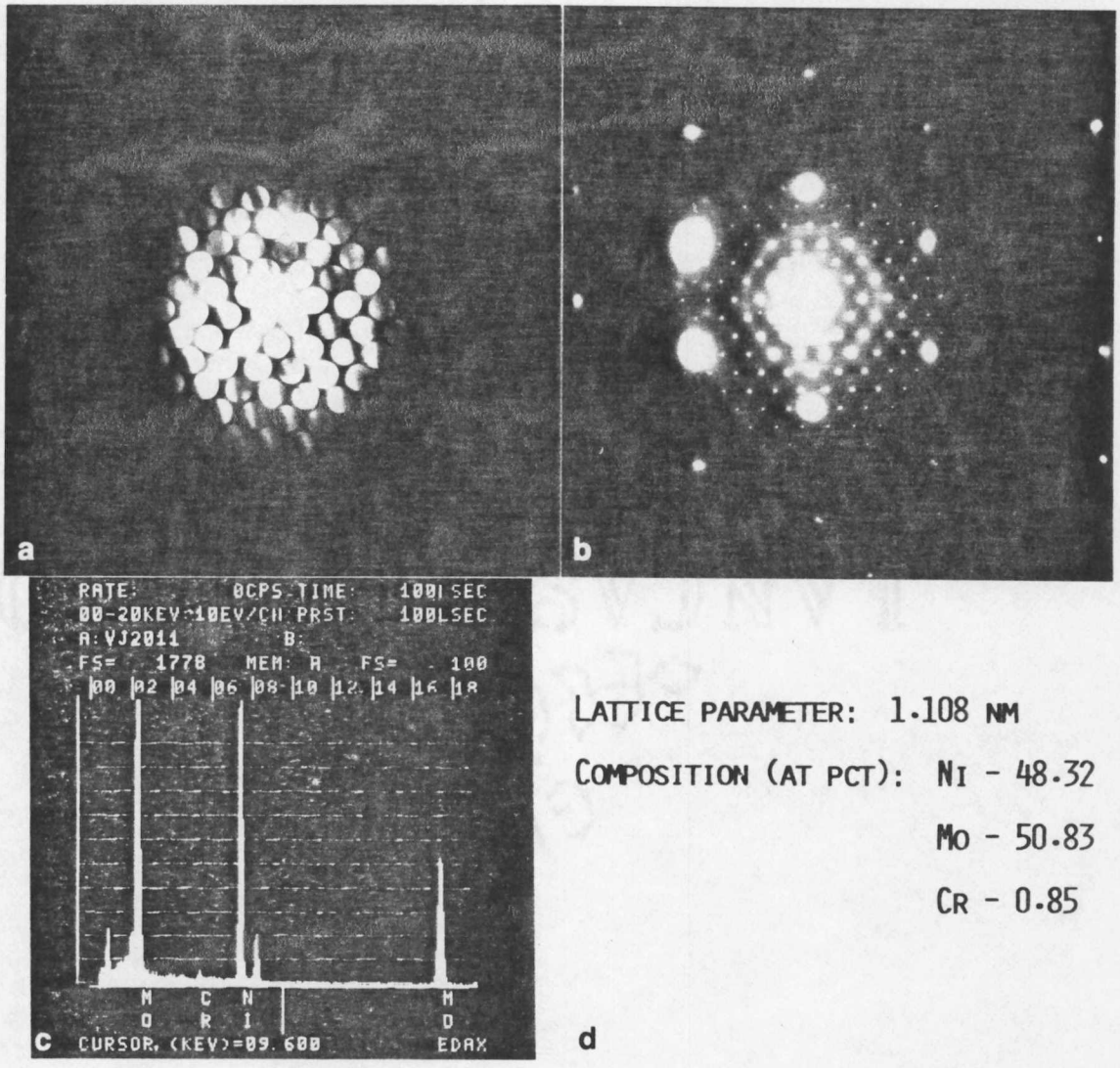


Figure IV-47. Diffraction and composition analyses of particle B in Figure IV-45. a) [011] CBED pattern; b) [011] SADP; c) EDAX intensity spectrum; d) Lattice parameter and composition.

hours. The effects of third elements on the lattice parameter of eta-carbides are not well known (264). Since it has been observed that the lattice parameter of the α phase Ni_4Mo alloys increases slightly with increasing chromium (9), it is conceivable that the presence of chromium has a similar effect on the eta-carbide. The observed a_o's of the carbides in the present study are only slightly above that for $M_{12}C$, but lower than that of M_6C. Moreover, the extent of precipitation is quite high and the carbon content of the alloys is quite low--in the range 0.008 to 0.01 wt pct (Chapter III, Table III-1, page 165). Tawancy (30) has also reported that thermal treatments at 900 and 955^oC lead to precipitation of the NiMo phase at the grain boundaries; however, this phase was not observed in any of the cases examined in this research. In view of these observations, it is believed that a major portion of the precipitates involved in the discontinuous precipitation reaction as well as those along the grain boundaries are eta-carbides of type $M_{12}C$, that is, Mo_6Ni_6C. A detailed explanation for the discontinuous precipitation reaction in Ni_4Mo-based alloys containing chromium is not sought, since their occurrence is felt to be incidental in relation to the overall transformation behavior.

In the following, the results of fine-grained specimens are presented. Other than the occurrence of the grain boundary discontinuous precipitation reaction, the types of second phases observed in the coarse-grained specimens are the same; only the volume percentage of the Ni_3Mo phase is larger and its formation is seen at shorter times. Effectively, the fine-grained specimens approach the

equilibrium condition faster. Therefore, the results for the coarse-grained samples establishing the presence of second phases such as the Ni_2Mo, DO_{22} and Ni_3Mo are not presented, although evidence for these has been obtained. The phase transformations occurring in the 2.08 wt pct Cr alloy were studied in detail at 850, 800, 700 and 600°C for aging times to 4500 hours and the results are extended to the 2.97 and 3.84 wt pct Cr alloys, which were investigated in comparatively less detail.

The schematic (001) and (112) reciprocal lattice sections identifying the relative locations of the SRO, Ni_4Mo, Ni_2Mo, and DO_{22} reflections were shown in Figures IV-36a and -36b (page 284). The (001), (100) and (010) reciprocal lattice sections for the orthorhombic Ni_3Mo were presented in Chapter II, Figure II-12 (page 52). All beam directions, unless indicated otherwise, refer to the fcc lattice. Reference should be made to these figures for correlation with electron diffraction patterns taken from regions containing one or more of the above phases.

Aging at 850°C. In all three alloys, Ni_3Mo forms at the grain boundaries. Throughout the aging period of 4500 hours, the microstructure within the grains is short-range ordered α. Only the TEM results for the 2.08 wt pct Cr alloy are presented. In 96 hours, both the DO_{22} and Ni_3Mo phases were present as large plates at the grain boundaries. The Ni_3Mo formed directly from the DO_{22}. Two twin variants of Ni_3Mo are identified as 1 and 2 in Figure IV-48a relative to the corresponding diffraction pattern in Figure IV-48b. The diagonal band

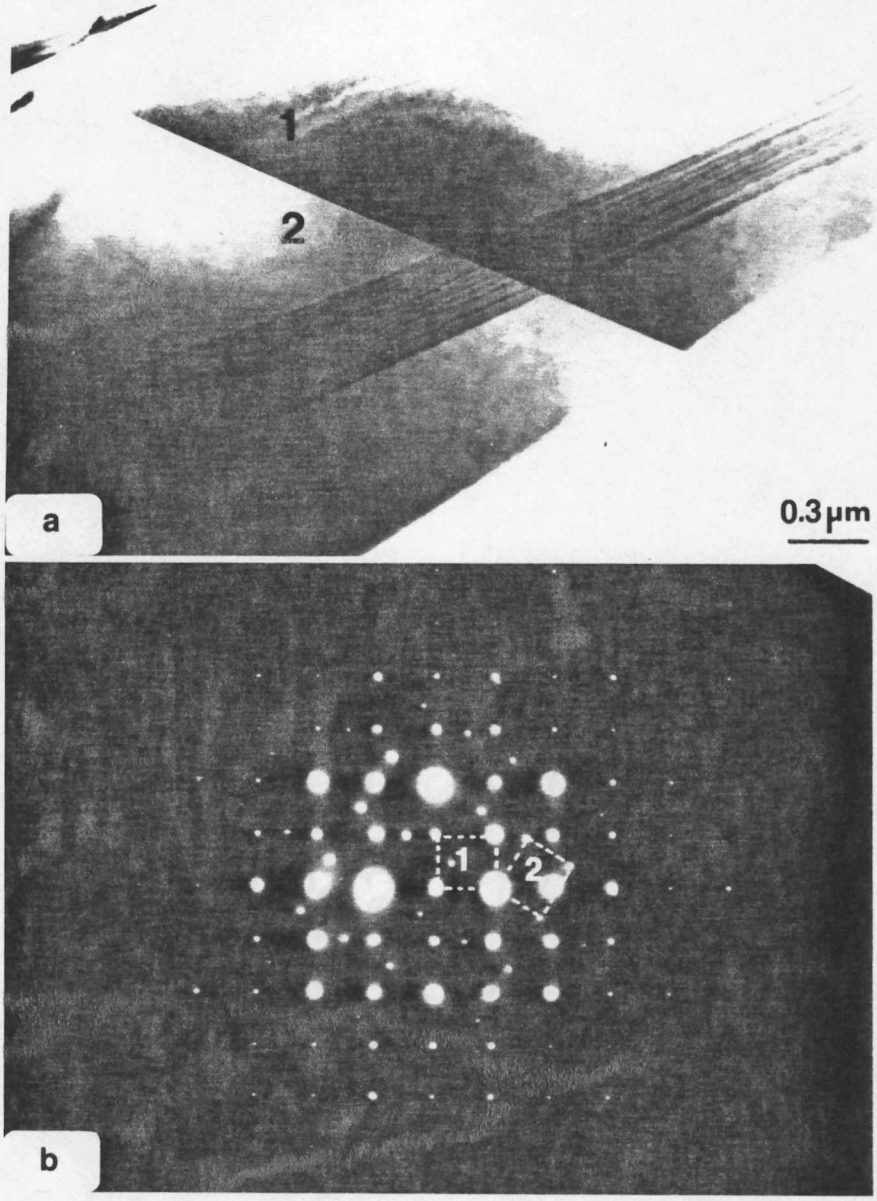


Figure IV-48. Micrographs of the 2.08 wt pct Cr alloy aged at 850°C. Aged 96 hrs. a) BF of two Ni_3Mo twins labelled 1 and 2 relative to the $[100]_\gamma$ SADP in b) (dashed lines outline the two variants of Ni_3Mo).

in Figure IV-48a, although not positively identified, is probably a stacking fault. With time, additional formation of Ni_3Mo occurred at the grain boundaries.

Aging at 800°C. In the 2.08 wt pct Cr alloy, within 16 hours, the DO_{22} phase forms (Figure IV-49a); domains of Ni_4Mo in a SRO matrix surrounding the DO_{22} were also present. The DO_{22} phase usually develops as multiple or single striations parallel to annealing twin boundaries, which are traces of {111} fcc planes; these subsequently transform to Ni_3Mo. An example of such a transformation to Ni_3Mo is illustrated in Figures IV-49b-d. The diffraction pattern in Figure IV-49c (indexed in Figure IV-49d) shows reflections from Ni_3Mo as well as those from the fcc lattice. The DF micrograph (Figure IV-49b) taken from the encircled Ni_3Mo spot in Figure IV-49c images Ni_3Mo domains aligned along bands; the intervening dark regions between bands are fcc. The diffraction pattern also shows intense streaking in the $[11\bar{1}]_{fcc}$ ($[010]_\gamma$) direction, which is normal to the thin dimension of the plates. The orientation relationship between the Ni_3Mo and the fcc lattice is confirmed (125) as:

$$[100]_\gamma \;//\; [011]_{fcc}$$
$$(010)_\gamma \;//\; (11\bar{1})_{fcc}$$
$$(001)_\gamma \;//\; (\bar{2}1\bar{1})_{fcc}$$

Coexistence of the DO_{22} and Ni_3Mo phases (Figures IV-50a-b) provided further evidence for the direct transformation from DO_{22} to Ni_3Mo. The dark field micrograph in Figure IV-50a was obtained from the $(1\bar{2}\ \bar{1}\ 0)$ DO_{22} spot, whereas that in Figure IV-50b was obtained

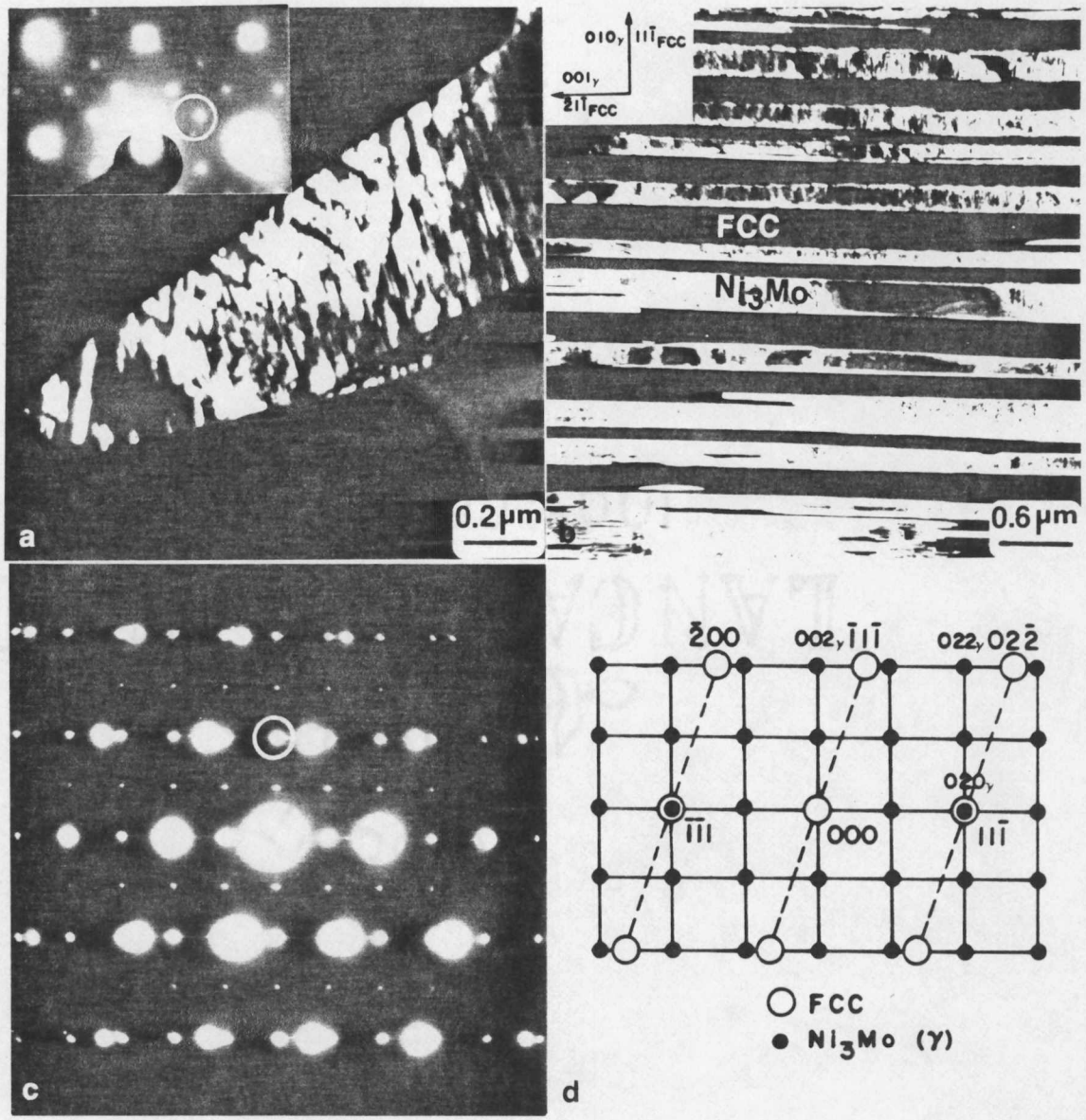


Figure IV-49. Micrographs showing DO_{22} and Ni_3Mo in the 2.08 wt pct Cr alloy aged at 800°C. a) 16 hrs--DF from DO_{22} spot encircled in the inset [001] SADP; b) 96 hrs--DF from Ni_3Mo spot encircled in the $[100]_\gamma//[011]_\alpha$ SADP in c); d) Indexing of of c) (dashed and solid lines outline the fcc and Ni_3Mo spots, respectively).

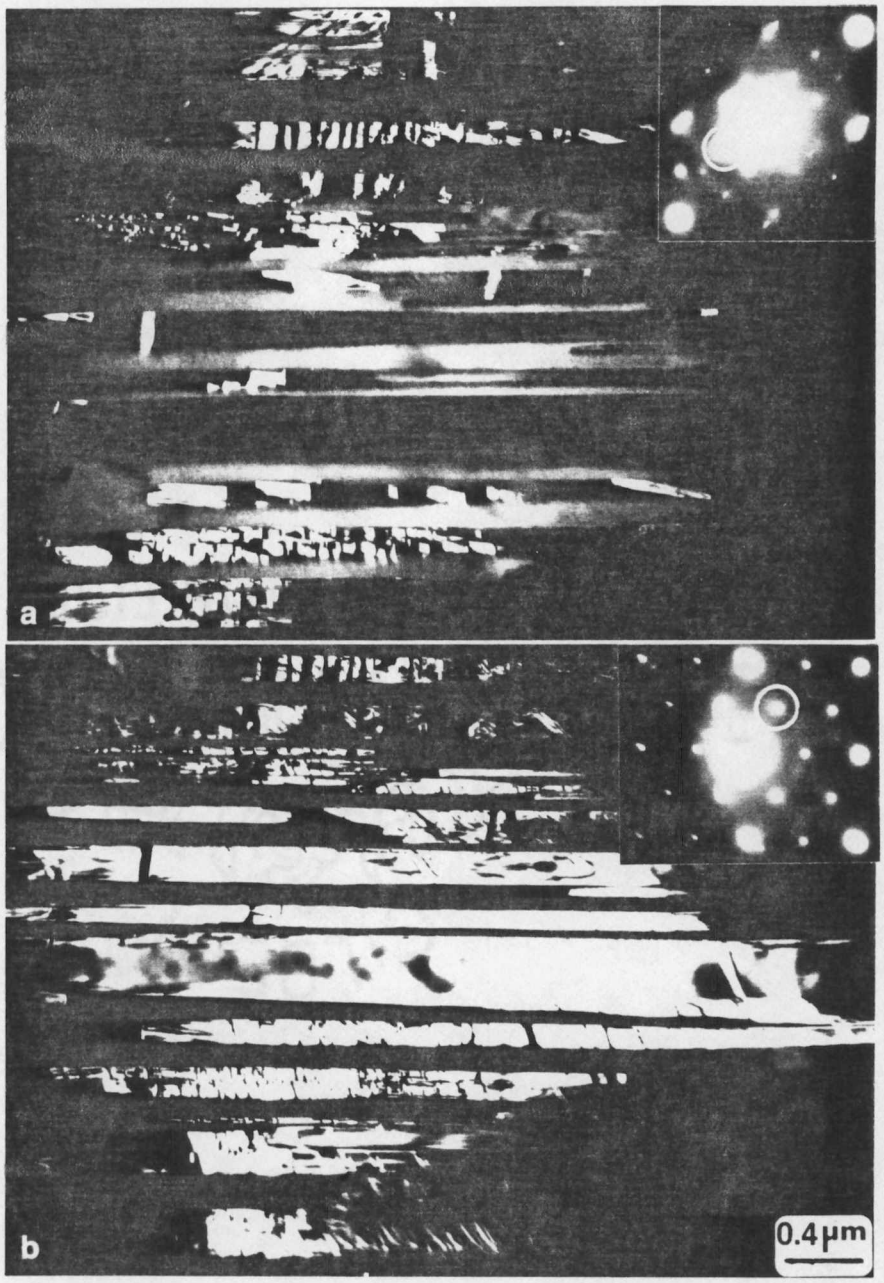


Figure IV-50. Micrographs showing the coexistence of DO_{22} and Ni_3Mo in the 2.08 wt pct Cr alloy aged at 800°C. Aged 400 hrs.
a) DF from DO_{22} spot encircled in the inset [001] SADP;
b) DF from Ni_3Mo spot encircled in the inset $[010]_\gamma$ SADP.

from the (101) Ni_3Mo spot (see inset diffraction patterns). There was also evidence for the formation of Ni_3Mo as a secondary coarsening reaction at the grain boundaries as shown in the Figures IV-51a and IV-51b for a sample aged for 4500 hours. In the BF and DF micrographs in Figures IV-51a and -51b, strips of remnant fcc material (indicated by arrows) are present within the Ni_3Mo as confirmed by additional fcc spots (indicated by arrows) in the inset $[100]_\gamma$ SAD pattern.

The Ni_4Mo domains are generally lenticular in shape when the c-axis of the domains lies in the plane of observation, and are rectangular-shaped when the c-axis is normal to this plane, as shown in the BF image in Figures IV-52a for a sample aged for 96 hours. An example of the domain morphology at other orientations is shown in Figures 52b (note the presence of SRO in the inset [112] SADP). These observations confirm the three dimensional model proposed (8,171) for single domains of Ni_4Mo. With time, the Ni_4Mo domains coarsened into rectangular blocks (Figure 53a), indicating that the lenticular shape of the domains is a transient morphology. However, none of these domains are orientated for diffraction (see inset [001] SAD pattern). Thin bands of the DO_{22} are also present in Figure IV-53a. The domains within these bands are shown in the DF image in Figure IV-53b taken from the encircled (110) DO_{22} spot in the inset SAD pattern.

In the 2.97 and 3.84 wt pct Cr alloys, no Ni_4Mo is observed at any stage of aging. Instead, groups of DO_{22} domains form parallel to {111} fcc planes. Examples of the DO_{22} structure are shown in the BF and DF images in Figures IV-54a-b for the 2.97 wt pct Cr alloy aged for 4500 hours. Similar to the behavior of the 2.08 wt pct Cr alloy,

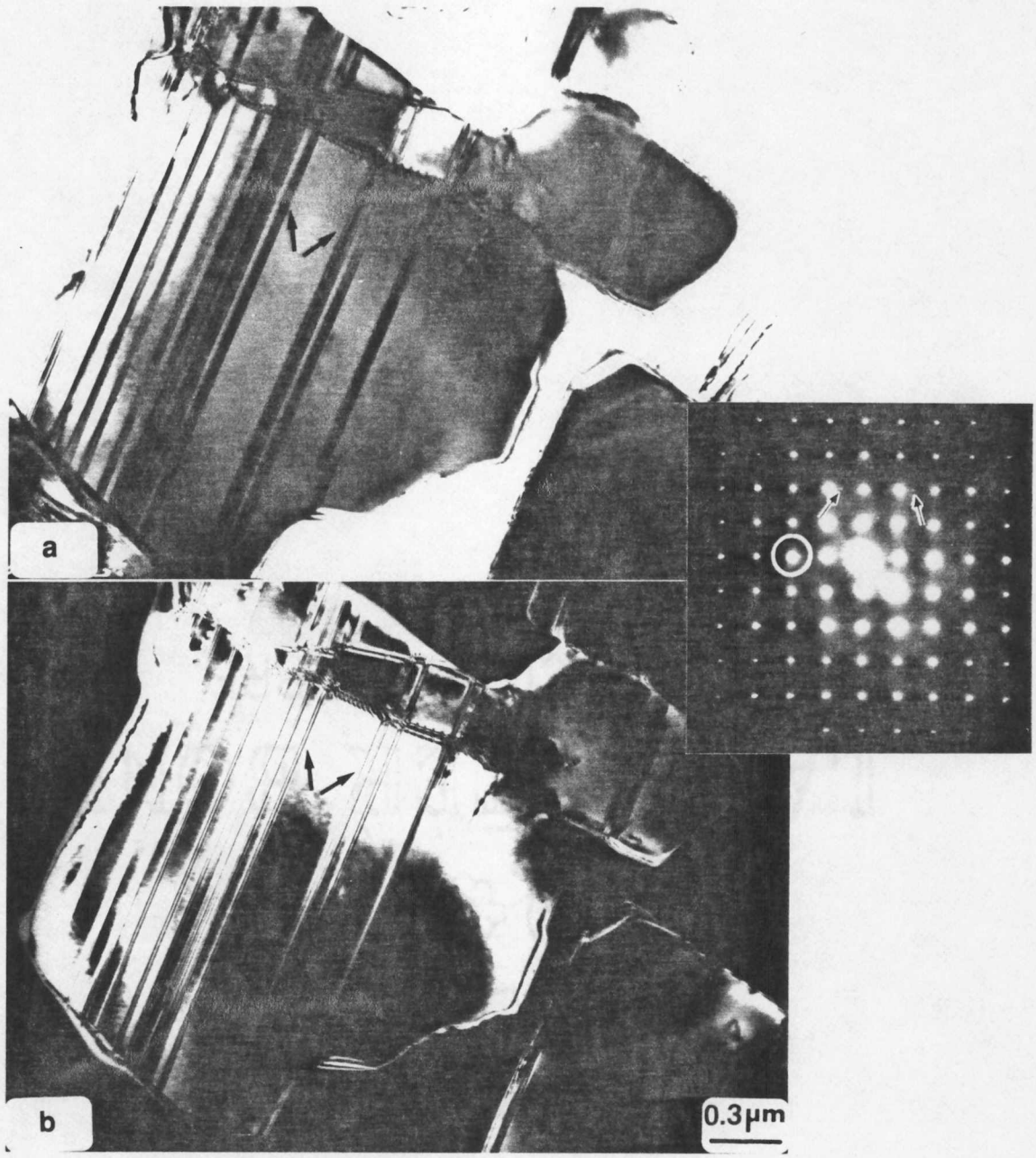


Figure IV-51. Micrographs showing the secondary coarsening reaction of Ni_3Mo at grain boundaries in the 2.08 wt pct Cr alloy aged at 800°C. Aged 4500 hrs. a) BF; b) DF from Ni_3Mo spot encircled in the inset $[100]_\gamma$ SADP.

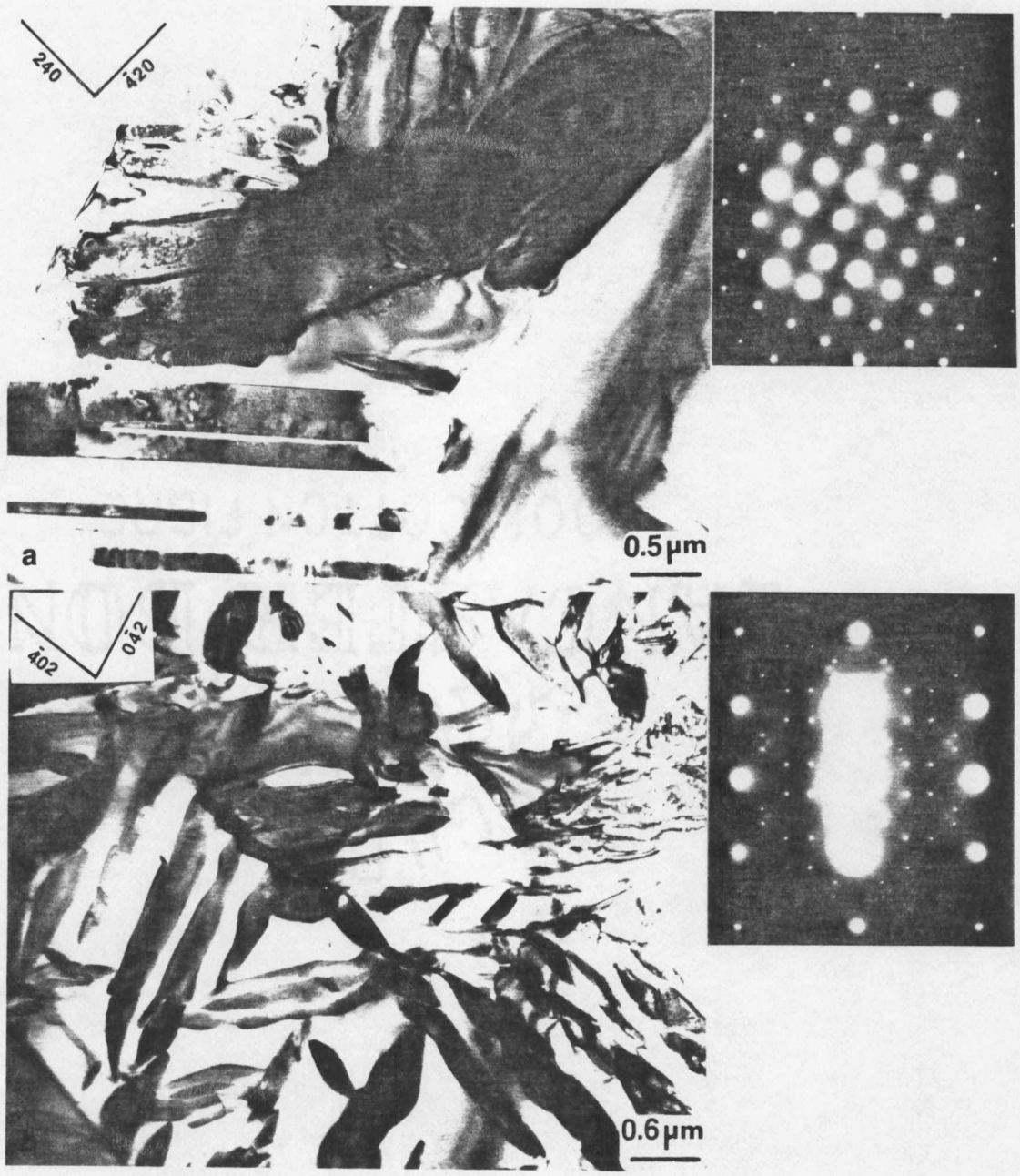


Figure IV-52. Micrographs showing the morphology of Ni_4Mo domains in the 2.08 wt pct Cr alloy aged at 800°C. Aged 96hrs. a) BF (inset [001] SADP); b) BF (inset [112] SADP).

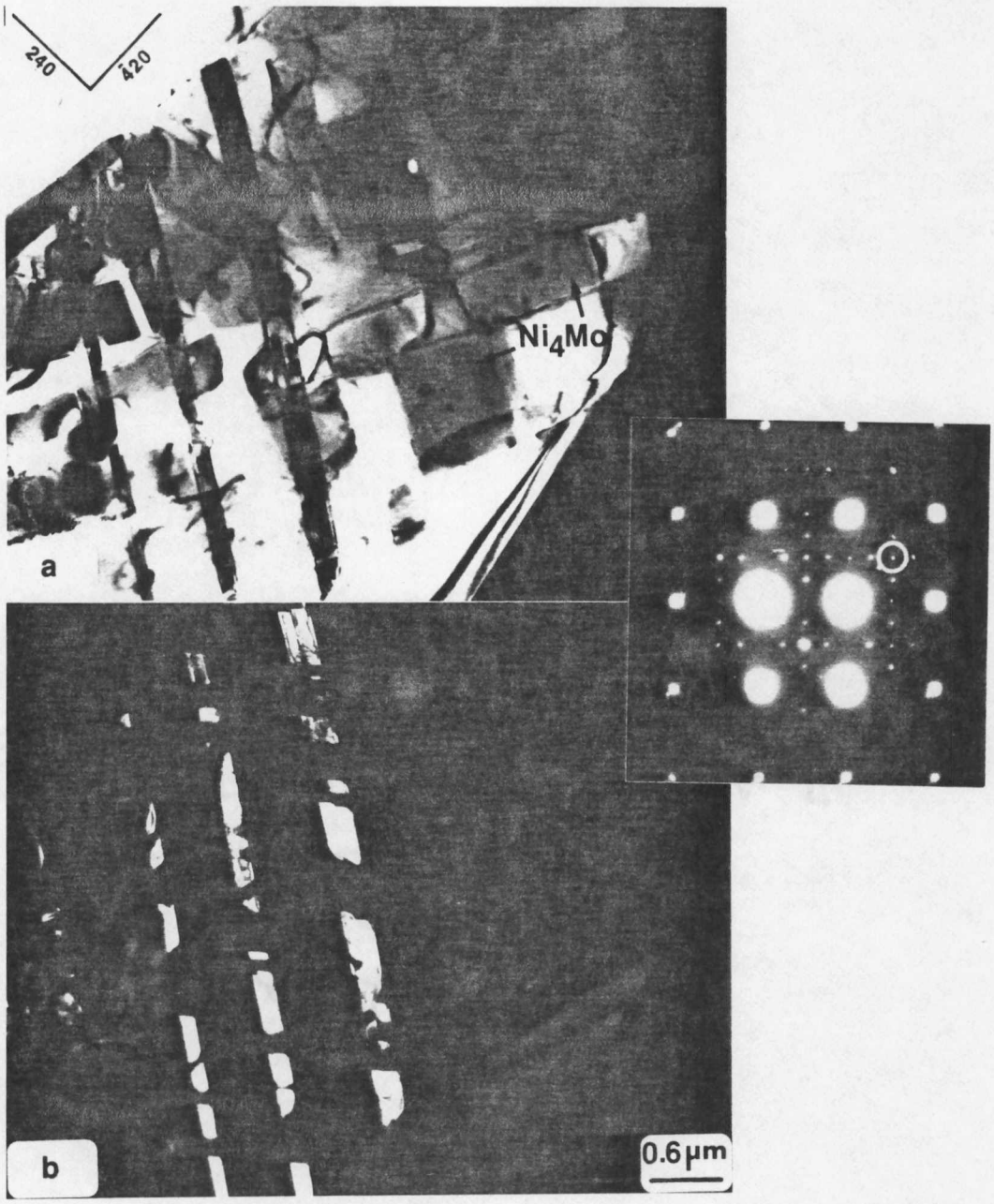


Figure IV-53. Micrographs showing the change in morphology of Ni_4Mo domains in the 2.08 wt pct Cr alloy aged for longer times at 800°C. Aged 4500 hrs. a) BF; b) DF from DO_{22} spot encircled in the inset [001] SADP.

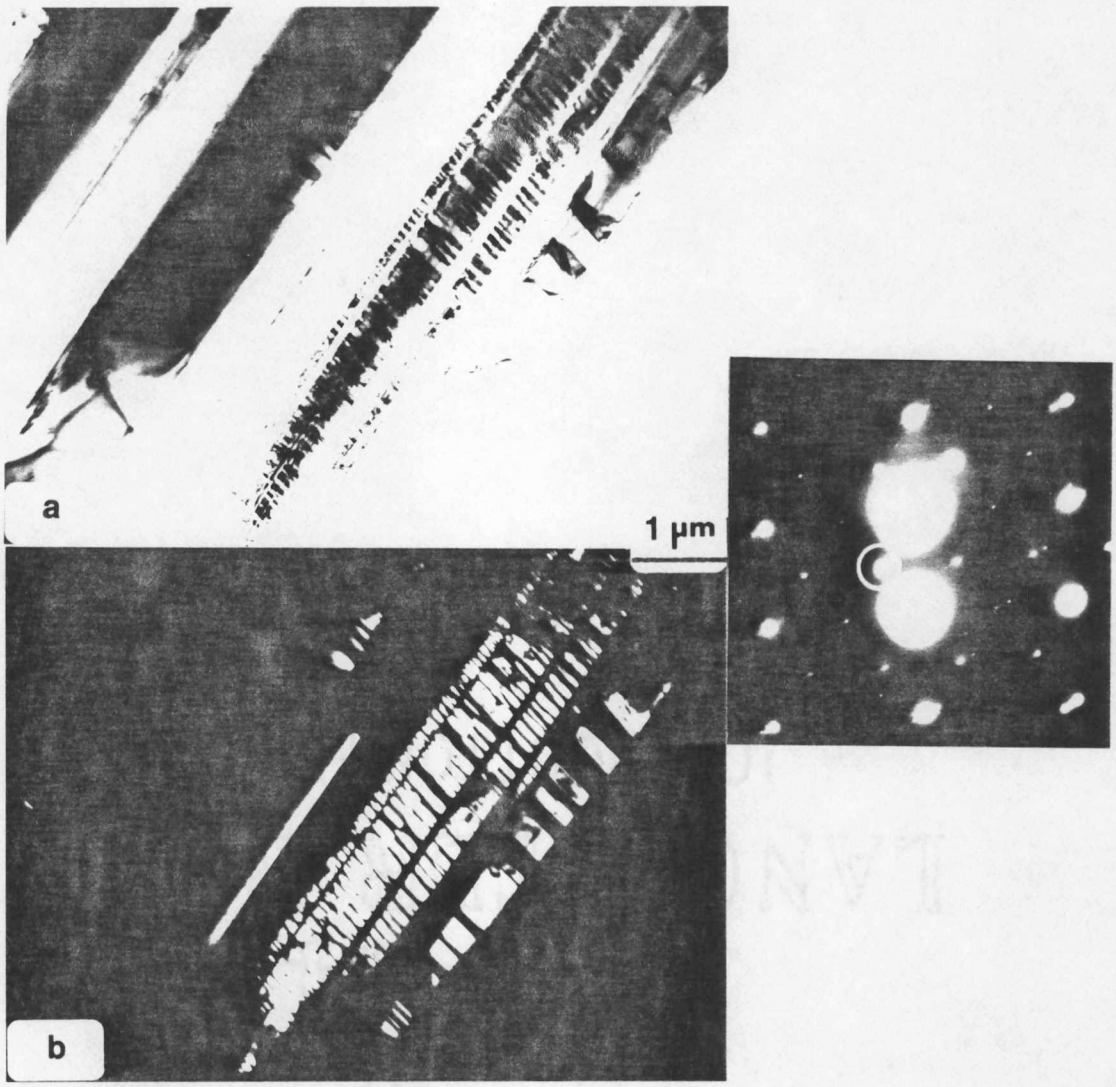


Figure IV-54. Micrographs illustrating the DO_{22} structure in the 2.97 wt pct Cr alloy aged at 800°C. Aged 4500 hrs. a) BF; b) DF from DO_{22} spot encircled in the inset [112] SADP.

the DO_{22} phase transforms directly to Ni_3Mo. This is shown in the DF image, Figure IV-55a, obtained from the encircled $(020)_\gamma$ fundamental spot in the $[100]_\gamma$ SAD pattern in Figure IV-55b (indexed in IV-55c). The SAD pattern reveals Ni_3Mo spots together with twin-related fcc spots. Such patterns have been reported by Yamomoto et al. (125) in the binary Ni_3Mo alloy. In Figure IV-55a, the Ni_3Mo plates are separated by fcc plates; the fcc plates on both sides of a Ni_3Mo plate are in twin relationship, as confirmed by DF images obtained from the fcc twin spots in Figure IV-55b. The behavior of the 3.84 wt pct Cr alloy is the same as that of the 2.97 wt pct Cr alloy. A BF micrograph and the associated $[100]_\gamma$ SAD pattern obtained from a specimen of this alloy aged for 4500 hours, showing parallel plates of Ni_3Mo with intervening fcc regions, is depicted in Figures IV-56a and -56b. In this case, only one set of fcc spots are present; the twin reflections are absent (Figure IV-56b). The orientation relationship between the Ni_3Mo and fcc is once again confirmed as that stated earlier in relation to the 2.08 wt pct Cr alloy (page 307).

Aging at 700°C. The transformation behavior is somewhat more complicated at this temperature. In the 2.08 wt pct Cr alloy, within 16 hours, both Ni_4Mo and Ni_2Mo develop, as evident in the [112] SAD pattern in Figure IV-57. Moreover, diffuse streaks are observed extending from one Ni_4Mo position to the neighboring one along the <420> direction and passing through the Ni_2Mo and SRO positions. Similar streaking has been reported in Ni_3Mo-based ternary alloys and is a manifestation of continuous (spinodal) ordering (265,266).

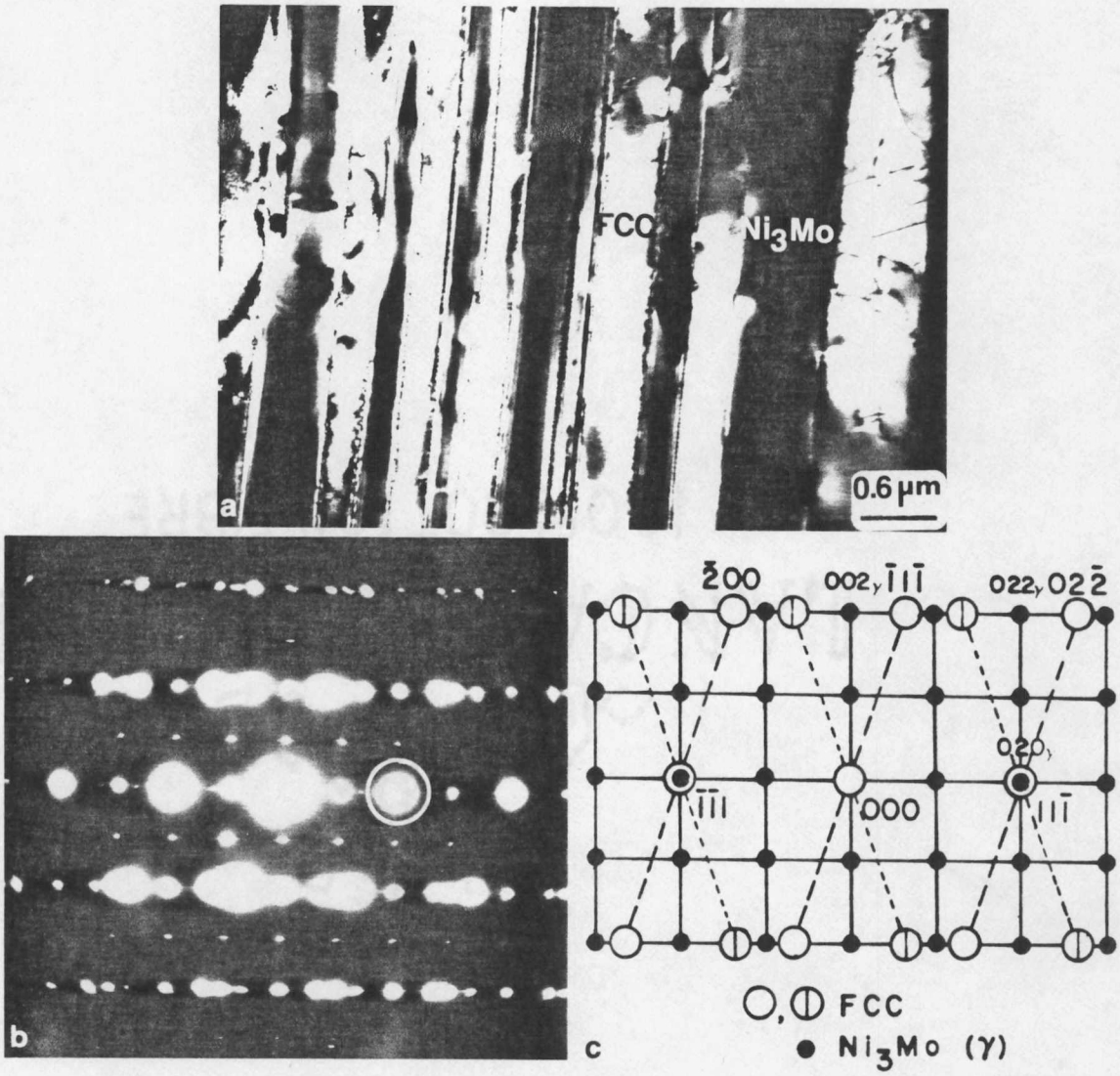


Figure IV-55. Micrographs showing the formation of Ni_3Mo in the 2.97 wt pct Cr alloy aged at 800°C. Aged 4500 hrs. a) DF from Ni3Mo fundamental spot encircled in the $[100]_\gamma//[011]_\alpha$ SADP in b); c) Indexing of b).

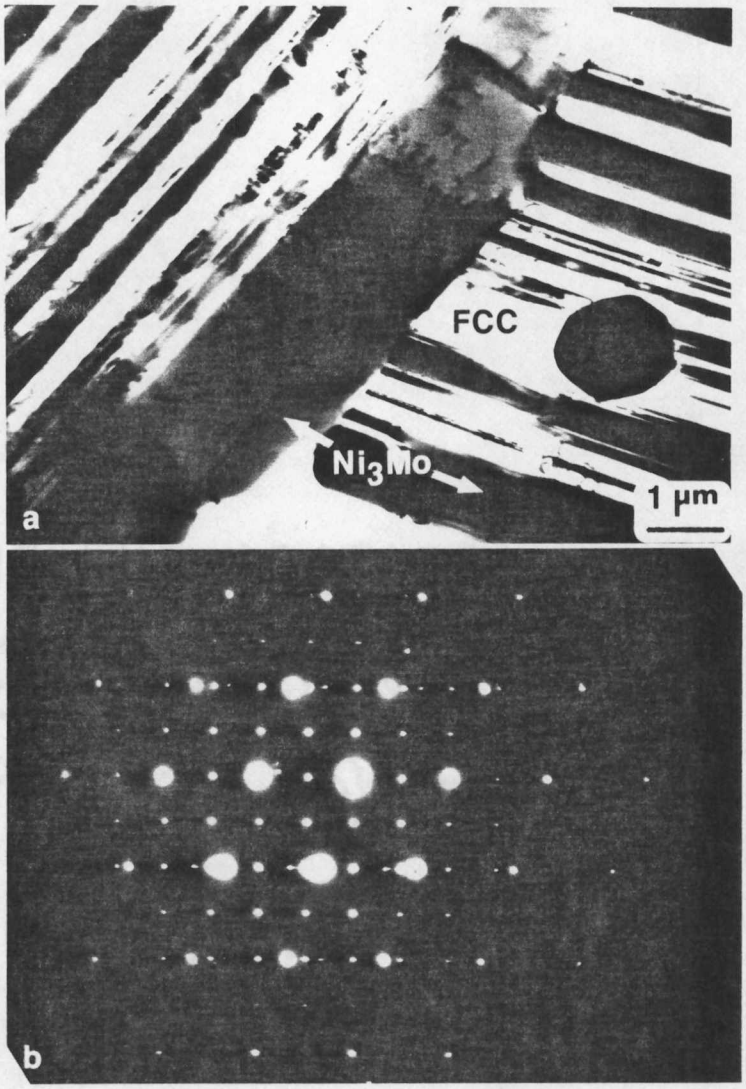


Figure IV-56. Micrographs showing the formation of Ni_3Mo in the 3.84 wt pct Cr alloy aged at 800°C. Aged 4500 hrs. a) BF; b) $[100]_\gamma//[011]_\alpha$ SADP of region to the right in a).

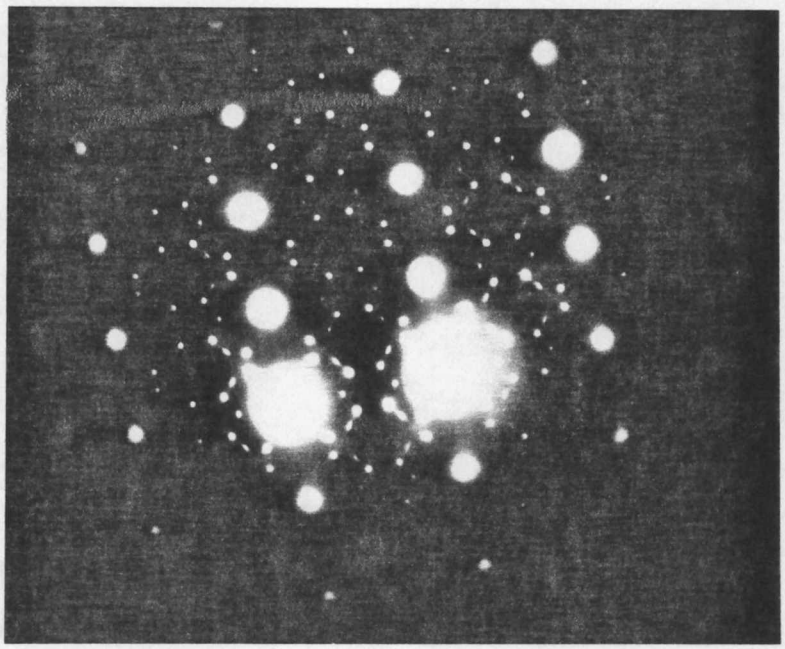


Figure IV-57. [112] SADP of the 2.08 wt pct Cr alloy aged at 700^{o}C for 16 hrs.

At 400 hours, the DO_{22} phase forms as thin striations parallel to {111} fcc planes. Examples of the morphology of different phases present at this time are shown in Figures IV-58a-d. In the inset [001] diffraction pattern, the DO_{22} spots are streaked in the [110] direction, which is the direction for the traces of {111} fcc planes. Examination at other orientations, such as the [112], showed similar streaking in the <111> direction. This streaking is normal to the thin dimension of the DO_{22} and confirms that it forms parallel to {111} fcc planes. There was evidence that the DO_{22} phase formed from bands containing Ni_4Mo and Ni_2Mo; these bands, which were parallel to {111} fcc planes, often appeared in a twin relation relative to the parent matrix. The Ni_4Mo domains appear rectangular and crystallographic (Figure IV-58b), and moreover, neighboring domains are separated by Ni_2Mo precipitates. The inset SAD pattern also shows streaking of the Ni_2Mo spots in the <420> direction. This streaking is caused by the plate-like shape of the Ni_2Mo precipitates (Figure IV-58c). The grain boundary reaction leading to the formation of large Ni_4Mo domains observed in the binary Ni_4Mo occurred to a limited extent in this alloy. Some of these regions had transformed to Ni_3Mo. This feature is described later.

The microstructures at later times (4500 hours) provided considerable insight into the formation mechanisms of different phases. Many subtle diffraction effects occur. The BF micrograph in Figure IV-59a shows Ni_2Mo precipitates in several orientations in a Ni_4Mo (light) matrix. A DF image, Figure IV-59b, from the Ni_2Mo spot encircled in the [001] diffraction pattern in Figure IV-59c images

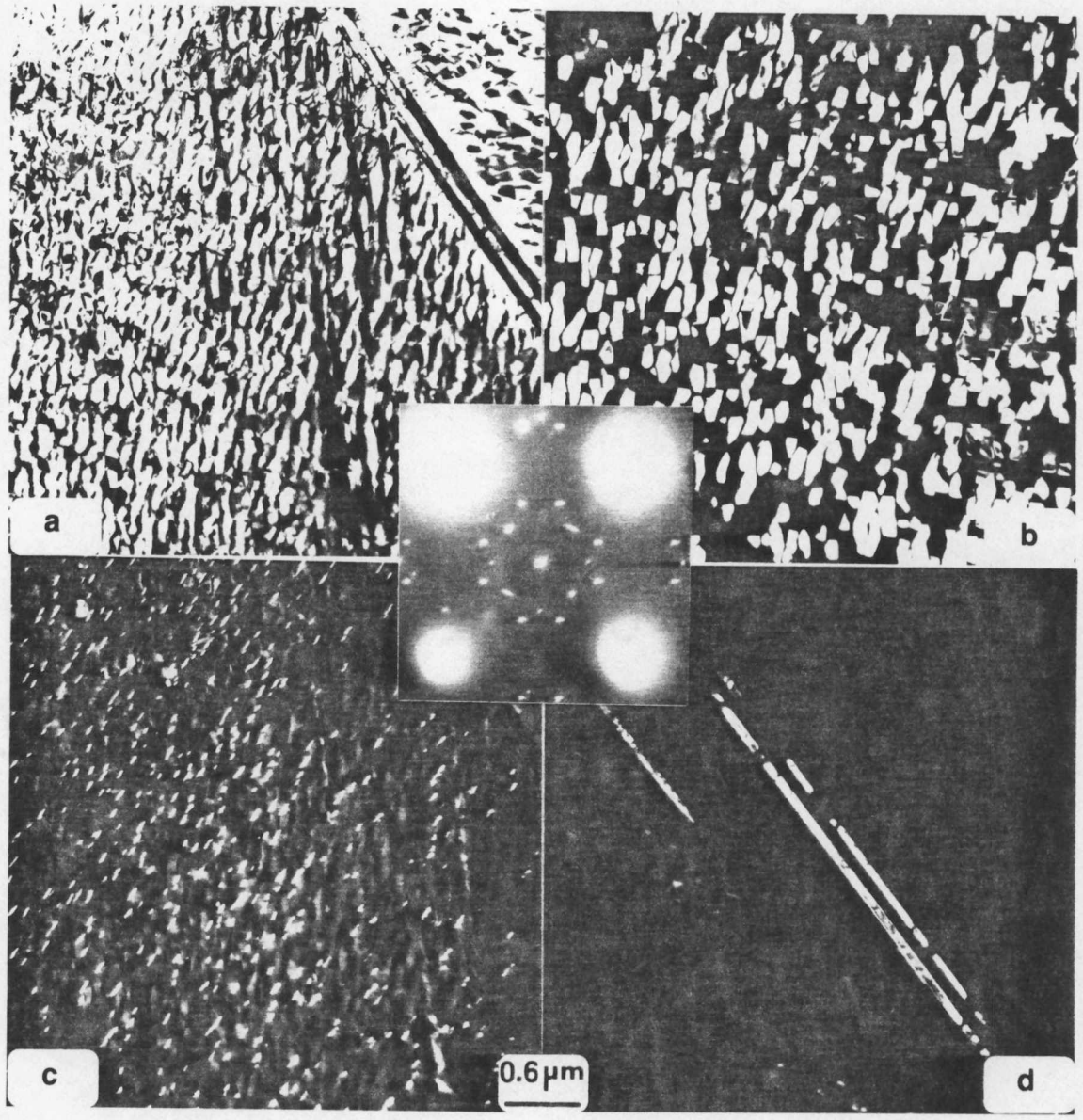


Figure IV-58. Microstructures of the 2.08 wt pct Cr alloy aged at 700°C for intermediate aging times. Aged 400 hrs. a) BF micrograph; b), c), and d) are respectively DF micrographs from Ni_4Mo, Ni_2Mo and DO_{22} spots. The [001] SADP is shown an inset.

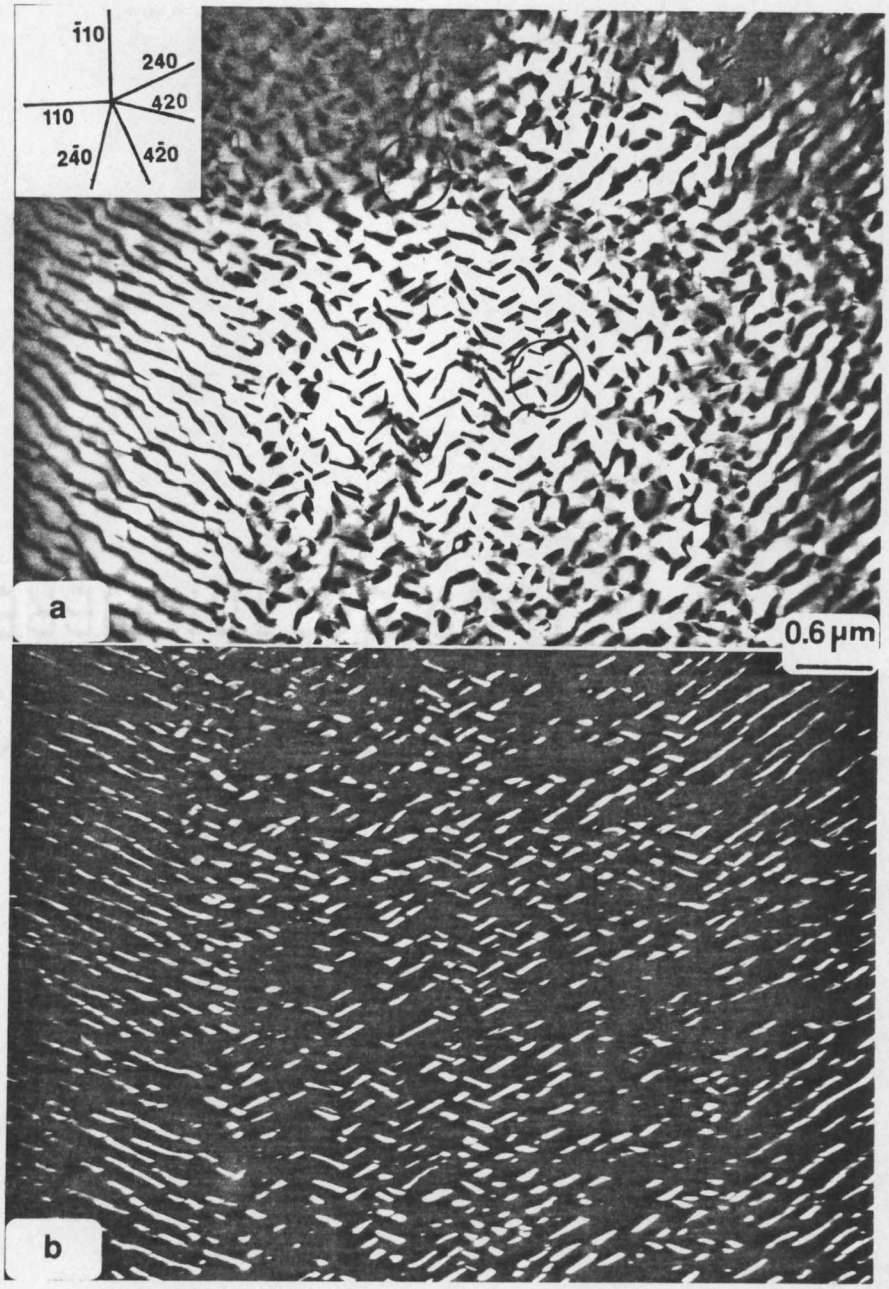


Figure IV-59. Micrographs showing the morphologies of Ni_4Mo and Ni_2Mo in the 2.08 wt pct Cr alloy aged at 700°C. Aged 4500 hrs. a) BF of Ni_2Mo precipitates in Ni_4Mo (light) matrix; b) DF from Ni_2Mo spot encircled in c); c), d), and e) Are respectively [001), [011] and [112] SADP's of a).

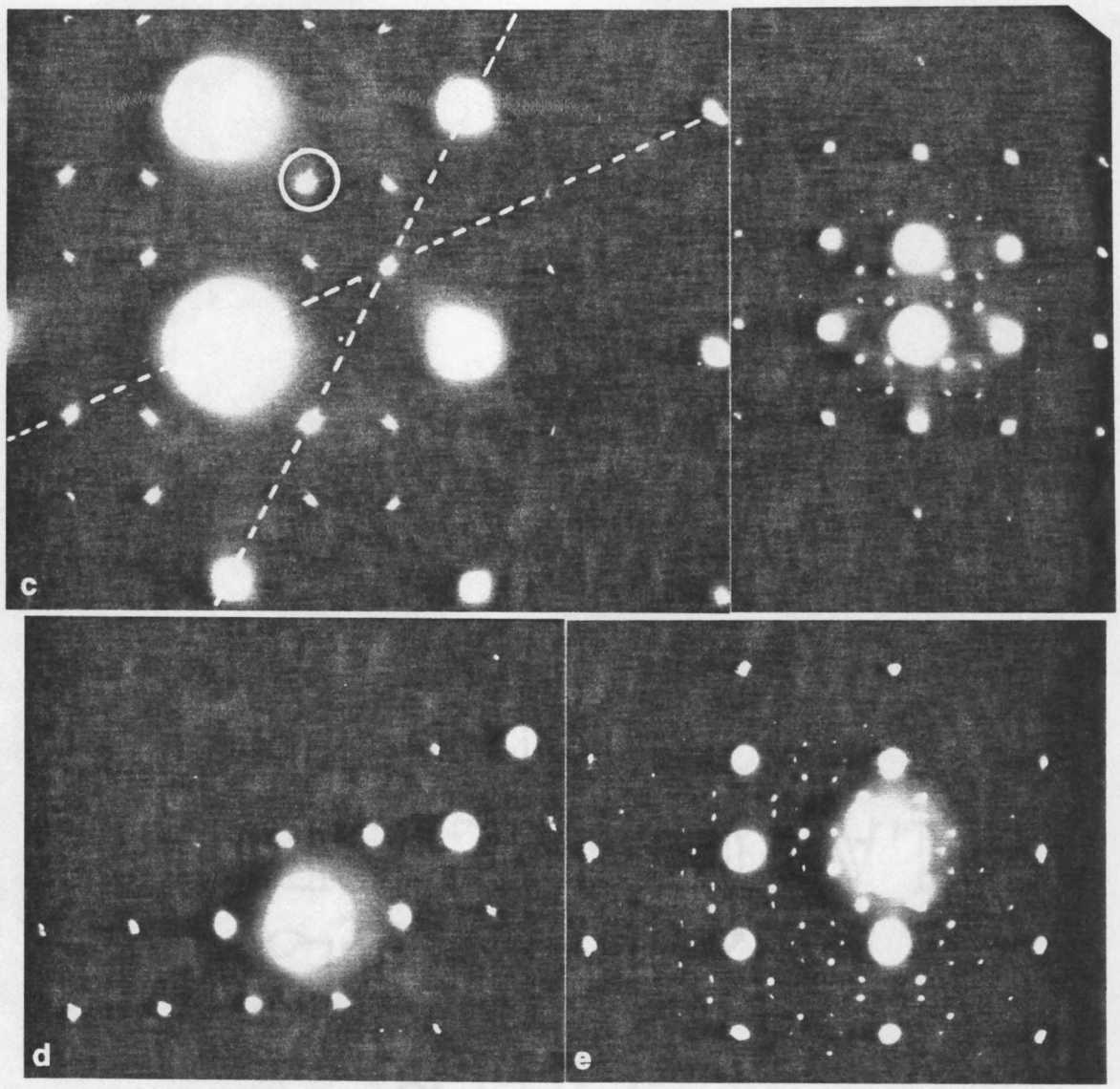


Figure IV-59. (Continued).

Ni_2Mo precipitates in several orientations. Closer inspection of the diffraction pattern (also see inset in Figure IV-59c) reveals streaking of the Ni_2Mo spots in two <420> directions as well as splitting of the spots. The fundamental spots are broadened in the <110> directions; the higher order spots clearly show splitting in pairs in <110> directions; for example, the (420) and (440) spots are split in the $[\bar{1}10]$ direction, whereas the $(2\bar{4}0)$ and $(\bar{4}40)$ spots are split in the [110] direction. To determine if these diffraction effects were caused by twins on {111} planes, the same region was examined in a number of <011> orientations, a representative example of which is shown in Figure IV-59d. Other than a splitting of the fundamental spots, no evidence was obtained for extra twin spots along <111> directions in either the [011] SAD pattern shown in Figure IV-59d or in the other possible <011> orientations.

These diffraction effects can be explained on the basis of perpendicular twin boundaries or δ-boundaries (118). Gevers et al. (267) have formulated a theory for explaining the origin and nature of the fine structure of diffraction spots associated with coherent domain boundaries, that is the δ-boundary. Since this type of interface separates two crystal parts which differ in lattice parameters, the associated misorientation causes splitting of the fundamental spots in diffraction patterns obtained therefrom in a direction perpendicular to the interface (267). When the electron beam is incident at a shallow angle, this interface will exhibit δ-fringes; when nearly parallel, the interface will be appear on edge, that is, will show few or no fringes (118,267). Based on these observations, it

is concluded that the fine diffraction effects in Figure IV-59c are associated with perpendicular twins. Thin lines (see arrows) representing the PT boundaries are visible in Figure IV-59a in two orientation roughly normal to each other. The traces of the two {110} fcc planes appearing in this orientation are indicated in Figure IV-59a. It is evident from the geometry that the perpendicular twin boundaries appearing vertical in Figure IV-59c are parallel to the $(\bar{1}10)$ plane, and those horizontal are parallel to the (110) plane. In fact, these are the coherent twin planes observed in practice for the PT boundaries in ordered Ni_4Mo (118,185). Optically, the boundaries in Figure IV-59a correspond to the {110} fcc striations discussed earlier in connection with the binary Ni_4Mo alloy. The streaking of the Ni_2Mo spots in Figure IV-59c is associated with the thin, plate-like shape of the precipitates. The traces of the four {420} fcc planes appearing in this orientation are also designated in Figure IV-59a, after due rotation corrections. It is clear that the Ni_2Mo precipitates form parallel to {420} fcc planes.

On tilting to the [112] orientation, Figure IV-59e, PT-related Ni_4Mo spots appear, as confirmed by DF images from the spots. The Ni_4Mo domains within each perpendicular twin are delimited by the Ni_2Mo precipitates at the domain boundaries. The domains and the precipitates appear with a perpendicular twin relation to those across the boundaries identified in Figure IV-59a.

Similar to the observations made in the specimen aged for 384 hours, the DO_{22} phase was observed to form from broad bands composed of Ni_4Mo domains and Ni_2Mo precipitates. These bands were parallel to

prior annealing twin boundaries, which are traces of {111} fcc planes. A representative example elucidating this transformation is illustrated in the BF micrograph in Figure IV-60a. The Ni_4Mo domains, Ni_2Mo precipitates and the DO_{22} are identified in the micrograph. Additional examples are presented in Figures IV-61a-c. This feature was also confirmed by SEM observations of the microstructure. A SEM micrograph depicting this feature, as well the perpendicular twins (PT's) described earlier is shown in Figure IV-60b. All relevant features are described on the micrograph.

The Ni_3Mo forms by two independent mechanisms. One mechanism involves direct formation from bands of DO_{22}. A BF micrograph illustrating this transformation is shown in Figure IV-61a. The associated [112] SAD pattern, Figure IV-61b, reveals DO_{22} as well as Ni_3Mo spots (see arrows); both spots are streaked in the $[\bar{1}\bar{1}1]$ direction, which is normal to the thin dimension of the bands containing DO_{22} and Ni_3Mo in Figure IV-61a. A DF image, Figure IV-61c, obtained from a DO_{22} spot labelled 1 in Figure IV-61b reveals domains within the bands; similarly, a DF image from the Ni_3Mo spot indicated by the arrow in Figure IV-61b revealed Ni_3Mo domains in other parts of the bands. This is taken as evidence for a direct transformation from DO_{22} to Ni_3Mo. The intervening regions between bands are composed of Ni_4Mo domains, as verified by the DF micrograph in Figure IV-61d obtained from the Ni_4Mo spot labelled 2 in Figure IV-61b. No Ni_2Mo is present in the region of the bands, as evident in the DF image in Figure IV-61e taken from the spot labelled 3 in Figure IV-61b. Similar to earlier observations, bands containing Ni_4Mo and Ni_2Mo (which have

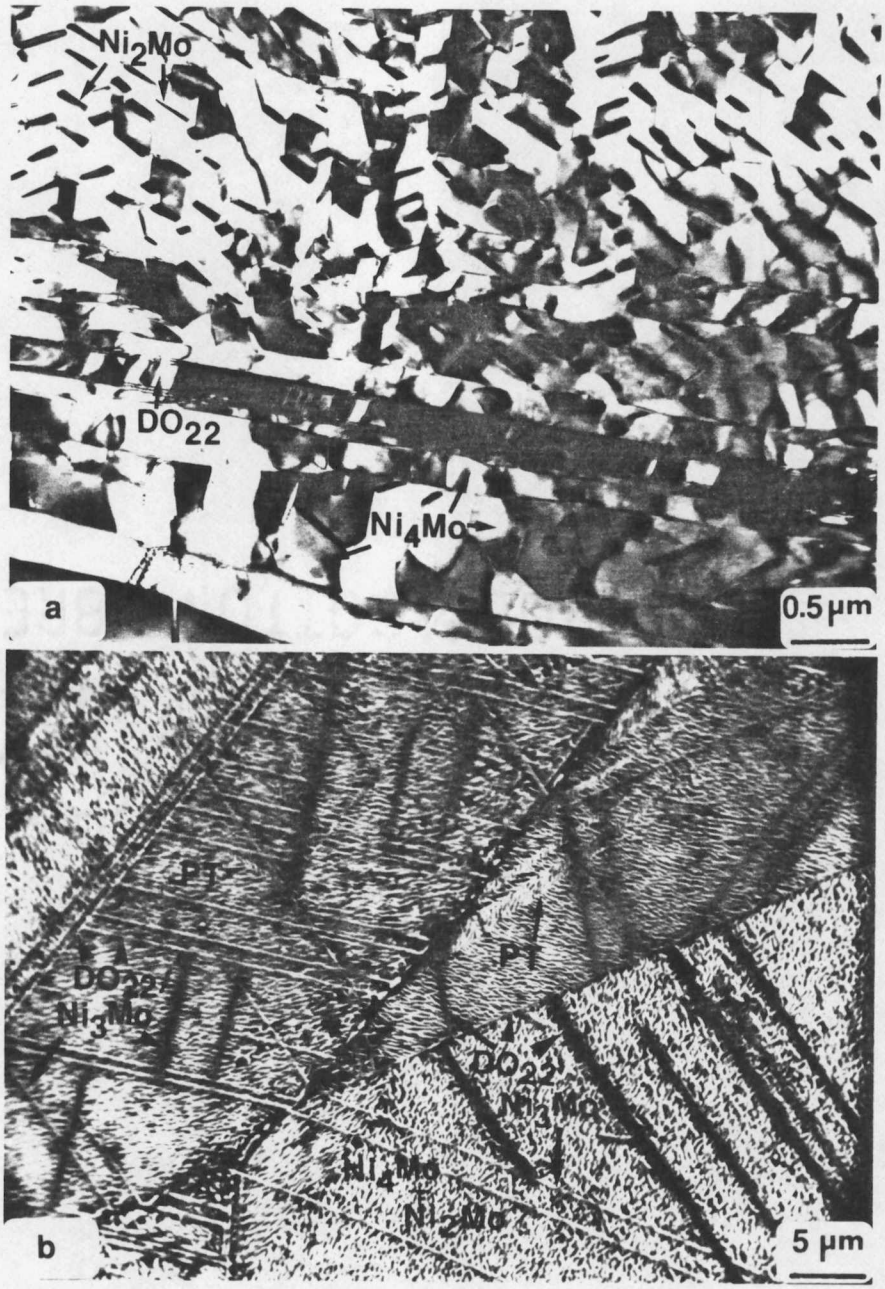


Figure IV-60. Micrographs illustrating the formation mechanism of DO_{22} in the 2.08 wt pct Cr alloy aged at 700°C. Aged 4500 hrs. a) BF showing that DO_{22} forms from bands composed of Ni_4Mo and Ni_2Mo; b) SEM micrograph.

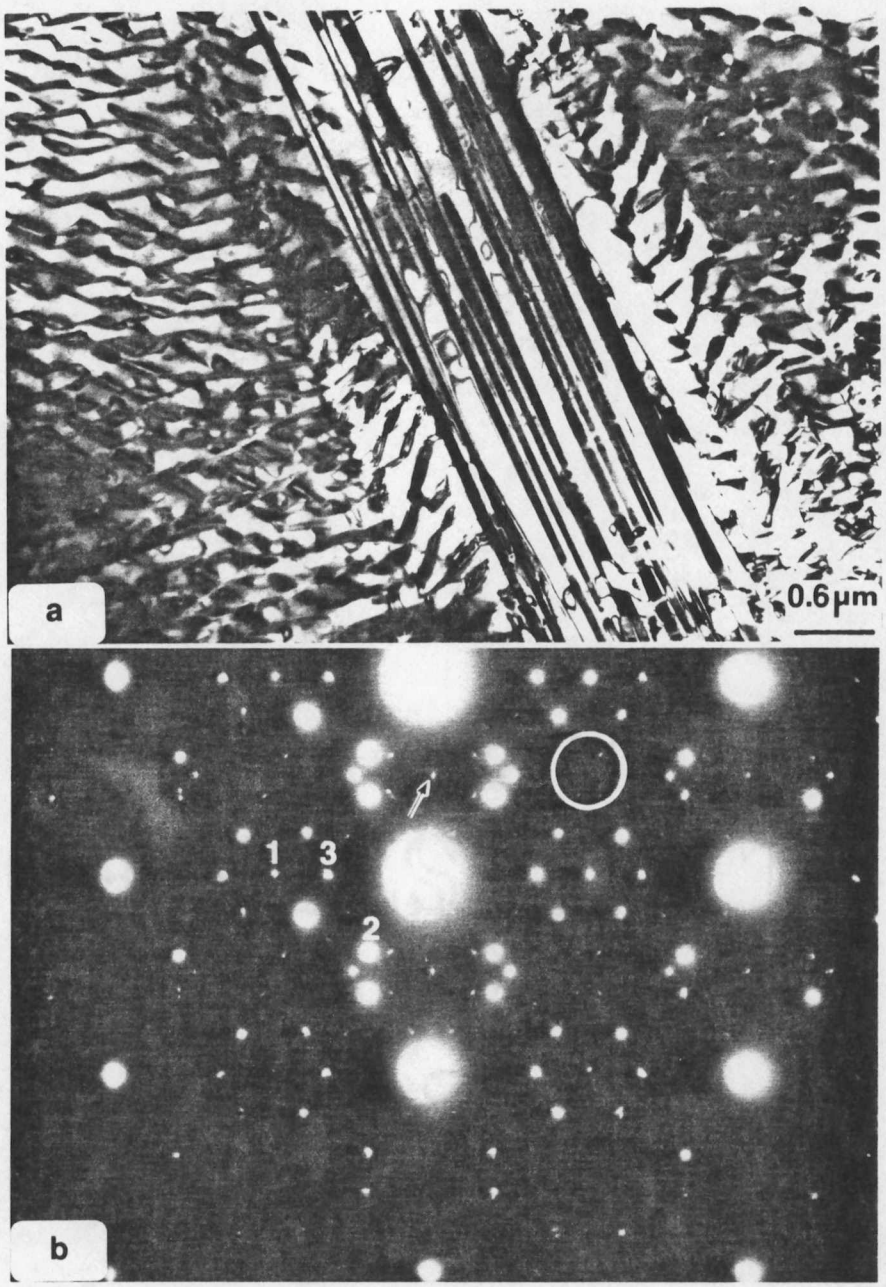


Figure IV-61. Micrographs illustrating the formation mechanism of Ni_3Mo from DO_{22} in the 2.08 wt pct Cr alloy aged at 700°C. Aged 4500 hrs. a) BF; b) [112] SADP from region to left in a) but covering portion of the DO_{22}/Ni_3Mo bands; c), d), and e) Are DF micrographs from the DO_{22}, Ni_4Mo and Ni_2Mo spots labelled 1, 2, and 3, respectively in b).

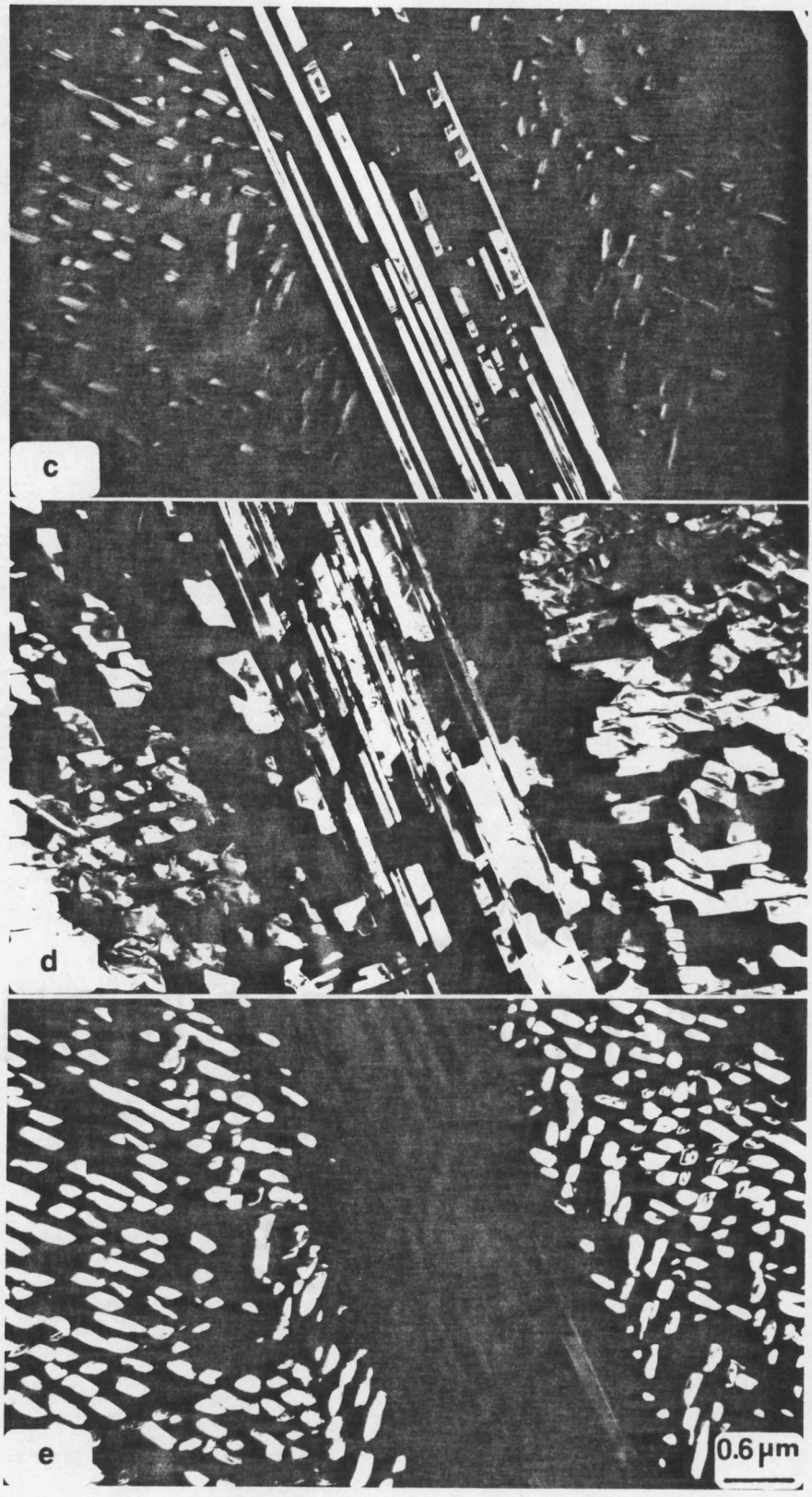


Figure IV-61. (Continued).

transformed to DO_{22}) are often twinned on {111} fcc planes in relation to the parent matrix. The faint spots encircled in Figure IV-61b occurring at locations other than those of Ni_4Mo, Ni_2Mo, DO_{22}, Ni_3Mo and Ni_4Mo double diffraction, are presumably due to double diffraction by the Ni_2Mo precipitates.

A second formation mechanism of Ni_3Mo was prevalent at grain boundaries and closely follows the conventional sequence observed at lower temperatures (<800°C) in the binary Ni_3Mo alloy (122,123, 127-129). This mechanism involves initial formation of large domains of Ni_4Mo at the grain boundaries (Figures IV-62a-b) by the grain boundary domain coarsening process that was described earlier in connection with the binary Ni_4Mo. These regions subsequently transform directly to Ni_3Mo. During this shear transformation from the fcc-based Ni_4Mo to the hcp-based Ni_3Mo numerous stacking faults are produced (Figure IV-62c). The faults form parallel to (010) Ni_3Mo planes, similar to that reported during ordering in the binary Ni_3Mo and appear to be periodic. The mean spacing of the faults is 5.2 nm, which is closely comparable to that reported in the binary (122,127,128). The stacking faults are apparently gradually removed as shown in Figure IV-62d, where fewer faults together with APB's are visible within the large Ni_3Mo plate. These APB's form roughly parallel to (100) Ni_3Mo planes (122,123,127-129) and in Figure IV-62d are almost normal to the stacking faults. There was no evidence at any stage for the formation of the LPAPB structure observed in the binary Ni_3Mo (122,123,127-129) prior to the coarsening process which produces the APB's observed in Figure IV-62d. In Figure IV-62d, subsequent growth

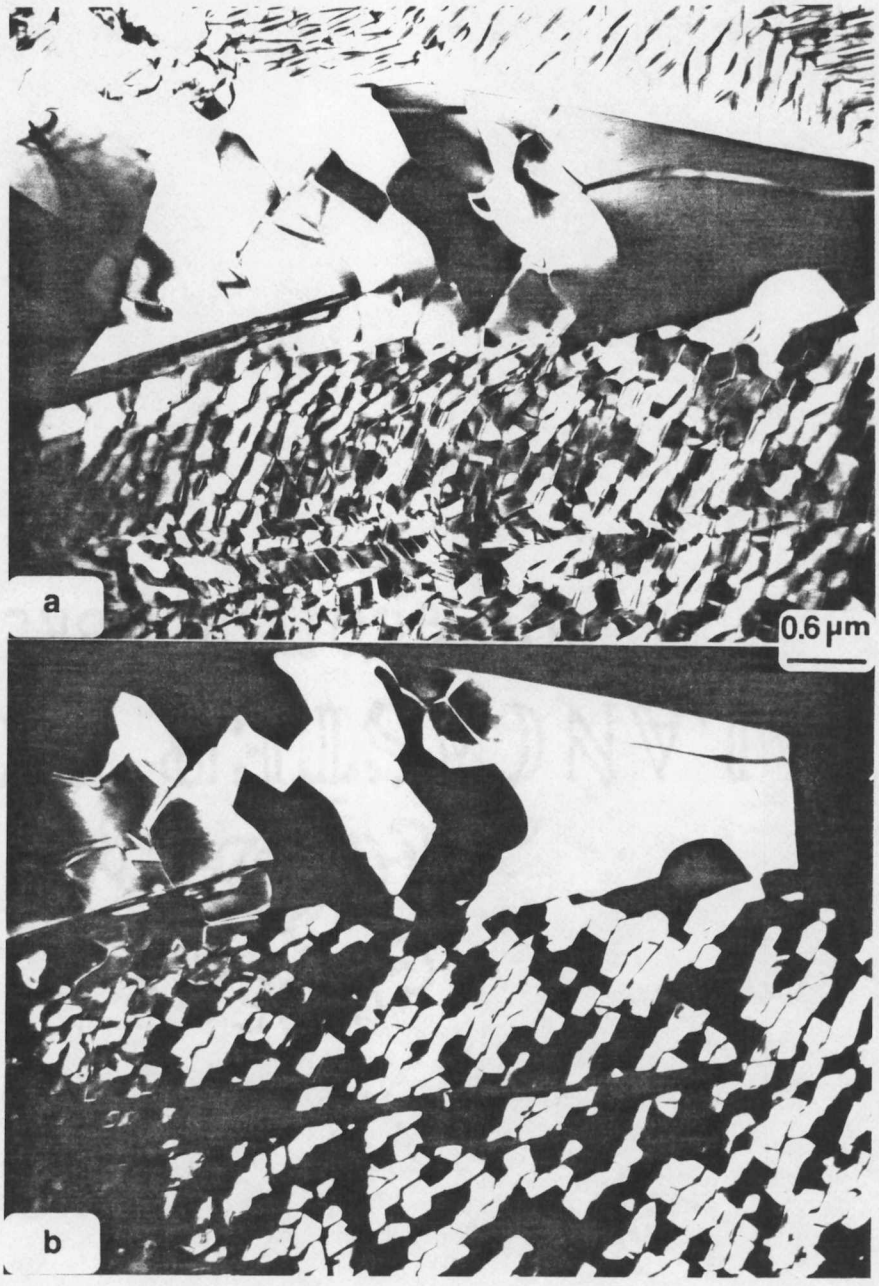


Figure IV-62. Micrographs illustrating the formation of Ni_3Mo at grain boundaries in the 2.08 wt pct Cr alloy aged at 700°C. Aged 4500 hrs. a) BF and b) DF of large Ni_4Mo domains at grain boundaries; c) DF of Ni_3Mo plate containing stacking faults; d) BF of grain boundary Ni_3Mo showing APB's and few stacking faults.

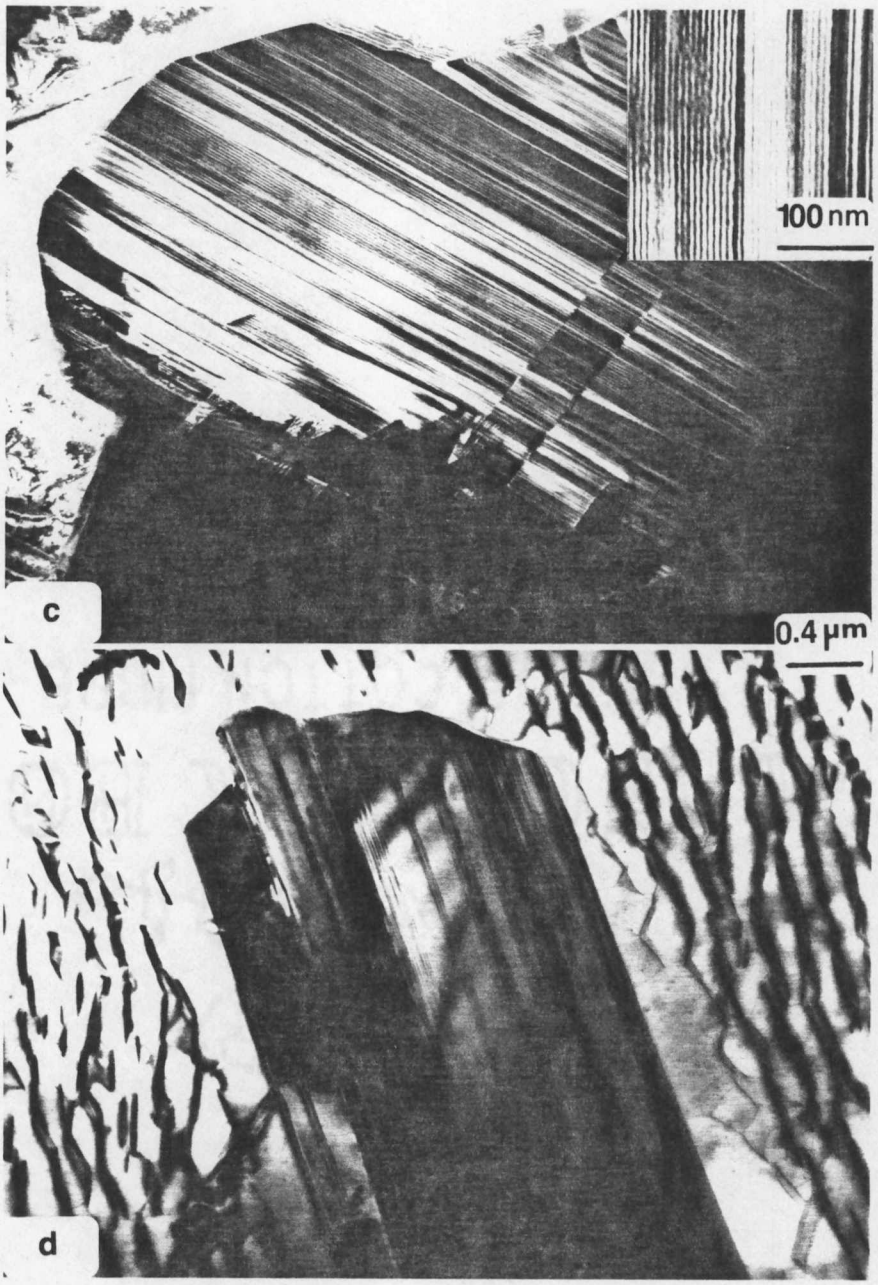


Figure IV-62. (Continued).

of the Ni_3Mo plates is accomplished by redissolution of the Ni_2Mo and formation of large domains of Ni_4Mo in the immediate vicinity of the advancing plate, followed by transformation of the Ni_4Mo to Ni_3Mo, with the simultaneous presence of stacking faults. More positive evidence for this second formation mechanism of Ni_3Mo discussed in the foregoing is presented later in connection with the results at 600°C.

The behavior of the 2.97 wt pct Cr alloy is by and large similar to that of the 2.08 wt pct Cr alloy. In difference, much larger amounts of DO_{22} and Ni_3Mo and much lower amounts of Ni_4Mo and Ni_2Mo are present. Moreover, a small amount of SRO α phase is also observed. Representative examples are shown in Figures IV-63a-f for a sample aged for 4500 hours. In the BF micrographs in Figures IV-63a and -63c, polyphase regions containing α, Ni_4Mo, Ni_2Mo, DO_{22} and Ni_3Mo are identified. The [112] SAD patterns obtained from the regions encircled in Figures IV-63a and -63c, shown in Figures IV-63b and -63d respectively, establish the presence of the Ni_4Mo, Ni_2Mo and DO_{22}. Similarly, the presence of Ni_3Mo and α were established by diffraction. The large Ni_3Mo plates observed in Figures IV-63a and -63c form by the grain boundary mechanism and reveal stacking faults similar to those in the 2.08 wt pct Cr alloy. A BF micrograph from another region, Figure IV-63e, reveals multiple bands of DO_{22} which have transformed to Ni_3Mo. The associated $[100]_\gamma//[011]_{fcc}$ SAD, Figure IV-63f, is reminiscent of those seen at 800°C and reveals that the intervening spaces between the bands are fcc; two successive fcc regions are in twin relationship as confirmed by DF images from the fcc twin spots in Figure IV-63f. The streaking in Figure IV-63f in the

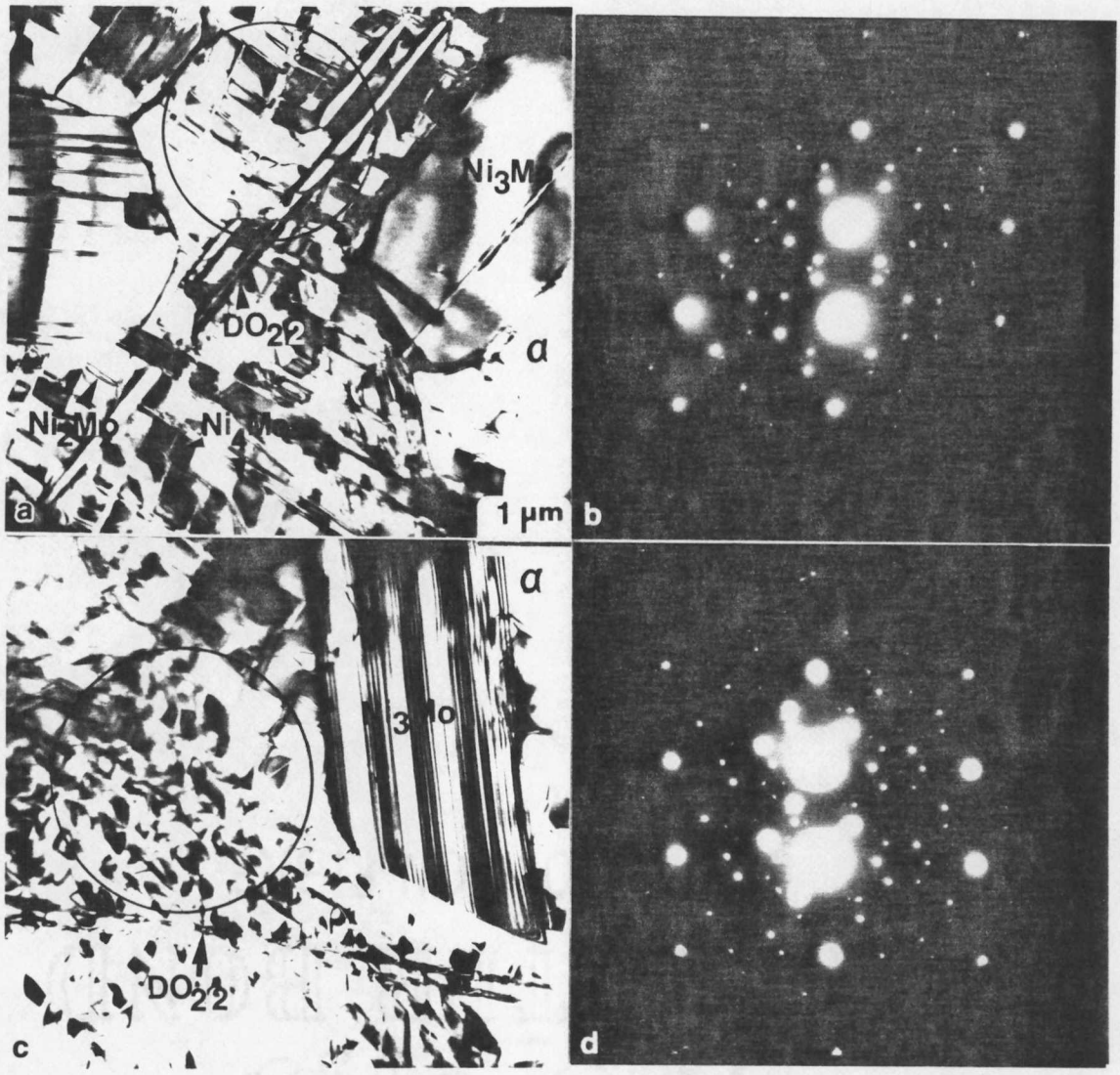


Figure IV-63. Microstructures of the 2.97 wt pct Cr alloy aged at 700°C. Aged 4500 hrs. a) BF micrograph; b) [112] SADP of a) BF micrograph showing Ni_3Mo plate containing stacking faults; d) [112] SADP of region to the left of the Ni_3Mo plate in c); e) BF micrograph showing bands of DO_{22} which have transformed to Ni_3Mo; f) $[100]_\gamma$ //$[0\bar{1}1]_\alpha$ SADP of e).

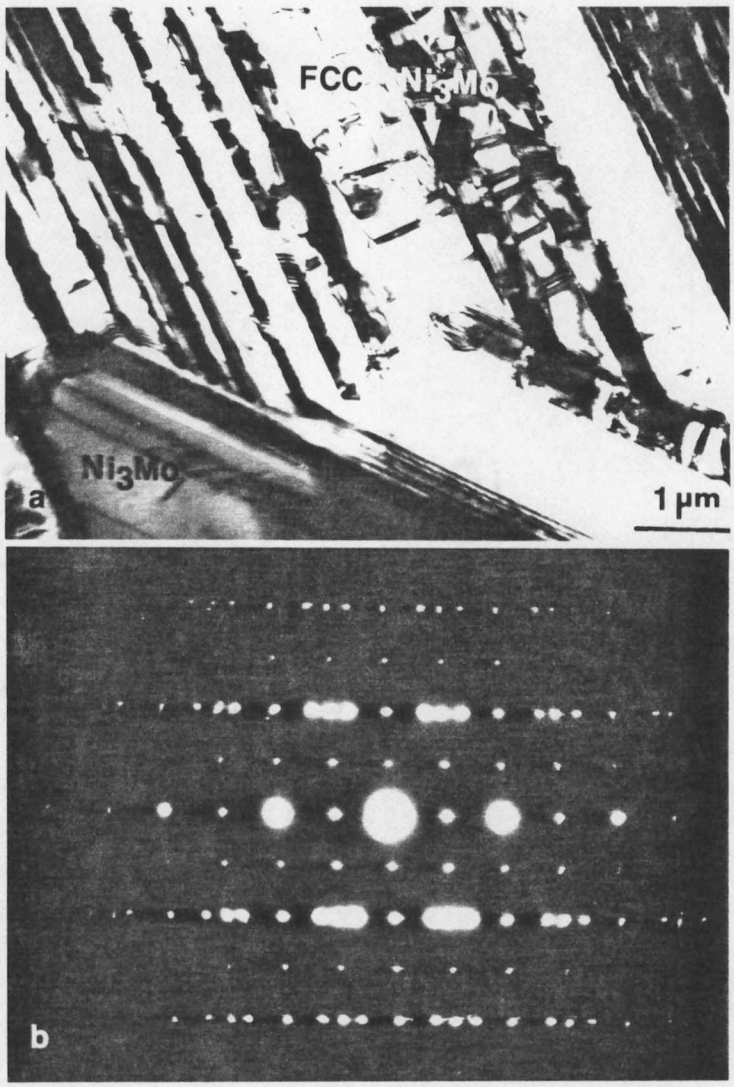


Figure IV-63. (Continued).

$[010]_\gamma//[111]_{fcc}$ is normal to the thin dimension of the bands. Although the fcc regions show some residual contrast characteristic of Ni_4Mo and Ni_2Mo, these were not detected in SAD patterns in other orientations where they would otherwise provide diffraction. Examination of the DO_{22} bands in other regions once again established that similar to the behavior of the 2.08 wt pct Cr alloy they form from bands composed of Ni_4Mo and Ni_2Mo aligned parallel to {111} fcc planes.

In the 3.94 wt pct Cr alloy, no Ni_4Mo or Ni_2Mo is observed after 4500 hours, although these were present at shorter times. The microstructure, Figure IV-64a, is entirely composed of alternate bands of Ni_3Mo and fcc α, as confirmed by the $[100]_\gamma//[011]_{fcc}$ SAD pattern in Figure IV-64b. The Ni_3Mo forms predominantly from the DO_{22}; there was very little evidence for the grain boundary mechanism noted in the 2.08 and 2.97 wt pct Cr alloys.

Aging at 600°C. The transformation behavior in all three alloys in terms of types of second phases and their formation mechanisms are identical. Ordering proceeds much slower at this temperature in comparison to that at 700°C and other than indications of a grain boundary reaction, the microstructural changes are too fine to be observable optically. In the following, only the results of TEM observations of the 2.97 wt pct Cr alloy aged for 4500 hours are presented.

The microstructure within the grains is very fine and is composed of only Ni_4Mo and Ni_2Mo, as confirmed by the [112] SAD

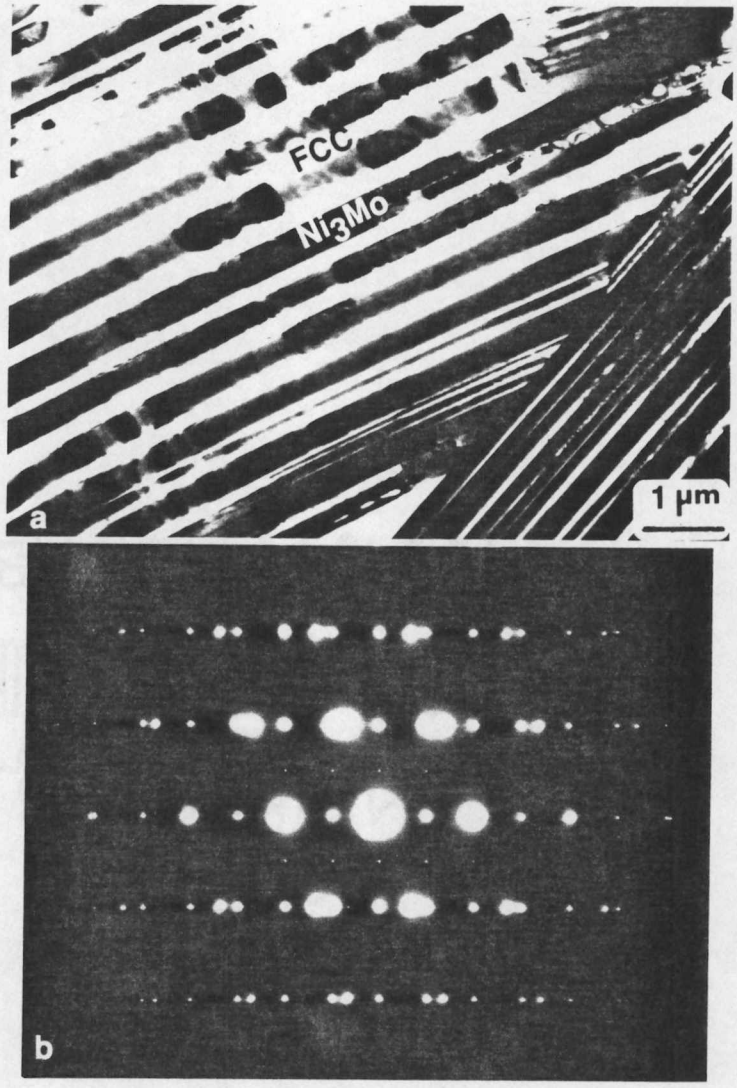


Figure IV-64. Microstructures of the 3.84 wt pct Cr alloy aged at 700°C. Aged 4500 hrs. a) BF micrograph showing alternate bands of Ni3Mo and fcc; b) $[100]_\gamma//[011]_\alpha$ SADP of region at top in a).

pattern shown in Figure IV-65a. No evidence was obtained for the DO_{22} phase in any parts of the microstructure. At the grain boundaries, large domains of Ni_4Mo form by the grain boundary domain coarsening process discussed earlier in connection with the binary Ni_4Mo alloy. An example of this coarsening reaction is illustrated in the BF micrograph in Figure IV-65b. The DF micrograph, Figure IV-65c, obtained from a superlattice Ni_4Mo spot establishes that these regions are composed Ni_4Mo domains, which are much larger than those within the grains. Frequently, many dark particles were present among the domains. Presumably, these are NiMo, but this could not be positively ascertained. The coarsened Ni_4Mo domains subsequently transform to Ni_3Mo, as shown in the BF micrograph in Figure IV-65d. Within the Ni_3Mo plate, stacking faults as well as APB's are visible.

To understand the formation mechanism of Ni_3Mo, other regions of the sample containing Ni_3Mo were examined. An enlarged view of a large Ni_3Mo plate is shown in Figure IV-66a. This micrograph is a DF image obtained from the encircled (020) Ni_3Mo spot in the associated [100] Ni_3Mo SAD pattern in Figure IV-66b. The micrograph reveals very thin stacking faults which produce intense streaks in the [010] Ni_3Mo direction in the SAD in Figure IV-66b. After due rotation corrections, it is established that the direction of streaking is perpendicular to the thin dimension of the faults. Thus, these stacking faults form parallel to (010) Ni_3Mo planes and are associated with the shear transformation from the fcc-based Ni_4Mo to the hcp-based Ni_3Mo, in agreement with the reports of Van Tendeloo and co-workers (122,127,128). Also note in Figure IV-66b that the (001) Ni_3Mo double

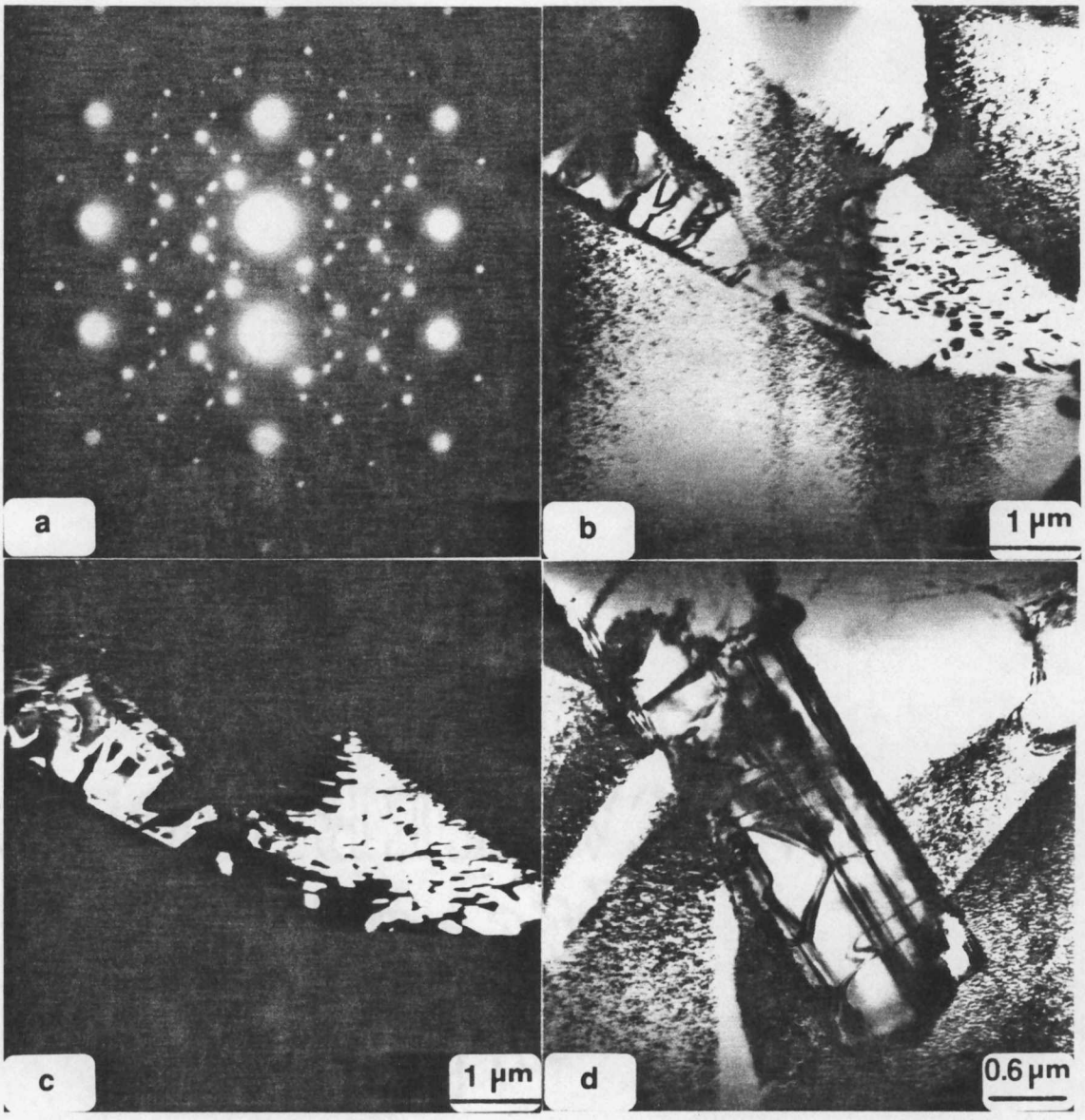


Figure IV-65. Microstructures of the 2.97 wt pct Cr alloy aged at 600°C. Aged 4500 hrs. a) [112] SADP from inside grains; b), c) BF and DF micrographs showing large Ni_4Mo domains at grain boundaries; d) BF micrograph of grain boundary Ni_3Mo plate containing stacking faults and APB's.

diffraction spots are absent, and moreover, many smaller spots are present along the [010] Ni_3Mo directions at locations in between the Ni_3Mo spots. These spots are associated with polytypes of the hcp structure (122). In fact, but for fewer such spots, Figure IV-66b is identical to Figure 8 of Van Tendeloo et al. (122).

When the same region is tilted to the [010] Ni_3Mo orientation, APB's within the plate are imaged, as shown in the DF image in Figure IV-66c obtained from the $(\bar{2}00)$ Ni_3Mo spot encircled in the SAD in Figure IV-66d. After making due allowances for rotation, it is seen that the APB's form parallel to (100) Ni_3Mo planes, which is the defect plane reported for these in the binary Ni_3Mo (121-123,127-129). It is evident from Figures IV-66a and -66c that the stacking faults and the APB's are rougly normal to each other, as expected. Another example of the stacking faults and the APB's on (100) Ni_3Mo planes is depicted in the DF image in Figure IV-67a obtained from a (200) Ni_3Mo spot encircled in the corresponding [011] Ni_3Mo SAD pattern in Figure IV-67b. The APB's have the appearance of the dissociated non-conservative APB's reported in the binary Ni_3Mo (121,122,127,128). Thus, the observation of stacking faults on (010) Ni_3Mo planes and non-conservative APB's on (100) Ni_3Mo planes are in good agreement with the reports on the binary Ni_3Mo alloy (121-123,127-129). However, no evidence was obtained in any of the three chromium alloys for the LPAPB structure (of 1.39 nm spacing) observed in the binary Ni_3Mo alloy prior to the coarsening process that produces the non-conservative APB's on (100) Ni_3Mo planes (121-123,127-129).

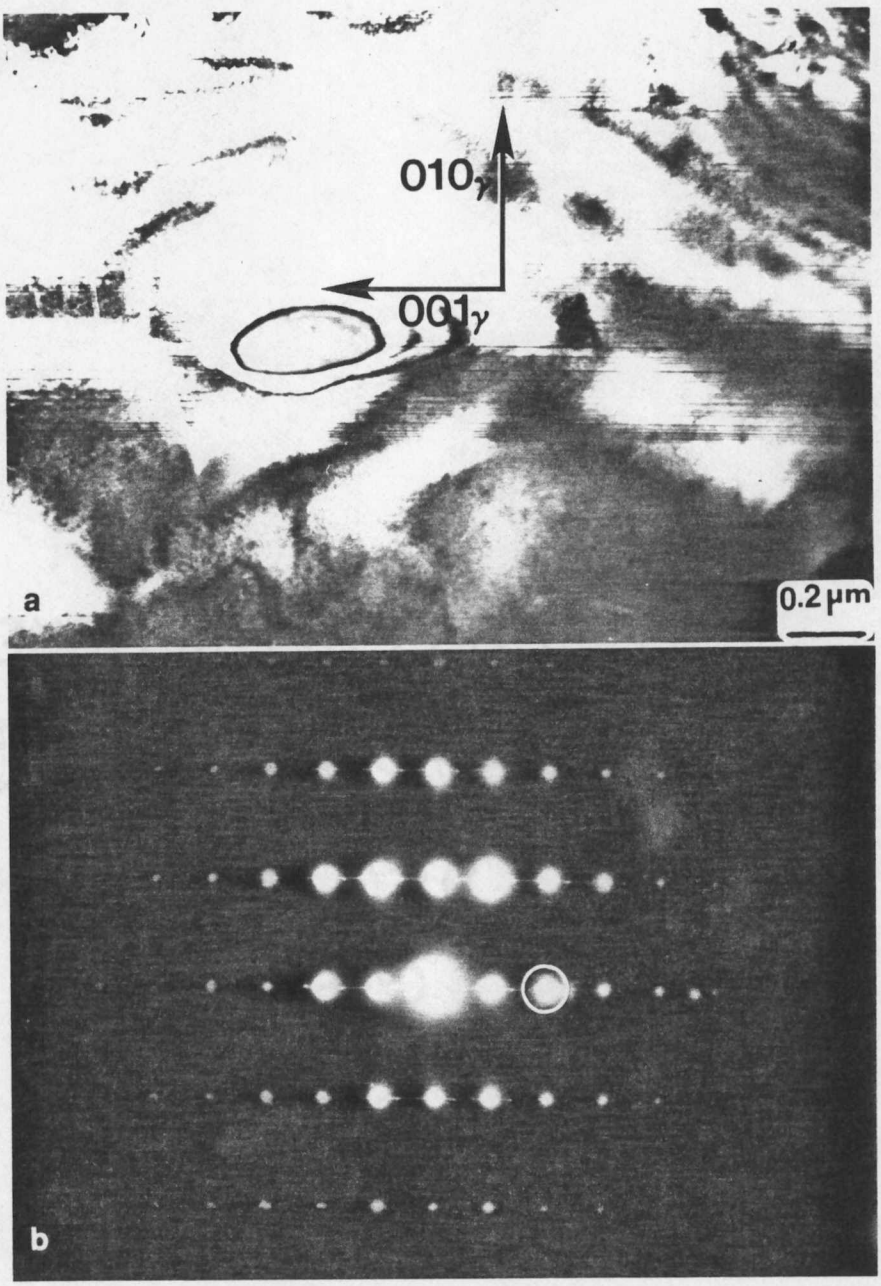


Figure IV-66. Micrographs illustrating the formation of Ni_3Mo at grain boundaries in the 2.97 wt pct Cr alloy aged at 600°C. Aged 4500 hrs. a) DF from encircled spot in $[100]_\gamma$ SADP in b); c) DF from encircled spot in [010] SADP in d).

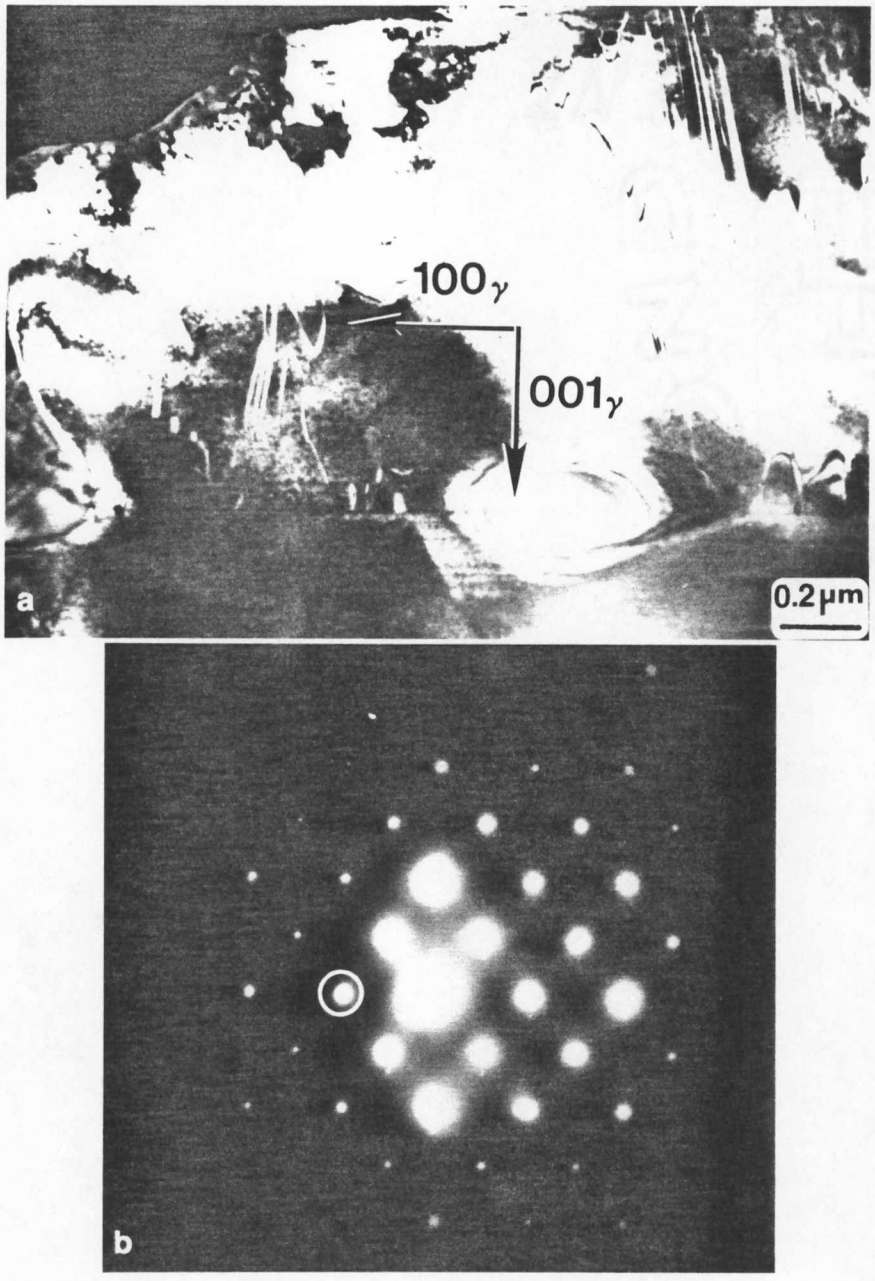


Figure IV-66 (Continued).

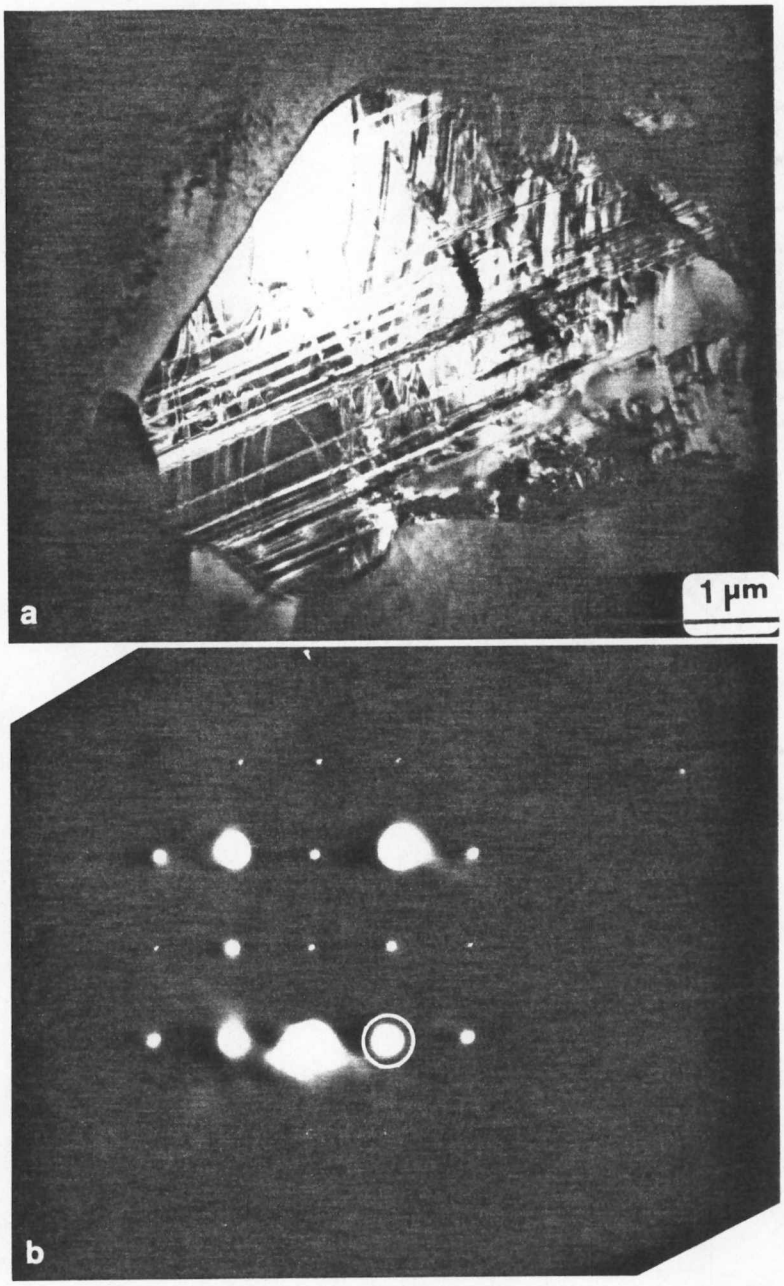


Figure IV-67. Example of stacking faults and APB's in grain boundary Ni_3Mo in the 2.97 wt pct Cr alloy aged at 600oC. a) DF from (200) Ni_3Mo spot encircled in the $[011]_\gamma$ SADP in b).

Composition Analyses of Phases by TEM-EDAX

The compositions of various phases present in the three chromium alloys after aging 4500 hours at 850, 800, 700 and 600°C were determined with the use of EDAX in the Philips EM400, as described in Chapter III (pages 180-186). The phases observed at each temperature, as well as their compositions are summarized in Table IV-3 for the 2.08, 2.97 and 3.84 wt pct Cr alloys. The compositions of the Ni_4Mo and Ni_2Mo at 600°C could not be determined, since these were present on too fine a scale. The data shown for every individual phase represents values approximately at the middle of a range of values obtained from 3 to 6 measurements. Several consistent changes in the compositions of phases as a function of chromium content (in alloy) and temperature are evident.

First, for a particular phase α, β, or γ and at any given temperature, with an increase in chromium content in the alloy, the nickel content remains nearly the same, whereas the molybdenum content decreases and chromium content increases. Second, for each alloy, with a decrease in temperature, the composition of a particular phase α, β, or γ shows almost no change in the nickel content, whereas the molybdenum content decreases and the chromium content increases. For example, compare the compositions of the phase at each temperature. Third, the phase has the lowest solubility for chromium and the α phase the highest (exception is Ni_2Mo (ε)). These observations clearly establish that chromium predominantly substitutes for the molybdenum in Ni_4Mo alloys.

TABLE IV-3

Chemical Compositions of Phases* as a Function of Chromium Content in Alloy and Temperature

Temperature (°C)		Wt Pct Chromium in Alloy								
		2.08			2.97			3.84		
		Phase	At Pct	Wt Pct	Phase	At Pct	Wt Pct	Phase	At Pct	Wt Pct
850	Ni	α	78.5	70.7	α	78.1	70.6	α	77.4	70.2
	Mo		18.0	26.5		17.5	25.9		17.0	25.3
	Cr		3.5	2.8		4.4	3.5		5.6	4.5
	Ni	γ	75.5	66.3	γ	75.2	66.0	γ	74.5	65.6
	Mo		22.6	32.4		22.3	32.0		22.2	31.9
	Cr		1.9	1.4		2.5	2.0		3.3	2.5
800	Ni	α	79.6	72.3	α	78.6	71.8	α	78.0	72.0
	Mo		16.7	24.7		16.0	23.9		14.6	21.9
	Cr		3.7	3.0		5.4	4.3		7.4	6.1
	Ni	β	79.7	71.0	---	---	---	---	---	---
	Mo		19.2	28.1						
	Cr		1.1	0.9						
	Ni	γ	75.8	66.6	γ	75.5	66.7	γ	76.1	67.7
	Mo		22.2	31.9		21.5	31.1		20.2	29.3
	Cr		2.0	1.5		3.0	2.2		3.7	3.0
700	Ni	---	---	---	α	78.7	72.4	α	78.3	72.6
	Mo					14.8	22.3		13.8	20.9
	Cr					6.5	5.3		7.9	6.5
	Ni	β	79.2	70.8	β	78.6	70.5	---	---	---
	Mo		19.0	27.7		18.6	27.3			
	Cr		1.8	1.5		2.8	2.2			
	Ni	γ	75.6	66.8	γ	75.0	66.5	γ	75.6	67.4
	Mo		21.3	30.7		20.8	30.1		20.0	29.1
	Cr		3.1	2.5		4.2	3.4		4.4	3.5
	Ni	ε	72.0	63.1	ε	66.8	57.7	---	---	---
	Mo		23.3	33.3		26.2	37.0			
	Cr		4.7	3.6		7.0	5.3			
600	Ni	Matrix β+ε	77.3	69.0	Matrix β+ε	76.4	68.6	Matrix β+ε	72.0	64.5
	Mo		19.7	28.7		18.8	27.6		19.9	29.1
	Cr		3.0	2.3		4.8	3.8		8.1	6.4
	Ni	γ	75.5	66.8	γ	75.0	67.0	γ	75.4	67.5
	Mo		21.3	30.7		19.9	29.0		19.3	28.3
	Cr		3.2	2.5		5.1	4.0		5.3	4.2

*α - SRO FCC; β - Ni_4Mo; γ - Ni_3Mo; ε - Ni_2Mo

Discussions on the Effect of Chromium on Phase Relationships in Ternary Ni_4Mo-Based Alloys

The results presented in the foregoing have shown that additions of even small amounts of chromium dramatically changes the physical metallurgy and transformation behavior of Ni_4Mo-based alloys. A number of second phases, such as Ni_2Mo, DO_{22} and Ni_3Mo, which are richer in molybdenum than the binary Ni_4Mo, are observed. The types of phases observed are dependent on temperature and composition. On the other hand, the transformation mechanisms are governed more by the aging temperature than by composition. Several significant results have emerged from the present investigation. These are discussed in the following.

Mechanisms of Transformations

One significant result is the observed direct transformation from the DO_{22} phase to Ni_3Mo in all three chromium alloys at the higher temperatures, namely, 850, 800 and 700^{o}C. Ruedl (29) has also reported this transformation in Hastelloy B aged at 700^{o}C. A recent publication by Schryvers et. al. (129) has provided significant insight into the rather complex formation mechanism of Ni_3Mo. The transformation occurs in several steps; the exact sequence is dependent on temperature and was outlined in Figure II-32, Chapter II (page 124).

The Ni_3Mo is an orthorhombic superstructure of the close packed hexagonal basic structure, whereas the DO_{22} is a tetragonal superstructure of the face centered cubic structure, also with the

composition Ni_3Mo, but having a cubic stacking of the close packed layers (127-129). A rational basis for the observed direct transformation from DO_{22} to Ni_3Mo in the ternary Ni_4Mo + Cr alloys lies in the fact that the two structures can be generated, one from the other, by a reshuffling of ordered close packed planes (127-129). This is also consistent with the diffraction evidence that the close packed layers in the two structures, that is, $(111)DO_{22}$ and $(010)Ni_3Mo$ are parallel (128). Thus, conceivably, the reshuffling required to accomodate the direct transformation, although not observed in the binary Ni_3Mo, is favored by the presence of chromium in the ternary Ni_4Mo-based alloy. The physical processes involved have not been examined, but are most likely related to the fact that the chromium partially substitutes for the molybdenum.

A second result of significance is related to the formation of Ni_3Mo at grain boundaries. Besides the aforementioned direct formation of Ni_3Mo from DO_{22}, a second mechanism is observed at 700 and 600^{o}C at the grain boundaries, and closely follows the conventional sequence reported at lower temperatures in the Ni_3Mo binary alloy (129). Large domains of Ni_4Mo form at the grain boundaries by the process of domain coarsening that occurs in the binary Ni_4Mo alloy at low temperatures. These regions subsequently transform to Ni_3Mo by a combined diffusion and shear process, which leaves in its wake many stacking faults on (010) Ni_3Mo planes. In difference to the binary Ni_3Mo, the transformation from Ni_4Mo to Ni_3Mo does not involve the intermediate formation of the LPAPB structure. This is probably associated with the observation that the formation of the LPAPB structure in the binary

Ni_3Mo is partly composition driven (129), that is, due to the difference in composition between the Ni_4Mo and Ni_3Mo, and in the ternary Ni_4Mo-based alloys the chromium partially substitutes for the molybdenum and facilitates the diffusion processes required to accomplish the transition from Ni_4Mo directly to Ni_3Mo. A possible reason for a different mechanism at the grain boundaries, from that described in the previous paragraph, may be associated with the fact that Ni_3Mo generally nucleates at the grain boundaries (125) and the preexistence of Ni_4Mo at the grain boundaries allows easy transition by the mechanism discussed above. The driving force for either mechanism is expected to be related to thermodynamics, which dictates a certain volume percentage of Ni_3Mo in the alloys.

A third significant result originating from the present study is the formation of the DO_{22} structure at 700°C from bands containing Ni_4Mo and Ni_2Mo aligned parallel to {111} fcc planes. The mechanism by which this takes place can be understood on the basis of the atomic arrangement of nickel and molybdenum atoms in these structures. The Ni_4Mo, DO_{22}, and Ni_2Mo structures are structurally related and fall in the "420" category of alloys (92,126,127), that is, the structures can be described as appropriate sequences of pure nickel and pure molybdenum planes in the <420> fcc directions. The Ni_4Mo, DO_{22} and Ni_2Mo respectively contain four, three and two nickel planes followed by one molybdenum plane, and can be produced, one from the other, by the periodic removal/insertion of non-conservative antiphase boundaries in the {101} supersturucture planes (92,126,127). In the present study, at 700°C, unlike the binary Ni_3Mo, a reverse

transformation to DO_{22} from bands composed of Ni_4Mo and Ni_2Mo aligned along {111} fcc planes, takes place. Since the Ni_4Mo and Ni_2Mo are present adjacent to each other, a simple diffusion-driven exchange on {420} fcc planes of a row of nickel atoms and a row of molybdenum atoms from the Ni_4Mo to the Ni_2Mo at the boundary separating the two, will generate the DO_{22} structure. The realignment and/or the twinning that is observed on {111} fcc planes of the bands containing Ni_4Mo and Ni_2Mo is probably associated with the ease with which the transformation can proceed on the close-packed {111} fcc planes, which are also the close packed planes for these structures (127,128).

Relative Stability of Phases

Another important result in this study is the notable absence of the Ni_2Mo phase above 700°C (at 800 and 850°C) and of the DO_{22} structure below 700°C (at 600°C). The influence of ternary alloying additions on the relative stability of different phases in the Ni-Mo system can be qualitatively explained on the basis of the ground state structures in fcc based ordered alloys (268,269) and by invoking the concept of the V_2/V_1 ratio (ratio of second and first nearest neighbor interaction energies) in the theory developed by De Fontaine and co-workers (174,270,271). Several investigators (265,266,272) have used this approach to gain better understanding of the phase relationships in Ni_3Mo-based alloys containing a variety ternary additions.

Cahn and co-workers (268,269), working in framework of the Ising model, that is, by restricting atom pair interactions to first and

second nearest neighbors, derived the minimum energy (or ground state) structures at $0^{o}K$ for fcc and bcc-based ordering alloys. Their results showing the crystal structures stable at different compositions and values of V_2/V_1 for fcc-based ordering systems, reproduced from the work of Martin and Williams (266) with slight modifications to include the Ni_4Mo ($D1_a$) structure, is illustrated in Figure IV-68. The cross-hatched region between 0.16 and 0.25 atom fraction B is a region of multiphase equilibrium, that is, assuming no interactions beyond second nearest neighbors, mixtures of A_5B and A_4B or A_4B and A_3B (DO_{22}) have the same free energy as mixtures of A_5B and A_3B. Sanchez and DeFontaine (270,271) have derived phase diagrams applicable to the Ni-Mo system for the case of $0<V_2/V_1<0.5$. They utilized the fcc ground state structures determined by Cahn and co-workers (268,269) and calculated the configurational free energy using the cluster variation method. Basically, this method involves calculations of the number of possible configurations for different types of clusters having the same average energy and computing the phase diagram on the basis of the configuration that minimizes the free energy functional. Their results are reproduced in Figure IV-69 for three values of V_2/V_1: 0.25, 0.35 and 0.45. These diagrams were derived under the assumptions that 1). pair interactions beyond second nearest neighbors are zero, 2) the pair ineraction energies are independent of temperature and composition, 3) the internal energy of the system is due to pairwise interactions between the two kinds of atoms A and B, 4) the cluster is large enough and possesses the correct symmetry of the superlattice being modelled, and 5) all

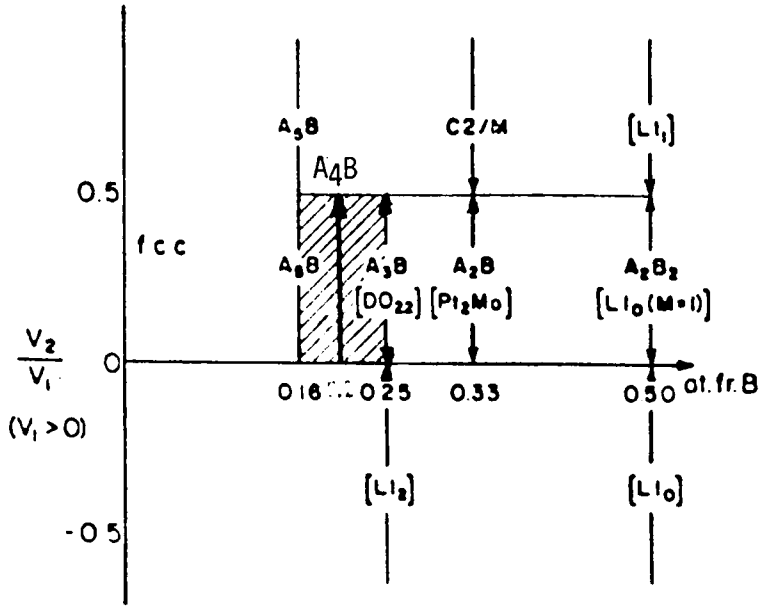


Figure IV-68. Ground state structures for fcc ordering alloys.

Source: M. J. Richards and J. W. Cahn, "Pairwise Interactions and the Ground State of Ordered Binary Alloys," Acta Met., 19, 1263-1277 (1971).

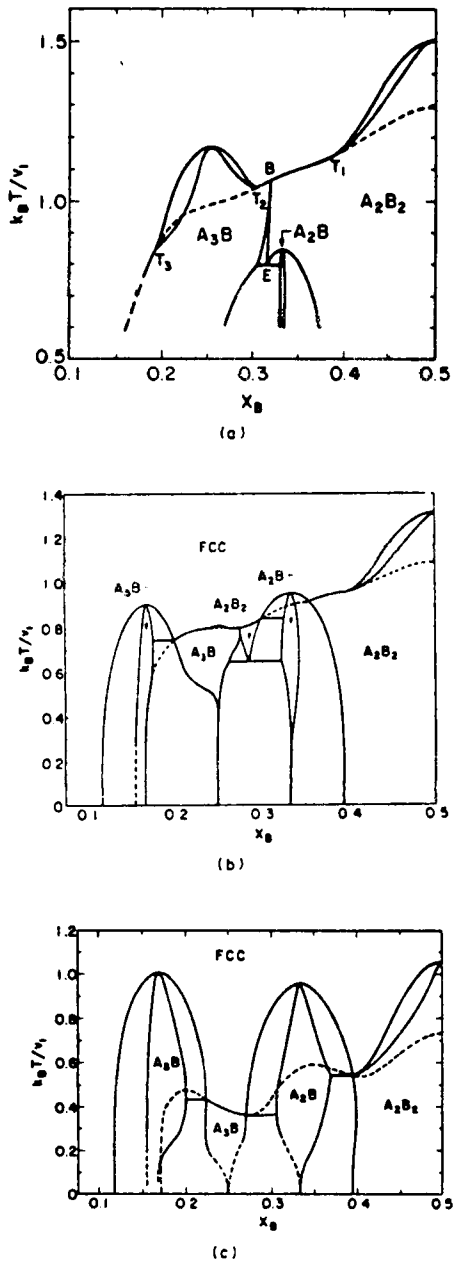


Figure IV-69. Temperature-composition phase diagrams calculated for three values of the ratio of second to first pairwise interaction parameters (V_2/V_1). a) 0.25; b) 0.35; c) 0.45. Dashed lines are locus of the {1 1/2 0} ordering spinodal.

Source: J. M. Sanchez and D. DeFontaine, "Ordering in Fcc Lattices with First- and Second-neighbor Interactions," Phys. Rev. B, 21, 216-228 (1980); ibid, "Ising Model Phase-Diagram Calculations in the FCC lattice with first- and second-neighbor Interactions," Phys. Rev. B, 25, 1759-1765 (1982).

vacancy, atom size and vibrational effects are ignored. The Ni_4Mo phase was not included in these calculations, since fourth nearest neighbor interactions have to be considered before it becomes a unique ground state structure (273). However, this phase is expected to be stable at low temperatures (271).

The phase diagrams in Figure IV-69 predict that a reduction of the V_2/V_1 ratio will cause an increase in the stability of the DO_{22} phase relative to the Ni_2Mo structure. In the present study, the DO_{22} structure is observed (at least initially, before it transforms to Ni_3Mo) at 850, 800 and 700°C, whereas the Ni_2Mo forms only at and below 700°C. Moreover, at 700°C a mixture of Ni_4Mo and Ni_2Mo transforms to DO_{22}, and also, with an increase in chromium content, the amount of Ni_4Mo and Ni_2Mo decreases and that of DO_{22} increases till eventually at 3.84 wt pct chromium neither Ni_4Mo nor Ni_2Mo are present. These results together with the composition analyses indicates that partial substitution of the molybdenum by the chromium probably leads to a reduction in the V_2/V_1 ratio, which in turn, renders the DO_{22} structure more stable relative to the Ni_2Mo, in accord with phase diagrams in Figure IV-69. However, present models do not permit prediction of the relative stability of either the DO_{22} or Ni_2Mo with respect to Ni_4Mo, which is observed upto 800°C. The absence of the DO_{22} structure at 600°C cannot be due a change in the behavior of the pair interaction energies (that is, the V_2/V_1 ratio), since these are justifiably independent of temperature (268-271). It is more probably related to the sluggish kinetics, since the low temperature does not provide sufficient diffusion required for formation of the DO_{22} from a mixture of Ni_4Mo and Ni_2Mo.

Ternary Ni-Mo-Cr Phase Diagram

On combining the results of the present investigation on the types and compositions of phases observed in alloys containing chromium in the range 2 to 4 wt pct with earlier results on the types of phases observed in alloys containing chromium in the range 0 to 1 wt pct (9), it is possible to propose a ternary Ni-Mo-Cr phase diagram for alloys near the Ni_4Mo composition. The phase relationships are somewhat straightforward at 850 and 800°C compared to that 700°C. At 850 and 800°C, increase in chromium content causes a progressive change from β to $\alpha + \beta + \gamma$ to $\alpha + \gamma$. At 700°C, increase in chromium changes the structure from β to $\beta + \gamma + \varepsilon$ to $\alpha + \beta + \gamma + \varepsilon$ to $\alpha + \gamma$. The Ni_2Mo (ε) phase, although metastable in the Ni-Mo binary phase diagram is present, together with Ni_4Mo, in large amounts in the ternary 2.08 wt pct Cr alloy. This indicates that the Ni_2Mo may be stabilized in this alloy. In comparison, there are four phases (α, β, γ, ε) present at the end of 4500 hours in the 2.97 wt pct Cr alloy, although the amounts of β and ε are substantially lower. Four phases can exist in equilibrium in a three-component system only at an invariant point. The chances of encountering such a point in practice are quite remote. In view of the small amounts of β and ε present, coupled with the appearance of the α phase in the 2.97 wt pct Cr alloy, and occurrence of only α and γ in the 3.84 wt pct Cr alloy, it is reasonable to expect that the 2.97 wt pct Cr alloy will also be eventually converted to α and γ. On this basis it is concluded that at 700°C, increase in chromium changes the phase relationships from β to $\beta + \gamma + \varepsilon$ to $\alpha + \gamma$.

Isothermal sections of the ternary Ni-Mo-Cr phase diagram at 850 and 800°C around the Ni_4Mo composition derived on the basis of this limited investigation are displayed in Figures IV-70 and -71. Since the phase relationships are quite complicated at 700°C, an isothermal section for this temperature has not been proposed. The present results suggest that the Ni_2Mo phase, although metastable in the binary Ni-Mo system, may be thermodynamically stable in the ternary Ni-Mo-Cr system at 700 and 600°C. The locations of the alloy compositions used in this study are identified by open circles. Closed circles represent data for the compositions of phases and dashed lines indicate approximate locations of phase boundaries not determined in the present study. The composition analyses (Table IV-3, page 345) reveals that with either an increase in chromium content in the alloy or more effectively a decrease in temperature, the composition of a particular phase shifts towards lower molybdenum and higher chromium contents, that of nickel remaining relatively unchanged. This behavior is clearly borne out in Figures IV-70 and -71. Despite the errors involved in the determination of the compositions of the phases, it is evident that Figures IV-70 and -71 predict the expected trend and provide a fairly good picture of the phase relationships at 800 and 850°C in Ni-Mo-Cr alloys near the Ni_4Mo composition. This demonstrates that analytical electron microscopy is indeed a powerful tool for providing fairly accurate determinations of ternary phase diagrams, even of relatively complex alloy systems.

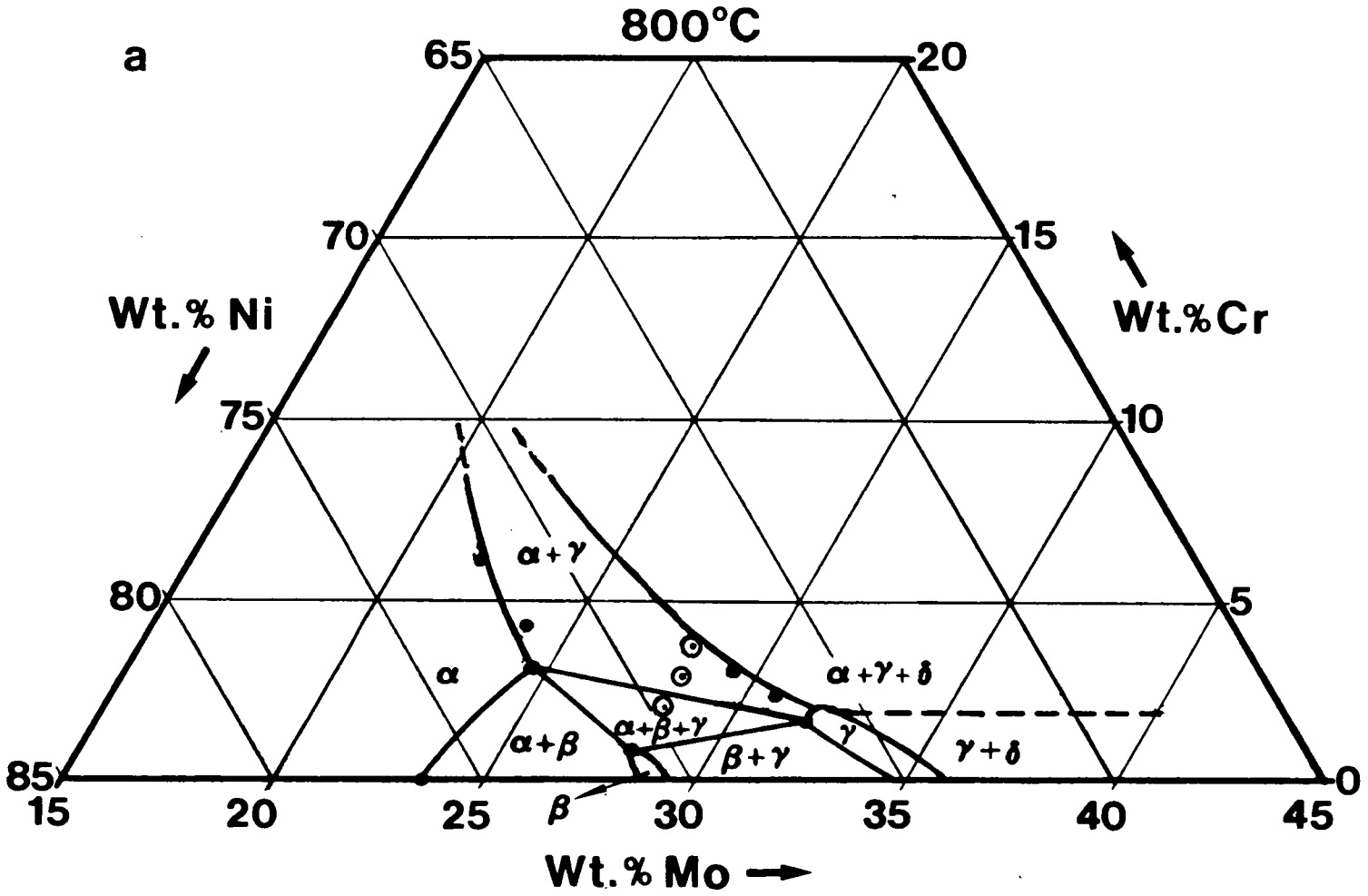


Figure IV-70. Isothermal sections of the ternary Ni-Mo-Cr phase diagram near the Ni_4Mo composition. a) 800°C; b) 850°C.

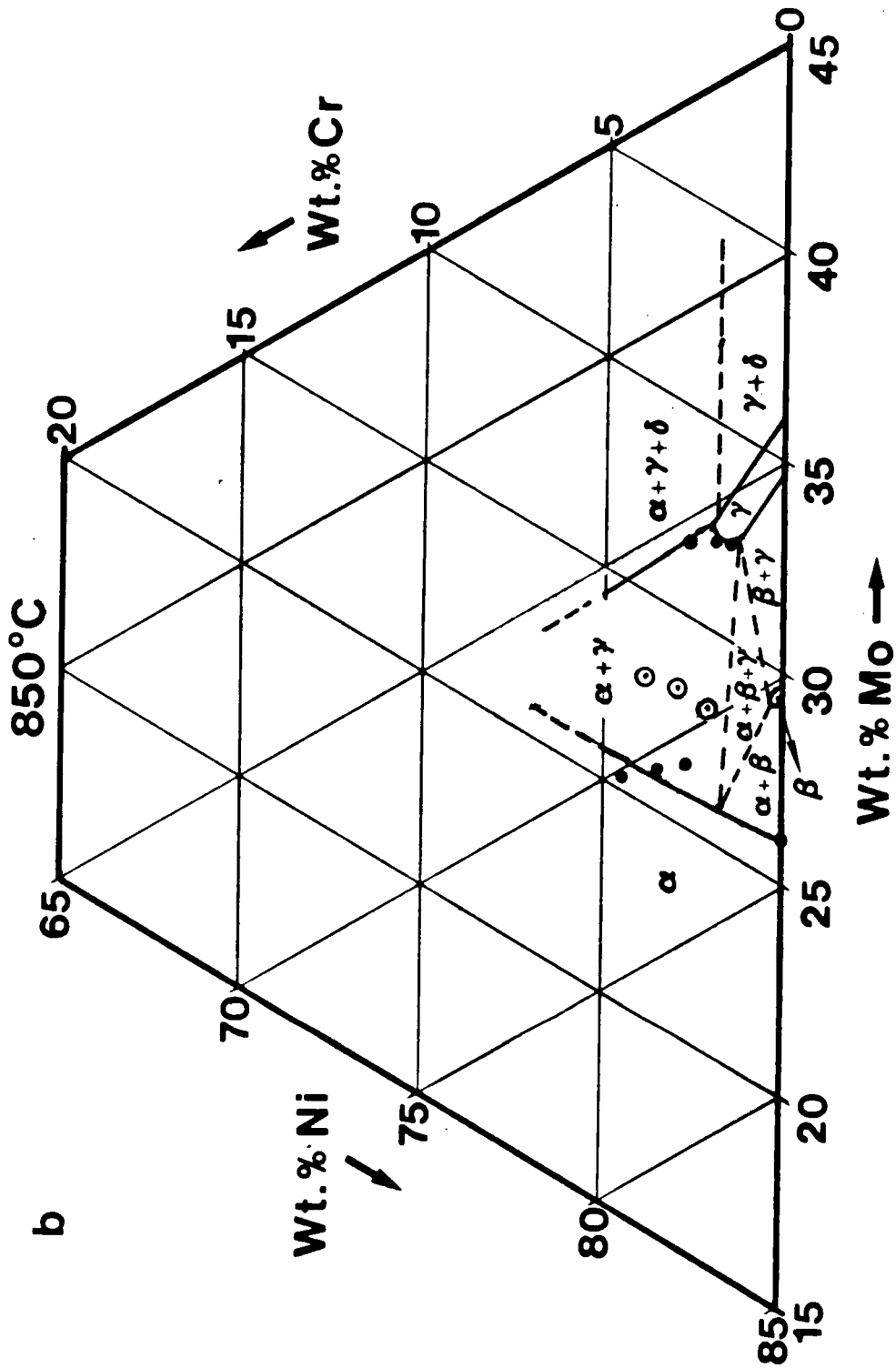


Figure IV-70. (Continued).

CHAPTER V

CONCLUSIONS

The objectives of this dissertation, which were outlined in Chapter I, have been completely fulfilled. Several major conclusions have resulted from this study. These are presented below in two sections: one for the binary Ni_4Mo and a second for the ternary Ni_4Mo-Cr alloys.

Binary Ni_4Mo Alloy

1. The resistivity changes associated with SRO and LRO in Ni_4Mo have been completely characterized. Salient features of these changes are:

1.1. Fast cooling from above the LRO-SRO transition temperature results in retention of SRO with resistivities of 144 and 139 micro-ohm-cm at 25 and -269^{o}C, respectively. The corresponding resistivities of the fully LRO state obtained by slow cooling are 48 and 8 micro-ohm-cm, respectively.

1.2 Increase in cooling rate within the range permitting LRO, results in an increase in the room temperature resistivity and a decrease in domain size. This increase in resistivity is attributed to the primary influence of a decrease in the degree of LRO with cooling rate.

1.3 The negative temperature coefficient of resistivity that is observed in the SRO state above the critical temperature is probably associated with the interaction between the change in the degree of

SRO with temperature and s-d electron scattering; decrease in the degree of SRO (increase in temperature) decreases such scattering and leads to a decrease in resistivity.

1.4 A decrease in slope of the LRO resistivity-temperature curve in the temperature range -150 to 600^{o}C is attributed to the temperature dependence of s-d electron scattering; increase in temperature decreases such scattering, thereby increasing n_{eff} and decreasing the slope.

1.5 The first order phase change in Ni_4Mo, indicated by the discontinuous change in the resistivity on continuous heating and cooling, permits quenching-in from near the ordering temperature specific degrees of LRO, as is evident from quenched-in increases in resistivity values.

2. The {111} fcc striations observed in the optical microstructure are intrinsic stacking faults/twins, and form primarily due to quenching stresses. The faults are usually overlapping and there is a one-to-one correspondence between the faults and the twins. The presence of these faults is explained on the basis of structural and nearest neighbor bond considerations.

3. The {110} fcc striations are an optical manifestation of the perpendicular twin boundaries. Each striation consists of groups of APT-related domains. An atomistic mechanism is proposed for the change in morphology of these striations from tapered at short aging times to straight at longer aging times.

4. Domain growth in Ni_4Mo can be described by the relationship $D^n = kt$, in a manner parallel to metallurgical grain growth. The value

of the exponent n (1/slope of the logD versus logt plot) changes from 2 at 850 and 800°C to 3 at 600°C. This change is attributed to domain orientation effects. The activation energy for domain growth is obtained as 80 kcal/mole.

5. The domain coarsening reaction that is observed at the grain boundaries on low temperature aging (700 and 600°C) involves formation of groups of domains separated by APB's on low energy {110} fcc planes. The primary driving force for this reaction is the reduction in interfacial energy obtained by elimination of the APB's between the small intragrain domains, in support of Chakravarti et al. (13). The difference in the degree of order between the coarse and fine domains also provides a contribution, at least initially, whereas ordering strains play a relatively insignificant role.

Ternary Ni_4Mo-Cr Alloys

1. Resistivity changes associated with ordering on continuous heating and slow cooling (9) have been explained using TEM. The Ni_4Mo domain size is decreased markedly by addition of chromium. The increase in LRO resistivity in the 2.08 wt pct Cr alloy (9) is attributed to the influence of increased electron scattering caused by chromium in solid solution, a decreased degree of LRO, and scattering caused by increased domain boundary area. The high resistivity of the 3.84 wt pct Cr alloy (9) is caused by a completely SRO state. In the 2.08 wt pct Cr alloy, both Ni_2Mo and Ni_3Mo are observed.

2. The isothermal transformation behavior at 850, 800, 700 and 600°C of ternary Ni_4Mo alloys containing chromium in the range 2 to 4

wt pct have been studied. Salient features are summarized in the following.

2.1 A variety of Mo-rich second phases, such as DO_{22}, Ni_3Mo, Ni_2Mo, and eta carbides are observed.

2.2 Prior grain size plays a significant role in governing the type, volume and distribution of phases. In coarse-grained specimens, a discontinuous precipitation of α and eta-carbides of type Mo_6Ni_6C (that is, $M_{12}C$) is observed on aging at 800 and 850°C. Other than the absence of this reaction in the fine-grained specimens, the types of phases observed in both cases are the same; only the amount of Ni_3Mo is greater in the fine-grained specimens, its formation is seen at shorter times, and the equilibrium state is attained faster.

2.3 At 850, 800 and 700°C, the DO_{22} structure is observed to form parallel to {111} fcc planes, from which Ni_3Mo forms directly.

2.4 At 700°C, the DO_{22} forms from bands composed of Ni_4Mo and Ni_2Mo aligned parallel to {111} fcc planes.

2.5 A second mechanism of formation of Ni_3Mo is observed at the grain boundaries on aging at 700 and 600°C, and closely follows the conventional sequence observed at lower temperatures (<800°C) in the binary Ni_3Mo alloy. Large domains of Ni_4Mo form at the grain boundaries. These domains subsequently transform to Ni_3Mo, with the simultaneous presence of stacking faults on (010) Ni_3Mo planes. In contrast to the binary Ni_3Mo, no evidence was obtained for the LPAPB structure (122,123,127-129) during this step.

2.6 Composition analyses of the phases has established that chromium predominantly substitutes for the molybdenum in Ni_4Mo-Cr alloys.

2.7 The relative stability of the DO_{22} with respect to the Ni_2Mo (ε) is probably associated with the reduction in the V_2/V_1 ratio (ratio of second to first pair interaction energies) caused by substitution of the molybdenum by the chromium.

2.8 With increase in chromium content, the phase relationships at equilibrium progressively change from β to $\alpha + \beta + \gamma$ to $\alpha + \gamma$ at 850 and 800°C, and from β to $\beta + \gamma + \varepsilon$ to $\alpha + \gamma$ at 700°C.

2.9 Isothermal sections at 800 and 850°C of the ternary Ni-Mo-Cr phase diagram near the Ni_4Mo composition have been proposed.

LIST OF REFERENCES

LIST OF REFERENCES

1. J. H. Westbrook, In: Order-Disorder Transformations in Alloys, H. Warlimont (ed.), Springer-Verlag, Berlin, New York, pp. 494-539 (1974).

2. K. Aoki and O. Izumi, Nippon Kinzaku Gakkaishi, 43 (12), pp. 1190-1195 (1979).

3. C. T. Liu and C. C. Koch, In: Technical Aspects of Critical Materials Used by the Steel Industry, National Bureau of Standards, Gaithersburg, IIB, pp. NBSIR 83-2679-2 (1983).

4. C. T. Liu, C. L. White, C. C. Koch, and E. H. Lee, In: Proc. Symp. High Temperature Materials Chemistry II, Z. A. Munir and D. Gubicciotti (eds.), The Electrochemical Society, Pennington, NJ, 83-7, pp. 32-41 (1983).

5. F. C. Hodge and R. W. Kirchner, Materials Performance, 15, pp. 40-45 (1976).

6. D. Harker, J. Chem. Phys., 12, p. 315 (1944).

7. P. V. Guthrie and E. E. Stansbury, "X-Ray and Metallographic Study of the Nickel-Rich Alloys of the Nickel-Molybdenum System," ORNL-Report 3078, Oak Ridge National Laboratary: , Oak Ridge, Tennessee (1961).

8. T. S. Lei, "The Effect of 0-8 Wt.% Iron on Transformations of Alpha Phase Ni-Mo-Fe Alloys with Ni:Mo Ratio Equal to 4:1," Ph.D. Dissertation, University of Tennessee, Knoxville (1979).

9. K. Vasudevan, "The Effect of 0-4 Weight Percent Chromium on Transformations of Alpha Phase Ni-Mo-Cr Alloys with Nickel: Molybdenum Atom Ratio Equal to 4:1," M.S. Thesis, University of Tennessee, Knoxville (1982).

10. E. E. Stansbury, K. Vasudevan, and T. S. Lei, In: Microstructural Science, S. A. Shiels, C. Bagnall, R. E. Witkowski and G. F. Vander Voort (eds.), 13, pp. 197-219 (1985).

11. T. S. Lei, K. Vasudevan, and E. E. Stansbury, In: High-Temperature Ordered Intermetallic Alloys, C. C. Koch, C. T. Liu and N. S. Stoloff (eds.), Materials Research Society, Pittsburg, 39, pp. 163-172 (1985).

12. W. B. Snyder and C. R. Brooks, In: Ordered Alloys - Structural Applications and Physical Metallurgy, B. H. Kear, C. T. Sims, N. S. Stoloff and J. H. Westbrook (eds.), Claitor's, Baton Rouge, pp. 275-296 (1970).

13. B. Chakravarti, E. A. Starke, and B. G. LeFevre, J. Mats. Sci., 5, pp. 394-406 (1970).

14. K. C. Chen, F. W. Ling, and E. A. Starke Jr., Mat. Sci. Eng., 13, pp. 255-262 (1974).

15. T. Saburi, H. Fujii, and S. Nenno, J. Phys. Soc. Japan, 35, pp. 1386-1393 (1973).

16. G. I. Nosova and N. A. Polyakova, Phys. Met. Metallog., 48, pp. 178-180 (1978).

17. G. I. Nosova and N. A. Polykova, Fiz. Met. Metalloved., 39, pp. 837-843 (1975).

18. G. I. Nosova and N. A. Polyakova, Phys. Met. Mettalog., 42, pp. 98-104 (1976).

19. C. R. Brooks, J. E. Spruiell, and E. E. Stansbury, Inter. Met. Rev., 29 (3), pp. 210-248 (1984).

20. W. E. Norem and E. E. Stansbury, "An Investigation of Nickel-Rich Alloys Containing Molybdenum and Iron," Report to Union Carbide, Oak Ridge National Laboratary, Oak Ridge, Tennessee (1963).

21. K. Vasudevan and E. E. Stansbury, Scripta Met., 19 (9), pp. 1101-1106 (1985).

22. C. P. Fryer, "The Effect of One-Half and One Atomic Percent Additions of Iron, Aluminum, Silicon and Chromium on the Ordering Reaction of Ni_4Mo," M.S. Thesis, University of Tennessee (1982).

23. V. I. Kiriyenko, E. E. Poplavskaya, and L. P. Potapov, Phys. Met. Metallog., 33, pp. 132-138 (1972).

24. E. N. Vlasova, Y. D. Tyapkin, and V. D. Plakhiti, Sovt. Phys. Dokl., 19, p. 32 (1974).

25. Hastelloy--Development Alloy B-2, Stellite Division, Cabot Corporation, Kokomo, Indiana.

26. R. E. Clausing, P. Patriarca, and W. D. Manly, Trans. ASM., 51, p. 123 (1959).

27. D. Y. Roan, "Microstructure and Mechanical Properties of Hastelloy B-2 and its Wear Behavior Against Graphite in a Simulated Mechanical Face Seal," M.S. Thesis, University of Tennessee (1969).

28. G. N. Flint, J. Inst. Metals., 87, p. 303 (1958/59).

29. E. Ruedl, Mat. Res. Bull., 10, p. 1267 (1975).

30. H. M. Tawancy, J. Mat. Sci., 15, pp. 2597-2604 (1980).

31. H. M. Tawancy, Scripta Met., 18, pp. 343-346 (1984).

32. H. M. Tawancy and A. I. Asphahani, In: High-Temperature Ordered Intermetallic Alloys, C. C. Koch, C. T. Liu and N. S. Stoloff (eds.), Materials Research Society, Pittsburg, 39, pp. 485-494 (1985).

33. J. E. Spruiell, "X-Ray Study of Short Range Order in Nickel Alloys Containing 10.7 and 20.0 Atomic Percent Molybdenum," Ph.d. Dissertation, University of Tennessee, Knoxville (1963).

34. G. Tammann, Z. Anorg. Allgem. Chem., 37, p. 303 (1903).

35. G. Tammann, Z. Anorg. Chem., 45, p. 24 (1905).

36. G. Tammann, Z. Anorg. Chem., 47, p. 296 (1906).

37. G. Tammann, A. Anorg. Chem., 107, p. 1 (1919).

38. V. I. Smirnov and N. S. Kurnakov, Z. Anorg. Allgem. Chem., 72, p. 31 (1911).

39. N. S. Kurkanov, S. F. Zhemchuzhni, and M. Zasedatelev, Izv. St. Petersburgskogo Politekh. Inst., 22, p. 487 (1914).

40. E. C. Bain, Chem. Met. Eng., 28, p. 21 (1923).

41. E. C. Bain, Trans. AIME, 68, p. 625 (1923).

42. C. H. Johannson and J. O. Linde, Amer. Physik, 78, p. 439 (1925).

43. F. C. Nix and W. Shockley, Rev. Mod. Phys., 10 (1), pp. 1-71 (1938).

44. H. Lipson, Progr. Mater. Sci., 2, pp. 1-52 (1950).

45. L. Guttman, Solid State Phys., 3, pp. 145-223 (1956).

46. T. Muto and Y. Takagi, Solid State Phys., 1, p. 193 (1955).

47. C. S. Barrett and T. B. Massalski, The Structure of Metals Third Edition, McGraw Hill, New York (1966).

48. J. B. Cohen, In: Phase Transformations, American Society Metals, Metals Park, Ohio, pp. 561-625 (1970).

49. J. W. Christian, The Theory of Transformations in Metals and Alloys, Pergamon Press, Oxford (1975).

50. M. A. Krivoglaz and A. Smirnov, The Theory of Order-Disorder in Alloys, Macdonald, London (1964).

51. J. H. Westbrook (ed.), Intermetallic Compounds, Wiley, New York (1967).

52. H. Warlimont (ed.), Order-Disorder Transformations in Alloys, Springer-Verlag, Berlin/New York (1974).

53. B. H. Kear, C. T. Sims, N. S. Stoloff, and J. H. Westbrook (eds.), Ordered Alloys--Structural Applications and Physical Metallurgy, Claitor's, Baton Rouge (1970).

54. C. C. Koch, C. T. Liu, and N. S. Stoloff (eds.), High-Temperature Ordered Intermetallic Alloys, Materials Research Society, Pittsburg (1985).

55. N. S. Stoloff and R. G. Davies, Prog. Mater. Sci., 13 (6), pp. 1-84 (1966).

56. N. S. Stoloff, In: Strengthening Methods in Crystals, A. Kelly and R. B. Nicholson (eds.), Elsevier, New York, pp. 193-259 (1971).

57. A. G. Khachaturyan, Progr. Mater. Sci., 22, pp. 1-150 (1978).

58. F. Reynaud, Phys. Stat. Sol. (a), 72, pp. 11-59 (1982).

59. N. S. Stoloff, Int. Met. Rev., 29, p. 123 (1984).

60. W. L. Bragg and E. J. Williams, Proc. Roy. Soc., London, A145, p. 699 (1934).

61. H. A. Bethe, Proc. Roy. Soc., London, A150, p. 552 (1935).

62. J. E. Spruiell and E. E. Stansbury, J. Phys. Chem. Sol., 26, p. 811 (1965).

63. T. P. Chang, "Investigation of Ordering in Nickel-10 and -20 Atomic Percent Molybdenum by Electrical Resistivity Measurements," M.S. Thesis, University of Tennessee, Knoxville (1965).

64. Landolt-Bornstein, Springer-Verlag, Berlin/New York (1971).

65. J. M. Cowley, Phys. Rev., 77, p. 669 (1950).

66. J. M. Cowley, J. Appl. Phys., 21, p. 24 (1950).

67. J. M. Cowley, Phys. Rev., 120, p. 164 (1960).

68. G. J. Dienes, Acta Met., 3, p. 549 (1955).

69. R. Kikuchi, Phys. Rev., 81, p. 988 (1951).

70. M. Kurata, R. Kikuchi, and T. Watari, J. Chem. Phys., 21, p. 434 (1953).

71. L. D. Landau and E. M. Lifshitz, Statistical Physics, Addison-Wesley, Reading, MA (1958).

72. E. V. Kozlov and V. M. Dementev, Fiz. Met. Metalloved., 35, p. 500 (1973).

73. F. Gautier, F. Ducastelle, and J. Giner, Phil. Mag., 31, p. 1373 (1975).

74. I. G. Batirev, A. A. Katsnelson, L. Kertesz, and A. Szasz, Phys. Stat. Sol. (b), 101, p. 163 (1980).

75. F. Brouers, J. Giner, and J. van der Rest, J. Phys. F: Metal Physics, 4, p. 214 (1974).

76. F. Ducastelle and F. Gautier, J. Phys. F: Metal Physics, 6, p. 2039 (1976).

77. W. Hume-Rothery and H. M. Powell, Z. Kristallogr., 23, p. 91 (1935).

78. G. V. Raynor, In: Progress in Metal Physics I, London (1949).

79. H. Sato, R. S. Toth, and G. Honjo, J. Phys. Chem. Solids, 28, p. 137 (1967).

80. J. W. Gibbs, Scientific Papers, Dover, New York., 1, (1961).

81. L. A. Nesbit and D. E. Laughlin, Acta Met., 26, p. 815 (1978).

82. R. S. Irani, Contemp. Physics, 13, p. 559 (1972).

83. J. B. Newkirk, A. H. Geisler, D. L. Martin, and R. Smoluchowski, Trans. AIME, 188, p. 1249 (1950).

84. P. S. Rudman, In: Intermetallic Compounds, J. H. Westbrook (ed.), Wiley, New York (1967).

85. J. W. Steeds, In: Introduction to Analytical Electron Microscopy, J. J. Hren, J. I. Goldstein and D. C. Joy (eds.), Plenum Press, New York, pp. 387-422 (1979).

86. D. B. Williams, Norelco Reporter, 30 (2), pp. 24-53 (1983).

87. M. Raghavan, J. Y. Koo, and R. Petkovic-Luton, Norelco Reporter, 31 (1), pp. 32-38 (1984).

88. J. I. Goldstein, In: Introduction to Analytical Electron Microscopy, J. J. Hren, J. I. Goldstein and D. C. Joy (eds.), Plenum Press, New York, pp. 83-120 (1979).

89. R. W. Newman and J. J. Hren, Phil. Mag., 16, pp. 211-214 (1967).

90. V. I. Kiriyenko and L. P. Potapov, Phys. Met. Metallog., 31, pp. 102-108 (1971).

91. M. N. Chandrasekharaiah, S. Ranganathan, P. R. Okamoto, and G. Thomas, Mat. Res. Bull., 7, pp. 13-18 (1972).

92. P. R. Okamoto and G. Thomas, Acta Met., 19, p. 825 (1971).

93. J. Vrigen, P. M. Bronsveld, J. van der Veen, and S. Radelaar, Z. Metallk., 67, p. 473 (1976).

94. A. M. Moisin, Phys. Stat. Sol. (a), 47, p. 305 (1978).

95. C. Sykes and H. Evans, J. Inst. Metals, 58, p. 235 (1936).

96. R. Feder, M. Mooney, and A. S. Nowick, Acta Met., 6, pp. 266-277 (1958).

97. J. Rothstein, Phys. Rev., 94, p. 1429A (1954).

98. G. H. Vineyard, Phys. Rev., 102, pp. 981-992 (1956).

99. A. S. Nowick and L. R. Weisberg, Acta Met., 6, pp. 260-265 (1958).

100. H. Yamuchi and D. de Fontaine, In: Order-Disorder Transformations in Alloys, H. Warlimont (ed.), Springer-Verlag, New York (1974).

101. H. Sato and R. Kikuchi, Acta Met., 24, p. 797 (1976).

102. H. E. Cook, D. De Fontaine, and J. E. Hilliard, Acta Met., 17, p. 765 (1969).

103. D. De Fontaine and H. E. Cook, In: Critical Phenomena in Alloys, Magnets and Superconductors, R. E. Mills, E. Ascher and R. I. Jaffee (eds.), McGraw-Hill, New York, p. 257 (1971).

104. F. W. Ling and E. A. Starke Jr., Scripta Met., 5, pp. 741-748 (1971).

105. L. E. Tanner and H. J. Leamy, In: Order-Disorder Transformations in Alloys, H. Warlimont (ed.), Springer-Verlag, Berlin, pp. 180-239 (1974).

106. J. W. Cahn, Acta Met., 9, pp. 795-801 (1961).

107. R. Muto, Phys. Chem. Research Sci. Papers, Tokyo, 30, p. 99 (1936).

108. G. J. Dienes, J. Appl. Phys., 22, pp. 1020-1026 (1951).

109. G. Grube and H. Schlect, Z. Elektrochem., 44, p. 413 (1938).

110. N. Baar, Z. Anorg. Chem., 70, p. 353 (1911).

111. Dreibholz, Z. Physik Chem., 108, p. 8 (1924).

112. W. Koster and W. Schmidt, Arch. Eisenhutten, 8, p. 413 (1934-35).

113. F. H. Ellinger, Trans. AIME, 30, p. 607 (1942).

114. M. Hansen, Constitution of Binary Alloys, Second Ed., McGraw-Hill, New York (1958).

115. R. E. W. Casselton and W. Hume-Rothery, J. of the Less Common Metals, 7, p. 212 (1964).

116. P. R. Okamoto and G. Thomas, Mat. Res. Bull., 6, pp. 45-50 (1971).

117. E. Ruedl, P. Delavignette, and S. Amelinckx, Mat. Res. Bull., 2, pp. 1045-1054 (1967).

118. E. Ruedl, P. Delavignette, and S. Amelinckx, Phys. Stat. Sol., 28, p. 305-328 (1968).

119. S. Saito and P. Beck, Trans. Met. Soc. AIME, 215, pp. 938-941 (1959).

120. E. Ruedl and S. Amelinckx, Mat. Res. Bull., 4, pp. 361-368 (1969).

121. G. Van Tendeloo, P. Delavignette, R. Gevers, and S. Amelinckx, Phys. Stat. Sol. (a), 18, p. 85 (1973).

122. G. Van Tendeloo, J. Van Landuyt, P. Delavignette, and S. Amelinckx, Phys. Stat. Sol. (a), 25, pp. 697-707 (1974).

123. G. Van Tendeloo, P. Delavignette, J. Van Landuyt, and S. Amelinckx, Phys. Stat. Sol. (a), 26, pp. 299-304 (1974).

124. T. Saburi, K. Komatsu, M. Yamamoto, S. Nenno, and Y. Mizutani, Trans. Met. Soc. AIME, 245, pp. 2348-2349 (1969).

125. M. Yamamoto, S. Nenno, T. Saburi, and Y. Mizutani, Trans. Japanese Inst. of Metals, 11, pp. 120-126 (1970).

126. S. K. Das and G. Thomas, Phys. Stat. Sol. (a), 21, p. 177 (1974).

127. G. Van Tendeloo, R. De Ridder, and S. Amelinckx, Phys. Stat. Sol. (a), 27, p. 457 (1975).

128. G. Van Tendeloo, Mater. Sci. Eng., 26, pp. 209-220 (1976).

129. D. Schryvers, G. Van Tendeloo, and S. Amelinckx, Phys. Stat. Sol. (a), 87, pp. 401-415 (1985).

13Q. C. B. Shoemaker, A. H. Fox and D. P. Shoemaker, Acta Cryst., 13, 585-587 (1960).

131. C. B. Shoemaker and D. P. Shoemaker, Acta Cryst., 16, p. 997 (1963).

132. G. Van Tendeloo and S. Amelinckx, Mat. Res. Bull., 8, pp. 721-732 (1973).

133. L. E. Tanner, Acta Met., 20, pp. 1197-1227 (1972).

134. J. Mayer and K. Urban, Phys. Stat. Sol. (a), 90, pp. 469-475 (1985).

135. H. Thomas, Z. Physik, 129, pp. 219-232 (1951).

136. G. V. Starikova and A. A. Presnyakov, Phys. Met. Metallog., 10, pp. 943-945 (1960).

137. V. S. Meskin, R. I. Sergienko, and L. A. Potapov, Phys. Met. Metallog., 13, pp. 113-117 (1962).

138. P. Chevenard, J. Inst. Metals, 36, p. 46 (1926).

139. E. E. Stansbury, C. R. Brooks, and T. L. Arledge, J. Inst. Metals, 94, pp. 136-138 (1966).

140. H. G. Baer, Z. Metallkde., 56, p. 79 (1965).

141. B. T. Lampe, "An Investigation of the Order-Disorder Transformation in the Nickel-29.9% Molybdenum Alloy by Electrical Resistivity Measurements," M. S. Thesis, University of Tennessee, Knoxville (1965).

142. B. G. LeFevre, A. G. Guy, and R. W. Gould, Met. Trans., 242, p. 788 (1968).

143. W. H. Aarts and A. S. Houston-Macmillan, Acta Met., 5, pp. 525-527 (1957).

144. H. J. Logie, J. Jackson, J. C. Anderson, and F. R. N. Nabarro, Acta Met., 9, p. 707 (1961).

145. H. G. Muller and P. Muth, Z. Metallk., 50, p. 217 (1959).

146. W. Chen and M. E. Nicholson, Acta Met., 12, p. 687 (1964).

147. A. C. Damask, J. Phys. Chem., 1, pp. 23-26 (1956).

148. A. C. Damask, J. Appl. Phys., 27, pp. 610-616 (1956).

149. B. Chakravarti, E. A. Starke, C. J. Sparks, and R. O. Williams, J. Phys. Chem. Sol., 35, pp. 1317-1326 (1974).

150. T. Saburi, K. Komatsu, and S. Nenno, Phil. Mag., 20, pp. 1091-1094 (1969).

151. S. K. Das, P. R. Okamoto, P. M. J. Fischer, and G. Thomas, Acta Met., 21, p. 913 (1973).

152. S. K. Das and G. Thomas, In: Order-Disorder Transformations in Alloys, H. Warlimont (ed.), Springer-Verlag, New York/ Berlin, pp. 332-343 (1974).

153. G. Thomas and R. Sinclair, Acta Met., 25, p. 231 (1977).

154. G. Thomas and M. J. Goringe, Transmission Electron Microscopy of Materials, John Wiley, New York, pp. 106-108 (1979).

155. J. P. A. A. Chevalier and W. M. Stobbs, Acta Met., 24, p. 535 (1976).

156. W. M. Stobbs and J. P. A. A. Chevalier, Acta Met., 26, p. 233 (1978).

157. J. P. A. A. Chevalier and W. M. Stobbs, Acta Met., 27, pp. 1197-1217 (1979).

158. J. P. A. A. Chevalier, J. Microsc., 119, pp. 113-124 (1980).

159. S. Banerjee, K. Urban, and M. Wilkene, In: Solid-Solid Phase Transformations, H. I. Aaronson, D. E. Laughlin, R. F. Sekerka and C. M. Wayman (eds.), Met. Soc. AIME, Pittsburg, pp. 311-315 (1982).

160. S. Banerjee, K. Urban, and M. Wilkens, Acta Met., 32, pp. 299-311 (1984).

161. J. Mayer and K. Urban, Acta Met., 33 (4), pp. 539-543 (1985).

162. B. G. LeFevre, M. Grenga, and B. Ralph, Phil. Mag., 18, p. 1127 (1968).

163. B. G. LeFevre and R. W. Newman, Georgia Inst. Tech., Atlanta, GA, (1968).

164. M. Yamamoto, S. Nenno, M. Futamoto, and S. Nakanura, Japanese Jnl. of Applied Physics, 11, pp. 437-444 (1972).

165. M. Yamamoto, S. Nenno, and F. Shohno, Jpn. J. Appl. Phys., 16, pp. 2045-2046 (1977).

166. M. Yamamoto, T. Hashizume, and T. Sakurai, Scripta Met., 19, pp. 357-360 (1985).

167. P. C. Clapp and S. C. Moss, Phys. Rev., 142, p. 418 (1966).

168. P. C. Clapp and S. C. Moss, Phys. Rev., 171, p. 754 (1968).

169. P. C. Clapp and S. C. Moss, Phys. Rev., 171, p. 764 (1968).

170. J. M. Cowley, In: The Chemistry of Extended Defects in Non-Metallic Solids, L. Eyring and M. OKeeffee (eds.), North-Holland, Amsterdam/New York (1970).

171. E. E. Stansbury, In: High-Temperature Ordered Intermetallic Alloys, C. C. Koch, C. T. Liu and N. S. Stoloff (eds.), Materials Research Society, Pittsburg, 39, pp.93-107 (1985).

172. R. De Ridder, G. Van Tendeloo, and S. Amelinckx, Acta Cryst., 32, pp. 216-224 (1976).

173. A. G. Khachaturyan, In: Order-disorder Transformations in Alloys H. Warlimont (ed.), Springer-Verlag, New York, pp. 114-131 (1974).

174. D. De Fontaine, Acta Met., 23, pp. 553-571 (1975).

175. H. E. Cook, Mater. Sci. Eng., 25, p. 127 (1976).

176. L. N. Larikov, V. V. Geichenko, and V. M. Fal'chenko, Diffusion Processes in Ordered Alloys, Amerind Pub. Co., New Delhi, India, (1981).

177. R. S. Irani, F. W. Ling, and R. W. Cahn, Metallography, 6, pp. 141-153 (1973).

178. F. W. Ling and E. A. Starke Jr., Acta Met., 19, pp. 759-768 (1971).

179. N. S. Stoloff and R. G. Davies, Acta Met., 12, pp. 473-485 (1964).

180. V. S. Arunachalam and R. W. Cahn, J. Mater. Sci., 2, p. 160 (1967).

181. R. S. Irani and R. W. Cahn, Acta Met., 21, pp. 575-584 (1973).

182. F. W. Ling, R. S. Irani, and R. W. Cahn, Mat. Sci. Engr., 15, pp. 181-186 (1974).

183. J. E. Spruiell, L. M. Ruch, and C. R. Brooks, Met. Trans., 6A, p. 1301 (1975).

184. J. W. Goodrum and B. G. LeFevre, Met. Trans., 8A, p. 939 (1977).

185. T. Saburi, E. Kanai, and S. Nenno, J. of Less Common Metals, 37, p. 59 (1974).

186. L. A. Nesbit and D. E. Laughlin, Acta Met., 28, pp. 989-998 (1980).

187. Yu. D. Tyapkin, G. I. Nosova, E. N. Polyakova, and V. D. Plakhtiy, Fiz. Met. Metalloved., 41, pp. 441-443 (1976).

188. D. Harker, Trans. ASM, 32, pp. 210-238 (1944).

189. V. I. Kiriyenko and L. P. Potapov, Phys. Met. Metallog., 38, pp. 817-821 (1974).

190. L. F. Artisishevskaya, I. B. Malysheva, and YA. P. Selisskiy, Phys. Met. Metallog., 33, pp. 144-148 (1978).

191. L. E. Tanner, Phys. Stat. Sol., 30, pp. 685-701 (1968).

192. E. E. Stansbury, Unpublished research, The University of Tennessee, Knoxville (1966).

193. A. Bazorgzard and C. R. Brooks, Unpublished research, University of Tennessee, Knoxville (1977).

194. A. C. Fraker and H. H. Stadelmaier, Trans. Met. Soc. AIME, 245, pp. 847-850 (1969).

195. C. P. Heijwegen and G. D. DiRieck, Met. Trans., 4, pp. 2159-2167 (1973).

196. H. M. Tawancy, J. Mater. Sc. Letters, 16, pp. 1117-1118 (k1981).

197. J. S. Koehler and F. Seitz, J. Appl. Mech., 14, p. A217 (1947).

198. W. Bell, W. R. Roser, and G. Thomas, Acta Met., 11, p. 1247 (1964).

199. B. H. Kear, Acta Met., 12, p. 555 (1964).

200. M. J. Marcinkowski, Phil. Mag., 6, p. 871 (1961).

201. M. J. Marcinkowski and R. M. Fisher, J. Appl. Phys., 34, p. 2135 (1963).

202. M. J. Marcinkowski and H. Chessin, Phil. Mag., 10, p. 837 (1964).

203. N. S. Stoloff, In: High-Temperature Ordered Intermetallic Alloys, C. C. Koch, C. T. Liu and N. S. Stoloff (eds.), Materials Research Society, Pittsburg, 39, pp. 3-27 (1985).

204. P. A. Flinn, Trans. AIME, 218, p. 145 (1960).

205. W. J. M. Tegart, The Electrolytic and Chemical Polishing of Metals in Research and Industry, Pergamon, New York (1959).

206. L. E. Murr, Electron Optical Applications in Materials Science, McGraw-Hill, New York (1970).

207. G. Thomas and M. J. Goringe, Transmission Electron Microscopy of Materials, Wiley-Interscience, New York (1979).

208. P. J. Goodhew, Specimen Preparation for Transmission Electron Microscopy of Materials, Oxford University Press, Oxford (1984).

209. G. Cliff and G. W. Lorimer, J. Microscopy, 110, p. 107 (1975).

210. R. Tixier and J. Philibert, In: Proc. Fifth Int. Cong. on X-ray Optics and Microanalysis, G. Mollenstedt and K. H. Gaukler (eds.), Springer-Verlag, Berlin, p. 180 (1969).

211. J. Goldstein, J. L. Costley, G. W. Lorimer, and S. J. B. Reed, In: SEM/77, O. Johari (ed.), IITRI, Chicago, 1, p. 315 (1977).

212. B. M. Korevaar, Acta Met., 9, pp. 297-303 (1961).

213. B. G. Livshits and R. A. Rymashevskii, Phys. Met. Metallog., 13 (2), pp. 41-49 (1962).

214. E. A. Starke Jr, V. Gerold, and A. G. Guy, Acta Met., 13, p. 957 (1965).

215. A. van den Beukel, A. P. Matthijsen, J. M. J. Ritzen, and R. den Buurman, Acta. Met., 16, pp. 435-441 (1968).

216. C. J. van der Wekken, R. Taggart, and D. H. Polonis, Metal Science J., 5, pp. 219-223 (1971).

217. E. Torfs, L. Stals, J. van Landuyt, P. Delavignette, and S. Amelinckx, Phys. Stat. Sol. (a), 22, pp. 45-51 (1974).

218. R. J. Willey, J. Mater. Sci., 13, pp. 871-875 (1978).

219. Ye. N. Babanova, I. B. Klyuyeva, L. S. Chemerinskaya, and F. A. Siderenko, Phys. Met. Metallog., 49 (3), pp. 184-186 (1980).

220. F. Brouers and A. V. Vedyayev, Phys. Rev. B, 5 (2), pp. 348-360 (1972).

221. R. P. Vasilyeva, N. N. Narkulov, V. P. Fadin, and YU. N. Arkhipov, Phys. Met. Metallog., 48 (3), pp. 671-672 (1979).

222. M. K. Sardar and K. P. Gupta, Scripta Met., 14, pp. 835-838 (1980).

223. P. Meisterle and W. Pfeiler, Acta Met., 31, pp. 1543-1547 (1983).

224. J. B. Gibson, J. Phys. Chem. Solids, 1, pp. 27-34 (1956).

225. P. L. Rossiter and P. Wells, J. Phys. C: Solid St. Phys., 4, pp. 354-363 (1971).

226. P. L. Rossiter, J. Phys. F: Metal Phys., 7 (3), pp. 407-418 (1977).

227. D. Nicholson, Private communication, Oak Ridge National Laboratory, Oak Ridge, Tennessee (1984).

228. J. H. Mooji, Phys. Stat. Sol. (a), 17, pp. 521-530 (1973).

229. J. Richter and W. Schiller, Phys. Stat. Sol. (b), 92, pp. 511-517 (1979).

230. V. A. Phillips, Acta Met., 9, pp. 976-978 (1961).

231. Ye. V. Pal'guyev, A. A. Kuranov, P. N. Syutkin, and F. A. Siderenko, Phys. Met. Metallog., 41 (6), pp. 72-76 (1976).

232. M. J. Marcinkowski and R. Smoluchowski, J. Phys. Chem. Solids, 26, pp. 185-189 (1965).

233. M. Brauwers, J. Giner, J. Van der Rest, and F. Brouers, Solid State Comm., 17, pp. 229-232 (1975).

234. V. Christoph, J. Richter, and W. Schiller, Phys. Stat. Sol (b), 100, pp. 585-602 (1980).

235. P. L. Rossiter, J. Phys. F: Metal Phys., 9, pp. 891-901 (1979).

236. P. L. Rossiter, J. Phys. F: Metal Phys., 10, pp. 459-465 (1980).

237. P. L. Rossiter, J. Phys. F: Metal Phys., 11, pp. 615-621 (1981).

238. M. J. Whelan, In: Diffraction and Imaging Techniques in Material Science, S. Amelinckx, R. Gevers and J. Van Landuyt (eds.), North-Holland, Amsterdam/New York, Volume I: Electron Microscopy, pp. 43-106 (1978).

239. M. H. Loretto and R. E. Smallman, Defect Analysis in Electron Microscopy, Chapman and Hall, London (1975).

240. R. Gevers, A. Art, and S. Amelinckx, Phys. Stat. Sol., 3, p. 1563 (1963).

241. A. Art, R. Gevers, and S. Amelinckx, Phys. Stat. Sol., 3, p. 697 (1963).

242. H. P. Kao, "Dislocation Structure, Deformation Structure, Strengthening Mechanisms and Embrittlement Causes of Ordered Ni_4Mo Alloy," Ph.D. Dissertation, University of Tennessee, Knoxville, (1986).

243. J. A. Venables, In: Deformation Twinning, R. E. Reed-Hill, J. P. Hirth and H. C. Rogers (eds.), Gordon & Breach, New York, (1964).

244. V. Paidar, Phil. Mag., 52 (1), pp. 73-82 (1985).

245. R. E. Reed-Hill, Physical Metallurgy Principles, Van Nostrand Reinhold, New York pp. 202-212 (1972).

246. G. E. Poquette and D. E. Mikkola, Trans. Met. Soc. AIME, 245, pp. 743-751 (1969).

247. K. Hirano, R. P. Agarwala, and M. Cohen, J. Appl. Phys., 33, p. 3049 (1962).

248. J. Askill, In: Diffusion in Body-Centered Cubic Metals, ASM, Metals Park, pp. 247-252 (1965).

249. R. H. Moore, In: Diffusion in Body-Centered Cubic Metals, ASM Metals Park, pp. 275-281 (1965).

250. A. J. Ardell, N. Mardesich, and C. N. J. Wagner, Acta Met., 27, pp. 1261-1269 (1979).

251. R. Gevers, J. van Landuyt, and S. Amelinckx, Phys. Stat. Sol., 18, pp. 343-361 (1966).

252. J. van Landuyt, R. Gevers, and S. Amelinckx, Phys. Stat. Sol., 18, pp. 363-378 (1966).

253. G. Van Tendeloo and S. Amelinckx, In: Electron Microscopy in Material Science, G. E. Ruedl and U. Valdre (eds.), pp. 775-826 (1975).

254. S. Amelinckx, J. Less Common Metals, 28, pp. 325-355 (1972).

255. J. W. Cahn and R. Kikuchi, J. Phys. Chem. Solids, 20, p. 94 (1961).

256. R. Kikuchi and J. W. Cahn, J. Phys. Chem. Solids, 23, p. 137 (1962).

257. H. Gleiter, Acta Met., 17, pp. 565,853 (1969).

258. V. I. Gomankov, I. M. Puzey, Y. e. I. Mal'tsev, and E. D. Petrenko, Phys. Met. Metallog., 29 (2), pp. 212-215 (1970).

259. V. I. Gomankov, I. M. Puzey, and Y. e. I. Mal'tsev, Phys. Met. Metallog., 30 (1), pp. 237-240 (1970).

260. M. F. Collins and G. G. Low, Proc. Phys. Soc. (London), 86, pp. 535-548 (1965).

261. I. M. Puzey, V. I. Gomankov, and A. A. Loshmanov, Phys. Met. Metallog., 25 (1), pp. 30-37 (1968).

262. K. H. Kuo, Acta Met., 1, p. 301 (1953).

263. K. H. Kuo and C. L. Jia, Acta Met., 33 (6), pp. 991-996 (1985).

264. H. L. Yakel, Int. Metals Rev., 30 (1), pp. 17-40 (1985).

265. P. L. Martin and J. C. Williams, Acta Met., 32, pp. 1681-1693 (1984).

266. P. L. Martin and J. C. Williams, Acta Met., 32, pp. 1695-1702 (1984).

267. R. Gevers, J. van Landuyt, and S. Amelinckx, Phys. Stat. Sol., 26, pp. 577-590 (1968).

268. M. J. Richards and J. W. Cahn, Acta Met., 19, pp. 1263-1277 (1971).

269. S. M. Allen and J. W. Cahn, Acta Met., 20, pp. 423-433 (1972).

270. J. M. Sanchez and D. De Fontaine, Phys. Rev. B, 21 (1), pp. 216-228 (1980).

271. J. M. Sanchez and D. De Fontaine, Phys. Rev. B, 25 (3), pp. 1759-1765 (1982).

272. M. Yamamoto, F. Shohno, and S. Nenno, Trans. Japan Inst. Metals, 19, p. 475 (1978).

273. J. Kanamori and Y. Kakehashi, J. Phys. (Paris), 38, pp. Suppl. C7-274 (1978).

APPENDIX

TABLE A-1

Magnification Calibration of Philips EM300

CONDITIONS:

1. Operating Voltage = 100 KV.
2. Performed zero magnification setting as outlined in the manual.
3. Diffraction, intermediate and objective lenses reversed atleast twice ending in the '+' position; interval of 5 secs between reversals.

Selector #	M	SA
1	525*	9630
2	1050*	9630
3	1575*	9630
4	2100*	9630
5	2625*	9630
6	3150	9630
7	3676*	9630
8	4600*	9630
9	5800	9630
10	7523*	9630
11	10200	7485
12	13320*	8928
13	16500	10800
14	20640*	13122
15	25500	16046
16	31320*	19636
17	39250	23520
18	49779*	27772
19	59500	32760
20	72847*	40841
21	93500	51051
22	120255*	61262*
23	140000*	76500*
24	160000*	92500*
25	180000	107500

*Inter/extrapolated values

TABLE A-2

Rotation Calibration of Philips EM300

The rotation calibration was accomplished by using the standard method of double exposing the image and the diffraction pattern of a MoO_3 particle. The calibration was performed at 100KV for the conditions listed below:

1. Intermediate lens fine control on '0'--designated "STD."
2. Intermediate lens fine control on 'max,' coarse on 1--designated "IL1."
3. Intermediate lens fine control on 'max,' coarse on 4--designated "IL4."

The rotation angles as a function of SA selector number are tabulated below. For a given magnification, rotate diffraction pattern relative to the image by the indicated number of degrees and in the indicated direction (CW or CCW). Also, whether an additional 180^{o} rotation is required or not (depends on the condition 1, 2 or 3) is indicated at the bottom of the table.

	Rotation Angle, Degrees		
SA Selector #	STD	IL1	IL4
10	25 CW	20 CW	36 CCW
11	100 CCW	105 CCW	19 CW
12	100 ,,	106 ,,	18 ,,
13	98.5 ,,	106.5 ,,	18.5 ,,
14	98.5 ,,	105 ,,	21 ,,
15	96 ,,	101.5 ,,	22 ,,
16	93.5 ,,	99.5 ,,	25 ,,
17	90 ,,	95 ,,	28 ,,
18	87.5 ,,	91 ,,	31.5 ,,
19	82.5 ,,	--	--
20	77.5 ,,	82 ,,	42 ,,
22	--	65.5 ,,	59.5 ,,

	STD and IL1	IL4
SA 1 - 10	180^{o} Inversion	No inversion
SA 11-25	No inversion	180^{o} Inversion

TABLE A-3

Camera Constant* Calibration of Philips EM300

The camera constant was determined using an aluminum diffraction standard for two different settings. The measurements were made for an operating voltage of 100 KV for two positions of the intermediate lens (I.L.) fine control. The diffraction pattern was focussed using the diffraction lens (D.L.) coarse and fine controls.

I.L. Fine control	I.L. coarse control	D.L. coarse control	$_{o}\lambda L$ A-mm	L mm
"0"	---	---	53.7	1452
	1	7	25.54	690
	4	21	23.7	641
"max"	5	18	44.58	1205
	6	17	68.89	1862
	7	16	93.86	2537

* λL

VITA

K. Vasudevan was born in Tamil Nadu, India on March 7, 1956. He attended high school in Bombay, India, and graduated from the Our Lady of Perpetual Succour High School in March 1972. After attending two years of junior college, he entered the Indian Institute of Technology, Kharagpur, India, and received a B.Tech. degree in Metallurgical Engineering in May 1979. In the Winter of 1980, he accepted a research assistantship at the University of Tennessee, Knoxville and began study toward a Master's degree in metallurgical engineering. This degree was awarded in August 1982.

He continued his graduate education toward a Ph.D. at the University of Tennessee, Knoxville. This degree was awarded in June 1986.

The author is a student member of The American Society for Metals, The Metallurgical Society of AIME, and The Materials Research Society. K. Vasudevan will be taking up employment as a Research Associate at the University of Illinois at Urbana-Champaigne after graduation. His ultimate goal is a career in applied research.